Interaction of
Ionising Radiations with Nanoparticles

A Thesis

Submitted for the Degree of

Doctor of Philosophy

In the Faculty of Engineering

By

B H M Darukesha

Department of Instrumentation and Applied Physics

Indian Institute of Science

Bangalore – 560 012, India

July 2023

Declaration

I hereby declare that, the work embodied in this thesis entitled "**Interaction of Ionising Radiations with Nanoparticles**" is entirely original and is the result of investigations carried out by me in the Department of Instrumentation and Applied Physics, Indian Institute of Science, Bangalore, India and U R Rao Satellite Centre, Indian Space Research Organisation under the supervision of Professor K. Rajanna, Professor Abha Misra, Dr. M Ravindra, and Dr. Radhakrishna V

I further declare that this work has not formed the basis for the award of any degree, diploma, fellowship, associateship or similar title of any other university or institution. In keeping with the general practice of reporting scientific observations, due acknowledgement has been made wherever the work described is based on the findings of other investigators. Any omission that might have occurred by oversight or error in judgment is regretted.

July 2023 B H M Darukesha

--submitted online--

Certificate

This is to certify that the thesis entitled "**Interaction of Ionising Radiations with Nanoparticles**" by B H M Darukesha is a record of original bonafide work carried out under my guidance and has not been submitted to any other university or institute.

Prof. K. Rajanna
Instrumentation and Applied Physics
Indian Institute of Science
Bangalore – 560012, India

Prof. Abha Misra
Instrumentation and Applied Physics
Indian Institute of Science
Bangalore – 560012, India

Dr. Radhakrishna V.
U R Rao Satellite Centre
Department of Space, Govt. of India
Bangalore – 560017, India

Dr. M. Ravindra
U R Rao Satellite Centre
Department of Space, Govt. of India
Bangalore – 560017, India

--submitted online--

A special note….

I sincerely express my gratitude to Prof. Manjunath M Nayak at Centre for Nano Science and Engineering (CeNSE), IISc for his help, support and inspiration. He has been my mentor even before I joined IISc as a student. He suggested the area of work and provided constant motivation and guidance.
Thank you Sir.

I also thank Dr. S T Aruna, Scientist at Council of Scientific and Industrial Research – National Aerospace Laboratories (CSIR-NAL), Bengaluru. She generously provided nanoparticles that we needed for the studies and offered several suggestions, tips and cautions that helped the studies.
Thank you Madam.

Acknowledgements

My sincere thanks to

- *Indian Space Research Organisation (ISRO) for the opportunity for higher studies*
- *Dr. Radhakrishna V, for guidance, encouragement, support, unparalleled amount of academic freedom to pursue a variety of scientific ideas*
- *my guides Prof. K. Rajanna, Prof. Abha Misra, Dr. M Ravindra for the guidance and support*

- *Staff at Space Astronomy Group members, at U R Rao Satellite Centre, ISRO Srikar Tadepalli, Koushal Vadodra, Lalitha Abraham, Anurag, Manoj Bug, Manjunath Olekar. I am very grateful to Koushal and Srikar for their kind help to perform experiments and for many discussions and suggestions*
- *members of Sensor Lab and Nano-lab of IAP: Dr. Venki, Dr. Nagarjuna, Dr. Vinay, Dr. Puspita, Dr. Rituparna, Dr. Buddha Boruka.*

- *Dr. M Annadurai then Director of URSC for enabling us to conduct neutron interaction studies at IGCAR, Kalpakkam.*
- *Dr. M T john, Shri Danasekharan, Dr. Venkataraman at IGCAR for providing Am-Be neutron source and Pulse-shape discriminator for the studies.*
- *Shri Varun Kashyap, Noki Technologies, Hyderabad for the access to liquid scintillation counter and technical help*

- *my friend academicians Dr. Thipperudrappa, Dr. Murugesh, Dr. Nagaswarupa, Dr. Prashant for providing various nanoparticles for the study*
- *Micro and Nano Characterization Facility (MNCF), CeNSE, IISc; Dr. Sarat Kumar Dash and Shri Richard Pinto at U R Rao Satellite Centre; Dr. Kennedy at SNN College of Enigneering, Chennai; Dr. Nagabhushan at CNR Rao Centre for Nanosciece and technology. Tumkur University; Centre for Nano and Soft Matter (CeNS) for the characterisation support*

- *colleagues at URSC Shri M P Bhat, Shri Sriram Bhat, Dr. Girish Gowda, Dr. M S Giridhar, Shri Naik, Shri Bhaskar K V, Shri NS Murali, Shri Prashant Bagalakot, Dr. M Aravinda Kumar, Dr. Renji, Dr. R Ranganath, Shri A Rajendra, Shri Abdual Rahman Khan Ashok, M Narayanaswamy, Rashmi, Ankita, Srinivas Bollu, Nagesh and many others for help in various aspects of the study*
- *Shri V Venkatesh, my superior, mentor and a source of inspiration*
- *office staff at IAP Smt. Vijaya, Shri Natrajan, Shri Govinda for the kind help*

- *my father Lingaikya Mahadevaiah, my teacher, a role-model for whom I have dedicated this thesis. my mother Suvarnamma for seeding virtuous goals in life.*

- *my wife Savitha without whose support and toiling I could not have completed this task. I respect her for the unconditional love and care she took of my family during these times.*
- *affectionate daughter Manasapriya for understanding the requirement and supporting me. Special thanks to daughter Akshayamrutha for kindly sparing me.*

I am blessed to have such support from all walks of life.

List of Publications (from the work reported in this thesis)

1. **Darukesha, B. H. M**., Radhakrishna, V. & Rajanna, K. *Direct determination of the outcomes of interaction of X-rays/gamma-rays with nanoparticles*. Nucl. Instruments Methods Phys. Res. Sect. A Accel. Spectrometers, Detect. Assoc. Equip. **1048**, 167922 (2023).
2. **Darukesha, B. H. M**., Radhakrishna, V. & Rajanna, K. *Enhancing the Gamma-Counting Efficiency of a Liquid Scintillation Cocktail by Incorporation of Nanoparticles*. *Radiochemistry* **64**, 393–398 (2022).
3. **Darukesha, B. H. M**., Radhakrishna, V. & Rajanna, K. *Suitability of nanoparticles for gamma-ray applications*. *Appl. Radiat. Isot.* **191**, (2023).

4. **Darukesha, B. H. M**., Radhakrishna, V. & Rajanna, K. Non-emission of photoelectrons from selected nanoparticles (Under review)

Table of Contents

List of figures

List of tables

Abbreviations:

AuNP	:	Gold Nanoparticle
CSDA	:	Continuously Slowing Down Average
CSPA	:	Charge Sensitive Power Amplifier
DI	:	De-Ionised
EDS	:	Energy Dispersive Spectroscopy
HV	:	High Voltage
LLD	:	Low Level Discriminator
LSC	:	Liquid Scintillation Counter
MCA	:	Multi-Channel Analyser
NPRS	:	Nanoparticle Radiosensitization
PHS	:	Pulse Height Spectrum
PMT	:	Photomultiplier Tube
SA	:	Shaper Amplifier
SEM	:	Scanning Electron Microscopy
TEM	:	Transmission Electron Microscopy
UHV	:	Ultra High Vacuum
XPS	:	X-ray Photoelectron Spectroscopy
XRD	:	X-ray Diffraction

Conventions followed:

The conventional unit of radiation energy, eV, is used in the thesis. 1 eV is the kinetic energy an electron gains upon its acceleration through a potential difference of 1 volt [1]. It is equivalent to 1.602×10^{-19} J.

^{241}Am and ^{241}Am(α) indicate gamma and alpha sources, respectively.

The convention followed is PHS *of* (radiation) *with* (the detector).

Liquid scintillators are also referred to as cocktails. These terms are used in the thesis interchangeably.

The nanoparticle-loaded plastic scintillators are referred to as nanocomposites. For instance, Gd_2O_3 nanoparticle-loaded plastic scintillator is a Gd_2O_3 nanocomposite.

Abstract

The interaction of ionizing radiations such as alpha, beta, gamma, and X-rays with *matter-at-bulk* has been studied intensively for many decades. However, the interaction of ionizing radiations with *matter-at-nanoscale* is studied sparsely due to the lack of experimental techniques. Thus, there exists a gap in knowledge. The present thesis contributes to the development of an experimental technique for determining the outcomes of the interaction of given ionizing radiation with given nanoparticles. The technique involves obtaining pulse height spectra of ionizing radiation with a liquid scintillator before and after loading the nanoparticles under identical conditions and observing the variations in spectra to infer the outcomes of the interactions.

The study investigates the outcomes of interactions of gamma-rays, X-rays, beta- and alpha-radiations with about twenty-five types of nanoparticles. It ascertains the effects of the nature and energy of radiations, species, size, and concentration of nanoparticles on the outcome of interactions. It demonstrates that the interaction of ionizing radiations with nanomaterials differs from those with their bulk counterparts. The interaction of low-energy photons (X-rays from ^{55}Fe or a 40 kVp gun or gamma-rays from ^{241}Am or ^{133}Ba) with nanoparticles of Gd_2O_3, HfO_2, and ZrO_2 leads to the emission of numerous electrons from the nanoparticles. However, the nanoparticles of Au, Fe_2O_3, Pd, W, and WO_3 interact with low-energy photons but inhibit the exit of electrons from them. Thus, the interaction of low-energy photons varies with the species of nanoparticles. Further, photons of a given energy range interact with the nanoparticles intensely. These are the two new results from this study. High-energy gamma radiations seldom interact with nanoparticles. The interactions of beta- and alpha-radiations result in the emission of electrons from all species of nanoparticles.

Practical applications like –nanoparticle radiosensitization for cancer treatment; the development of efficient-fast-large-affordable gamma-detectors; and the development of Pb-free, efficient, light-weight gamma-ray shields—rely on the interaction of ionizing radiations with nanoparticles. They either seek or benefit from empirical knowledge of the outcome of interactions. As the lack of mechanistic understanding of nanoparticle radiosensitization has delayed its field implementation, researchers seek the outcomes of 'physical interaction of ionizing radiations with nanomaterials'. Since the process-related challenges have hindered the upscaling of detectors or shields and have kept their studies in exploratory mode, certainty gained on the outcome of interactions offers much-needed directions.

Nanoparticles of Gd_2O_3, HfO_2, and LaF_3 suit as dopants in plastic scintillators for developing efficient-fast-large-affordable gamma detectors. Those of WO_3, Sn, and Fe_2O_3 suit as dopants for developing Pb-free, efficient gamma-ray shields. The results reason why the enhancement of photon detection efficiency of plastic scintillators is repeatedly reported with doping of only selected species of nanoparticles. They reason how nanoparticle-loaded polymers offer impressive shielding efficiencies for diagnostic photons.

1 Chapter 1: Introduction

The radiations capable of removing electrons from atoms or molecules of typical materials are called ionizing radiations [1]. While they enable numerous benefits, they also pose dangers that necessitate adequate shielding. They get emitted from a source and strike or can penetrate the matter on their way [2]. Ionizing radiations examined in this thesis include gamma-rays, X-rays, and beta- and alpha-radiations.

Nanomaterials are a novel class of physical entities being investigated rigorously [3]. They are a collection of few atoms and manifest several unique properties due to their smaller size and large surface-to-volume ratio [4]. Nanomaterials have renewed the interest in most scientific disciplines because they offer novel solutions for several long-standing practical problems like cancer therapy, nuclear non-proliferation, Pb-free shields, and Gamma-ray radioimmunoassay. These applications are detailed in section 1.2.

1.1 A gap in knowledge

The interaction of ionizing radiations with matter-at-bulk has been studied for over a century [1]. Experimental techniques built on physical phenomena like ionization, scintillation, thermoluminescence etc., have enabled these studies. They have enabled us to comprehend both radiation and matter. Ionizing radiations have facilitated practical applications. The knowledge has capacitated the protection from the damaging effects of radiation [1,5]. However, the studies and the knowledge of the interactions of ionizing radiations with nanoparticles have been sparse [6–8]. Experimental techniques to study such interactions are non-existent [7,9,10]. Therefore, there exists a gap in knowledge.

In the absence of empirical evidence, the interactions of ionizing radiations with the nanoparticles are assumed to be analogous to those of ionizing radiations with their bulk counterparts [8,11,12]. It may be reasonable to assume so since the interactions occur at the atomic level. However, the environment within the nanomaterials may differ from that within the bulk. It could dictate and alter the outcome of the interactions.

As discussed in the literature, the bonding configuration in surface atoms differs from that in the atoms of the bulk counterparts [13]. The nanoparticles may interact differently with electromagnetic radiation than their bulk counterparts owing to their smaller size and the larger surface-to-volume ratio [14]. The nanoparticles interact with the surroundings on the chemical level affecting the charge and ion transfer from and onto the surface of the nanoparticle [6]. The behavioral differences between bulk and nanoparticles prescribe that the latter must be treated differently from isolated atoms [7].

Besides, the matter-at-nanoscale exhibits distinct responses when interacting with non-ionizing radiations like visible light [2]. X-rays or gamma-rays interact with matter varying with the energy of the photons [1]. Therefore, scrutinizing such an assumption is imperative.

1.2 Practical applications seeking the empirical knowledge

Three widely pursued applications that rely on the interaction of ionizing radiations with nanoparticles are introduced in the following sections. A fourth application that is enabled using the nanoparticles is introduced and discussed in chapter 5.

1.2.1 Nanoparticle Radiosensitization (NPRS) for cancer treatment

Cancer is a dreaded disease. Currently, radiotherapy – irradiation of the malignant cells or tissues with high-energy X-ray or gamma-ray photons – is the mainstream approach for cancer treatment, used in about 50% of other cases [8,15–19] and up to 80–90% in breast and central nervous system cancers [16,20]. The photons striking the tissues interact with water and biological materials to release electrons into the surroundings leading to the eradication of the cancerous cells [8,9,16,21–23]. However, conventional radiotherapy lacks selectivity and damages co-located tissues. The cells develop radio-immunity, and patients require progressively higher dosages [8,15,16,19,24–28]. Enhancing the efficacy of radiotherapy, by some means, can reduce the dose delivered to the patients[8].

NPRS is an innovative method to enhance the efficacy of radiotherapy. Here, radiotherapy is performed with nanoparticles administered into the malignant tissues. As per the widely pursued hypothesis, the nanoparticles interact more readily with the incoming radiations than the tumor materials and emit photoelectrons or Auger electrons into the tumor to cause chemical and biological effects that eradicate the cancerous cells or inhibit their growth [8,9,17,22–24,28–31], (Figure 1-1). Nanoparticles render themselves as target materials with greater interaction probability than atoms. The smaller size feature of the nanoparticles facilitates their injection/clearance into/outside the tissues and ensures electrons exit from the nanoparticles into the tissues. NPRS is considered a major breakthrough [8,31–33] and is endorsed as “the new dogma” in cancer treatment [34].

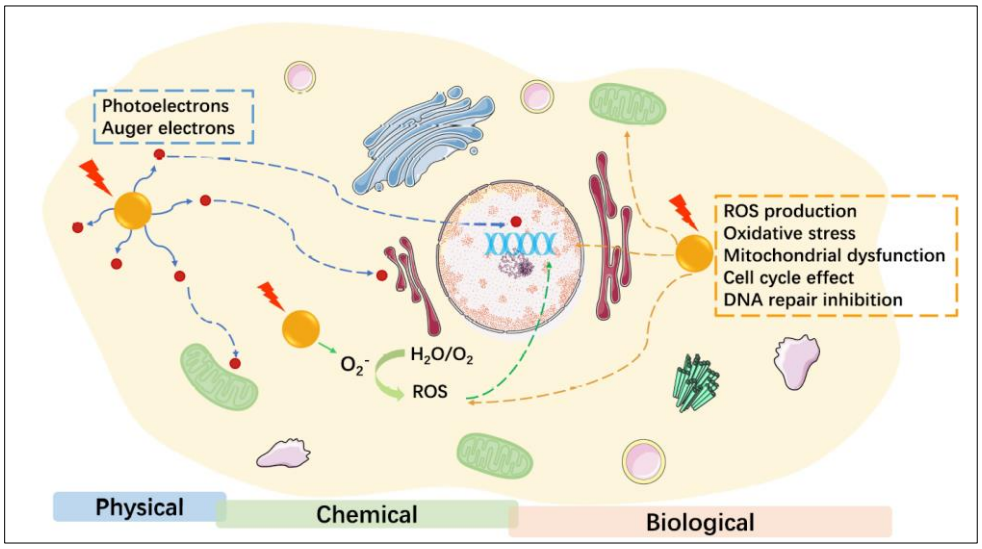

Figure 1-1 Nanoparticle radiosensitization to enhance the efficacy of radiotherapy. Reproduced from[28].

The historical aspects leading to the development of NPRS are reviewed in reference [15]. In the 1970s, the practice of administering the solutions of Au, Fe, and I began with a goal to enhance the contrast in medical imaging[15]. Soon, it became apparent that the presence of these solutions advantageously enhances the efficacy of radiotherapy[15]. In 1980, Matsudaira et al. hypothesized that primarily the photoelectric effect with the atoms of these materials causes the emission of additional electrons into the tissues and thus originates 'radiosensitization'[35]. In the 1990s, as they emerged, the nanoparticles began replacing the contrast agent solutions[15,36,37].

In a seminal work in 2004, Hainfeld et al. increased mice's 'one-year survivability' from 20% to 86% by injecting Au nanoparticles (AuNPs) into cancer-induced mice tissues and irradiating the tissues with 250 kV X-rays[29]. This work generated enormous interest receiving over 1800 citations till now. Since then, numerous studies have established NPRS. They involve various species, sizes, and concentrations of nanoparticles; cancer types and radiations like X-rays, gamma-rays, beta-radiations, etc., conducted in-vitro (cells cultured in Petri dishes) or in-vivo (in cells, primarily rats) or in-silica (simulations)[7,8,16,26]. The logical next step was the clinical implementation of the technique.

However, inconsistent or surprising results started emerging soon[7,9,38]. For instance, while some studies demonstrate radiosensitization with MeV photons[27,37,39–41], some failed to observe radiosensitization with ^{60}Co [35]. Under identical conditions, two similar tissues irradiated with 220 kVp X-rays exhibited different sensitizations (40% versus 75% cell survivals) [33]. While 1 wt.% concentration is predicted to be optimal, the enhancements achieved at even lower loadings are greater by the orders of magnitude [35,38].

As understanding the mechanism(s) responsible for NPRS is a prerequisite for clinical implementation of the technique, researchers vigorously debate the precise mechanism of NPRS [7–10,15–17,19,22,24,26,31,32,37,38,42–47]. Journal articles titled *Actual questions raised by NPRS* [7]. *Radiosensitization by gold nanoparticles: Will they ever make it to the clinic?* [16]. *Radiosensitizing Nanoparticles as Novel Cancer Therapeutics — Pipe Dream or Realistic Prospect?* [42] capture the essence of the debate. Some researchers consider NPRS with MeV impractical [8,9] due to the low probability of interaction of MeV photons with nanoparticles [1]. Researchers propose diverse mechanisms like disrupting biological processes [43], endoplasmic reticulum stress [7], induction of autophagy [44], thioredoxin reductase[26], increasing apoptosis[45], etc., which may originate or contribute to the dose-enhancing effects. Thus, the NPRS studies remain exploratory [7,32,46], and the clinical implementation of NPRS is delayed [7,8,31,47–50], despite the large body of work.

Nevertheless, the researchers are univocal in ascertaining the need for empirical knowledge for the mechanistic understanding of NPRS[6,7,51–53,8,19,22,26,31,46,47,50]. A 2020 article by 39 eminent researchers in NPRS emphasizes the need for mechanistic study more than ever before [8]. The challenge in gaining mechanistic understanding is that the NPRS studies involve multi-process and multi-variable experiments. The efficacy of a combination of ionizing radiation and nanoparticles is determined only at the end of the physical, chemical, and biological -processes

involving variables such as the energy of photons and the extent of loading (Figure 1-1). The degree of complexity is greater than that first thought[7].

The physical interaction of ionizing radiations with nanomaterials forms the first process in NPRS. Though the knowledge of physical interactions may not be sufficient to provide mechanistic understanding, it eliminates the uncertainties till that point. However, the empirical results on the outcome of this step are unavailable due to the lack of experimental techniques to determine them. [7,8,10,54]. The literature states that the "actual distribution of electrons emitted from isolated metal nanoparticles (MNPs) of different sizes, interacting with high-energy ionizing radiation does not exist" [8,55]. It ascertains that a "simple physical interaction between nanoparticle and Radiation" would provide a better insight into the working mechanism of NPRS [7].

1.2.2 Development of efficient, fast, large, and affordable gamma-ray detectors

Efficient-fast-large-affordable gamma-ray detectors are needed in multiple applications. Modern synchrotrons can generate an intense, narrowband beam of radiation pulses ranging from infrared to hard X-rays to ~67 keV at pulse rates as high as 10^{10} photons s^{-1} [56]. The full utilization of their potential gamma detectors that are efficient, fast, large, and economical are needed [57–60]. In addition, highly intense lasers are proposed as the source of X-rays, gamma-rays, and neutrons for various scientific, industrial, and medical applications [61,62]. Efficient and fast detectors facilitate such applications. [63,64] Thirdly, radiation portals established at the ports and national borders for nuclear security and non-proliferation require such detectors for rapid and unambiguous detection of special radionuclides or their offspring [65,66]. Adapting fast detectors in positron-emission tomography (PET) or time-of-flight (ToF) imaging can reduce exposure duration and, consequently, the dose patients receive [66,67]. Efficient and large-area gamma detectors can contribute to space-based X-ray astronomy [67,68].

Inorganic scintillators presently used for X-ray or gamma-ray detection are efficient but slow [1]. Their decay time is long, typically 230 ns [1]. The decay time in inorganic scintillators is constrained by the time required for electron-hole transmission. [1]. Therefore, there is little scope for its improvement [64]**.** Solid-state detectors, another class of detectors used today, are either efficient or fast, depending on the thickness of the active layer [57,58]. For example, the active layer in Silicon Avalanche Photodiodes (Si-APDs) ranges from 10 µm to 150 µm. For faster resolutions of 1 ns and <100 ps, the active thicknesses needs to be 100 µm and <10 µm, respectively[60]. For faster timing resolution, thinner detectors are required. For better efficiency active layer should be thicker. Also, the inorganic scintillators and solid-state detectors can be realized only in small sizes [1,67].

On the other hand, organic scintillators are fast, scalable, and affordable but less efficient [64,69]. Their decay times are short, typically 2-3 ns[1]. They are mainly used as liquid or plastic scintillators. Plastic scintillators as large as meters are realized[12,66]. Organic scintillators owe low gamma detection efficiency to their low-Z constituents C, H, O, and N [1,12,67,70,71]. If only the efficiency of organic scintillators is enhanced, they render themselves desirable detectors [12,67,70].

It was demonstrated in the 1960s that loading high-Z materials into liquid and plastic scintillators enhances the gamma-detection efficiency of the scintillators [72–74]. High-Z materials were loaded through organometallic ligands, where the atoms of high-Z materials get attached to one end of a long chain [74,75]. However, severe deterioration of light yield, limited possible loading, and stability issues limited the success [12,65,67,68,76]. In a new approach that began around 2005, the 'nanoparticles' of high-Z materials are loaded into the plastic scintillators for enhancing the gamma-detection efficiency of the hosts [12,57,58,60,64,65,67,77–79]. The dopant nanoparticles interact with incoming gamma-radiations, presumably emitting electrons into the scintillator to cause additional scintillation and thereby enhancing the gamma-detection efficiency of the hosts [57,79] (Figure 1-2). Nanoparticles offer greater gamma-ray stopping power to the hosts. Further, the smaller size feature of the nanoparticles facilitates the exit of electrons from the nanoparticles and helps maintain the transparency of nanoparticle-loaded scintillators[60,79].

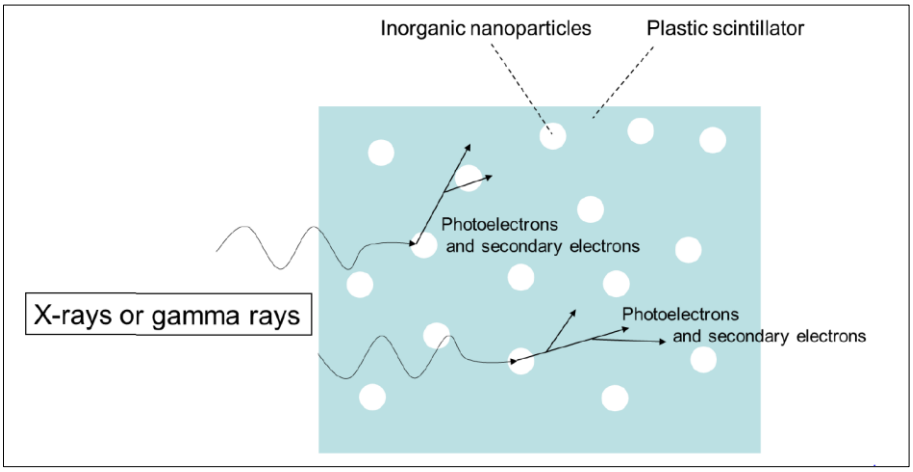

Figure 1-2 Enhancement of scintillation counts inside the plastic scintillators by incorporating nanoparticles. Reproduced from [67].

Studies so far have demonstrated that incorporating Bi_2O_3, Gd_2O_3, HfO_2, $Hf_xSi_{1-x}O_2$, and ZrO_2 nanoparticles enhances the gamma detection efficiency of the host scintillators [57–60,65,77,80–82]. The detection efficiency of the hosts is increased by about 200%[60,70], 640%[83], and 720%[60]. Retention of the fast decay time of nanoparticle-loaded scintillators is confirmed[58,60,66,67,77,84]. In terms of the size of loaded scintillators, the demonstrations have remained on a laboratory scale of about a centimeter in size [65,69,76]. For instance, the detectors developed by Cai et al. have a diameter of 14 mm and a thickness of 3 mm [65] representing the typical sizes. However, practical applications demand detectors of useful sizes, at least a few inches [12].

The realization of large detectors is hindered by process-related challenges, such as the generation of a physical gap of the order of micrometers between the nanoparticle and the host that adversely affects the transmission of electron or scintillation [85], material and optical inhomogeneity, aggregation of nanoparticles [78,86] excessive sedimentation of the nanoparticles inside the scintillators [70], and, thermal instability of nanocomposites [87], loss of transparency[65,87]. The efforts to surmount the process-related challenges are underway[12,66,74]. Researchers prefer that such efforts involve nanoparticles interacting with incoming photons and emitting numerous energetic electrons [58,67]. An experimental technique that determines the

nanoparticles that interact with photons and emit numerous energetic electrons would benefit the researchers to focus their efforts.

1.2.3 Development of Pb-free, efficient, lightweight gamma-ray shields

Ionizing radiations are a boon and bane. Highly energetic ionizing radiations, particularly gamma rays, enable multiple applications encompassing industries, food irradiation, medical diagnostics, nuclear reactors, research facilities, high-energy physics experiments, scientific research, space exploration, and biological investigations [36,88–91]. However, they can potentially harm biological organisms and sensitive microelectronics hardware [92–97]. Prolonged exposure or a higher dose of ionizing radiation causes cancer, cell mutations, organ dysfunction, or even premature mortality [18,89,98]. On the other hand, approximately 0.4% of diagnosed cancers are because of exposure to diagnostic and medical X-rays in humans [99]. Microelectronic hardware suffers upsets, latch-ups, or catastrophic failures upon over-exposure [89]. Thus, shielding proves essential for space applications [95,99,100]. Thus, while ionizing radiations are a necessary evil, efficient shielding of personnel and hardware against harmful radiations is needed to sustain the applications and facilitate the development of even advanced applications[18,99,101–106].

Conventional gamma-ray shields utilize Pb due to its high-Z and higher density that favors the photoelectric interaction mechanism for the greatest attenuation [1,100,107–110]. However, Pb is toxic, heavy, and causes health issues [100,105,111]. Pb is inexpensive, but its recycling is costly [95]. Current-day aprons weigh approximately 4.5 to 5.0 kg and last about ten years with proper care [100,104,112]. Efforts to reduce the weight by embedding the powders of Pb, W, or other materials in conformable polymers yield discouraging results as the composites suffer aging, embrittlement, and cracking of the polymer, drastically curtailing their service life [104].

In an ongoing approach, the nanoparticles of high-Z materials are embedded into conformable polymers (Figure 1-3) to realize Pb-free, efficient, light-weight gamma-ray shields [18,87,95,108,109,113]. The nanoparticles convert the gamma rays into electrons that would be absorbed by the polymer[95,114–116]. The smaller size feature of nanoparticles facilitates their dense packing inside the polymers, which is believed to cause more efficient attenuation of the photons than the powders[100,108,110,117]. Exceptional attenuation of diagnostic photons (versus high-energy photons) enabled by nanoparticles (versus microparticles) demonstrated in several works is motivating further studies[87,91,96,100,102,105,106,109,113,117–123]. Additionally, nanoparticle-loaded shields are economical, easy to process, chemically stable, durable, and radiation tolerant[95,108,124,125].

So far, impressive radiation shielding has been achieved by incorporating nanoparticles of Bi, CuO, Fe_2O_3, Gd_2O_3, HfO_2, Pb, W, Zn, and ZrO_2 into various conformable polymers [71,87,100,104,107–109,114,117,119,126].

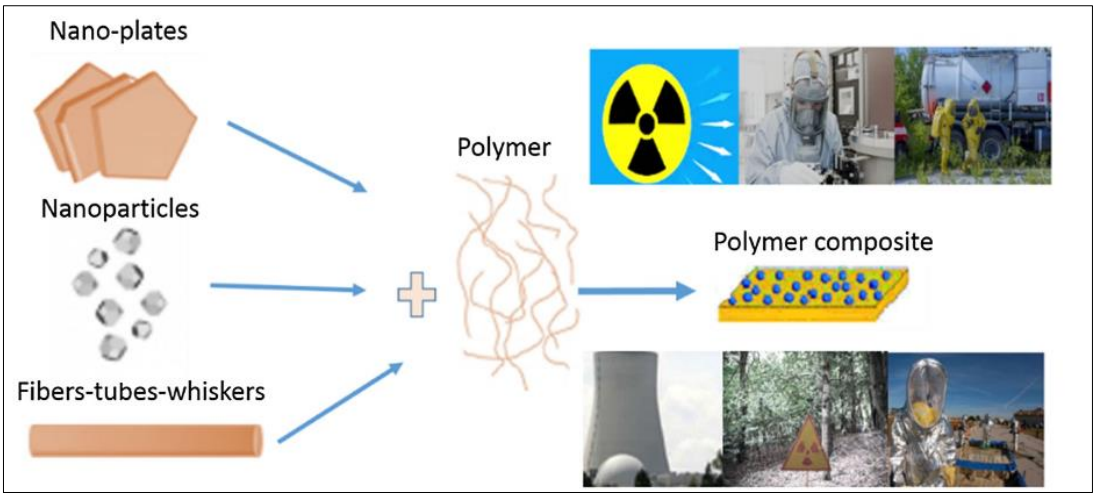

Figure 1-3 Illustration showing the incorporation of nanoparticles into conformable polymers to develop Pb-free, efficient, light-weight gamma-ray shields. Reproduced from [127].

Studies continue to investigate gamma-ray shielding with nanoparticles of various species, synthesis routes, size, loading, and energy of gamma-radiations. Even the particulate size, coating, and concentration also play dependent roles in the preparation of composite [124]. The nanoparticles efficiently converting the gamma-rays into electrons are suitable for regular applications not involving delicate electronics or humans.

In particular applications like space electronics, the shields require nanoparticles that do not emit energetic electrons. Modern space electronics hardware is susceptible to even a single electron fault in binary systems [94], and the emission of the energetic electron would pose health risks to humans[18,92,117]. Additional material to shield them adds to the bulk and costs [100]. There are no techniques to identify nanoparticles that suit better. An experimental technique to determine the energy profile of electrons, at least qualitatively, is necessitated in the first place. Secondly, although laboratory-scale shields are demonstrated[71,87,100,109,117], realizing their scalable versions remains a goal [95,102,107]. The goal can be achieved after overcoming process-related challenges such as restricted loading, embrittlement, tear, crack, split, and mechanical and chemical instability[99,100,104,107]. Test selection of suitable nanoparticles benefits future studies attempting to overcome process-related challenges [107].

As a summary of section 1.2, an experimental technique to determine the outcome of the interaction of ionizing radiations with the nanoparticles, one that enables the study of the effect of species, size of nanoparticles, and the energy of ionizing radiation on the outcomes, would provide crucial inputs and benefit the practical applications.

1.3 Earlier attempts to study the interactions

Earlier, Casta et al. examined specific variations in the number of electrons released from AuNPs, and Au bulk surfaces to complement experimental findings for the modeling studies for NPRS [10,11]. They used X-ray Photoelectron Spectroscopy (XPS) and illuminated the Au targets with ~1.5 keV (Figure 1-4). and ~1.3 keV X-rays in two studies.

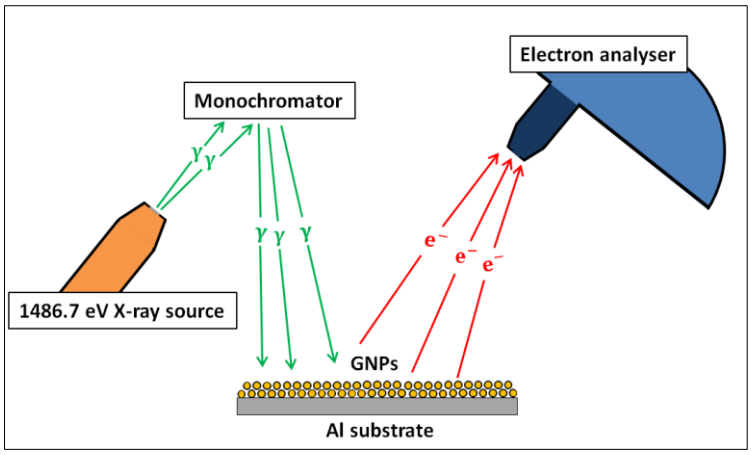

Figure 1-4 Earlier work by Casta et al. AuNPs and Au bulk surface irradiated with ~1.5 keV X-rays. Reproduced from [10]. GNPs stands for gold-nanoparticles.

Contrary to the expectation, they found that the number of electrons emitted by AuNPs was only a small percentage higher than that the bulk Au surface emitted, lower than the expected [10]. They attributed the limited enhancement in the number of electrons emitted from AuNPs to a "nanoscale effect" and asserted that it is intrinsic to AuNPs. These studies identified the behavior difference between a bulk gold surface and AuNPs and concluded that nanoparticles must be treated differently from isolated atoms [7]. Notably, they pointed out the scarcity of empirical results, which was subsequently emphasized by Brun et al. [7,10]. No further studies are reported in this direction [128].

The interactions in materials characterization techniques do not correspond to those in practical applications. Among the current materials characterization techniques, XPS uses about 1.5 keV X-rays, XRD uses about 6 keV, and SEM uses up to about 40 keV. Radiotherapy and NPRS utilize high-energy X-rays from ~40 keV to 6 MeV [7,8] and sometimes even 25 MeV since the photons need to pass through human skin [15,100]. The targeted energy range for efficient and fast detectors is up to about ~64 keV emitted by synchrotrons [80] or gamma-rays of 14 and 60 keV emitted by ^{241}Am, a progeny of a special radioactive source ^{241}Pu or 511 keV photons used in tomographs [66]. Diagnostic X-rays used in radiography that demand novel shields range from 40 kV to 150 kV[99,100,104] or 25 MeV X-rays used in radiology [100]. Since the photon-matter interactions strongly depend on the energy of radiation and materials [1], new techniques than those used for materials characterization are necessitated.

1.3.1 Potential outcomes of interactions

The relevant outcomes of the interaction of ionizing radiation with a nanoparticle include the attenuation of ionizing radiation within the nanoparticle, the emission of electrons and/or photons of different energies from the nanoparticles, and the transmission of radiations through the nanoparticle without interaction [1,99]. The outcomes may vary with the nature and energy of the radiation, species, and size of the nanoparticles [7–9,76,124]. The number and energy profile of the electrons emitted may also vary.

1.4 Motivation, Evolution, Aims, Objectives, & Scope of the thesis

Nanoparticles offer unique advantages over their bulk counterparts, making them valuable for various applications. Their smaller size, large surface-to-volume area, and other distinctive properties enable novel functionalities. Nanoparticle radiosensitization is attempted since the administration of nanoparticles into biological systems and their clearance through renal routes is feasible due to smaller size. Within biological systems, electrons emitted from atoms within nanoparticles have a higher probability of exiting the nanoparticle due to the shorter distance to the particle's edge. This effect is further enhanced by the presence of a larger number of surface atoms in nanoparticles. Moreover, nanoparticles can be easily functionalized to enhance their properties. The introduction of nanoparticles into scintillators will enhance the efficiency of detection thereby offering advantages of different sizes and shape of detectors. The introduction of nanoparticles into polymers enhances attenuation and an optimum loading can match the efficiency of a bulk shield (like lead) but reduced weight.

Along with the nanoparticles' unique properties, this potentially renders them superior to using their bulk counterparts. Further, understanding the behavior and effects of ionizing radiation on nanoparticles leads to newer possibilities for advancements in various fields. This motivated for studying the interaction of ionizing radiations with nanoparticles – in contrast to their bulk counterparts –.

The present thesis work evolved as it progressed. The work began with the goal of realizing efficient, fast, and large gamma-ray detectors for space science applications. To determine the best available nanoparticles for this application, nanoparticles were embedded into conventional plastic scintillators, and their relative gamma-to-electron conversion efficiencies were measured. It yielded an unexpected result that instead of increasing, the WO_3 and PbO nanoparticles decreased the gamma-detection efficiency of the hosts. The literature review indicated that a technique to directly determine the outcome of the interaction of photons with nanoparticles is currently non-existing and also that other applications are seeking empirical knowledge on such interactions. In response, an experimental technique to determine the outcome of the interaction of given ionizing radiation with given nanoparticles was developed, and the validity of the results was established. The outcomes of interactions of gamma-rays, X-rays, beta, and alpha radiations with about 25 types of nanoparticles were investigated. The effects of various parameters were evaluated. The new results were identified. Efforts were made to explain them. The results were compared with those in the literature, and the inputs for practical applications were identified. Using the knowledge gained, a proof-of-concept was demonstrated to enable gamma-ray radioimmunoassay within the conventional liquid scintillation counters.

The aims of the thesis work are outlined here. This dissertation aims to address and fill the gap in knowledge on the outcome of the interaction of given ionizing radiation with given nanoparticles. It seeks to contribute the inputs for the studies related to the practical applications involving the interaction of ionizing radiations with nanoparticles such as NPRS, the development of efficient-fast-large-affordable gamma-ray detectors, and the development

of Pb-free, efficient, light-weight gamma-ray shields. The work intends to determine the outcome of beta and alpha radiations and their utility in addressing potential applications. The work intends to apply the knowledge to resolve other challenges in the field. One such challenge is enhancing the gamma-counting efficiency of cocktails [75,129,130]. The present thesis aims to demonstrate the enhancement by loading nanoparticles into scintillation cocktails.

The thesis targets to fulfill its aims through the following five objectives:

The **first objective** is to evaluate whether the outcome of the interaction of gamma rays varies with the species of nanoparticles. It was necessitated since the nanoparticles of Gd_2O_3, HfO_2, and Bi_2O_3 loaded into a plastic scintillator enhanced the gamma-detection efficiency of the host, but those of WO_3, PbO, under identical conditions, reduced it. It includes an examination of the artifacts, comparing and contrasting them to other reports in the literature, hypothesizing possible explanations, and ascertaining the ways to authenticate the results directly.

The **second objective** is to devise an experimental technique to directly determine the outcome of the interaction of given ionizing radiation with given nanoparticles to validate the results observed with plastic scintillators directly. Further, the technique should facilitate the study of interactions of radiations used in practical applications. It should determine the effect of species, size, and concentration of nanoparticles and the nature and energy of the ionizing radiations.

The **third objective** is to acquire empirical knowledge on the interaction of given ionizing radiations with given nanoparticles using the technique developed. This objective examines the effects of species, size, and concentration of nanoparticles and the nature and energy of the ionizing radiations on the outcome of interactions. It also includes identifying new results and offering pointers for their explanation.

The **fourth objective** is to analyze the outcomes of the study in contrast and comparison to the existing results in the literature obtained. It also includes the identification of the inputs from the present work for the studies concerning basic knowledge and practical applications involving the interaction of ionizing radiations with nanoparticles.

The **fifth objective** entails utilizing the knowledge obtained to demonstrate proof-of-principle for achieving gamma-ray radioimmunoassay within the standard LSCs, an enduring goal in the field. This objective covers enhancing the gamma-counting efficiency of a conventional cocktail by loading nanoparticles into it.

In the scope of thesis work, nanoparticles are treated here as a collection of atoms or molecules. They are considered physical entities. Only spherical nanoparticles are studied. The outcomes considered include electron emission from nanoparticles, the transmission of radiations without interaction, and attenuation of the radiations within nanoparticles. Other outcomes like radioluminescence and thermal dissipation are not considered. Practical applications relying on the emission of electrons from the nanoparticles and attenuation of radiations within the

nanoparticles are considered. Pointers to explain the new results are proposed for additional basic studies.

The scope of this work excludes the incorporation of nanoscintillators or luminescent quantum-dots or high-bandgap nanomaterials into transparent polymers to develop fast, efficient, large gamma-ray detectors pursued by researchers [12,64,65,74]. Here, the nanoparticles convert the radiations into electrons or effectively absorb the radiations with themselves. Among the radiation shields, since the development of wearable shields overwhelmingly dominates other applications, only that is considered. The discussion, however, applies to developing gamma-shielding glass or concrete. Overcoming process-related challenges constraining the application implementation, such as restricted loading, embrittlement, tear, crack, split, and mechanical and chemical instability, are not addressed in the thesis. Instead, the thesis work helps identify better-suited nanoparticles for the applications and the forthcoming studies to overcome such challenges better use the selected nanoparticles. The work is a qualitative and comparative study. The measurement of absolute efficiencies or the numerical analysis for the precision of the spectra has not been part of the present work.

1.5 Outline of the thesis

A brief outline of the thesis is given below:

Chapter 2 provides a pertinent theoretical context for the thesis work. The fundamental aspects of ionizing radiations and the interaction mechanisms of ionizing radiations with matter are described. The types, principles, features, advantages, and shortcomings of current techniques determining the outcome of the interaction of ionizing radiations with matter-at-bulk are briefed. Relevant properties of the nanomaterials are presented.

Chapter 3 presents the study conducted to determine better-suited nanoparticles as dopants in plastic scintillators to realize efficient, fast gamma-scintillators. As the study yielded an unexpected result, an investigation and analysis were conducted to establish that the result was genuine. This chapter presents the same. It reveals a new result that not all the species of nanoparticles enhance the gamma-detection efficiency of the plastic scintillator. This study warranted the development of a new technique presented in the next chapter. The first objective of the thesis is addressed in this chapter.

Chapter 4 presents the technique being contributed for determining the outcome of the interaction of given ionizing radiation with given nanoparticles. It presents the first empirical results on the outcome of gamma-rays, X-rays, and beta- and alpha-radiations with nanoparticles. The effects of nature and energy of the ionizing radiations and species, size, and concentration of the nanoparticles are provided. This chapter discusses the features, strengths, and limitations of the technique; compares the results with those in the literature; offers inputs for practical applications and basic knowledge concerning the interaction of ionizing radiations with nanoparticles; and mentions the pointers for further basic studies to explain the new results obtained in the study. This chapter addresses the second, third, and fourth objectives of the thesis.

Chapter 5 presents a work that applies the knowledge gained in chapter 4 to overcome an enduring radiation physics challenge. The gamma-counting efficiency of a liquid scintillator is enhanced by loading Gd_2O_3 nanoparticles into the scintillator as a proof-of-principle for enabling the gamma-ray radioimmunoassay within the standard LSCs. The fifth objective of the thesis is addressed in this chapter.

Chapter 6 provides a summary of the thesis. It presents an account of how the aim and objectives of the thesis are accomplished and outlines the scope for future work.

Appendix-I presents a brief study conducted on the interaction of neutrons with nanoparticles. This work could not be continued within the time-frame due to limited access gained to the neutron source. Appendix-II proves that the nanoparticles respond more distinctly than the nanofilms conducted in the beginning.

2 Chapter 2: Theoretical background

This chapter provides a pertinent theoretical context for the thesis work. The fundamental aspects of ionizing radiations and the interaction mechanisms of ionizing radiations with matter are described. The types, principles, features, advantages, and shortcomings of current techniques determining the outcome of the interaction of ionizing radiations with matter-at-bulk are briefed. Relevant properties of the nanomaterials are presented.

2.1 Introduction: Ionising radiation

Radiations are energy in transit. They originate from radionuclide materials, X-ray guns, or particle accelerators and travel until they are absorbed by the medium (matter). Their energy is transformed into secondary radiations, light, heat, etc. [89]. They are broadly classified, as shown in Figure 2-1.

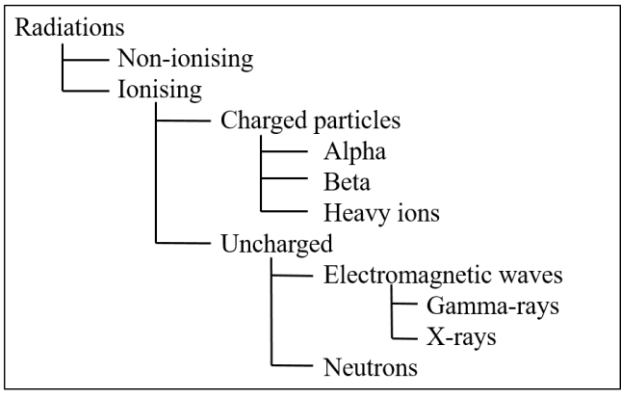

Figure 2-1 Broad classification of radiations.

The radiations capable of ionizing the medium are termed 'ionizing' [1]. They include gamma-rays, X-rays, beta, alpha, neutrons, fission fragments, etc. Ionizing radiations occur naturally or are created artificially -intentionally or otherwise [1,131]. At least 60 natural sources of ionizing radiations exist in air, water, or soil in the form of isotopes [91]. The abundance of radiation varies with place and time.

Each variety of ionizing radiation is specified by its charge, mass, and energy [1]. Alpha radiations are identical to helium nuclei, possessing mass and positive charge. They are emitted from natural radioactive sources, usually by heavy elements like U, Th, Ra, etc. Alpha particles possess energy in the range of 4 MeV to 9 MeV [131]. All natural sources of alpha radiations invariably emit gamma-rays [1]. Alpha particles are artificially produced by extracting electrons from helium atoms in a vacuum environment.

Beta-radiations are equivalent to electrons in mass and charge. They emerge from the nucleus when a neutron decays into a proton and an electron [131]. They can be generated by accelerating the low-energy electrons in a vacuum called fast electrons. Once in the medium, differentiating a beta-radiation from a fast-electron is impossible. The beta radiation spectrum is continuous, spanning the energy to a maximum [1,132]. The end-point energies for different sources vary from

18.6 keV of ^{3}H to several MeV of other sources [1,5,133]. Each spectrum has average energy, roughly one-third of the end-point energy [131].

Gamma rays are electromagnetic waves of exceptionally high frequency. They possess neither charge nor mass. They are emitted naturally from the nuclei of radioactive elements or generated through the annihilation of positrons and electrons [1,101]. Their energies range from tens of keV to tens of MeV [1,5,133].

X-rays are electromagnetic waves of very high frequency. They are produced by bombarding high-Z material targets with energetic electrons or by accelerating or decelerating charged particles in an electric field of a nucleus [1,5]. Their origin involves the rearrangement of electron shells of atoms or the transitions within the nucleus. Advanced synchrotrons and accelerators produce X-rays with extremely high energies, as high as 18 MeV[95]. In terms of generating an intense, narrowband beam of radiation pulses, they generate from infrared to hard X-rays up to 67 keV at pulse rates as high as 10^{10} photons per second [56]. A radioactive source ^{55}Fe emits X-rays with principal energies of 5.8 keV and 6.5 keV. On the other hand, X-rays from a gun are a continuum with a set peak energy but having weighted-average energy much lesser than the peak energy. A gun with 40 kVp emits X-rays from 0 to 40 keV with a weighted average of approximately 10 keV.

2.2 The interaction of ionizing radiations with matter-at-bulk

2.2.1 The interaction of charged species radiations

Alpha and beta-radiations are the charged species radiations studied in the present work. They interact mainly through the coulomb force between them and the orbital electrons of the absorber atoms or rarely with the nuclei [1]. The interaction commences right at the point of contact and persists throughout. The target material absorbs the radiation energy within a small thickness, close to the point of interaction. Energy is transferred through collision and radiation, with over-domination of the former. Collisional loss results in ionization, excitation, and molecular damage [134].

When alpha or energetic beta radiation strikes a solid surface, either from inside or outside, a few electrons that gain enough energy get released from the atom and migrate to the surface, resulting in their eventual emission. These electrons are called *secondary electrons.* Secondary electrons possess all possible energies, but their mean energy is comparatively much lower than that of the incident particle [1]. The interactions with materials exhibiting low work function (the minimal energy required to remove an electron from the surface of a specific solid to infinity) or substantial escape distances will result in a large yield of secondary electrons [1]. Secondary electrons interact with matter like the primary ones of corresponding energy.

Acceleration or deceleration of charged particles in the electric field of a nucleus emanates a portion of radiation as a photon [5]. The phenomenon is termed *bremsstrahlung.* The interaction of bremsstrahlung-generated photons with matter would be similar to that of X-rays.

2.2.1.1 *Interaction of alpha radiations*

Alpha radiations striking a material attract many nearby electrons. They drag many electrons along the trajectory, leading to energy loss through multiple simultaneous collisions. Each collision reduces the energy of alpha radiation by typically < 100 eV [1]. Alpha radiations ionize heavily due to heavy mass and charge. Thus, they are easily absorbed, confining the interaction mainly to the surface [1,135,136]. The alpha radiations of given energy penetrate a fixed depth in a given material [131]. They typically produce ten or fewer secondaries per particle.

2.2.1.2 *Interaction of beta radiations*

Beta radiations impinging a material surface generate an electrostatic repulsive force between themselves and the orbital electrons of the material atoms. This force slows down the radiation. The interaction of low-energy beta radiations is similar in trend to that of alpha radiations. Nevertheless, due to their 7000-fold smaller mass and 2-fold lower charge, beta radiation penetrates a substance more deeply than alpha radiation. [135]. A similar mass between a fast electron and an orbital electron causes the radiation to deflect continuously as it moves through the material. A small thickness of matter can attenuate beta-radiations. The thickness of the target material that absorbs a beta-radiation or fast-electron thoroughly is characterized as continuously slowing down the approximation (CSDA) range in that material [137]. Typical interactions of beta-radiations with matter are shown in Figure 2-2.

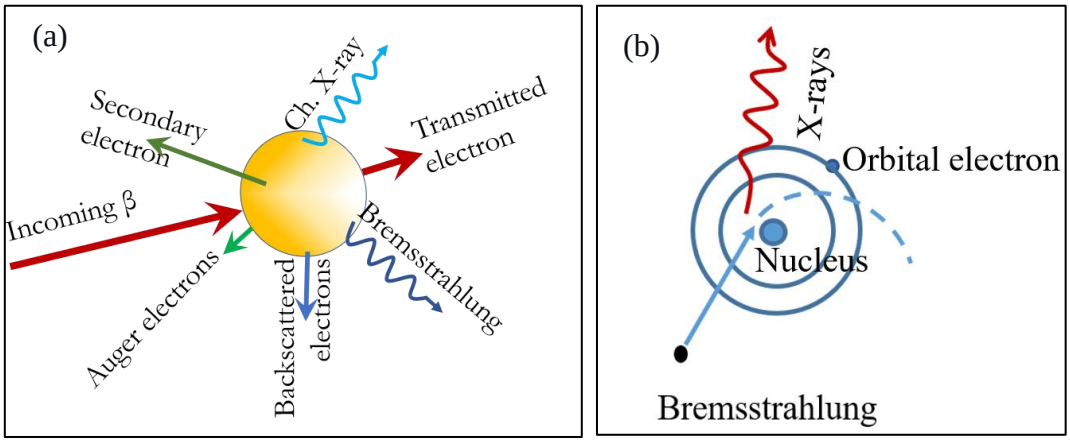

Figure 2-2 (a) Prominent outcomes of beta-radiation interaction with the matter (b) Bremsstrahlung

The interaction of beta radiations produces secondary electrons [1]. Numerous electrons backscatter from matter located in proximity to the point of interaction after deflecting by about 180°. Backscattering is more probable when low-energy betas strike high-Z material targets [1]. Energetic beta radiation often interacts with K-orbital electrons and causes the ejection of an orbital electron. Filling the gap by L, M, N, etc., orbital electron most likely follows the production of a K_α characteristic X-ray [68]. Auger electrons emanate in a competing process to produce X-rays [1]. The energy of Auger electrons is a characteristic of the target material. Bremsstrahlung occurs along the trajectory and bears a continuum [1]. The material absorbs low-energy bremsstrahlung to produce new fast-electrons. Highly energetic beta-radiations get transmitted through the whole thickness of the matter after losing their partial energy. The

electrons emitted into the surrounding from the entry and exit of the nanoparticle get detected in the system.

2.2.2 Interaction of uncharged species radiations

Gamma-rays, X-rays, and neutrons constitute uncharged species of ionizing radiations. Their interaction with matter is probabilistic and independent of history. These features are marked differences in their interaction from that of the charged species radiations.

2.2.2.1 *Interaction of X-rays or Gamma-rays (Photons)*

A photon striking an atom may get scattered, absorbed, or transmitted without any interaction. When interaction occurs, it occurs with a whole atom or an orbital electron [1]. It follows one of the three primary mechanisms: Photoelectric effect, Compton Scattering, and Pair-production, depending on the energy of the photon, Z, and density of the target material [1]. The schematic representation of the mechanisms is given in Figure 2-3.

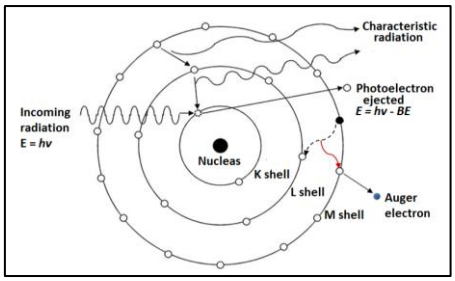

Photoelectric effect

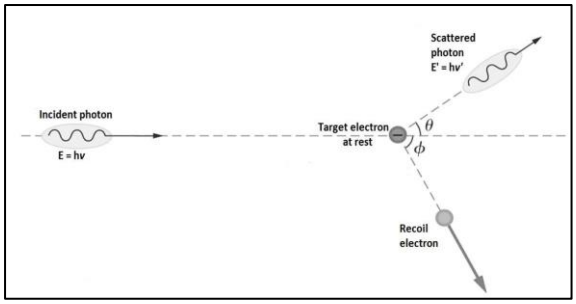

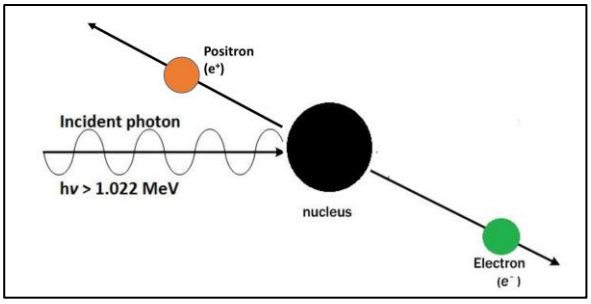

Compton scattering Pair Production

Figure 2-3 Prominent mechanisms of interaction of gamma-rays or X-rays with matter.

Photoelectric effect

In this process, the photon interacts with an atom [1,5]. The entire electron cloud participates in the process rather than an individual corpuscular electron [5]. The atom ejects an electron called a photoelectron from one of its bound shells. As it requires the presence of an atomic nucleus to satisfy the conservation of momentum, it occurs only with the bound electrons [9] rather than with a free electron. The probability of photoelectric absorption is greater for more tightly bound electrons, such as K-shell electrons, than for other orbital electrons. Over 80% of the photoelectric absorption involves the ejection of K-shell electrons when incoming photon energy is greater than K-shell energy [5]. All the energy of the incoming photon minus the binding energy is transferred to the photoelectron.

Estimating the probability of the photoelectric effect usually utilizes empirical formulae due to challenges involved in theoretical calculations [5]. The photoelectric effect varies roughly as $(Z/E)^3$, where Z is the atomic number of the target material, and E is the incident photon energy. This Z dependency arises due to the electron density in the valence shell. The photoelectric effect is prevalent when photons < 500 keV interact with materials of high atomic number [5] [15,138].

The photoelectric interaction results in the ionization of a target atom, creating a vacancy within its bound shells [1]. A characteristic X-ray emerges when an electron from the outer shell fills the gap in K-shell [1]. The vacancy in the outer shell is immediately filled by capturing a free electron from the target material and/or rearrangement of electrons among other atom shells. Thus, more characteristic X-rays may get emitted. An Auger electron may be emitted as an alternative consequence of the characteristic X-ray emission, which occurs when an electron from an outer shell fills the vacancy created at either step. All photoelectrons, X-ray, or Auger electrons continue interacting with material according to their characteristics.

Compton scattering

In Compton scattering, the incident photon interacts with an electron bound to the atom (not the free electron). It transfers part of its radiation energy to the electron (initially supposed to be at rest) (Figure 2-3)[1]. The electron receiving the energy is called a *recoil electron.*

Arthur Holly Compton provided a theoretical framework for this interaction. The recoil electron energy ($E\gamma$) and scattering angle of the photon (θ) are related as

$$E_\gamma = \frac{E_{\gamma 0}}{1 + \frac{E_{\gamma 0}}{m_0 c^2\ (1 - \cos\theta)}}$$

where m_0c^2 is the rest-mass energy of an electron (0.511 MeV), and $E\gamma_0$ is the energy of the incident photon. Thus, the energy distribution in Compton scattering is determined only by the scattering angle of photon [1]. Since all scattering angles are possible, the energy shared with the recoil electron varies from zero to the incident photon energy. The incident energy is transferred when the scattering angle is 180°. The incident photon can undergo multiple interactions and finally be absorbed entirely. The Compton scattering per atom of the target material varies with the number of electrons present as scattering targets and thus increases proportionately with Z.

Pair production

In pair production, a high-energy incident photon is annihilated, and in its place, two oppositely charged particles (positron and electron) get emitted and traverse in orthogonal directions (Figure 2-3) [1]. This interaction can occur only in the electrostatic field generated by a nucleus. Pair production is possible when the photon energy exceeds 1.02 MeV, which is double the rest-mass energy of an electron. The probability of pair production is very low until the photon energy reaches several MeV, and thus it is mainly limited to high-energy photons [1]. All the

energy the photon carries over 1.02 MeV is transferred as kinetic energy shared by each charged particle. A simple equation cannot indicate the probability of this interaction per nucleus; however, it can be approximated as being proportional to the square of the atomic number (Z) of the target material[1].

Figure 2-4 presents the relative probabilities of occurrence of the photoelectric effect, Compton scattering, and pair-production as a function of Z of the target material and photon energy. Areas indicate the dominance of a given mechanism. The lines intersecting the areas present where the probability of occurrence of two mechanisms intersected is equally probable.

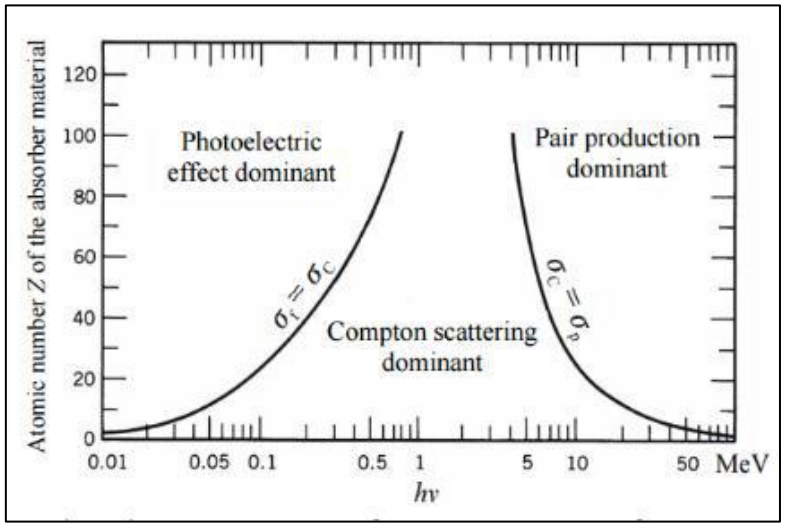

Figure 2-4 Probabilities for mechanisms of interaction of photons with matter. Reproduced from [139]

Thus, interactions of gamma-rays and X-rays mainly manifested in the emission of scattered X-rays/photons, photoelectrons, Compton electrons, Auger electrons, and characteristic photons [24]. The product photons again interact with matter, and the ultimate products are fast-electrons. Photon detectors are devised to promote material interactions and to detect the secondaries so that their total energy forms the output signal [1].

2.3 Radiation detection: principles and instruments

Ionizing radiations can be detected through the effects they cause upon interacting with matter [140]. Such effects include thermoluminescence, ionization, emulsion tracks, scintillation, Cherenkov radiation, artificial radioactivity, and thermal dissipation. Every kind of radiation detector exploits a specific effect to produce a discernable signal in the measurement system [5]. Radiation detection ranges from simple detection of the presence of radiation or quantifying the radiation to determining the radiation energy, type, or location [69]. While detectors offer an understanding of the radiations, the knowledge thus gained enables the development of better detectors. Thus, both the detectors and detection methods undergo development and investigation [5]. Figure *2-5* illustrates the various types of radiation detectors commonly employed. The following section outlines the fundamental concepts associated with these detectors.

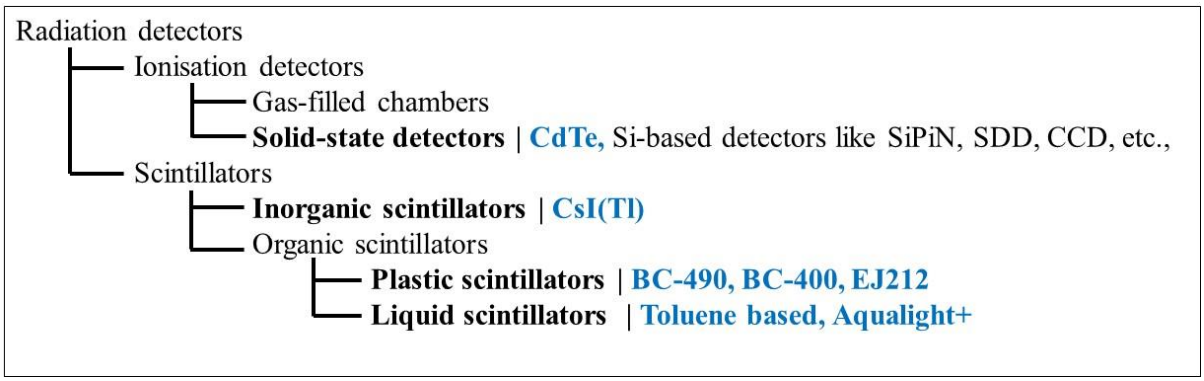

Figure 2-5 Types of popular radiation detectors. Highlighted ones are used in this work. SiPiN is Silicon-PIN diode, SDD is Silicon Drift Detector, CCD is Charge Coupled Device

2.3.1 Ionization detectors

Ionization detectors are gas-filled chambers. They present easily ionizable materials to incoming radiations and detect the electrons from the interactions (Figure 2-6).

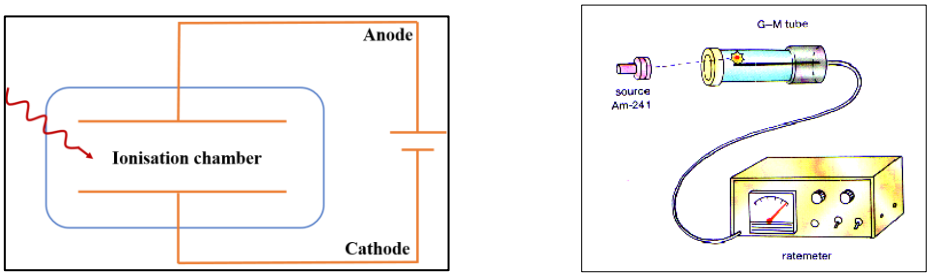

Figure 2-6 Ionization chamber type detector.

In its basic form, an ionization detector is a metallic cylinder filled with a gas (like air or argon) at a specific pressure. Radiations interact and ionize the matter leading to the generation of electrons and ions in the medium. The cylindrical surface and the metallic wire drawn in the center of the cylinder along the axis are connected to negative and positive terminals of a voltage supply, respectively. The wire is connected through a load resistance. The electrons generated experience the electric field and get accelerated towards the wire. The flow of electrons in the wire constitutes a current pulse that gets detected as a potential drop across load resistance. The strength of the pulse measures the quantum of radiation deposited in the medium.

2.3.2 Solid-state detectors

Solid-state detectors offer semiconductor material to the incoming radiations. Essentially, these detectors are p-n junction diodes operated in reverse bias[1]. The incoming photon interacts with the semiconductor material and generates electron-hole pairs (Figure 2-7). The electrons are accelerated to constitute an electrical signal. Since the active region for radiation detection remains free of charge carriers, current flowing is exclusive to that created by the interaction of radiation. The amplitude of the current pulse is proportional to the energy of incident radiation.

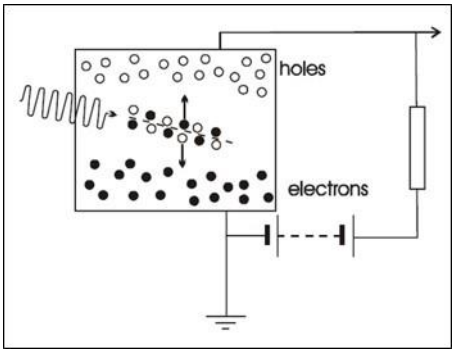

Figure 2-7 Principle of solid-state detectors

Solid-state detectors offer the best possible low energy detection threshold and energy resolution. The number of electron-hole pairs created for given radiation is the greatest since the energy necessary for creating an electron-hole pair is as low as 3 eV[1]. The corresponding energy in the gas ionization chamber is ~35 eV. However, solid-state detectors are either efficient or fast, depending on the thickness of the depletion layer [57,59].

2.3.3 Scintillation detectors

Scintillation is a short-lived flash of light [131]. Scintillation occurs when radiations excite certain substances called scintillators. Substances that scintillate efficiently in UV or visible range are used widely. A scintillation detector offers suitable material for incoming radiation, converts a fraction of radiation energy into detectable light photons, and turns light photons into an electrical signal [5]. Scintillators are characterized by several parameters, including stopping power, photoelectric generation, proportionality, transparency, decay time, light yield, emission wavelength, stability, and physical form. No scintillator meets all features` [1,141]. The selection of a scintillator always depends on the practical application. Based on their composition, there are two types of scintillators: inorganic and organic. *The present work employs organic scintillation detectors extensively.*

2.3.3.1 *Inorganic scintillators*

These were the first scintillators identified. ZnS plates served as scintillation detectors in the discovery of X-rays by Roentgen. Rutherford and his students used ZnS extensively. They counted the number of scintillations manually using a spinthariscope (Figure 2-8). Robert Hofstadter, in 1948, discovered the scintillation response in thallium-doped sodium iodide crystal NaI(Tl). This discovery enabled the spectroscopic detection of gamma photons by compact detectors s[1].

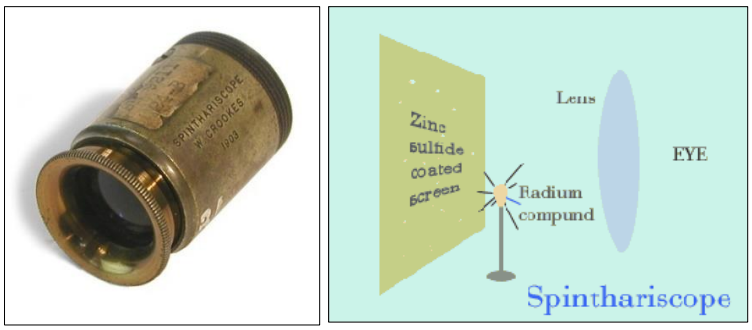

Figure 2-8 Spinthariscope, used by Rutherford and his students.

Inorganic scintillators necessitate a regular crystalline lattice for operation. Though single crystal scintillators exist, most inorganic scintillators use crystals like NaI doped with luminescent center-forming materials like Tl. The mechanism of scintillation in inorganic scintillators is sketched in Figure 2-9.

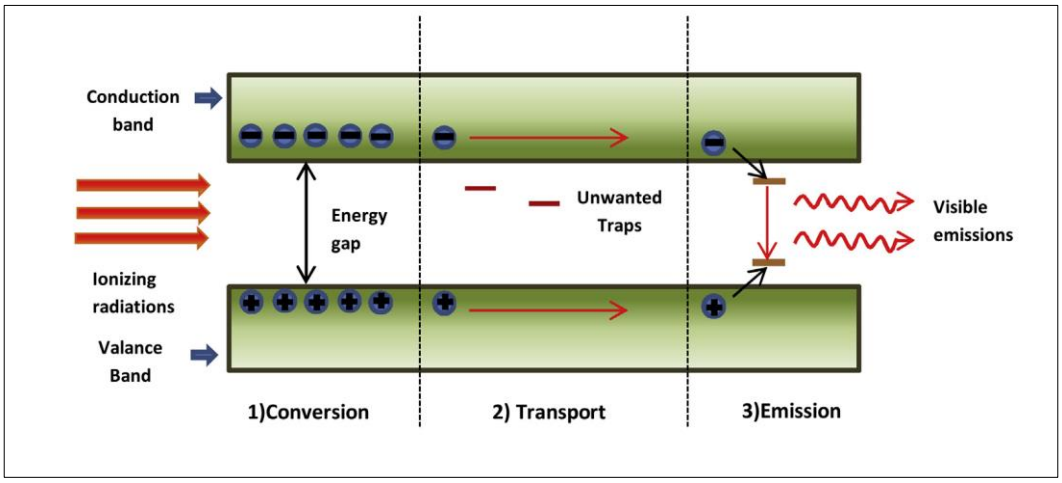

Figure 2-9 Mechanism of scintillation in inorganic materials. Reproduced from [142]

When ionizing radiation interacts with the lattice of scintillator material, it generates multiple electrons. Each electron generates a hole. An electron receiving energy less than the ionization threshold stays at the bottom of the conduction band, and the corresponding hole stays at the top of the valence band. The electron-hole pair, called an exciton, migrates through the lattice and recombines at another point radiatively, leading to a scintillation pulse.

Inorganic scintillators offer high light yield and, thus, better energy resolution [1]. However, they are inadequate for applications requiring fast detection due to their long decay time. Some inorganic crystals are hygroscopic and need special environmental protection, resulting in greater operational costs. Despite these limitations, they are the first choice as detectors in medical diagnostics or radiography, medical imaging, dosimetry, radiation portals, and high-energy physics experiments [143], for the lack of fast and efficient detectors.

2.3.3.2 *Organic scintillators*

Organic scintillators are composed of C, H, N, and O. They can scintillate with a single molecule for scintillation as the phenomenon occurs from electronic transitions within a single molecule. Thus scintillation in organics is independent of their physical state [1]. Pure organic scintillation crystals like anthracene exist. However, they are generally not used in practice since their scintillation efficiency is anisotropic, they lack mechanical integrity, and they are available in small volumes [144]. Practical organic scintillators typically contain a solvent organic material that exhibits a π-electronic structure into which efficient scintillators and wavelength shifters are dissolved. Selected organic materials like benzene and toluene offer the π-electronic structure. Nominally, the solvent absorbs radiation energy and shares it with the scintillator. The scintillator converts the energy into light. The scintillation occurs typically around 300 nm. The wavelength shifter absorbs it and re-emits in a higher wavelength overlapping with

the maximum sensitivity of the light-sensitive device like PMTs. The detailed mechanism of scintillation in organic scintillators is sketched in Figure 2-10.

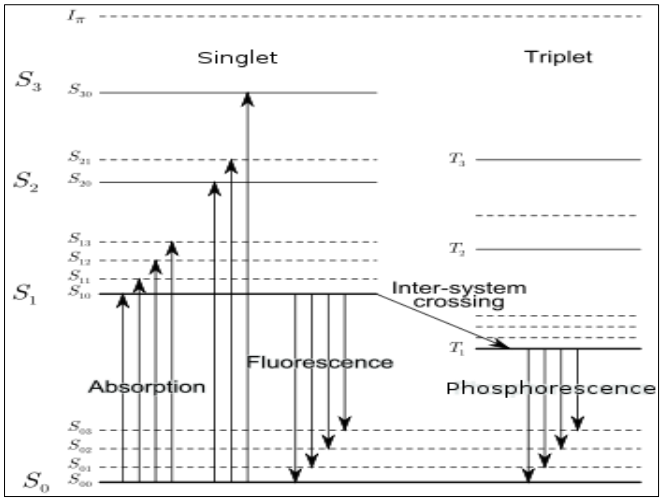

Figure 2-10 Mechanism of scintillation in organic materials. Reproduced from [1].

In Figure 2-10, *So, S1, S2, . . .* represent the series of singlet states (spin 0) and *T1, T2, T3,* the triplet (spin 1) electronic states. The energy spacing between S_o and S_1 is typically about 3 or 4 eV. That between higher-lying states is usually smaller[1]. Each of these singlet and triplet electronic configurations possesses various vibrational states that are represented by subdivided levels. The second subscript denotes the vibrational states. Thus, the second vibrational state of the first electronically-excited state is designated by S12. The spacing between the vibrational states is large relative to the average thermal energies, typically 0.025 eV. Hence, nearly all molecules stay in the S_{oo} state at room temperature.

When ionizing radiations interact with a scintillator, radiations deposit specific energy in a molecule. Excited (not ionized) molecules exchange energy amongst themselves and with a fluorophore or wavelength shifter. This excitation elevates the electrons to any of the excited states. Upward pointing arrows denote this phenomenon. As estimated, ~10% of the energy is transferred to excited singlet and triplet molecular states [145]. Singlets de-excite within picoseconds radiatively to their ground state S_1. Triplets lose their energy non-radiatively through internal conversion. Molecules excited to a state with excess vibrational energy (like S_{11} or S_{12}) quickly lose vibrational energy, unable to maintain thermal equilibrium with their neighbors. Thus, the absorption of radiation energy eventually leads to a state where more molecules stay in an excited state S_{10}. Scintillation occurs when molecules transit from S_{10} to one of the vibrational states of the ground electronic state. The photons emitted from the excited flour molecules in an event constitute the scintillation. The processes continue until the radiation energy is transformed into light, trapped by a solute, or dissipated as thermal energy.

Organic scintillators are solid crystalline, amorphous solids (plastic), and liquid scintillators. Plastic scintillators are a mare solid solution version of their liquid counterparts [76].

Crystalline solid scintillators:
Anthracene and stilbene are examples of crystalline solid organic scintillators. They are pure organic crystals. Anthracene exhibits the greatest scintillation efficiency that benchmarks the efficiencies of other organic scintillators.

Plastic scintillators:
Plastic scintillators are amorphous solid organic scintillators. The solvents are aromatic groups (usually benzene or toluene rings) or their derivatives. Polyvenyltoluene is a popular solvent. Plastic scintillators are the only viable choice for large-area detection (several m^2) with a spatial resolution [69]. They display better radiation tolerance compared to crystal scintillators. This study employed plastic scintillator EJ212 sourced from Eljen Technologies. It used a semi-polymerized Saint-Gobain's BC-490 resin to realize unloaded and nanoparticle-loaded plastic scintillators.

Liquid scintillators:
A liquid scintillator has a homogenous mixture of aromatic rings as solvents into which a primary scintillator and wavelength shifter are dissolved. *The present thesis work utilizes liquid scintillators extensively.*

2.3.3.3 ***Liquid scintillation counting technique***
Using liquid scintillators as a radiation counting technique is long-established and well-researched. Hartmut Kallmann discovered UV-induced and radiation-induced scintillation in certain organic materials in 1937 and around the mid-1940s [146]. Two original independent papers appearing in the same issue of a journal in 1950 by Kallmann and Reynolds established the LSC as an instrument for quantitative radioactivity analysis [132]. LSCs contain a vial with PMT placed adjacent to it (Figure 2-11). The sample under test is mixed with the liquid scintillator and poured into the vial. Radiations emitted from the sample into the liquid generate the scintillation to be counted by the PMT.

Liquid scintillators became standard for detecting and quantitatively measuring radioactivity, particularly from low-energy beta-radiations. The 4π geometry of the liquid scintillators enables high detection efficiency (~100%) for beta-radiations. By innovative use of liquid scintillation counting, Rosalyn Yalow developed a radioimmunoassay technique for which she received the 1977 Nobel Prize in Physiology or Medicine. LSCs are continued being used for biological radio-assays and high-energy physics experiments [67] due to the absence of afterglow [63] and a high degree of automation [75].

Packard Instruments commercialized LSCs in 1953. Since then, many companies have offered them with rigorous data-processing tools [145]. LSCs became useful in physical and chemical sciences ranging from low-level activities in environmental monitoring to higher-level activities in nuclear plants [132]. They remained the only practical approach to counting low-energy beta emissions for a long time [147], until the emergence of mass spectrographs[148].

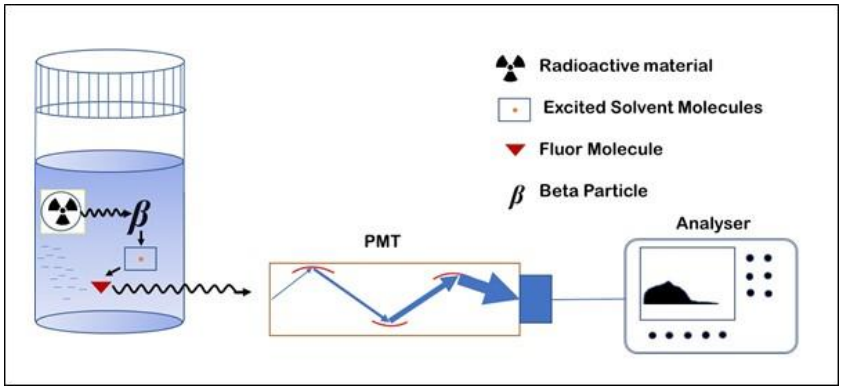

Figure 2-11 Principle of liquid scintillation counting.

Two phenomena in the liquid scintillation counting technique relevant to the study are quenching and loss of transparency. Any physical or chemical process reduces the light yield (ratio of the number of scintillation photons to the energy deposited) of the scintillator, classified as the photon, chemical, and optical [132,149]. Photon quenching occurs when a material other than the solvent unduly absorbs the radiation energy. In chemical quenching, the excitation energy is transferred to a material other than fluorescent or solvent. Optical quenching (color quenching) occurs when any colored substance in the scintillator absorbs the scintillation photons.

2.3.4 Instrumentation for organic scintillation detectors

This section presents the principles and the instrumentation leading to generating a pulse height spectrum (PHS) with a liquid scintillator. A typical configuration for pulse-counting mode scintillation-based detection is illustrated in Figure 2-12, and the generation of a voltage pulse is sketched in Figure 2-13.

The interaction of ionizing radiation with a scintillator generates a scintillation pulse. Scintillation propagation is omnidirectional, and some impinge on the PMT. A PMT is a vacuum tube generally made from borosilicate glass. One inner end of the PMT is coated with a thin film of bialkali material called photocathode. This end is oriented towards the scintillator. The photocathode converts the scintillation light into electrons emitted into the vacuum. The number of electrons emitted would be proportional to the scintillation strength. PMT hosts a series of electrodes collectively called dynodes. The electrons emitted from the photocathode are directed towards the first dynode. As the electrons strike the dynode, a proportionally multiplied number of secondary electrons are emitted from the first dynode into the vacuum. All dynodes are maintained at a positive voltage, and every dynode is kept at a higher voltage than its predecessor using a high-voltage supply. Now, the second dynode attracts, accelerates, and multiplies the electrons. The process continues till the last dynode (called the anode) multiplies the electrons. PMTs can routinely multiply by 10^6 times. The electrons thus multiplied constitute a current pulse, the magnitude of which is proportional to the energy deposited in the scintillator.

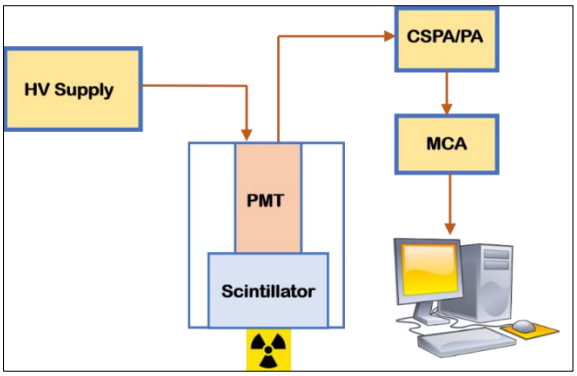

Figure 2-12 Typical scintillation detector set-up

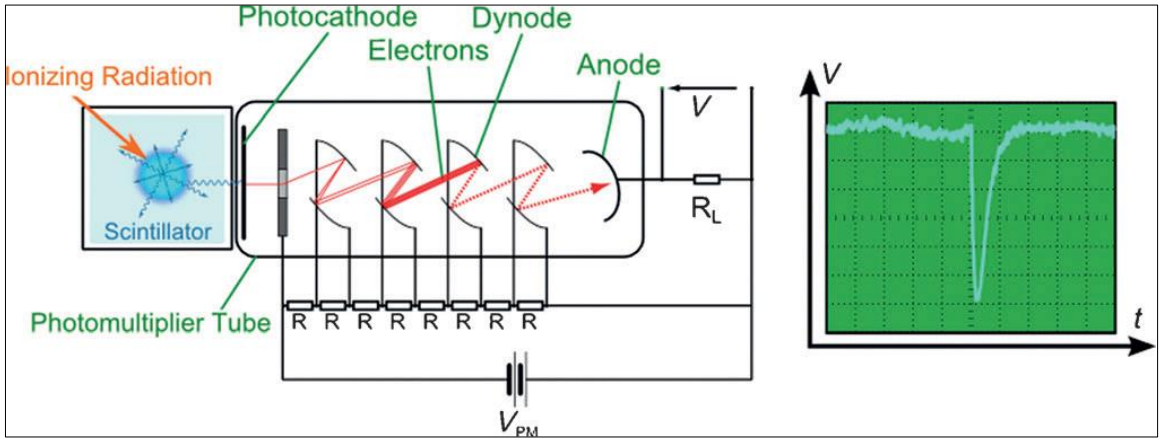

Figure 2-13 Generation of a voltage pulse in scintillation detectors. Reproduced from [74]

The output current pulses from the PMT are integrated through a CSPA and amplified/shaped with the SA. Shaped pulses are discriminated according to their strengths by MCA and are converted from analog to digital. As successive pulses occur, the analyzer sorts and construct a histogram of their amplitudes displayed as the PHS acquired for a given time. The PHS is a function of ionizing radiation, detector medium, detector size, acquisition time, and settings in readout electronics.

2.4 Gamma-ray shielding

Gamma-ray shielding is a particular utilization of the interaction of gamma rays with matter. It is achieved by inserting the materials having a greater probability of interaction between the source and item to be safeguarded. Unlike charged particles, photons are characterized by an infinite range and, thus, penetrate deeply into matter [125]. Each interaction, viz. photoelectric effect, Compton scattering, and pair-production, removes a gamma-ray photon from the beam either by absorption or scattering away from the direction of the item to be protected [1]. Gamma-ray attenuation follows exponential pattern decay. The probability of attenuation of gamma-rays is the sum of probabilities of all three mechanisms. The efficacy of the attenuation increases with an increase in Z, density, and thickness of the material.

2.5 Nanoparticles

Nanoparticles are the tiniest entity of bulk matter that can be manipulated independently. They constitute an ensemble of atoms or molecules. American Society for Testing and Materials (ASTM) standards defines them as particles with lengths that range from 1 to 100 nm in at least one dimension. [150]. Some researchers define them as particles with at least one dimension smaller than 1 μm and as small as atomic and molecular lengths (~0.2 nm) [151]. Some justify an upper size limit as that size where the particles begin to behave like the bulk [151].

Nanoparticles are realized through different routes such as mechanical milling, electrospinning, lithography, sputtering, the arc discharge method, laser ablation among top-down approaches and chemical vapor deposition, solvothermal and hydrothermal methods, sol–gel method, soft and hard templating methods, reverse micelle methods among the bottom-up approaches [152]**.** The choice of synthesis method depends on factors such as the desired nanoparticle material, size, shape, and surface properties. Nanoparticles prone to aggregation or agglomeration are synthesized and/or buffered in neutral solutions. Nanomaterials vary in composition, purity, size, size distribution, surface charge, shape (particles, rods, tubes, sheets/films), and structure (hollow, core-shell, surface functionalized). Nanoparticles used in this study were synthesized through chemical routes. For the present study, species, size, and coating are relevant.

Various techniques characterize nanoparticles for structural, morphological, and chemical properties like size, composition, shape, and purity. Common characterization techniques include transmission electron microscopy (TEM), scanning electron microscopy (SEM), X-ray diffraction (XRD), dynamic light scattering (DLS), Fourier-transform infrared spectroscopy (FTIR), and surface area analysis.

Nanotechnology is the utilization of nanomaterials for practical applications. Nanotechnology is conceptualized as the engineering of structures, devices, and systems through the precise manipulation of their size and shape at the nanometer scale [150]. The European Medicines Agency defines nanotechnology as using structures with sizes less than 1000 nm designed with specific purposes. Nanotechnologists tailor the size of matter at nanoscales to obtain at least one novel property that enables the design and fabrication of new devices, structures, and systems. Though artisans have practiced nanotechnology since 2600 BC, mostly by trial-and-error, it gained significance when the synthesis, manipulation, and characterization of matter at the nanoscale became feasible [13,50].

The invention of the scanning tunneling microscope (1981), the discovery of fullerene (1985), etc., provided foundational knowledge that enabled the eventual commercialization of nanotechnology in the 2000s. Understanding several aspects of nanoscience and nanotechnology is rigorously pursued. Nanostructures are difficult to explain using either solid-state physics or quantum chemistry. Nanoparticles are larger than atoms or molecules governed by quantum physics but smaller than the bulk governed by classical Newtonian physics [13]. Physical laws governing the bulk and nanomaterials of the same element are different[4]. Generally, nanoparticle research is interdisciplinary, involving physics, chemistry, and

sometimes biology [6]. Novel areas of applications of nanoparticles include electronics, energy storage, environmental remediation, and biomedical engineering[153].

2.5.1 Nanoscale effects

Though not in every aspect, nanomaterials exhibit some unique properties. Predominantly, the quantum confinement and surface effects induce unique responses in nanomaterials.

Quantum confinement:

Nanoparticles confine the electrons and thus generate quantum effects [154]. The space occupied by the electrons floating around the outermost orbit, being significant in comparison to the dimensions of the particle, leads to quantum confinement [13]. Severe confinement of electrons and holes leads to the discretization and quantization of energy band levels[3]. The energy bandgap at the nano-level becomes much wider than in bulk [155]. It affects the optical, electrical, and magnetic properties of nanomaterials. For example, AuNPs look ruby red to black in buffer solution [154], and opaque copper turns transparent[156]. Reduction in binding energy per atom leads to the reduction in melting point by the Gibbs-Thomson equation [4]. For instance, a three nm-sized AuNPs melts 300 degrees lower than the melting temperature of bulk gold (1064 °C)[157]. Further, the quantum confinement effect leads to the display of magnetic moments in nanoparticles of materials that are non-magnetic at bulk, like gold, palladium, or platinum [4].

Surface effects:

The surface effects refer to the presence of a large fraction of atoms at the surface. While a 30 nm spherical nanoparticle has ~5% atoms on the surface, a 4 nm one has ~50% [158]. Since the surface atoms have fewer neighbors than bulk atoms, the binding energy per atom decreases with a reduction in particle size [4]. The high specific surface area makes electronic activity and its interaction with outside influences significant [13]. These effects impact the chemical reactivity, catalytic activity, and adsorption capacity of nanoparticles, making them suitable for applications such as heterogeneous catalysis, gas sensing, and environmental remediation[159]. Pertaining to the present study, the electrons have a defined escape depth for every material surface, the thickness of which depends on the energy of electrons and the material itself. For metal surfaces, this escape depth is approximately 10 nm; for insulators, it can be larger, up to 50 nm [160]. The number of “escape electrons” increases in nanoparticles compared to bulk surfaces due to lesser reabsorption of secondary electrons within the material [6].

Shape effects:

The shape of nanoparticles has an influence over their properties and behavior. Nanoparticles with different shapes, such as spheres, rods, tubes, and sheets/films exhibit distinct optical, electrical, and mechanical properties due to variations in their crystallographic orientation, surface curvature, and atomic arrangement[161]. Tailoring the shape of nanoparticles allows researchers to fine-tune their properties for specific applications, such as plasmonic sensing, drug delivery, and energy storage[159,162].

2.5.2 Functionalisation of nanoparticles

Nanoparticles are highly amicable for functionalization with different surface coatings or ligands, which can enhance their stability, dispersibility, and biocompatibility[8]. Surface functionalization involves attaching molecules or polymers to the nanoparticle surface, providing control over the particle's surface chemistry and interactions with the surrounding environment. This functionalization enables nanoparticles to be tailored for specific applications, such as targeted drug delivery, bioimaging, and biosensing[159,161,162].

2.5.3 Nanocomposites

Nanocomposites combine conventional materials with nanomaterials having one or more components engineered to extract the best attributes of both [108]. In this study, nanoparticles are loaded into plastic scintillators to obtain nanocomposites. While the nanoparticles offer better gamma-stopping power than the plastics, the host generates scintillation due to the interaction of incoming gamma-rays and nanoparticle-emitted electrons [79,80]. In nanoparticle-based radiation shields, nanoparticles attenuate the gamma-radiations while the conventional polymers provide conformability and shape ability [18,87,95,108,109,113].

2.6 Conclusions

Ionizing radiations enable several practical applications but harm living organisms and delicate hardware. The study of the interaction of ionizing radiations with matter generates useful knowledge for applications and protection from ionizing radiations. This chapter presented the interactions of alpha, beta, gamma- and X-rays with matter-at-bulk. It outlined the instrumentation involved in the detection of radiations using these interactions. It introduced the nanoparticles and presented the unique responses of the nanomaterials.

3 Chapter 3: Plastic scintillators loaded with nanoparticles for gamma detection

This chapter presents the study conducted to determine better-suited nanoparticles as dopants in plastic scintillators to realize efficient, fast gamma-scintillators. As the study yielded an unexpected result, an investigation and analysis were conducted to establish that the result was genuine. This chapter presents the same. It reveals a new result that not all the species of nanoparticles enhance the gamma-detection efficiency of the plastic scintillator. This study warranted the development of a new technique presented in the next chapter. The first objective of the thesis is addressed in this chapter

3.1 Introduction

The role of nanoparticles embedded into plastic scintillators to develop efficient, fast, large, and affordable gamma detectors scintillators is to efficiently convert the gamma-rays into electrons to cause additional scintillation inside the plastic scintillators [12,67,79]. Five different high-Z material nanoparticles were incorporated into plastic scintillators under identical process conditions. Pulse height spectra of ^{241}Am are obtained under identical measurement conditions. The extent of enhancement of the number of counts in PHS under the entire spectrum relative to those in PHS with unloaded plastic scintillators was compared. The enhancement in total counts indicates an increase in detection efficiency.

The nanoparticle species were selected based on their high-Z and/or wide usage in previous works. A radioactive source, ^{241}Am, was chosen since the energies emitted by this source (principal emission at 14 keV and 60 keV). Such energies are of interest in practical applications such as X-ray astronomy[12,66], the detection of photons from synchrotron X-rays ranging between 20 keV and 67 keV [57–60,84]. Incidentally, the diagnostic X-rays from which the shielding is sought typically span 40 kV to 150 kV. [99,100,104]. A literature survey finds that the higher loading of nanoparticles adversely affects the light-yield and gamma-detection efficiency of the nanoparticle-loaded plastic scintillators [60] due to loss of transparency [70,77]. Hence, the loadings were limited to a sufficiently low level of 2 wt.% to avoid any ambiguity.

3.2 Materials and Methods

3.2.1 Materials

For realizing plastic scintillators, commercially available Saint-Gobain's BC-490, a vinyl-toluene solvent-based partially-polymerized formulation, was used for its ready availability and higher viscosity. Though a polystyrene formulation was tried, initial trials incorporating Gd_2O_3 nanoparticles into it resulted in the sedimentation of nanoparticles due to the lower viscosity of the host. Sedimentation of ZrO_2 nanoparticles during the polymerization of polystyrene solvent-based plastic scintillators was reported earlier [70]. Higher viscosity formulation BC-490 enabled the suspension of the nanoparticles inside the plastic scintillator, even with 14-day long polymerization. The radioactive source of ^{241}Am was sourced from BRIT, India. EJ212 plastic scintillator was procured from Eljen Technologies as a reference

for the performance of scintillators realized in this work. A scintillator block of EJ212 was machined and polished to cylinders of 9 mm diameter and 9 mm thickness. The properties of the plastic scintillators used are tabulated in Table 3-1. Data is taken from their data-sheets.

Table 3-1 Plastic scintillators used in this study.

#	**Parameter**	**EJ-212**	**BC-490**
1.	Manufacturer	Eljen technology	Saint-Gobain
2.	Physical form	Fully polymerized plastic scintillator	Partially polymerized plastic scintillator
3.	Light output, % of Anthracene	65	55
4.	Wavelength of maximum emission, nm	423	425
5.	Rise time, ns	0.9	(not provided)
6.	Decay time, ns	2.4	2.3
7.	Polymer base	Polyvenyltolune	Polyvenyltolune
8.	Refractive index	1.58	1.58

PMT: The present study used PMT 9078B from ET Enterprises. It is 21 mm in diameter and 80 mm in length. It has a 19 mm diameter borosilicate-end window with a blue-green light-sensitive bialkali photocathode and ten numbers of high stability SbCs dynodes of linear focused design, achieving a gain of 0.8×10^6. This PMT offers better than 25% quantum efficiency over 320 nm and 425 nm with a peak efficiency of 28%. Its refractive index is 1.49, the same as that of the toluene.

Charge sensitive preamplifier (CSPA)/Shaping amplifier (SA): Amptek A-203 CSPA/SA was used in the study. It is a 16-pin surface-mount dual-in-line hybrid package mounted on a printed circuit board. The output of the preamplifier is internally connected to the shaping amplifier. CSPA has a rise time of 50 ns and a fall time of 30 μs. The time constant of SA was set at 250 ns for all measurements.

The multichannel analyzer (MCA): AmptekMCA8000A was used in the study. This pocket MCA has a conversion time of less than 5 μs. It provides output with data in real-time, live time, and count-rate.

CdTe detector: Amp-Tek XR-100T has a 5 x 5 x 1 mm3 CdTe diode detector packed in a TO-8 hermetically sealed package with a 100 μm thick Be window. CSPA is packaged within. The output is connected to Amp-Tek PX5 Digital Pulse Processor that provides PHS on a data acquisition screen.

The nanoparticles used (source, purity in %, average particle size in nm, polydiversity index) were Bi_2O_3 (Otto Chemie, 99.5, 119.8±2.1, 0.361), Gd_2O_3 (Nanoshel, 99.9, 55±0.8, 0.292), HfO_2 (Otto Chemie, 99.6, 76.6±3.2, 0.333) and PbO (Nanoshel, 99.9, 141±2.4, 0.299), WO_3 (Nanoshel, 99.9, 81.6±1.4, 0.351). The nanoparticles were characterized as detailed below.

3.2.2 Nanoparticle characterization

3.2.2.1 *Scanning Electron Microscopy (SEM)/ Energy Dispersive Spectroscopy (EDS).*

SEM generates a magnified image of the object using electrons instead of light waves. Electrons are emitted into an ultra-high vacuum, accelerated, and guided to the object. The electron beam is focused onto a fine probe and raster-scanned over a small rectangular area. Typical beam energy ranges from 500 eV to 40 keV. The interaction of the electron beam with the sample yields a variety of output signals (secondary electrons, internal currents, photon emission, etc.). Each type of electron is detected using an appropriate detector. SEM determines the elemental analysis and, thus, the purity of the sample when it is operated in photon detection mode, where the characteristic X-rays emitted by the target atoms are detected by ancillary detectors, such as Si(Li) scintillators. This mode is termed EDS.

This study used Oxford ESD INCA Pentafet attached to Carl Zeiss SEM EVO 50 to characterize the purity of nanoparticles. The EDS spectrum for Gd_2O_3 nanoparticles is displayed in Figure 3-1.

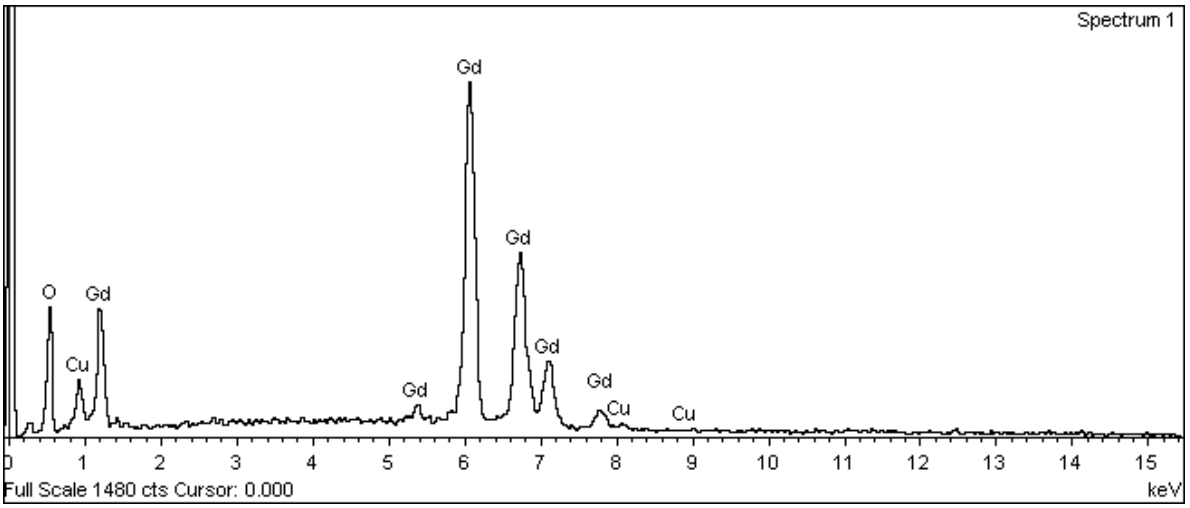

Figure 3-1 Energy Dispersive Spectrum of Gd_2O_3 nanoparticles

Further, in this study, the cross-sectional microscopic images of the nanocomposites were acquired by a Field Emission Scanning Electron Microscope (FE-SEM), Carl Zeiss Ultra 55, equipped with secondary electron detectors and a backscattered electron detector.

3.2.2.2 *Dynamic Light Scattering (DLS)*

DLS determines nanoparticle hydrodynamic size, size distribution, and polydispersity. In DLS, nanoparticles suspended in a solution are struck with monochromatic coherent laser light. The Brownian motion of particles leads to a variation in the intensity of scattering that is dependent on time, as the distance between the suspended scatterers continually fluctuates. The scattered light undergoes either constructive or destructive interference by the surrounding particles. Information contained in the time scale of movement of the scatterers is extracted by measuring the variations in scattered intensity over time at a given scattering angle (generally 90^o). The size of the particles is derived from the autocorrelation of the recorded intensity trace during the experiment.

The current study determined the sizes of nanoparticles through DLS. NanoBrook ZetaPALS (90°, 658 nm, 25 °C) was used with particle sizing software 5.23. The mixture was ultra-sonicated (at 35 kHz, with a 300 W sonicator) for about 15 minutes before filtering through a 0.22 µm PVDF filter directly to the cuvette. Triplicate measurements were carried out for one minute for each sample. The cuvettes were cleaned between the samples with ethanol, flushed thrice, air dried, and wiped clean with a lint-free tissue. The nanoparticles were suspended in toluene.

3.2.2.3 *X-ray Photoelectron Spectroscopy (XPS)*

XPS determines the elemental composition of a sample. It also determines the elemental oxidation states of the materials present within ~10 nm of the sample surface [163] or, conversely, detects the presence of surface contamination in bulk materials. In XPS, the sample is irradiated with monochromatic X-rays, and the photoelectrons emitted from the sample are detected and counted using appropriate detectors to infer surface composition and elemental oxidation states.

Survey spectra for the nanoparticles obtained are shown in Figure 3-2. The spectrum of each oxide shows core level spectra and Auger spectra of individual elements and oxygen, thereby confirming their presence in the oxides. The survey spectra were recorded with a SPECS spectrometer (SPECS Surface Nano Analysis GmbH, Germany) using non-monochromatic Al-Kα radiation (1486.6 eV) as an X-ray source operated at 300 W (12 kV, 12.5 mA). All the survey spectra were obtained with a pass energy of 50 eV with a step increment of 1 eV, and individual core level spectra of Gd 3d, Bi 4f, Pb 4f, and W 4f in Gd_2O_3, Bi_2O_3, PbO, and WO_3 nanoparticles were recorded with a pass energy and step increment of 40 and 0.05 eV, respectively. The binding energies reported here were referenced with C 1s peak at 284.6 eV. For XPS analysis, the nanoparticles sample powders were compacted, mounted on the sample holder, and kept in the preparation chamber at ultrahigh vacuum (UHV) at 8×10^{-8} mbar for 5 hours to desorb the volatile species present on the surface. After 5 hours, the sample was placed into the analyzer chamber with UHV at 5×10^{-10} mbar.

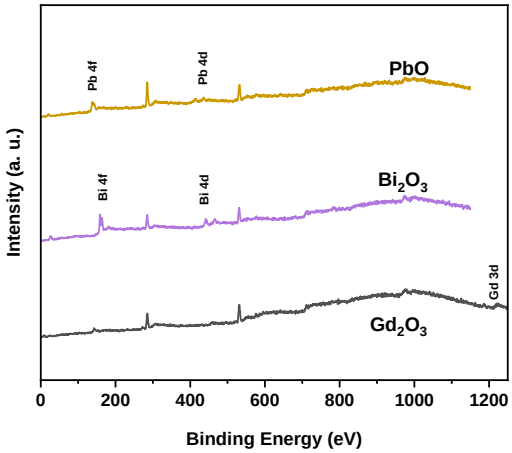

Figure 3-2 X-ray Photoelectron Spectrographs of nanoparticles

Further, the metal binding energy peak positions in individual core level spectra of oxides, as presented in Figure 3-3, show the presence of related oxides.

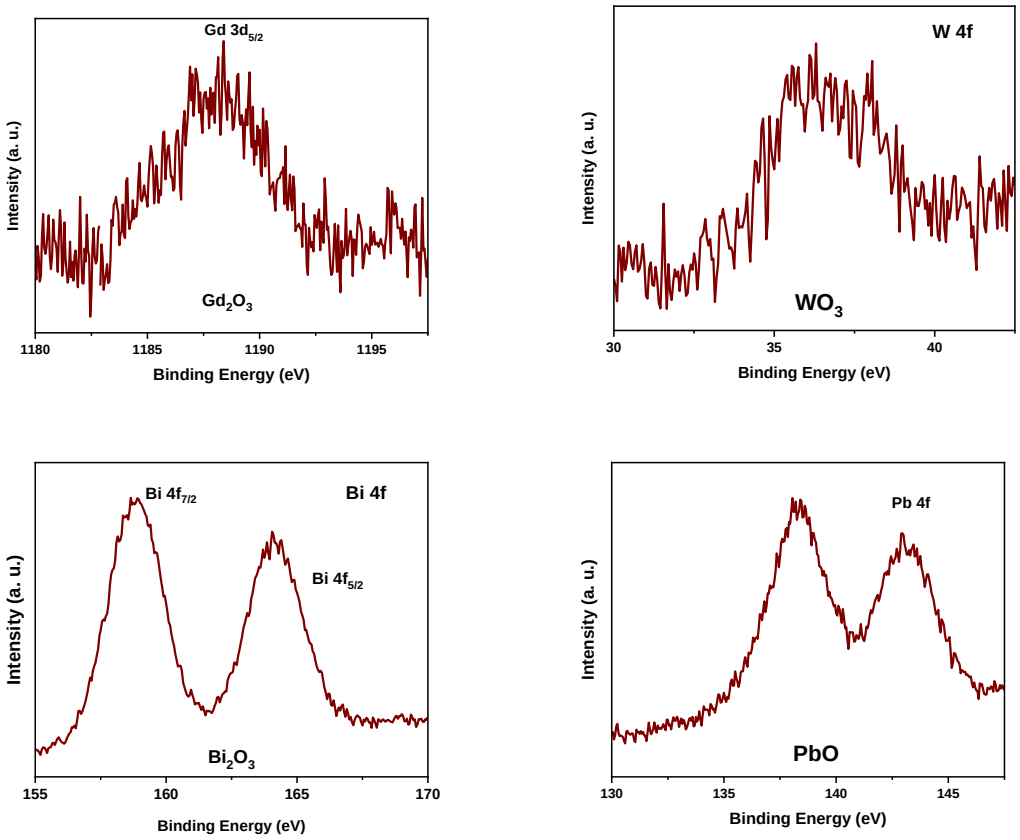

Figure 3-3 Metal-binding energy peak positions of individual core level spectra of oxides

3.2.2.4 *X-Ray Diffraction (XRD)*

In XRD, the sample is irradiated by a monochromatic X-ray beam. X-rays diffracted from the sample are collected. The angles of diffraction, along with corresponding intensities from the sample, are noted. The constructive interference of two scattered monochromatic X-rays is characteristic of the crystallinity of the sample since the constructive interference occurs when conditions satisfy Bragg's law ($n\lambda = 2d \sin\theta$) where n is an integer, λ is the wavelength of the X-ray, d is the distance between two atomic layers, and θ is diffraction angle or Bragg angle. XRD determines the crystalline structure, phase nature, lattice parameters, and crystalline grain size of the crystalline substances.

In this study, the crystalline phases were determined by the XRD system (Rigaku SmartLab) that uses Cu Kα X-rays in a 2θ–θ setup. Figure 3-4 displays the XRD patterns of the Gd_2O_3 nanoparticles. The crystallite size of the nanoparticles calculated from the Scherrer equation using powder X-ray analysis software (Rigaku SmartLab Studio II) was about 36 nm. The crystallinity was characterized since the interaction of low-energy gamma-rays varied with the species of nanoparticles. The nanoparticles studied were all found to be crystalline. The (hkl) parameters are identified as per JCPDS 43-1014 for Gd_2O_3, 24-0747 for WO_3, and 05-0570 for PbO nanoparticles.

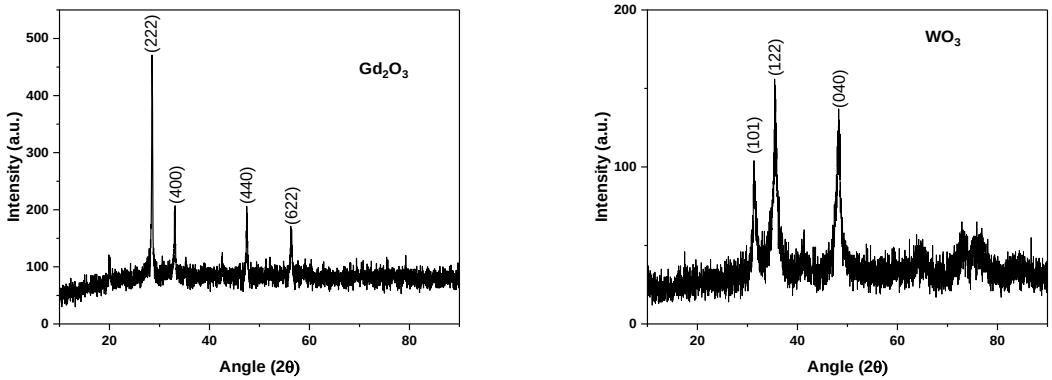

Figure 3-4 X-ray Diffraction patterns of nanoparticles

3.2.2.5 *Spectrophotometry*

Spectrophotometry measures the transmission, absorbance, and reflection of nanoparticle samples over a specified spectral range. The spectrophotometer measures the transmittance of the light at each wavelength. It is used for obtaining absorption spectra of the nanoparticles. The undispersed light of the halogen and/or the deuterium lamp transmits the sample and is partly absorbed by the sample. The thus altered light is spectrally dispersed in the polychromator by the holographic grating. In absorption measurements, the incident intensity (reference value) and the intensity attenuated by the sample are measured at every wavelength of interest.

In this study, the absorbance spectra of the nanoparticles were obtained with a Specord-S600 spectrophotometer. The spectra are shown in Figure *3-13*. It is a computer-controlled diode array spectrophotometer designed for measuring in the spectral range 190 – 1020 nm. Nanoparticles are loaded into DI water and mixed thoroughly. The mixtures of different nanoparticles were diluted to different extents to obtain appropriate spectra.

The spectrophotometry analysis revealed that none of the nanoparticles investigated exhibited an absorption peak within the specific wavelength region of interest, ranging from 350 nm to 450 nm. Moreover, the responses of the nanoparticles displayed similar trends, with no specific observations pertaining to WO_3 or PbO nanoparticles.

3.2.3 Methods

3.2.3.1 *Realization of nanocomposites*

Plastic scintillators were realized following the method mentioned in the datasheet of BC-490. All reagents were used as received. The solvent and the catalyst were mixed in proportion in a beaker. All mixing was manual. The mixture was added to the resin. Vacuum settling for 10 minutes at 10 mbar got rid of air bubbles. Nanoparticles were incorporated into the formulation at this stage. Nanoparticles were added to the mixture directly by weight at 2 wt.%, 1 wt.%, and 0.5 wt.%. The mixture was manually stirred and cast into glass test-tube molds (inner diameter of 9 mm and height of 12 mm) (Figure 3-5).

The scintillators thus realized were cut to 10 mm thickness. Each was 9 mm in diameter. All faces of all scintillators were polished using a micro-grinder and 0.05 μm sized alumina powder. The slab of plastic scintillator EJ212 was machined to the same dimensions, polished, and wrapped to serve as a reference for the unloaded plastic scintillator realized in this work. The representative samples are shown in Figure 3-6.

Figure 3-5 Molds made of glass tubes.

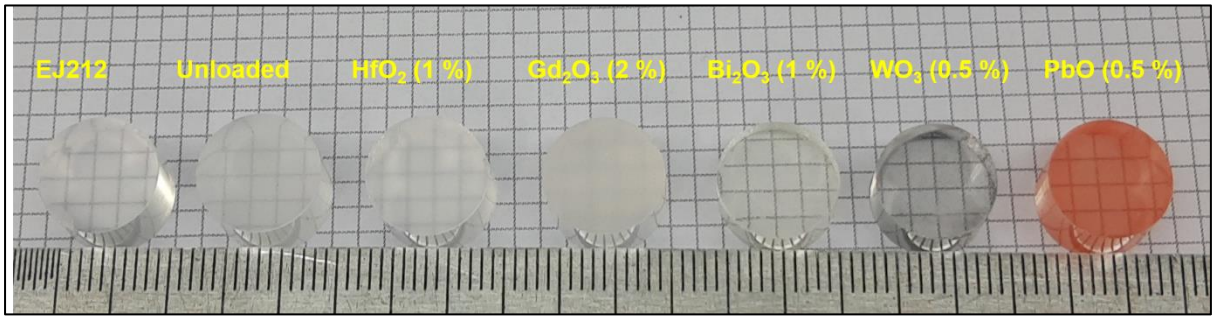

Figure 3-6 Unloaded and nanoparticle-loaded plastic scintillators realized in the study. The extent of loading is in wt.%

3.2.3.2 ***Measuring the relative gamma-to-electron conversion efficiencies***

The setup for measuring the gamma-to-electron conversion efficiency of the nanocomposites is shown in Figure 3-7. It is a standard set-up used for determining the extent of enhancement of detection efficiency. [58,164] The PMT was positioned vertically inside a light-tight enclosure. The scintillators were wrapped with reflecting aluminized mylar sheets on the side and top. The scintillators were placed over the PMT with their unwrapped side optically coupled to the PMT head with Dow-corning DC 3500 grease. An aluminum plate covered the enclosure from the top. The cover had an aperture of 10 mm in diameter in the center, optically closed with a 0.1 mm thick aluminum adhesive tape. The gamma-source disc was positioned right over the aperture. The output of PMT was fed to the MCA through the CSPA cum SA. PHS for unloaded, loaded, and standard plastic scintillators were obtained under identical measurement conditions. PHS were acquired for 60 s.

3.2.3.3 *Measuring the relative gamma-ray attenuation efficacy*

The measurement of gamma-attenuation efficiencies was not planned initially. It was determined using the standard procedure of measuring the transmitted portion of gamma rays through the nanocomposites as in [107], using a CdTe detector as in [122]. The detector was positioned over the source disc at a height of ~11 mm (Figure 3-7b). Each scintillator was placed in the gap between the source and the detector. CdTe detector output was connected to the AMP-TEK PX5 package, which provided the PHS. The PHS was acquired for 120 s. Greater the shielding of gamma-rays by the nanoparticles, the lesser the flux of gamma-rays reaching the detector. Thus, the greater the reduction of the number of counts in PHS, the greater the attenuation efficiency.

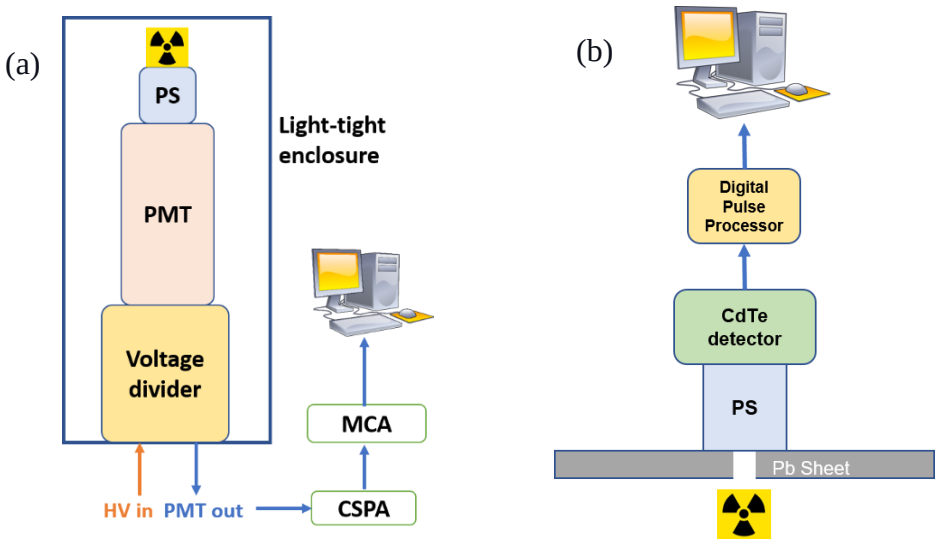

Figure 3-7 Schematics of experimental set-ups for measuring the relative (a) gamma-to-electron conversion efficiency and (b) gamma-attenuation efficiency of nanocomposites

3.3 Results

3.3.1 Nanocomposites realized

The nanocomposites realized are shown in Figure 3-6. The transparency is maintained for the nanocomposites for over 10 mm. The process has yielded good-quality unloaded, loaded, and standard plastic scintillators.

3.3.2 Effect of species on gamma detection efficiency of nanocomposites

Figure 3-8 displays pulse height spectra for scintillators for gamma-rays from ^{241}Am with 1 wt.% for all nanocomposites. All the samples exhibited the same response pattern. The figure displays the median of the three plots. Variations in PHS for the remaining two samples were within 2-3% of the counts.

The spectrum of unloaded plastic scintillators closely matched that of EJ212. The total counts under the PHS increased for nanocomposites of Gd_2O_3, HfO_2, and Bi_2O_3 but decreased for those of WO_3 and PbO. The number of counts increased or decreased at all channels for a given nanocomposite. The increase in counts was the greatest for Gd_2O_3 nanocomposites. Further,

full-energy peaks for the unloaded scintillator and EJ212 were located at channels approximately 100. Those for the nanocomposites shifted to lower channels.

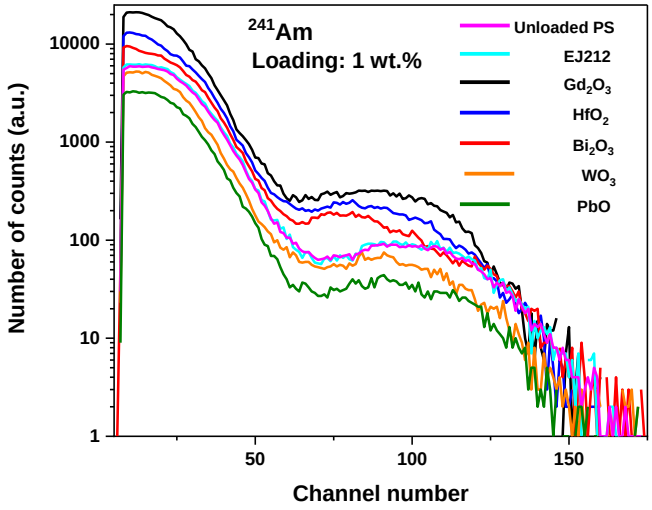

Figure 3-8 Variations in PHS of ^{241}Am in the unloaded plastic scintillator and in nanocomposites. PHS with EJ212 is included for comparison.

3.3.3 Effect of loading on gamma detection efficiency of nanocomposites

Figure 3-9 shows the effect of loading on the variations in PHS. (a) and (b) exhibit the same data. (b) is an enlarged view of (a) specifically focusing on the variations within the channel numbers 50. Notably, (a) and (b) are presented as semi-logarithmic and linear plot format, respectively. For Gd_2O_3, HfO_2, and Bi_2O_3 nanocomposites, counts increased with loading. A 2 wt.% Gd_2O_3 nanocomposite yielded the greatest increase in counts. The total counts in PHS increase by 4.2 times that of an unloaded plastic scintillator. Counts remained reduced for WO_3 and PbO nanocomposites at all loadings, and the variations in counts for different loadings were negligible.

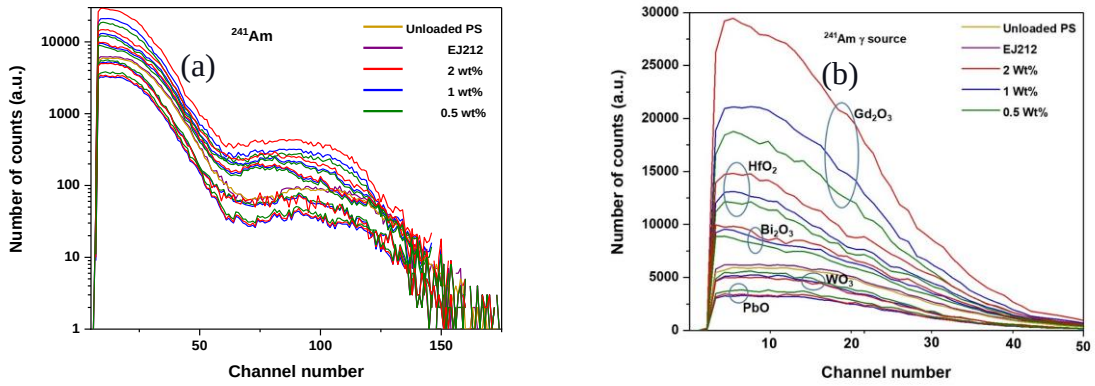

Figure 3-9 (a) Effect of loading of nanoparticles on the number of counts in PHS (b) enlarged version of (a)

3.3.4 Effects of species and loading on gamma attenuation efficiency

Figure 3-10 exhibits the relative gamma-attenuation efficiencies of nanocomposites. The variations in PHS were minute. Hence, the variations are presented in a histogram. The output flux of the EJ212 and unloaded plastic scintillators were approximately equal. The gamma-ray flux was reduced in varying degrees by all nanocomposites. All nanocomposites reduced the gamma-ray flux to varying extents. The extent of transmission varied between the nanocomposites. Increased loading of nanoparticles reduced the extent of transmission, in general.

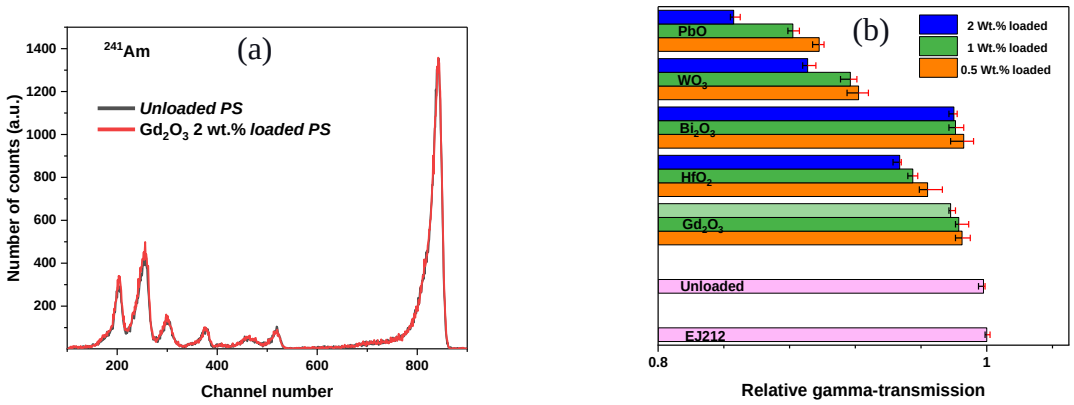

Figure 3-10 (a) pulse height spectra of ^{241}Am with CdTe detector for unloaded plastic scintillator and 2 wt.% Gd_2O_3 nanocomposite and (b) Relative gamma transmission efficiencies of nanocomposites for gamma-rays from ^{241}Am.

3.3.5 Discussion

3.3.5.1 *Inference of the results*

The PHS for the unloaded plastic scintillator (Figure 3-8) is formed due to the interaction of gamma-rays with constituent C, H, N, and O atoms. Nanoparticles loaded serve as additional sites for interaction for the gamma-rays. It is the outcome of the interaction of gamma rays with the dopant nanoparticles that leads to variations in PHS.

When a gamma-ray arrives at a nanoparticle, the interaction may or may not occur. If the interaction occurs, it could occur through the photoelectric effect or Compton scattering. The photoelectric effect may occur with an atom located at the surface or core of the nanoparticle. A photoelectron exiting the atom begins interacting with electrons inside the nanoparticle and/or with the plastic scintillator and/or other nanoparticles till it loses its energy. Compton scattering can occur with the electrons bound to any atom of the nanoparticle. The interaction of Compton scattered photons would be similar to that of the original gamma-ray of corresponding energy. The interaction of the recoil electron would be analogous to that of the photoelectron.

An electron leaving the nanoparticle with an energy greater than the scintillation threshold of the scintillator causes additional scintillation leading to increased counts in PHS. Counts vary at all channels as the electrons can exit the nanoparticles with all possible energies. This is true

for Gd_2O_3, HfO_3, and Bi_2O_3 nanocomposites but need not be for WO_3 and PbO nanocomposites. In all nanocomposites, the centroids of the full-energy peak positions shift towards lower channels due to a reduction in light yield. It is consistent with several studies reported in the literature [57,59,60,70,76,77,84]. The root cause of the reduction in light yield is being debated as fluorescence quenching and self-absorption loss due to light scattering by the nanoparticles[12,65,72,76].

Increased loading of nanoparticles increases the interaction events resulting in the enhancement of counts (Figure 3-9). This increase is despite the reduction in light yield. The literature indicates shifting of full-energy peaks with the extent of loading also [70,83]. However, such shifting is unobserved here since the variations in loading in the present study are relatively much smaller than those in the literature.

The interactions of gamma-rays with nanoparticles lead to gamma-ray attenuation in the nanocomposites (Figure 3-10). For gamma-attenuation measurements, the host plastic scintillator serves as a conformable polymer, and the effect of the interaction of electrons with the scintillators is ignored. Each interaction of gamma-ray with plastic scintillator and nanoparticle eliminates the gamma-ray from reaching the detector and thus contributes to the reduction in flux reaching the detector. Increased loading of nanoparticles increased the attenuation due to an increased number of interactions.

3.3.5.2 *Key observations for analysis*

Thus, there were five key observations for analysis.

The first four above observations are reasonable and concur with the literature. Cai *et al.* [65], Liu *et al.*[76], and Magi *et al.* [77] incorporated Gd_2O_3, HfO_2, and Bi_2O_3 nanoparticles and demonstrated enhanced gamma detection efficiencies for nanocomposites. Kishimoto and Toda achieved 7.2 times better detection efficiency with HfO_2 nanoparticles than a commercially available 5 wt.% Pb loaded plastic scintillator EJ-256 [84]. Magi et al. enhanced the detection efficiency of the scintillators for high-energy photons by incorporating Bi_2O_3 nanoparticles [77]. The effect of increased loading of Gd_2O_3, HfO_2, and Bi_2O_3 nanoparticles is in line with previous reports [57,59,60,70,83]. Thirdly, the enhancement of gamma-detection efficiency of the polymers is reported upon incorporating several species of nanoparticles, including Gd_2O_3, Bi_2O_3, and HfO_2 [87,105,106,108,110,117,123,125]. Increased loading of nanoparticles enhancing the extent of shielding concurs with all the earlier reports [108,109,113,117,122,165].

However, the fifth observation, the reduction in scintillation counts from a plastic scintillator upon incorporating WO_3 and PbO nanoparticles into the scintillator, has not been reported. It was an unexpected result. This observation necessitated scrutiny through a thorough investigation.

3.3.5.3 *Investigation of the new result*

A nanocomposite offers increased counts consequent to a series of processes: the nanoparticle interacts with the gamma-ray; the electron emitted from a constituent atom undergoing the

interaction exits the nanoparticle with enough energy to scintillate the medium; and finally, the nanocomposite does not absorb the scintillation before the scintillation reaches the PMT. These processes occur in Gd_2O_3, HfO_2, and Bi_2O_3 nanocomposites. In WO_3, PbO nanocomposites, the nanoparticles interact with the gamma-rays, as manifested by the reduction in counts. Otherwise, transmitting gamma-rays through nanoparticles without interaction leaves the number of counts unaltered. However, the commonalty in processes seems to end there for WO_3 and PbO nanoparticles.

On the other hand, the counts in PHS of a nanocomposite reduce due to one or many of the following reasons: optical quenching, generation of a gap between the host matrix and nanoparticle where the electron gets unduly absorbed though seems to be insignificant, the large initial or aggregated size of the nanoparticles attenuating the electron, loss of transparency due to the self-absorption of scintillation by the nanoparticles, or, as a speculation, the given nanoparticles absorb the energy of the electrons to the extent that electrons exit with energy insufficient to cause the scintillation. These reasons are analyzed next.

A nanoparticle inside the plastic scintillator causes optical quenching [149] (Section 2.3.3.3). All nanoparticles quench. However, if quenching were a determining factor in reducing the number of counts, the enhancement of counts by 4.2 times by Gd_2O_3 nanocomposite and the reduction of counts by 0.7 times for WO_3 and 0.5 times for PbO nanocomposites would be improbable. In the latter cases, additional scintillation, if it occurred, would balance the loss of counts due to optical quenching and thus at least maintain the number of counts, if not increase. This condition is true for any nanocomposite, particularly at these lower loadings. From Figure 3-9, the change in counts for increased loading is disproportionate to the concentration of the nanoparticles. Thus, quenching is not the reason for reduced counts.

A physical gap generated between the nanoparticles and the host can absorb the total or partial energy of the electrons. Literature reports the formation of gaps in the order of micrometers in nanocomposites (Figure 3-11)[85]. The block-polymerization technique currently followed for the realization of larger detectors [166] invariably leads to generating such cracks from stress relief during solvent drying [85,167].

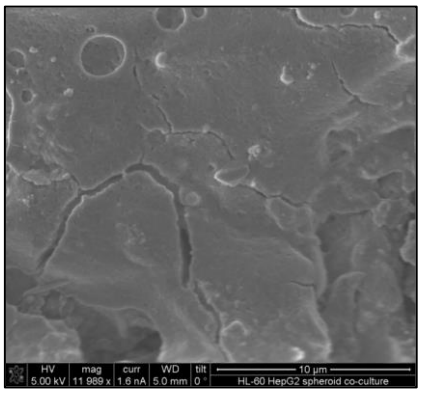

Figure 3-11 Cracks in a nanoparticle incorporated polymer. Reproduced from [85]

To analyze it, the nanocomposites were sliced, and the scanning electron micrographs of their plains were obtained for investigation (Figure 3-12). The Gd_2O_3 nanocomposites display a different texture, which requires further studies for an explanation. The micrographs of the other four nanoparticles and the magnified view in Figure 3-12 (f) show a fine dispersion of nanoparticles and only insignificant cracks between the nanoparticles and the host. The generation of gaps is not specific to WO_3 and PbO nanocomposites. Hence, this possibility is negated here.

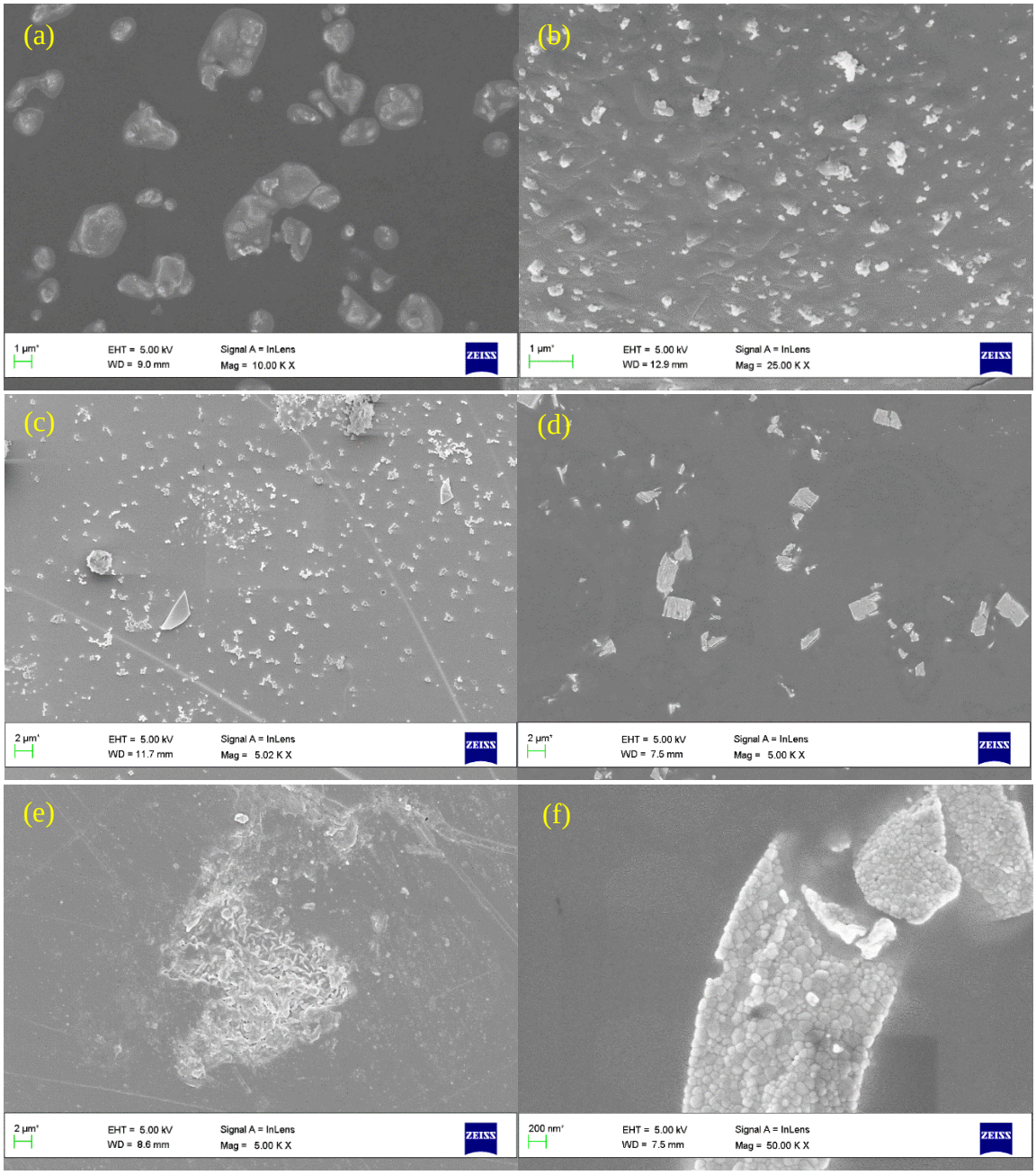

Figure 3-12 Scanning electron micrographs of a plain of (a) Gd_2O_3 (b) HfO_2 (c) Bi_2O_3 (d) WO_3 (e) PbO nanocomposites. (f) magnified view of the plain of WO_3 nanocomposite. All are 0.5 wt.% loaded nanocomposites.

Thirdly, a nanoparticle with a size exceeding the range of electrons inside the material can attenuate the electrons emitted from its atoms. Photoelectrons emitted from WO_3 and PbO atoms interacting with gamma-rays from ^{241}Am could be K_α energies of 48 keV and 44 keV from W and Pb atoms, respectively. The continuous-slowing-down approximation (CSDA) range of a 45 keV electron in W and Pb is about 42 µm and 76 µm, respectively. Thus, the starting size of currently used nanoparticles is not a deterrent. The nanoparticles aggregated during the realization of nanocomposites (Figure 3-12). They have aggregated to about half a micrometer. The aggregated sizes of WO_3 and PbO nanoparticles are comparable to those of the other nanoparticles. Alongside, the literature evidences the enhancement of counts from

nanocomposites containing $Hf_xSi_{1-x}O_2$ nanoparticles aggregated to hundreds of micrometers [60]. HfO_2 nanoparticles aggregated to sizes as large as 300 nm have enhanced the number of counts [58]. Hence, the aggregation of nanoparticles inside the plastic scintillators does not necessarily hinder the exit of electrons.

The loss of transmission due to self-absorption of scintillation by the nanoparticles could reduce the number of counts. The color of WO_3 and PbO indicates that these nanoparticles absorb light at some wavelength region, which may suppress the scintillation photons. To investigate this potential artifact, the absorption spectra were obtained for the nanoparticles (Figure 3-13). The spikes observed at 356 nm are noise generated during the change of lamps.

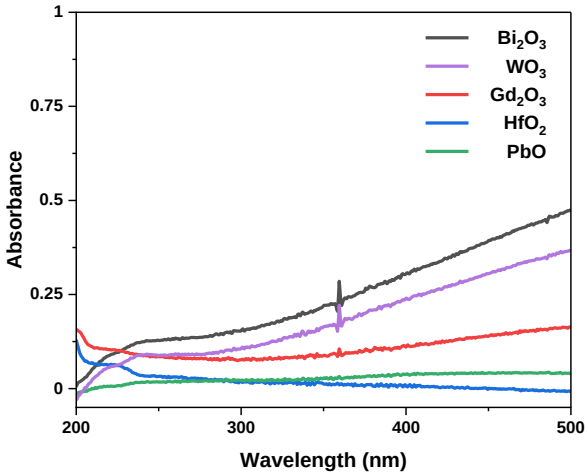

Figure 3-13 Absorption spectra of the nanoparticles used

PPO (fluor) scintillation occurs from 350 nm to 400 nm, with a peak at 360 nm. POPOP (wavelength shifter) emits light from 380 nm to 450 nm, with a peak at 420 nm. None of the nanoparticles exhibit absorption of photons at these wavelengths. No unusual response is observable in the absorption spectra of WO_3, and PbO nanoparticles, relative to the others. The absorption of scintillation would result in the shift of the full-energy peak to the lower channels. The color of WO_3 or PbO nanocomposites indicates that their absorption spectra may have peaks or tails in wavelengths outside the scintillation region. Thus, reduced counts in WO_3 and PbO nanocomposites are not caused by the self-absorption of scintillation by the nanoparticles.

It is possible that the electrons may exit PbO or WO_3 nanoparticles with energy insufficient to scintillate the host or the scintillation light generated is below the detection threshold of the PMT. The scintillation threshold of the PVT-based plastic scintillator used is typically 100 eV [168].

The literature offers inputs for further analysis. It repeatedly reports the enhancement of gamma-detection efficiency of a plastic scintillator by incorporating only selected species of nanoparticles such as Bi_2O_3, Gd_2O_3, HfO_2, $Hf_xSi_{1-x}O_2$, ZnO, ZrO_2 [56,57,83,58–60,65–67,70,80]. To the best of the survey, such enhancement by incorporating Pb, Sn, PbO, or WO_3 nanoparticles is not reported. Since the loading of Pb, Sn atoms (not their nanoparticles) into liquid and plastic

scintillators enhances the gamma-detection efficiency of the hosts, as demonstrated and utilized since the 1960s [75], the nanoparticles of these materials could have been the logical first choice as dopants in plastic scintillators for enhancing the gamma-detection of efficiency of the hosts. Meanwhile, the nanoparticles of Bi, Bi_2O_3, BiO, CuO, Fe_2O_3, Fe_3O_4, Gd_2O_3, HfO_2, Pb, Pb_3O_4, PbO, PbO_2, $PbWO_4$, Sm_2O_3, TiO_2, W, WO_3, Zn, ZnO, ZrO_2 have been loaded into conformable polymers to develop efficient gamma-ray shields [87,95,102,106,115,117,121,169].

The number of physical processes leading to increased or decreased scintillation counts from a nanocomposite is limited. After negating potential artifacts and critically analyzing the literature, explaining why and how WO3 and PbO nanocomposites reduce the number of counts with the existing knowledge is challenging. It is thus speculated that WO_3 and PbO nanoparticles interact with the gamma-rays; their constituent atoms emit electrons. However, these nanoparticles effectively absorb the electrons within themselves wholly or partially. Thus, selected species of nanoparticles interact with the gamma-rays but hinder the exit of electrons into the surrounding. Validation of this speculation requires more direct observations than those made with nanocomposites.

A literature survey indicated no experimental technique exists determining the outcome of the interaction of given gamma-rays with given nanoparticles. It also indicated that another practical application of nanoparticle radiosensitization also demands such a technique. The focus of the present study shifted towards developing one such technique.

Nevertheless, for the original purpose of the study, results determined that Gd_2O_3, HfO_2, and Bi_2O_3 nanoparticles convert the gamma rays into electrons more efficiently, with Gd_2O_3 offering the best conversion among them. Thus, they are better suited as dopants in plastic scintillators to develop efficient gamma-detectors. While all species of nanoparticle suit as dopants in conformable polymers to develop efficient gamma-ray shields, WO_3 and PbO were found suitable especially for space applications as they effectively absorb the gamma-rays within themselves.

3.4 Conclusions

A study conducted to measure the relative enhancement of the gamma-detection efficiency of a plastic scintillator upon loading different species of nanoparticles resulted in a revelation that not all nanoparticles enhance the gamma-detection efficiency of the hosts. It was established through the investigation that the outcome of gamma X-ray interaction varies with the nanoparticle species. The study hinted that selected species of nanoparticles interact with the gamma-rays but may hinder the exit of electrons into the surrounding. The data available from the experimental loading of nanoparticles into the plastic scintillators is limited. This revelation, however, motivated this thesis work to study the outcome in detail by develop a more direct experimental technique to determine the outcome of the interaction of gamma-rays with the nanoparticles for the same. The next chapter presents the development of such a technique and the results obtained using the technique.

4 Chapter 4 Interaction of ionizing radiation with nanoparticles

This chapter presents the technique developed for determining the outcome of the interaction of given ionizing radiation with given nanoparticles. It presents the first empirical results on the outcome of gamma-rays, X-rays, and beta- and alpha-radiations with nanoparticles. The effects of nature and energy of the ionizing radiations and species, size, and concentration of the nanoparticles are provided. This chapter also discusses the features, strengths, and limitations of the technique; compares the results with those in the literature; offers inputs for practical applications and basic knowledge concerning the interaction of ionizing radiations with nanoparticles; and mentions the pointers for further basic studies to explain the new results obtained in the study. This chapter addresses the second, third, and fourth objectives of the thesis.

4.1 Materials and methods

4.1.1 Materials

Radiation sources

The radioactive sources used in the study are listed in Table 4-1.

Table 4-1 Radiation sources used in this study

#	Source	Used as a source of	Principal energies [1,5,133]
1.	^{241}Am (encapsulated)	Gamma	14, 60 keV
2.	^{133}Ba	Gamma	81, 356 keV
3.	^{137}Cs	Gamma	662 keV
4.	^{22}Na	Gamma	511, 1270 keV
5.	^{60}Co	Gamma	1170, 1330 keV
6.	^{90}Sr/^{90}Y	Beta	540/2200 keV
7.	^{204}Tl	Beta	760 keV
8.	^{147}Pm	Beta	224 keV
9.	^{55}Fe	X-rays	5.8 keV, 6.5 keV
10.	X-ray gun	X-rays	40 kVp. The gun emits ~3 x 10^{11} photon/sr at 100 µA. It was always operated at 38 kVp and 50 µA.
11.	^{241}Am(α) (button)	Alpha Gamma	5.4 MeV 14 keV, 60 keV
12.	Am-Be	Gamma, Neutron	1 Ci, Neutron flux of 2.5 x 10^6 n/cm^2/s, continuous spectrum of maximum energy up to 10 MeV and the average energy of 5.5 MeV; Gamma flux of ~ 3.0 x 10^7 gammas/cm^2/s, major gamma energy 60 keV

The above sources were used due to their ready accessibility. They were standard sources in the form of discs (~ 3 mm thick x ~10 mm diameter). Except for the $^{241}Am(\alpha)$ button source, the radioactive sources were supplied by BRIT (britatom.gov.in). The $^{241}Am(\alpha)$ button source was retrieved from an outdated smoke detector. The X-ray gun was sourced from M/s Moxtek (Model: Magnum).

Liquid Scintillators

The main liquid scintillator used in this study was sourced from SRL Chemicals. (srlchem.com, product #46069). It consists of 6 g 2,5-diphenyloxazole (PPO) fluor and 0.2 g 1,4-bis(5-phenyloxazol-2-yl)benzene (POPOP) wavelength shifter dissolved in 1 litre of toluene. It was chosen for its classic combination and ready availability.

Dioxane-based liquid scintillator was also used. It was sourced from Mayochem (mayochem.com, product no. 23072). It has 1,4 dioxane solvent with 120 gm/l naphthalene, 4 gm/l PPO, and 50 mg/l POPOP. Initial measurements with a dioxane-based liquid scintillator yielded results similar in trend but lower in efficiency to those of a toluene-based one. Hence, the results obtained with the toluene-based liquid scintillator are reported here.

Au:Sn 80:20 sheets

Au:Sn 80:20 sheets were sourced from Indium Corporation of America. They helped obtain a PHS of gamma rays when they are attenuated externally. Each sheet is 25 μm thick. The composition of the sheets was better than Au:Sn 79:21 as characterized by energy-dispersive X-ray analysis.

Instruments

PMT, CSPA, SA, and CdTe detectors used are the same as those mentioned in section 3.2.1

Nanoparticles

The nanoparticles studied are listed in Table 4-2

The nanoparticles were chosen based on their usage in practical applications and ready availability. For example, Au, Gd_2O_3, HfO_2, and Fe_2O_3 are popular in NPRS [7,8,16]. Gd_2O_3, HfO_2, ZrO_2, and Bi_2O_3 are used to develop efficient, fast, large, and affordable gamma-ray detectors [12,56–60,67,70,80]. WO_3, Bi_2O_3, Sn, etc., are extensively studied to develop Pb-free, efficient, light-weight gamma-ray shields [95,100,108,115]. All nanoparticles were procured except for citrate-buffered AuNPs (29 nm) and $La_2Ce_2O_7$ nanoparticles

Table 4-2 Nanoparticles used in this study

#	Nanoparticle	Purity (%)	APS (nm)	PDI	Source
1.	Ag	99.2	81.7±0.6	0.332	Lab Chemie
2.	Au	99.9	73±3.3[#]	0.316	Nanoshel
3.	Au (buffered)	[*]	5±0.2[#]	[*]	Sigma-Aldrich
4.	Au (buffered)	[*]	28.9±0.3	0.352	(Synthesized by the author)
5.	Bi_2O_3 [$]	99.5	119.8±2.1	0.361	Otto Chemie
6.	CeO_2	99.9	38.5±1.7	0.287	Otto Chemie
7.	CuO	99.9	112.4±2.3	0.360	Otto Chemie
8.	Eu_2O_3	99.9	74.9±1.5	0.333	Mincometsal
9.	Fe_2O_3	99.4	32.9±0.1	0.250	High Purity Lab Chemie
10.	Gd_2O_3	99.9	55±0.8[#]	0.292	Nanoshel
11.	Gd_2O_3	99.9	12.96±[*]	0.428	Nanoshel
12.	Gd_2O_3	99.9	179.9±5.7	0.347	[&] (by sintering #10 at 900 °C for 4 hours)
13.	Gd_2O_3	99.8	1249.2±112.1	0.249	[&] (by sintering #10 at 1300 °C for 4 hours)
14.	HfO_2	99.6	76.6±3.2	0.333	Otto Chemie
15.	$La_2Ce_2O_7$ [$]	99.9	122.9±10.2	0.292	Synthesized at NAL[@]
16.	LaF_3	99.7	41.9±2.3	0.298	Lab Chemie
17.	PbO [$]	99.9	141±2.4	0.299	Nanoshel
18.	Pd	99.8	33.1±1.1	0.254	Lab Chemie
19.	Pr_2O_3	99.9	116.9±2.1	0.364	Mincometsal
20.	Sn [$]	99.7	150.5±8.9	0.297	Otto Chemie
21.	SnO_2	99.9	83.8±1.2	0.301	High Purity Lab Chemie
22.	TiO_2	98.7	36.3±2.9	0.262	Sigma-Aldrich
23.	W	99.8	70.7±1.6	0.320	High Purity Lab Chemie
24.	WO_3	99.9	81.6±1.4	0.351	Nanoshel
25.	WO_3	99.7	880.1±46.3	0.352	[&] (by sintering #24 at 1300 °C for 4 hours)
26.	Zn	99.7	128±5.1	0.308	Otto Chemie
27.	ZnO	99.9	73±3.3	0.316	Nanoshell
28.	ZnO	99.9	630.2±28.1	0.306	[&] (by sintering #27 at 1300 °C for 4 hours)
29.	ZrO_2	99.9	36.8±1.5	0.286	Tosho

APS – Average particle size, measured with dynamic light scattering

PDI – Polydiversity index

[#] unless specified otherwise, these are the sizes of nanoparticles referred to in the plots. Thus, the size of Gd_2O_3 nanoparticles was 55 nm, of AuNPs was 73 nm, and that of buffered AuNP was 5 nm core size with 14-25 nm mean hydrodynamic size.

[*] not measured

[$] these nanoparticles are filtered through a 0.22 μm filter

[&] these nanoparticles are sintered in a regular oven at a heating rate of 10°C per min

[@] National Aerospace Laboratories, Bengaluru, as acknowledged.

Citrate-buffered AuNPs (29 nm) were synthesized. They were synthesized using the Turkevich technique [170]. Au ribbons of 99.9999% purity, high-resistivity DI water, and electronic-grade high-purity chemicals were used. To prepare 500 ml of 0.1 mM $HAuCl_4$ solution, 0.5 g Au was dissolved in 2 ml of conc. HNO_3 and 8 ml of conc. HCl. 3 ml of this solution was dissolved in 500 ml of DI water. 50 ml out of this 503 ml was taken and dissolved in 500 ml of DI water. To prepare 38.8 mM $Na_3C_6H_5O_7$ solution, 1.14 g of Na_3Ci was dissolved in 100 ml of DI water. 30 ml of 0.1 mM $HAuCl_4$ mixed with 170 ml of DI water was heated in a mantle to about 85 °C for about 20 minutes. 20 ml of 38.8 mM $Na_3C_6H_5O_7$ solution was added to this hot solution. The mixture was boiled with continuous stirring till the color of the solution changed from pale yellow to colorless to pale red, which took ~15 minutes. The boiling was stopped to obtain sodium citrate buffered AuNPs.

$La_2Ce_2O_7$ nanoparticles were synthesized through a co-precipitation process using oxalic acid as the precipitant. 97.25 g of La_2O_3 was converted to lanthanum nitrate by adding 168 ml of nitric acid. To this mixture, 109.68 g of oxalic acid, dissolved in 462.78 ml of ethanol, was added and precipitated. In another beaker, 297.52 g of ceric ammonium nitrate was dissolved in 535.53 ml of DI water. To this aqueous solution, 297.52 g of oxalic acid, dissolved in 1225 ml of ethanol, was added and precipitated. Further, the precipitated solutions were thoroughly stirred. In order to adjust the pH of the solution, ethanol, and ammonia were taken in a ratio of 1:1 and added to the precipitated mixture until the pH reached 8. The obtained precipitate was then filtered and washed with distilled water thoroughly. The precipitate was dried in an oven at 120°C for 10 h, followed by calcination at 900°C for 4 h to get a fine powder.

The nanoparticles were received as nano-powders except for the buffered AuNPs (5 nm) sourced from Sigma-Aldrich and buffered AuNPs (29 nm) synthesized. The nanoparticles (unbuffered or buffered) were used as received/synthesized. Four types of nano-powders had aggregated by the time of experimentation. These nanoparticles were mixed in DI water, sonicated (35 kHz, 300 W) for 10 minutes, and filtered through Millipak® 0.22 µm units to filter and isolate smaller-sized nanoparticles. Since obtaining a species of nanoparticles that vary only in size was challenging, smaller nanoparticles were sintered to obtain large nanoparticles.

4.1.2 Characterization of the nanoparticles (additional)

The nanoparticles were characterized for purity, size, elemental composition, and crystalline nature. The details of techniques used were identical to those in section 3.2.2. The details of other techniques used are provided here.

4.1.2.1 *Transmission electron microscopy (TEM)*

TEM is a tool to image the atomic structure of the sample. Individual atoms of the crystal can be resolved at a very small scale (~0.5Å) using its High-Resolution mode. Electrons emitted from a source at the top of the microscope travel through a vacuum and get focused into a very thin beam which is then directed through the specimen of interest. Intensities of electrons passing through the sample are detected with a suitable detector to construct a micrograph.

Figure 4-1 shows the transmission electron micrograph of AuNPs synthesized.

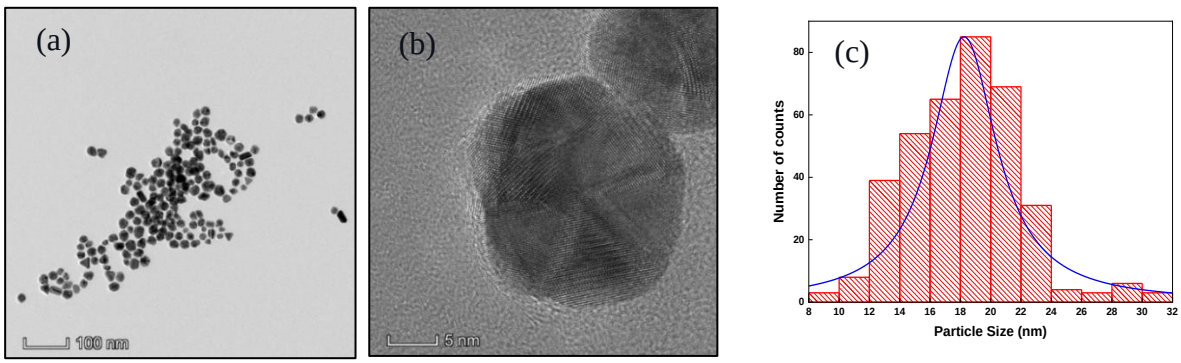

Figure 4-1 (a) Transmission electron micrograph of AuNPs synthesized in this work, (b) High-resolution transmission electron micrograph of AuNPs, (c) Histogram of size distribution as estimated by Image-J® tool

The average particle sizes of AuNPs obtained through the Image-J tool on TEM and DLS were 18 nm and 29 nm, respectively. This variation is possible as DLS uses aqueous dispersion of the nanoparticles where the hydrodynamic size of nanoparticles is measured while TEM characterizes the size of dry nanoparticles [6,171]. However, these variations in size measurements do not affect the rationale or inference in the present study.

4.1.2.2 *Photoluminescence (PL)*

Photoluminescence (PL) is the spontaneous light emission from a material when excited by an optical source [136]. In PL, the sample is excited by photons of a specific wavelength. The sample may absorb the optical photons and/or undergo photo-excitation. When the electrons return from the photo-excitation state to the equilibrium state, the excess energy is released in energy either in the form of light (a radiative process) or heat (a non-radiative process). The emission occurs at lower energy than the absorption as some of the absorbed energy is dissipated during internal energy transitions such as vibrational relaxation. The quantum yield of PL (PLQY) for a given nanoparticle incident with the light of a given wavelength is the percentage of light photons emitted as photoluminescence from sample [83].

In this study, PLQYs of Gd_2O_3 nanoparticles were determined, as nanopowders, outside the liquid scintillator. Internal PLQY (ratio of the number of photons emitted to the number of photons absorbed by the sample) was measured with a Hitachi F7000 spectrophotometer, and the external PLQY (ratio of the number of photons emitted to the number of photons incident on the sample) was estimated from it. External PLQYs at 269 nm and 420 nm were 9.32% and 9.83%, respectively. The samples were incident with these specific wavelengths as they are the wavelengths at which the emissions from the flour (PPO) and wavelength shifter (POPOP) peak, respectively.

4.1.3 The technique developed

4.1.3.1 *Set-up, rationale, and procedure of the technique*

Set-up

The set-up used is shown in Figure 4-2.

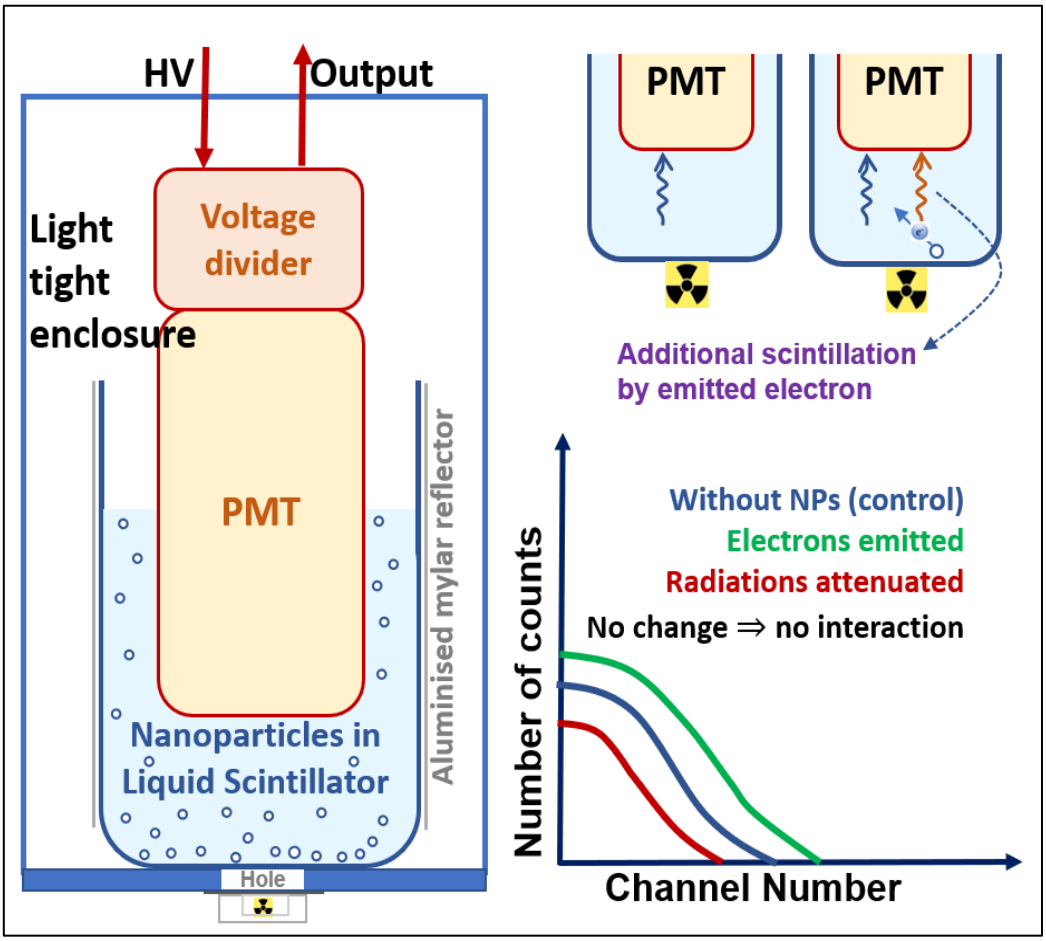

Figure 4-2 The set-up of technique contributed in this work for determining the outcomes of the interaction of given ionizing radiations with given nanoparticles

The light-tight enclosure was realized from stainless steel pipes (inner diameter 40 mm, thickness 1.5 mm) and flanges used in vacuum systems. A PMT was hung vertically down. The bottom cover of the enclosure (~3.5 mm thick aluminum) was kept detachable for repeated demounting and mounting of the beaker. A 12 mm diameter, 0.1 mm thick aluminum window was created at the center of the bottom cover. The radioactive source discs placed in steel enclosures were placed below the bottom cover such that the axis of the source, window, beaker, and PMT coincide. A glass beaker (~22 mm inner diameter, ~1.5 mm thick, ~80 mm long) was placed inside the enclosure so that a ~7 mm thick liquid scintillator stays beneath the PMT head. Its inner diameter was slightly larger than the outer diameter of the PMT. Efficient optical coupling between the PMT and liquid scintillator was ensured by immersing the PMT head into the liquid scintillator. The beaker was wrapped with a 0.05 mm thick aluminized mylar sheet to maximize the reflectivity of scintillation photons. The volume of the current setup was optimized between the need to detect the fast electrons expected to be released from the nanoparticles and to minimize the quantity of liquid scintillator used per experiment. The

output of PMT is connected to a data acquisition system through a charge-sensitive pre-amplifier cum pulse-shaper (Amptek A203) and a multichannel analyzer (MCA, Ametek, MCA-8000A) (Figure 2-12). ADMCA/Maestro software tool (www.amptek.com/software) acquired the data on a computer. Figure 4-3 and Figure 4-4 display the images of the experimental set-up.

The chart on the bottom right side of the set-up in figure 4-2 shows the rationale of the technique. The interaction of radiations with the nanoparticles causes variations in PHS of ionizing radiation with an unloaded liquid scintillator. The number of counts increases when the interaction results in the emission of electrons from the nanoparticles. Reduction in the number of counts occurs when nanoparticles attenuate the ionizing radiations. Transmission of ionizing radiations through the nanoparticles without interaction leaves the PHS unvaried. The shape of PHS discloses the energy profile of the electrons emitted with a nanoparticle-loaded liquid scintillator. Though the liquid scintillator is less efficient in detecting X-rays or gamma-rays, it is an efficient beta-radiation (fast-electron) detector.

The idea of loading the nanoparticles into a liquid scintillator evolved to overcome the practical issue of physical gaps generated between the nanoparticle and the host scintillator discussed in chapter 3. Such gaps in the micrometer range are reported in the literature [85] (Figure 3-11). The generation of gaps is known only after the realization of the mold and is irreversible. On the other hand, if the nanoparticles are loaded into a liquid scintillator, there would be no scope for generating a physical gap as the liquid surrounds the nanoparticles. The electrons emitted into the scintillator would then be constrained to interact with the liquid scintillator. Advantageously, the liquid scintillation counting technique is highly researched and is a practical means of quantitative analysis of low-energy betas [145]. Loading high-Z materials into liquid scintillators is pursued in several works for practical applications such as radioimmunoassay[75,172] or detecting high-energy particles[12,173]. Hence, loading the nanoparticles into a liquid scintillator emerged to develop the new technique.

The phenomena occurring inside an unloaded liquid scintillator are described in the literature [132,149] and are summarized in section 2.3.3.2. Those occurring inside the nanoparticle-loaded liquid scintillator are similar to those mentioned in section 3.3.5.1 since the liquid scintillator is functionally identical to a plastic scintillator.

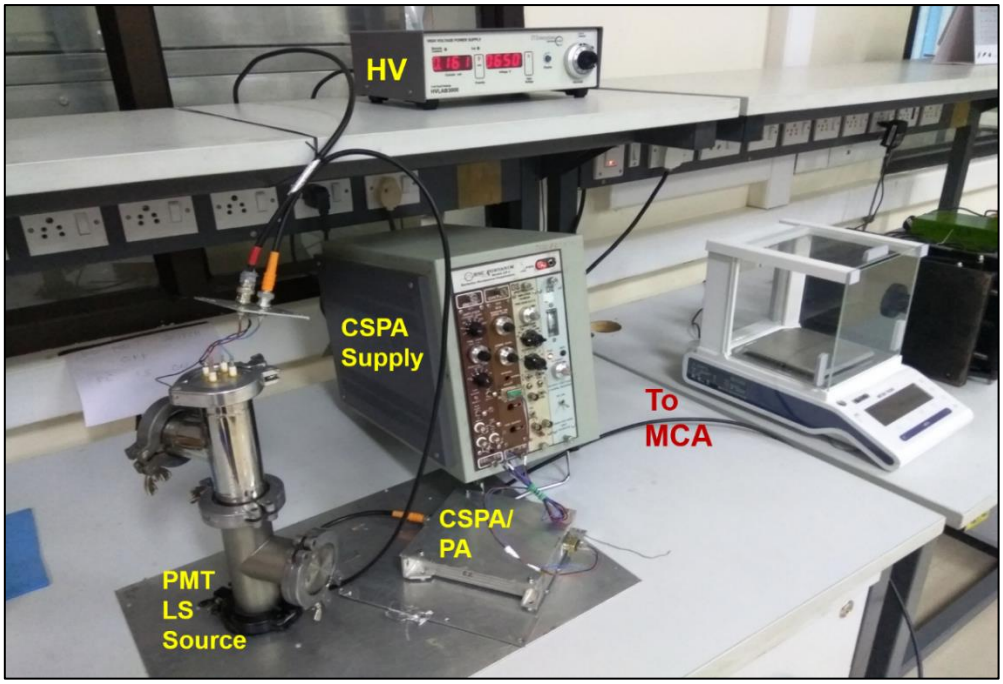

Figure 4-3 A view of a part of the experimental set-up.

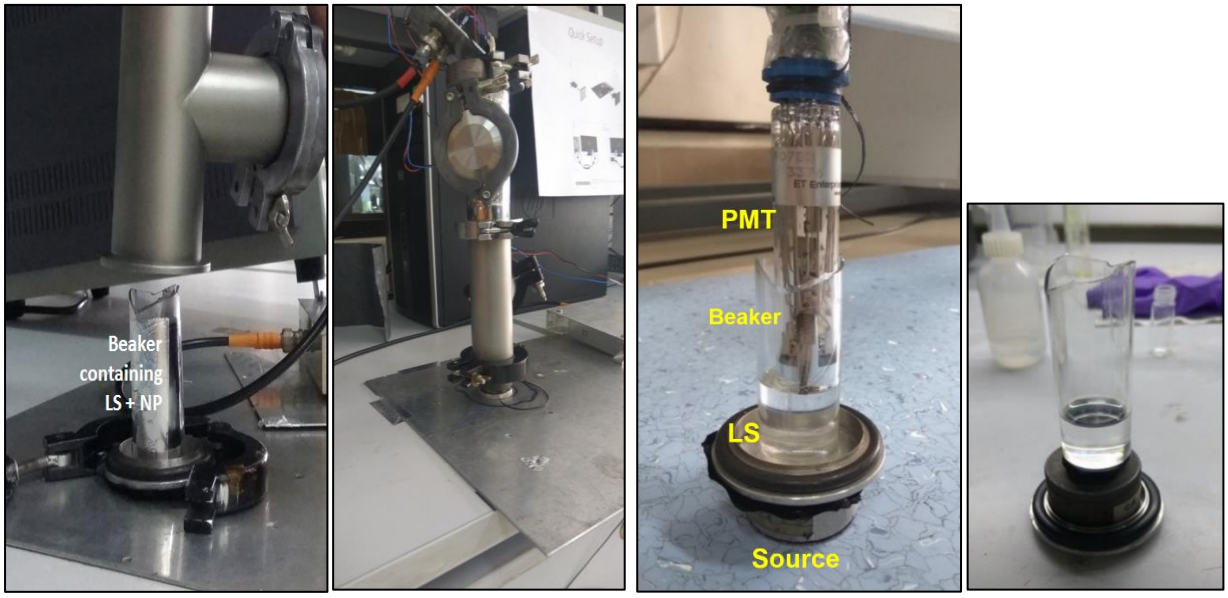

Figure 4-4 View of glass beaker containing the liquid scintillator.

Procedure

Initially, about 6 ml of liquid scintillator was dispensed into the beaker. This volume ensured the liquid scintillator filled up the gap underneath the PMT head in the present set-up. The PHS of ionizing radiation with the liquid scintillator was acquired. Acquisition time was 120 s. The low-level discriminator was set to 5 in all acquisitions. The given quantity of nanoparticles was loaded into the liquid scintillator by weight. Weight-based loading facilitated better control. The nanoparticles were weighed using Mettler Toledo ME204E series balance or Genius Sartorius 10 microgram resolution scales. While the powder nanoparticles were loaded through a spatula, buffered nanoparticles were loaded through a microsyringe. The minimum quantity of buffered AuNPs drawn once was 25 µl, with a corresponding weight of ~25 mg. The liquid

scintillator and nanoparticles mixture was sonicated (using a 300 W sonicator at 35 kHz for 15 minutes) and loaded into the beaker to be placed inside the light-tight enclosure. The PHS of ionizing radiation with the nanoparticle-loaded liquid scintillator was obtained under identical measurement conditions. The variations in PHS were studied, and outcomes were inferred. The process was replicated for various loadings.

Typical initial loading was ~5 mg. Suppose the number of counts increases with the initial loading of nanoparticles. In that case, the loadings are incremented till the number of counts in PHS reaches a maximum and starts reducing with further loading. If the number of counts decreased with the initial loading, the initial loading was reset to ~1 mg and then, if required, to sub-milligrams. Tinier loadings were achieved by diluting the mixture of liquid scintillator and nanoparticles. For dilution, the mixture is thoroughly shaken, and about half the mixture (about 3 ml) is decanted. About 3 ml of the fresh liquid scintillator is added to the beaker. Dilution was continued till PHS approached that of the unloaded liquid scintillator from the X-axis. Experiments with minute loadings were repeated using a microgram weighing scale. Further, for a few nanoparticles like TiO_2 loading 5 mg, the number of counts in lower channels increases while those in higher channels decrease. Upon loading 25 mg or more of TiO_2 nanoparticles, the number of counts increased at all channels. Thus, the primary outcome of the interaction of photons with nanoparticles is better studied at lower loadings to minimize the ensemble effect. The study of the interaction of beta-radiations invariably demanded dilution to sub-milligrams. This approach was maintained the same way for a given nanoparticle species.

Initially, HV to PMT was set high to obtain PHS for unloaded liquid scintillators with full-scale readings. Upon loading the nanoparticles, for instance, Gd_2O_3 nanoparticles, the channels get saturated by energetic electrons emitted from the nanoparticle. At higher loadings, the saturation would be even quicker. Then, the experiment was re-conducted by iteratively setting the HV to a value where any loading of nanoparticles does not saturate the channels. The operating HV was 800 V for experiments with ^{241}Am and X-rays, 600 V for that with ^{55}Fe, and 700 V for ^{133}Ba.

The background count rates were as low as 0.7, 2.4, 3.8, 7.1, 7.8 cps for HVs at 600 V, 700 V, 800 V, 900 V and, 1000 V, respectively. They were not subtracted while plotting. Count rates with radiation sources positioned below empty beakers were indistinguishable from the background count rates for all sources except for X-rays from the gun. The background count-rate for X-rays was high (35 cps) for 38 kVp X-rays from the gun. Possibly, X-rays strike the dynodes to cause the release of electrons. The count rate for X-rays was as high as 14850 cps when the beaker contained the liquid scintillator. Hence background counts were ignored.

The results were highly consistent. The number of counts varies over multiple acquisitions due to differences in the volume of liquid scintillator loaded, inaccurate positioning of radioactive sources below light-tight enclosure, differences in high-voltage setting, volatile reduction of volume of toluene etc. Such variations were within ~0.5% for unloaded liquid scintillators and ~1% for nanoparticle-loaded liquid scintillators at 800 V HV measured over a dozen

acquisitions. The variations were relatively lesser at high loadings. Counts vary within a single acquisition owing to statistical variance associated with radiation experiments. Those variations were within the above limits. Overall variations are included as error bars in Figure 4-7b.

Nanoparticles loaded into the liquid scintillator either stay suspended or sink to the bottom. The portion of them sinking in a liquid scintillator is a function of the quantity of loading, density of nanoparticles, and time. Most of the 10 mg Gd_2O_3 nanoparticles loaded stayed suspended in the current liquid scintillator for over 6 hours observed. When 25 mg of them were loaded, a few nanoparticles were visibly observed to settle at the bottom after an hour [Figure 4-5 (a)]. The effect of sinking on the number of counts in PHS was negligible [Figure 4-5(b)]. The acquisition time was as low as 2 minutes, and the acquisition always began immediately after loading. Thus, the distribution of nanoparticles inside the scintillator during the acquisition of PHS was practically the same or proportional.

The typical acquisition time was 120 s. For analysis, PHS was also acquired for longer durations of tens of minutes (Figure 4-5). The results were similar in trend. The counts at all channels increased proportionately. To minimize the time spent with radioactive sources in view of the large number of experiments planned, the acquisition time was limited to 120 s.

Interactions at greater loadings are studied only for a comprehensive one-time understanding of the technique or for determining the effect of loading. Such experiments were required only with selected species of nanoparticles (those in the third column of Table 4-3) and required large loadings.

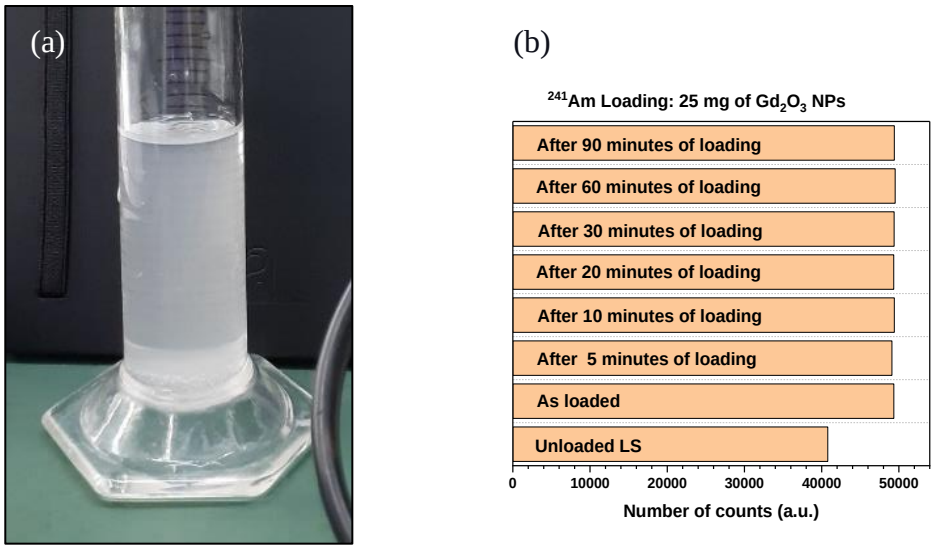

Figure 4-5 (a) Formation of a visibly thin layer of nanoparticles at the bottom after 1 hour of loading 25 mg of Gd_2O_3 nanoparticles into the liquid scintillator in a measuring jar (b) Variation in PHS counts over this time.

Specific modifications in the set-up

Nominally, radioactive sources and an X-ray gun were positioned directly beneath the aperture (Figure 4-2). However, the beaker attenuates X-rays from ^{55}Fe and beta-radiations from ^{204}Tl, ^{133}Pm. The glass beaker was substituted with a polytetrafluoroethylene (PTFE) beaker having a 0.1 mm thick bottom while studying the interactions of these radiations. As alpha-radiations cannot penetrate the thickness of the glass/PTFE beaker, the ^{241}Am(α) button source was immersed inside the liquid scintillator while obtaining both the reference PHS and nanoparticle-loaded PHS. Further, the ^{241}Am(α) source emits gamma-rays also. ^{241}Am gamma-source has an encapsulation that absorbs all the alpha radiations emanating from the source. When ^{241}Am was placed below the beaker, at an HV of 600 V or lower, the set-up could not generate PHS of ^{241}Am. Meanwhile, when the ^{241}Am(α) source was immersed in the liquid scintillator at an HV of 600 V to the PMT, the set-up could generate PHS of ^{241}Am(α). Thus, at HV of 600 V, only the outcomes of the interaction of alpha radiations with nanoparticles are manifested (Figure 4-6). Hence, the interactions of alpha radiation with the nanoparticles were studied at 600 V HV (section 4.2.4.)

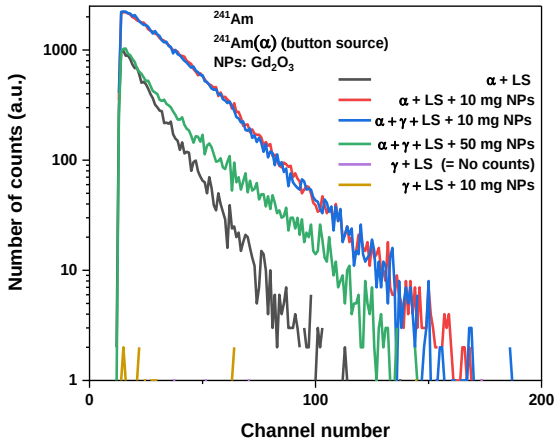

Figure 4-6 Variations in PHS of ^{241}Am(α) with liquid scintillator upon loading the nanoparticles at HV of 600 V

4.2 Results and inference: The outcomes of the interaction

The results are presented in the following sequence: Outcomes of interactions of low-energy photons, high-energy photons, beta- and alpha-radiations. Then, for each radiation, the effects of loading of nanoparticles, species of nanoparticles, size of nanoparticles, and energy of the radiations are sequenced.

4.2.1 Interaction of low-energy photons with nanoparticles

Gamma-rays from ^{241}Am, ^{133}Ba, and X-rays from ^{55}Fe and a 40 kVp gun are grouped as low-energy photons. Interactions involving ^{241}Am and Gd_2O_3 and AuNPs are chosen to represent the results as they offered higher sensitivity than with other nanoparticles.

The pulse height spectra of ^{241}Am with an unloaded liquid scintillator and Gd_2O_3 nanoparticle-

loaded liquid scintillator are displayed in Figure 4-7. In the PHS with an unloaded liquid scintillator, a number of counts appeared at channels until channel 400. Upon loading the nanoparticles, the number of counts in PHS increased. They increased at all channels. New counts appeared at higher channels than 400. Increased loading of nanoparticles increased the number of counts further. New counts appeared at even higher channels. This increase in the number of counts and appearance of counts at higher channels continued till a certain loading (800 mg). Beyond that, the number of counts started reducing across all channels, and counts appeared till lesser channels than the previous ones. At 2400 mg loading, the number of counts in lower channels (till ~50) reduced from those in PHS with an unloaded liquid scintillator, and the number of counts at higher channels reduced from those in PHS with a 10 mg nanoparticle-loaded liquid scintillator. The histogram presents the variations in the number of counts [Figure 4-7 (b)].

(a)

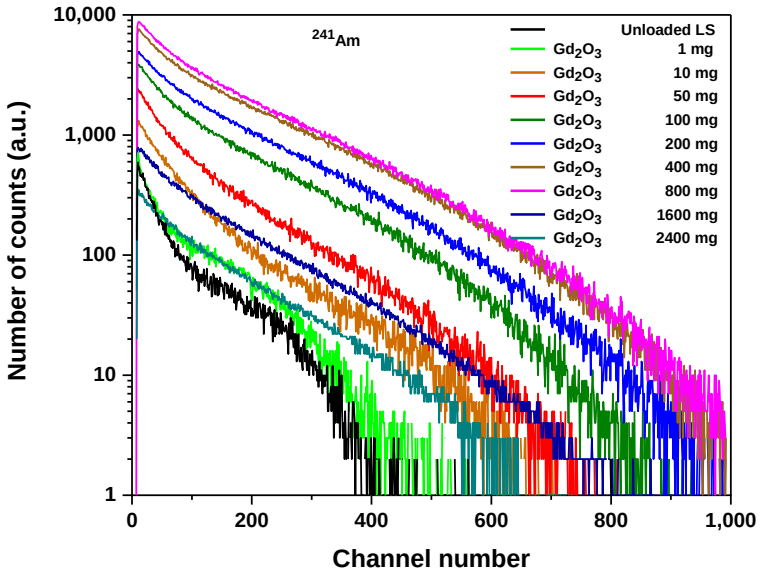

(b)

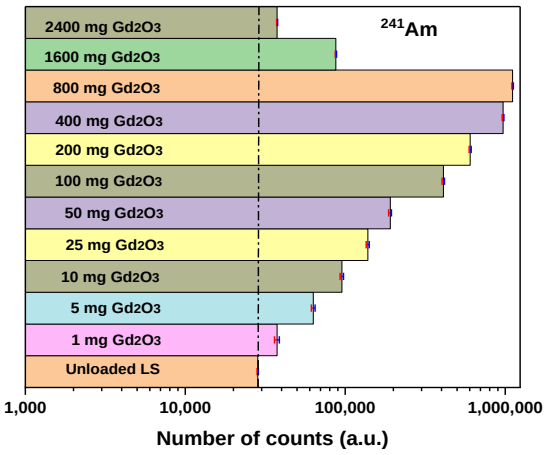

Figure 4-7 (a) Variations in PHS of ^{241}Am with liquid scintillator upon loading Gd_2O_3 nanoparticles. The error bars are included.

The results in Figure 4-7 are inferred here. The PHS of ^{241}Am for unloaded liquid scintillator is a characteristic. It essentially indicates the number and energy profile of electrons generated out of the interaction of gamma-rays with C, H, O, and N atoms of the liquid scintillator and thus serves as a reference PHS. Calibration of the channel numbers for energy could indicate the energies of the electrons. However, the calibration could not be performed due to the non-availability of suitable monoenergetic sources. The interaction mechanism is predominantly Compton scattering [132,149]. By the rationale of the technique, gamma rays from ^{241}Am interact with Gd_2O_3 nanoparticles to cause the emission of electrons from the nanoparticles.

Electron emission confirmation

To establish that the increase in the number of counts is due genuinely to the emission of electrons, the following experiments and analyses were conducted before inferring the results further.

The number of counts in PHS with an unloaded liquid scintillator appears till channel 400 (Figure 4-7), indicating that the energy of most energetic electrons released from the interaction of gamma-rays with C,H,N,O atoms corresponds to the energy at channel 400. The appearance of counts beyond channel 400 is possible only when even more energetic electrons are emitted from the nanoparticles into the liquid scintillator or longer integration time to detect a sufficient number of higher energy electrons emissions.

A test was performed using water. Figure 4-8 shows the increased number of counts in PHS upon loading 50 mg Gd_2O_3 nanoparticles into the liquid scintillator. Some nanoparticles are suspended in the liquid, while the rest have formed a layer at the bottom. About 5 ml of water was added to this mixture. Some nanoparticles were then suspended in water also. The number of counts got reduced. Water, immiscible and denser than the liquid scintillator, occupied the volume below the scintillator and thus separated the liquid scintillator from the layer of nanoparticles. Water attenuates most of the electrons emitted from the nanoparticles and some gamma rays from the source. As water molecules are non-fluorescent, their excitations are lost in radiation-less transitions.

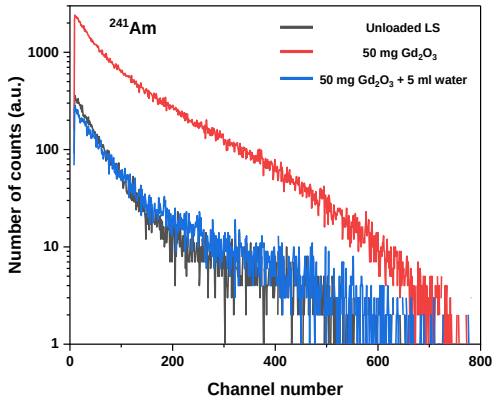

Figure 4-8 Variations in PHS of ^{241}Am with liquid scintillator upon loading Gd_2O_3 nanoparticles and then the water

Ruling out other artifacts required specific measurements. Withdrawal of the gamma-source during the acquisition reduced the count rate to the background. Thus, the nanoparticles used are not radioactive. Nanoparticles could be radio-luminescent. Irradiation of nanoparticles *alone* (without the liquid scintillator) inside the beaker returned a PHS identical to the level of the background of the scintillator without nanoparticles. Hence, the contribution of radio-luminescence of Gd_2O_3 nanoparticles to the increase in the number of counts is negligible. They could be photoluminescent. PLQYs of Gd_2O_3 nanoparticles at wavelengths of peak emission of the flour (360 nm) and the wavelength shifter (420 nm) were 9.32% and 9.83%, respectively. While the PL can account for about 10% increase in counts, the number of counts increased by about 4000% upon loading 800 mg of Gd_2O_3 nanoparticles. Thus, the contribution of the photoluminescence of the nanoparticles to the increase in the number of counts was negligible.

The interaction of Compton, scattered photons with the liquid scintillator contributes to the increase in counts. PHS of ^{241}Am with a CdTe photon detector was obtained without and with the nanoparticles positioned in-between the source and detector (Figure 4-9). The Amp-Tek XR-100T CdTe detector was hung vertically down inside the beaker with its Be window positioned closely over the bottom. The detector output was connected to a digital pulse processor AMP-TEK PX5. The source was placed beneath the beaker. Pulse height spectra were obtained with 0 mg, 10 mg, and 100 mg nanoparticles loaded into the beaker. The counts appear at well-defined channels. Upon positioning the nanoparticles, the number of counts in PHS was reduced. PHS shows the appearance of new counts at approximately channel 600. The variations in the number of counts also appear only at well-defined energies, and the shape of PHS is maintained.

The reduction in the number of counts upon insertion of nanoparticles affirms the interaction of gamma-rays with nanoparticles. The peaks in PHS without the nanoparticles correspond to specific energies of gamma rays emitted by ^{241}Am. The reduction in counts occurs only at these energies, and the number of counts does not vary at other channels or energies. Upon a rough calibration, channel 600 in PHS, where new counts appear upon placing the nanoparticles, corresponds to ~43 keV, the K_α X-rays from Gd. The photoelectric effect appears to be the dominant mechanism of interaction. Each photoelectric effect removes a gamma-ray from reaching the detector, and the photoelectrons traversing toward the detector get absorbed by the Be window. If Compton scattering was dominant, the recoil electrons would get attenuated by Be window, and the scattered photons would strike the detector if the detector is within the solid angle of Compton scattered photons. The number of counts would have increased across the channels. Though the contribution of Compton scattering could be finite, the possibility of enhancement of the number of counts by Compton scattered gamma-rays alone is invalidated.

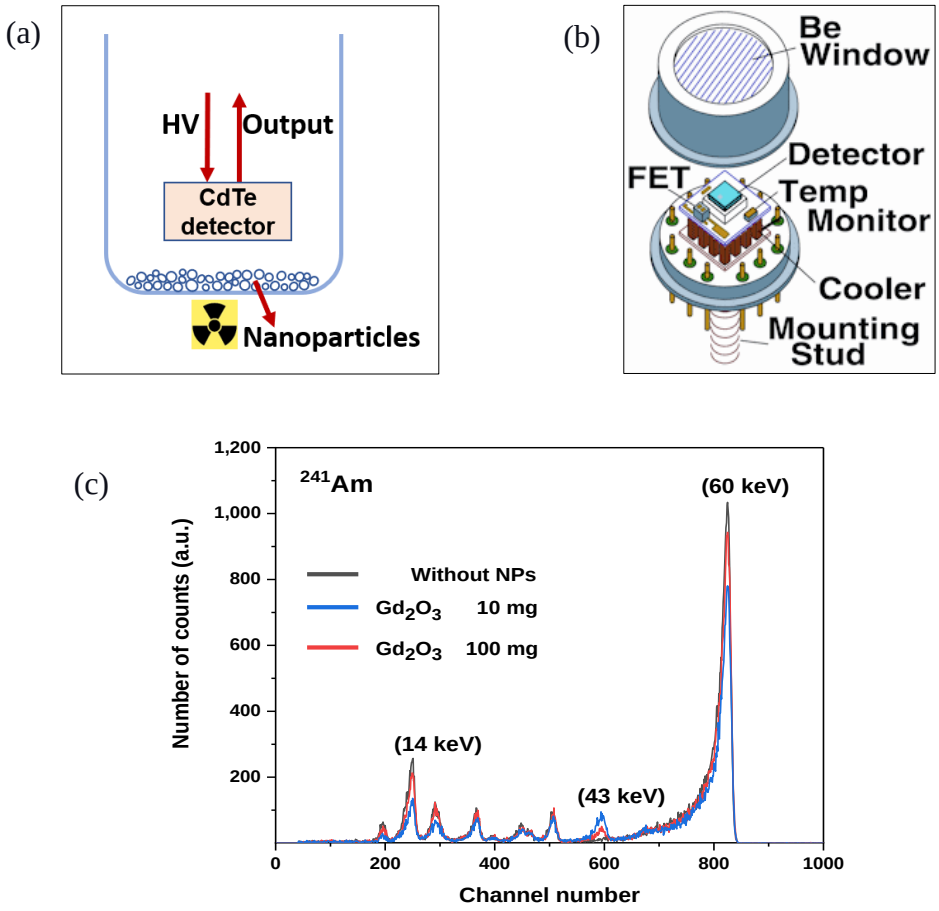

Figure 4-9 (a) Set-up (b) schematic of CdTe detector used (Amp-Tek XR-100T). (c) variations in PHS of ^{241}Am with CdTe detector upon loading Gd_2O_3 nanoparticles

The above experiments and analysis establish that the increase in the number of counts in PHS of ^{241}Am with nanoparticle-loaded liquid scintillator from those in PHS for unloaded liquid scintillator is due genuinely to the emission of electrons from the nanoparticles resulting from the interaction. The K-absorption edge of Gd being ~ 50 keV may facilitate the successful enhancement of interaction of gamma-rays from ^{241}Am (~60 keV). Meanwhile, for gamma-rays from other sources like ^{55}Fe, ^{133}Ba, X-rays used etc. also, among the species of nanoparticles, Gd_2O_3 nanoparticles offered the greatest enhancement.

Inference of results

The interpretation of the results in Figure 4-7 follows those for Gd_2O_3 nanocomposites in Figure 3-8. The liquid scintillator replaces the plastic scintillator in that study. Further, the exit of an electron depends on the ease with which the nanoparticle permits it to do so. The PHS with the nanoparticle-loaded liquid scintillator is featureless as the electrons share part of their energy unduly with other atoms inside the nanoparticle or with other nanoparticles. Scintillation photons undergo scattering or partial absorption with nanoparticles, as sketched in Figure 4-10.

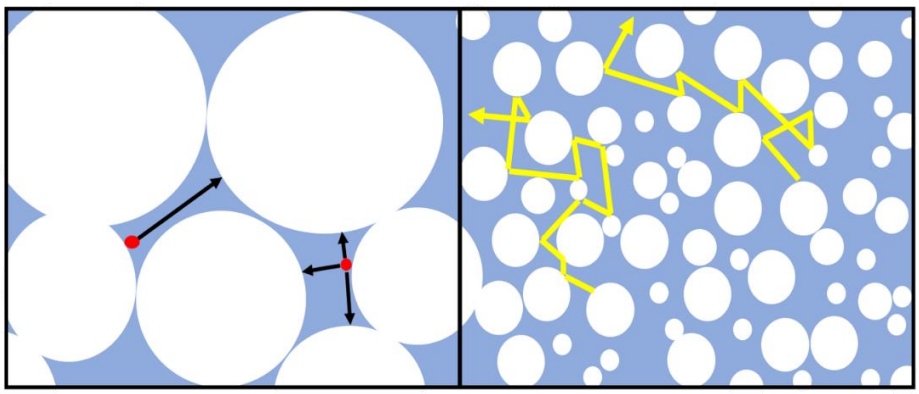

Figure 4-10 Scattering or absorption of scintillation and nanoparticle emitted electrons. Adapted from [174]. The red dots in the left image represent the electrons. Yellow arrows in the right image represent the movement of scintillation photons.

Additional loading of nanoparticles increases the packing density in the dispersed medium and at the bottom or the concentration of the nanoparticles in the liquid, leading to increased interactions. It results in the emission of energetic electrons. However, the loading also increases the attenuation and/or scattering of electron/scintillation (Figure 4-10). The relative increase of these events dictates the net counts at a given loading. In the current set-up, the concentration achieved by loading 800 mg of Gd_2O_3 nanoparticles resulted in the greatest number of counts. When nanoparticles form their layer at the bottom, the electrons exiting from nanoparticles settled in the top few contribute to increased counts. Beyond the optimum loading, the gamma-rays or the electrons emitted are attenuated within the settled nanoparticles layers. Thus, the number of counts starts reducing.

4.2.1.1 *Effect of species of nanoparticles: Interaction with AuNPs*

AuNPs are considered to represent the effect of species of nanoparticles. Among the species studied here, those that responded like Au include Ag, CuO, Fe_2O_3, PbO, Pd, Pr_2O_3, Sn, W, WO_3, and Zn. AuNPs are chosen to represent them as they are, by far, the most extensively investigated species of nanoparticles for nanoparticle radiosensitization [7,8]. Figure 4-11 presents the variations in PHS for unloaded liquid scintillators upon loading AuNPs. Upon loading the nanoparticles, the number of counts in PHS with a nanoparticle-loaded liquid scintillator got reduced. The reduction in the number of counts occurred at all channels. Additional loading of AuNPs reduced the number of counts further. The histogram displays the variations in the total number of counts in PHS.

(a)

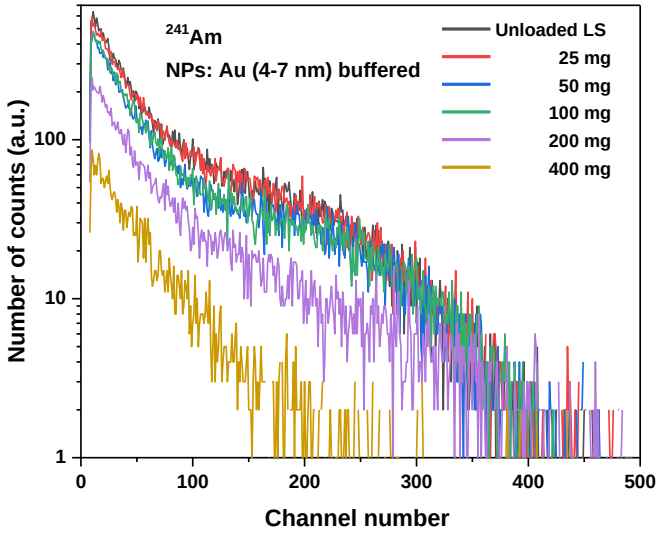

(b)

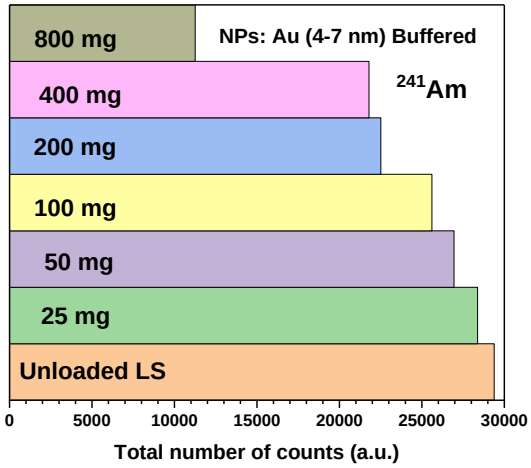

Figure 4-11 (a) Variations in PHS of ^{241}Am with liquid scintillator upon loading AuNPs (b) histogram displaying the variations in the total number of counts in PHS

Going by the rationale of the experiment, AuNPs absorb the gamma-rays within themselves. Specifically, AuNPs undergo interaction with gamma-rays from ^{241}Am, but the exit of electrons energetic enough to scintillate the medium into the liquid scintillator is not evidenced.

Confirmation of gamma-attenuation

Before inferring the results further, it was necessary to establish that the reduction in the number of counts in PHS is due only to the attenuation of gamma-rays within the Au nanoparticles. Following experiments and analysis were performed for the same.

The reduced counts in PHS upon loading the nanoparticles confirm the interaction of photons with the nanoparticles. Under identical conditions, Gd_2O_3 nanoparticles interacted with the photons and emitted numerous energetic electrons into the liquid scintillator. AuNPs (buffered)

may settle at the bottom of the beaker due to the higher density of citrate solution than that of the toluene and hence may not resemble the conditions as in the Gd_2O_3 nanoparticle-loaded liquid scintillator. However, unbuffered Au, and Pd nanoparticles follow the dispersion or settlement at the bottom, like that of Gd_2O_3 nanoparticles.

Maintenance of the shape of PHS at smaller loadings in Figure 4-11 suggests that the nanoparticles reduce the gamma-ray flux reaching the liquid scintillator. For an analogy, the variations in PHS with an unloaded liquid scintillator after inserting a known photon attenuator (Au:Sn 80:20 alloy sheet) were introduced between the source and liquid scintillator (Figure 4-12) studied. The variations resemble those observed after loading AuNPs into the liquid scintillator. This resemblance confirms that while Au:Sn 80:20 sheets attenuate a portion of gamma-rays before the rays strike the liquid scintillator, the nanoparticles attenuate the rays by staying inside the liquid scintillator.

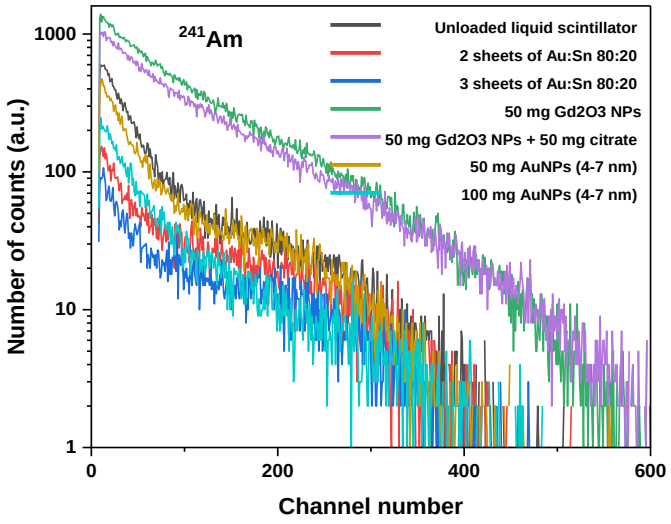

Figure 4-12 Variations in PHS of ^{241}Am in liquid scintillator upon inserting Au:Sn 80:20 sheets between the source and the beaker. Also displayed are the variations in the same PHS upon loading citrate solution into the liquid scintillator

Earlier studies with NPRS have found that the coating over the nanoparticles absorbs some electron energy [11,24,52,175]. To assess the extent of attenuation of electron energy by the buffer, the variations in PHS were obtained in three situations: loading citrate buffer alone, loading buffered AuNPs, and loading unbuffered Gd_2O_3 nanoparticles plus the neat citrate buffer solution. The results are included in Figure 4-12. Loading 50 mg of neat citrate to the neat liquid scintillator reduced the number of counts by about 1% (not shown due to the proximity of spectra). Loading 50 mg buffered 4-7 nm AuNPs reduced the number of counts by about 9%. Loading 50 mg Gd_2O_3 nanoparticles and 50 mg neat citrate increased the number of counts by about 330%. Due to its intermediate density, the citrate buffer separates the layer of Gd2O3 nanoparticles from the liquid scintillator. The number of counts increased upon loading Gd_2O_3 nanoparticles as these nanoparticles emit energetic electrons into the surrounding. Thus, the citrate coating is not a deterrent for the exit of electrons into the scintillator. If the electrons are

emitted from AuNPs with enough energy, like those emitted from Gd_2O_3 nanoparticles, electrons could traverse the citrate and strike the scintillator.

It is possible that the loading of 25 mg AuNPs forms a layer that was enough to stop all the gamma rays and the electrons emitted from the nanoparticles from entering the liquid scintillator and that the smaller loadings may facilitate the detection of electrons. The minimum quantity of buffered AuNPs drawn into the microsyringe was 25 µL weighing ~25 mg. The nanoparticles in powder form, such as AuNPs (unbuffered) and Pd nanoparticles, could be loaded in lesser quantities. Their loading could be further reduced with dilution. PHS was obtained by loading Pd nanoparticles with lesser loadings (Figure 4-13). Histogram was chosen to represent the variations since the spectra were indistinguishably close. The number of counts remained lower than that in reference PHS for all loadings. With each reduction in loading, the PHS approached that with an unloaded liquid scintillator but never yielded an increased number of counts than that in reference PHS.

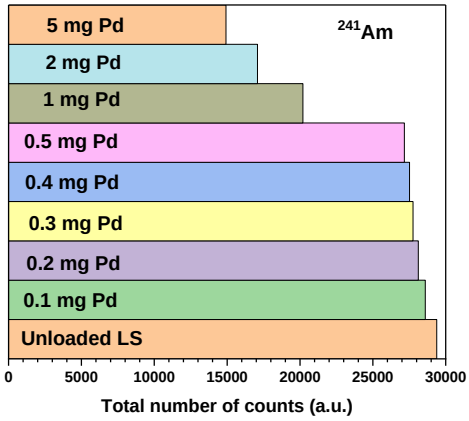

Figure 4-13 Histogram of the number of counts in PHS of ^{241}Am with liquid scintillator upon loading Pd nanoparticles

In another possibility, the electrons are emitted from the nanoparticles but go undetected at a given HV to PMT. To investigate, the experiments were conducted at higher HVs till 1000 V. However, the results were indifferent to those at 800 V HV (Figure 4-14).

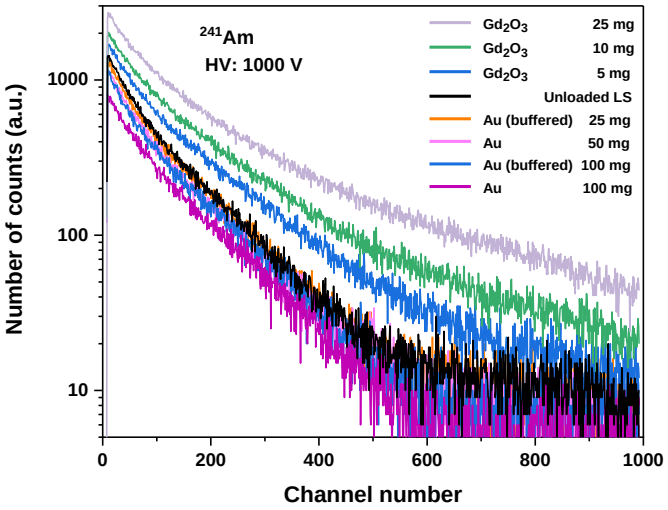

Figure 4-14 Variations in PHS of ^{241}Am with liquid scintillator upon loading AuNPs observed at higher HV of 1000 V. For clarity, the legend is arranged in the order of appearance of plots from top to bottom.

Inorganic materials are generally insoluble in toluene. However, an unacknowledged chemical effect on the surface of nanoparticles inducing the surface absorption of the electrons might cause a reduction in the number of counts. Further, the literature cites that the metals and metal oxide nanoparticles react heavily, especially in wet chemical environments [6]. As nanoparticles interact with molecules due to charge imbalance or Van-der-Waals attractive forces, a corona layer may get deposited on the nanoparticles' surface [176]. This layer can modify nanoparticle properties fundamentally in terms of agglomeration, surface structure, or charge [6] or mitigate the expected interactions [7]. The nanoparticles were irradiated with beta-radiations to investigate this possibility. The results obtained by replacing ^{241}Am with ^{90}Sr/^{90}Y beta source are shown in Figure 4-21 ahead. At lower loadings, the number of counts increased drastically. As shown in section 4.2.3 and section 4.2.4, the interaction of beta and alpha radiations with the nanoparticles results in the emission of electrons from the nanoparticles. Thus, the undue chemical/surface effect on the emission of electrons from the nanoparticles is negated.

Another possibility is quenching (section 2.3.3.3). The effect of quenching will shift the centroid of the full-energy peak to lower channels. The number of counts in PHS increase after interacting with beta- and alpha-radiations (sections 4.2.3 and 4.2.4). Buffered AuNPs form a few layers at the bottom with a large gap (~30 nm) between the nanoparticles as buffer solution separates them. Once the electron or scintillation leaves the layer of nanoparticles, chemical or optical quenching is practically avoided. Thus, quenching is insufficient in reducing the number of counts in PHS of gamma-rays with an AuNP-loaded liquid scintillator.

The gamma-ray flux striking the nanoparticles may be less. The estimated probability of interaction of gamma-rays of higher-energies employed in radio-sensitization with AuNPs is approximately 10^{-5} to 10^{-4} [8,177,178]. While over 99% of the nanoparticles available fail to convert

the rays, 75% of ionizations lead to the emission of only one or two electrons from the AuNPs [38]. Here, over 10^5 gamma-rays from ^{241}Am or 10^8 X-rays with 10 keV weighted average energy strike the target per second, providing enough flux.

Thus, the outcomes of the interaction of photons from ^{241}Am with WO_3, PbO nanocomposites and AuNPs, and other selected species are validated. Hence, the outcome of low-energy photons varies with the species of nanoparticles.

Two possibilities, however, remain. The electrons may exit AuNP nanoparticles but all with an energy lower than the scintillation threshold (the minimum energy needed by the electron to cause scintillation) of the liquid scintillator. Liquid scintillation counting theory estimates that the scintillation threshold for toluene-based liquid scintillators is about 100 eV [168]. In practice, the interaction of a beta particle of 1 keV or less with a liquid scintillator creates photons energetic enough to register a count in two oppositely placed PMTs in LSCs[149]. The theory also states that characterizing the scintillation threshold of a given liquid scintillator or a scintillation setup is challenging [132,149]. In most practical applications, a liquid scintillator is expected to detect the lowest energy beta-radiations from ^{3}H (average ~6 keV)[149]. Notwithstanding that, the present liquid scintillator set-up was tested for detecting low-energy X-rays from the available sources. The results of the interaction of X-rays from ^{55}Fe and an X-ray gun at 4 kV_p are displayed in Figure 4-15. The variations in PHS follow those with ^{241}Am. For Gd_2O_3 nanoparticles, the loading that results in the greatest number of counts in PHS is reduced to 50 mg.

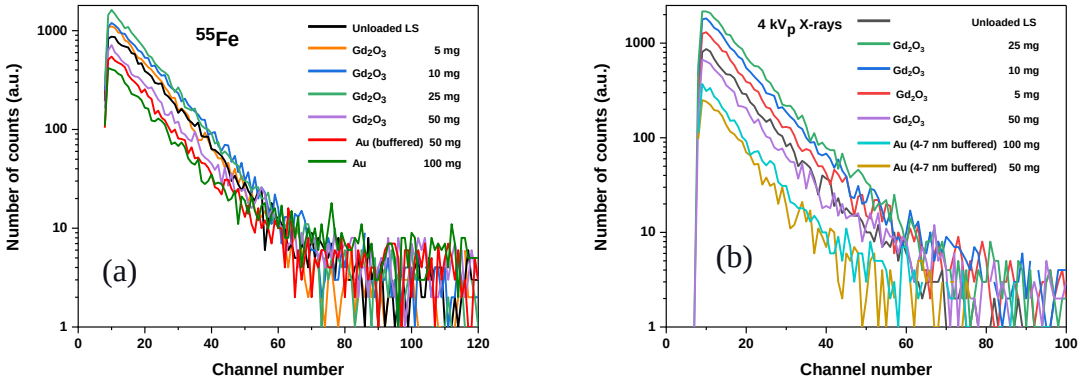

Figure 4-15 The variations in PHS of X-rays from (a) ^{55}Fe, (b) 4 kVp gun

For the current analysis, the unloaded liquid scintillator yielded a definite PHS. It testifies that the current setup can detect all electrons striking it with energy greater than at least 4 keV. The liquid scintillator and set-up could not be characterized for lower energies due to the non-availability of suitable sources., Further, if AuNPs emit electrons with energy insufficient to scintillate the liquid, electrons go undetected. That is a limitation of the present technique itself.

Secondly, electrons may exit from the smaller AuNPs than those studied here, as larger nanoparticles may attenuate the electrons within themselves. The present study could not test smaller AuNPs than 4 nm, as they were not readily available. This is the second limitation of

this work. However, though AuNPs of 1.4 nm or 1.9 nm are used, those of 14 nm, 50 nm, and 80 nm [7,8,37] is also used in the previous studies. The literature has not mentioned any specific performance change due to size variations of AuNPs.

Inference of the results

Figure 4-16 shows the interaction of gamma-rays from ^{241}Am with different species of nanoparticles. Distinct display of the PHS was given priority during the display of the responses than a common loading. Since the nanoparticles vary in species, size, and purity, no inference is attempted.

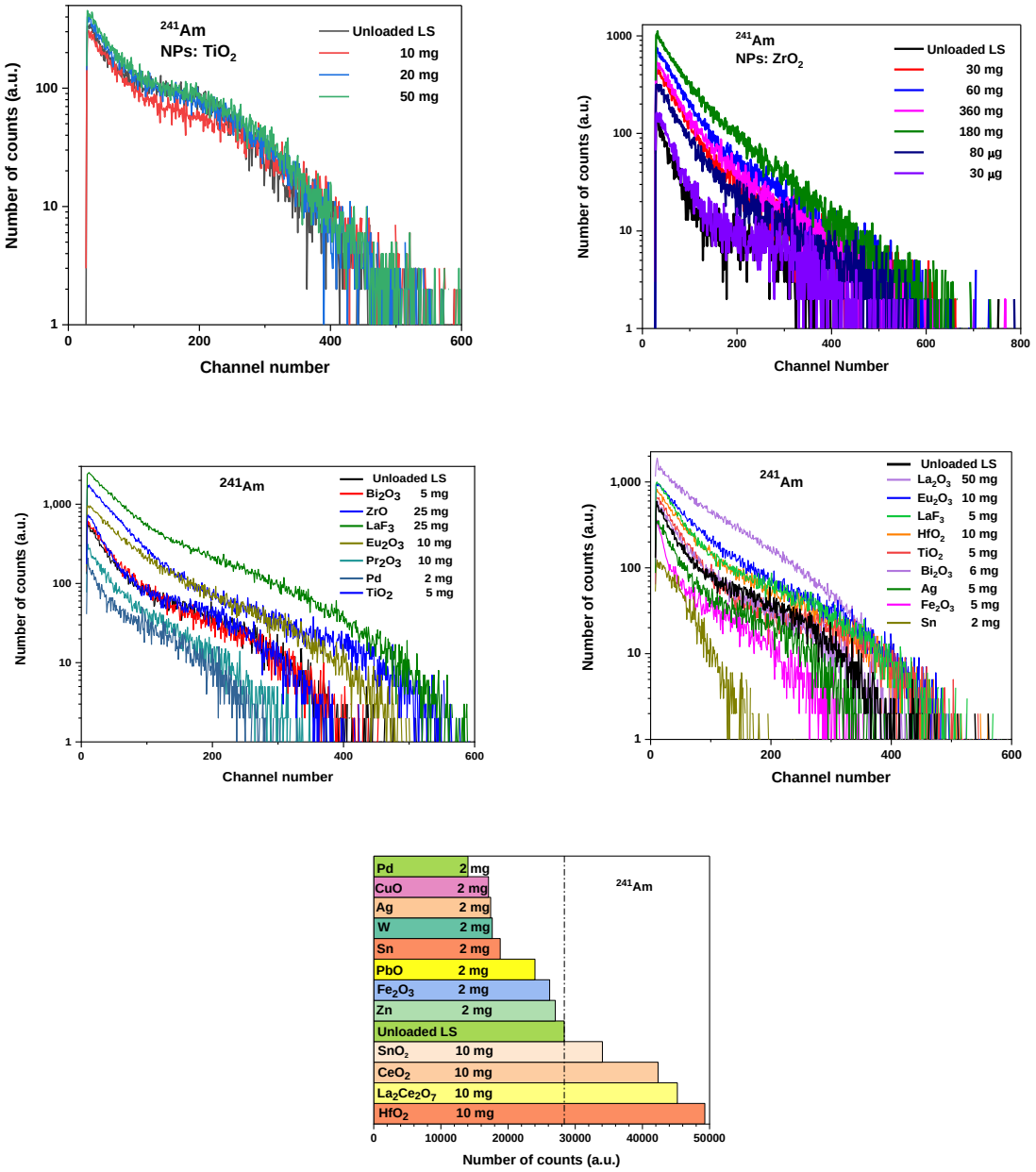

Figure 4-16 Variations in PHS of ^{241}Am with liquid scintillator upon loading different nanoparticles and histogram showing the variation in the total number of counts in PHS

Table 4-3 categorizes the species studies into 'electron-emitting' and 'photon-attenuating.'

Table 4-3 Categorization of nanoparticles as electron-emitting and photon-attenuating

#	Electron emitting nanoparticles*	Photon-attenuating nanoparticles
1	Bi_2O_3, CeO_2, Eu_2O_3, Gd_2O_3, HfO_2, La_2O_3, $La_2Ce_2O_7$, LaF_3, SnO_2, TiO_2, ZnO, ZrO_2	Ag, Au, CuO, Fe_2O_3, PbO, Pd, Pr_2O_3, Sn, W, WO_3, Zn

*For the sizes as in this study. The size of nanoparticles affects the outcomes (section 4.2.1.3). Their larger size versions could become photon-attenuating.

4.2.1.2 *Effect of loading or concentration of nanoparticles*

The effect of loading the nanoparticles is observable in Figure 4-7 and Figure 4-11. It is the effect of an ensemble of nanoparticles. The effect is noted and inferred in section 4.2.1. Thus, in electron-emitting nanoparticles, an optimum concentration yields the greatest number of electrons from the ensemble of nanoparticles. In gamma-absorbing nanoparticles, the effect of loading is to increase attenuation since the number of interactions increases.

4.2.1.3 *Effect of size of nanoparticles*

The variations in PHS of ^{241}Am with a liquid scintillator upon loading nanoparticles of different sizes are displayed in Figure 4-17.

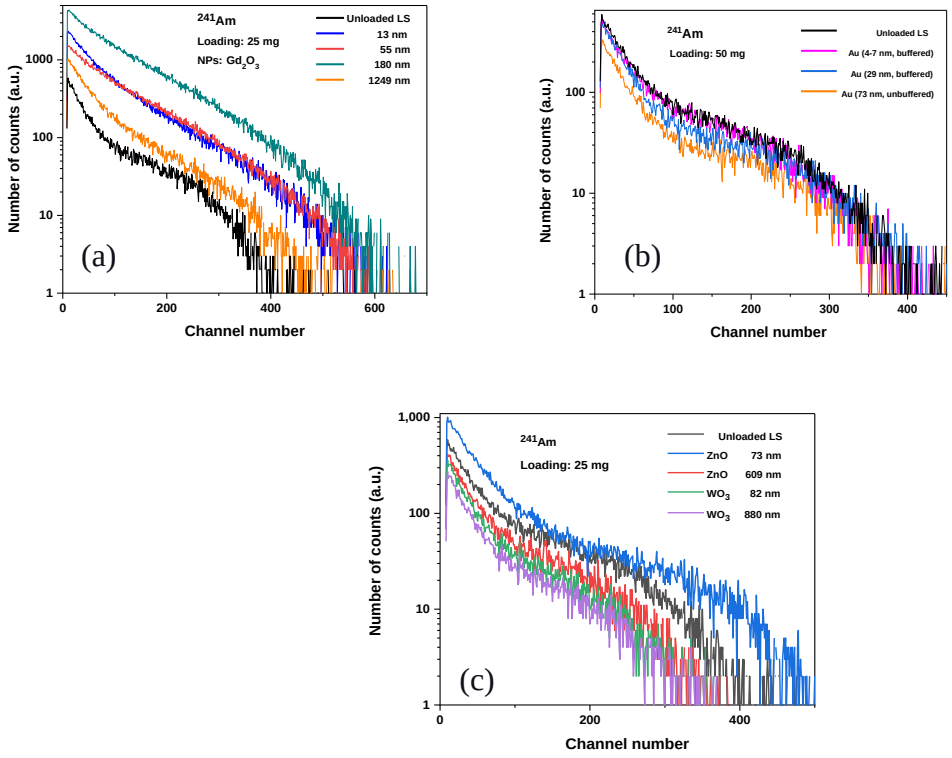

Figure 4-17 The variations in PHS of ^{241}Am in unloaded liquid scintillator upon loading (a) Gd_2O_3 (b) Au (c) ZnO and WO_3 nanoparticles of different sizes

The spectra in Figure 4-17 exhibit distinct variations in shape displaying the effect of size of the nanoparticles across different species. The shape of the spectra varies with the nature of nanoparticles as in Figure 4-17. The variations suggest that the energy of electrons emitted from the nanoparticles varies with the species of nanoparticles. The extent of reduction increased with the size of the WO_3 and Au nanoparticles.

In electron-emitting nanoparticles like Gd_2O_3 and ZnO, the increased size increases the probability of interaction within a single nanoparticle. The increased nanoparticle size, however, increases the probability of attenuation of emitted electrons within the nanoparticle. A photoelectron emitted from a core atom exits the nanoparticle when the distance from the interacting atom to the edge of the nanoparticle is shorter than the range of electrons inside the nanoparticle material. Optimum-sized electron-emitting nanoparticles facilitate the emission and exit of the greatest number of electrons. Notably, 180 nm need not be an optimum size for Gd_2O_3 species of nanoparticles. Larger-sized electron-emitting nanoparticles would effectively attenuate the gamma-rays. Thus, in electron-emitting nanoparticles, the size of the nanoparticles affected the outcome of interactions. In photon-attenuating nanoparticles, the extent of attenuation increased with the size of the nanoparticles.

4.2.1.4 *Effect of energy within low-energy photons*

Figure 4-15 and Figure 4-18 show the variations in PHS of different low-energy photons for unloaded liquid scintillators upon loading the electron-emitting Gd_2O_3 nanoparticles. The histogram in Figure 4-18 shows the extent of the count increase. The maximum number of enhancements when photons from ^{55}Fe, 38 kVp gun, ^{241}Am, and ^{133}Ba interacted with Gd_2O_3 nanoparticles were about 1.5, 3.8, 39.2, and 2.8 times, respectively. These trends were similar when any of the electron-emitting nanoparticles were loaded. Upon loading photon-attenuating nanoparticles, the number of counts in PHS upon loading reduced for all photon sources.

The extent of the increase or decrease in counts indicates the intensity of interaction. The extents of enhancement in counts with the energy of photons indicate that a range of energy within the low-energy photons leads to an intense interaction with electron-emitting nanoparticles. Currently, the greatest enhancement in counts is observed for X-rays from the gun and gamma-rays from ^{241}Am. Thus, the range energy exists between 10 keV (weighted average energy from 40 kVp gun) and 81 keV (one of the principal energies of ^{133}Ba), with 14 keV and 60 keV of ^{241}Am lying in-between. Determining the exact value of the energy of the photon that induces the most intense interaction requires studies with monoenergetic sources.

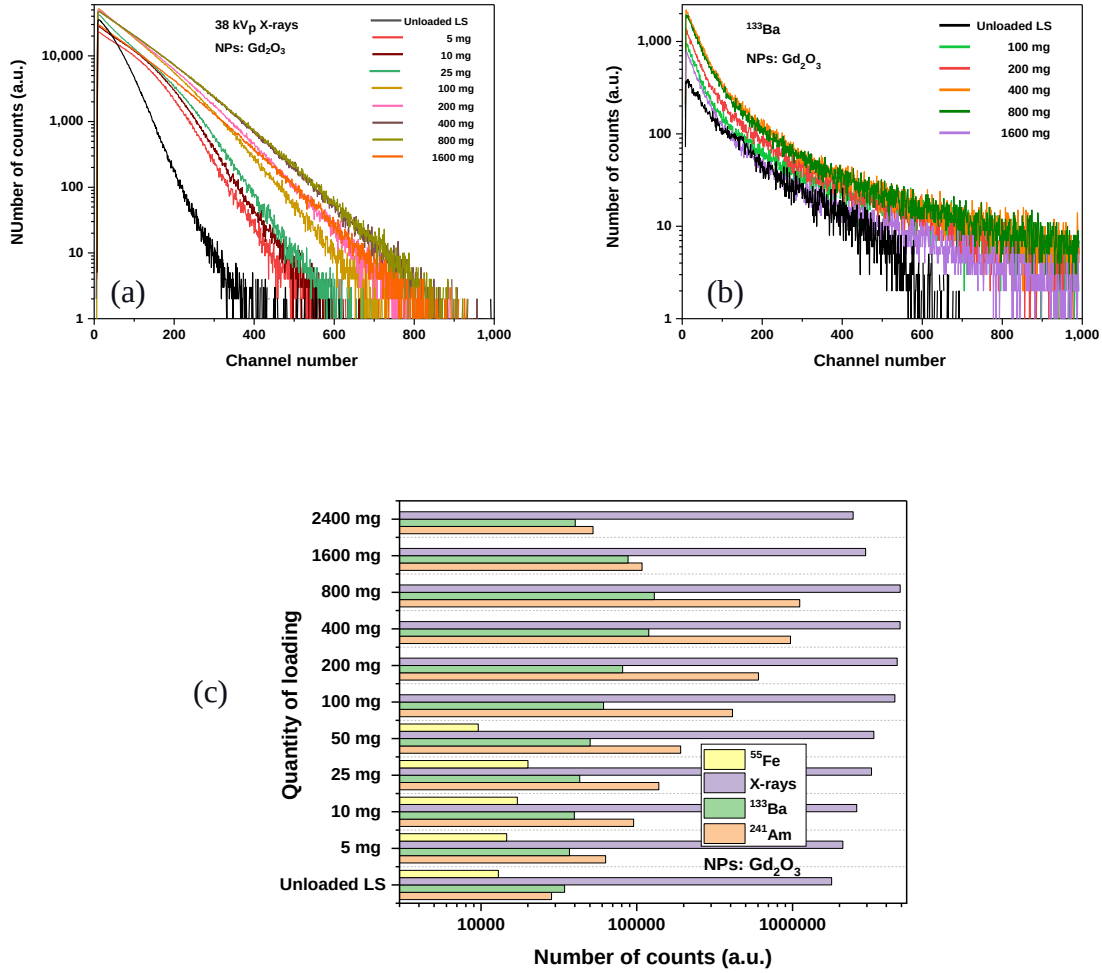

Figure 4-18 The variations in PHS of (a) X-rays from 38 kVp gun (b) gamma-rays from ^{133}Ba in liquid scintillator upon loading Gd_2O_3 nanoparticles at different concentrations (c) Histogram displaying the extent of enhancement of counts for low-energy photons all the loadings tried.

4.2.2 Interaction of high-energy photons with nanoparticles

Here, the gamma-rays emitted from ^{22}Na, ^{137}Cs, and ^{60}Co are considered high-energy photons. The outcomes of interactions of these radiations with Gd_2O_3 nanoparticles and AuNPs are shown in Figure 4-19. The extent of variation in the number of counts is displayed in the histogram. The extent of enhancement of counts upon loading Gd_2O_3 nanoparticles, if any, was insignificant compared to those with low-energy photons. The greatest variations in counts for loadings between 1 mg and 200 mg of Gd_2O_3 nanoparticles were about 1.1 and 0.8 times that for unloaded liquid scintillators, respectively. At higher loadings, the number of counts decreased upon loading the nanoparticles. The number of counts in PHS upon loading AuNPs was reduced for all loadings and all sources.

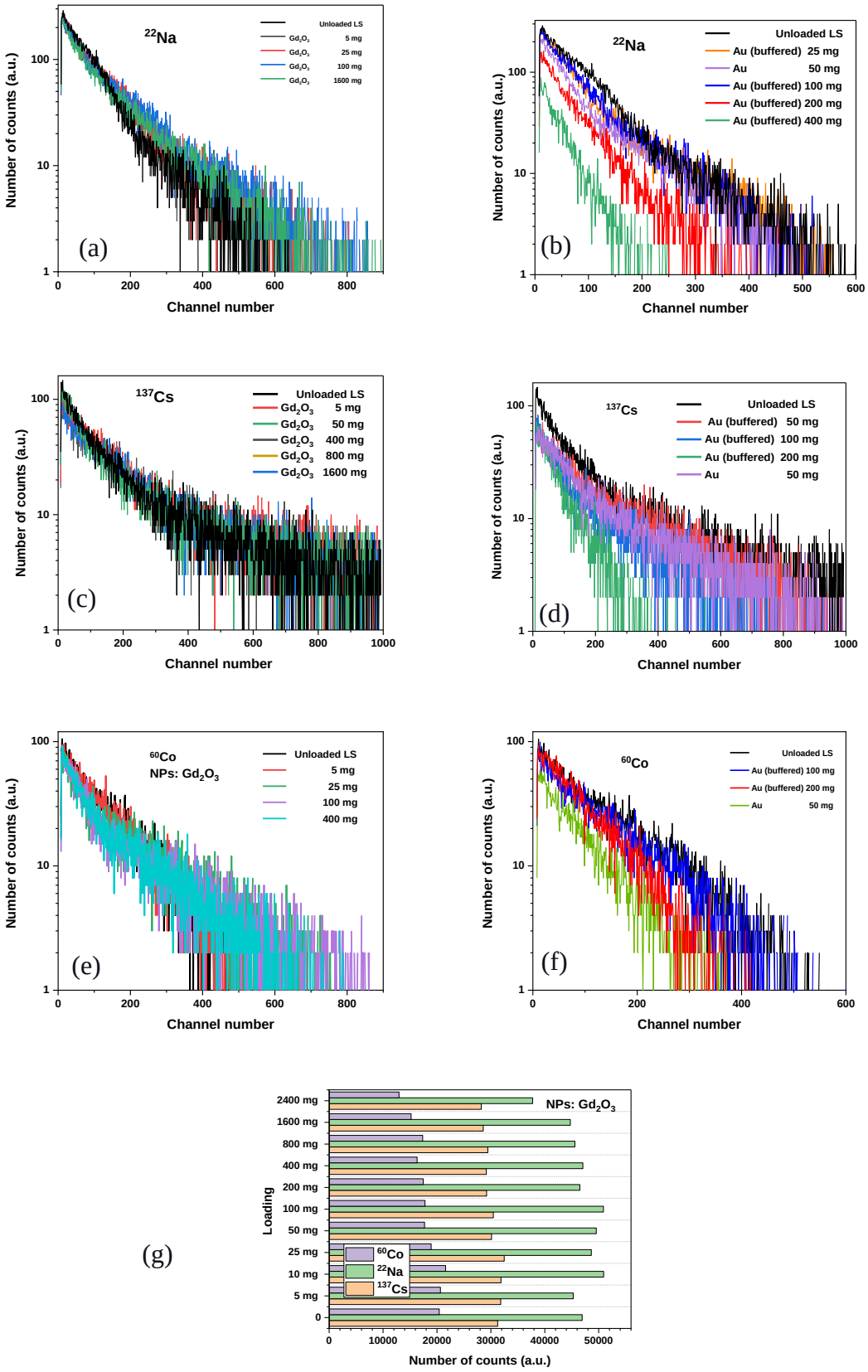

Figure 4-19 The variations in PHS of (a) & (b) ^{22}Na (c) & (d) ^{137}Cs (e) & (f) ^{60}Co with liquid scintillator upon loading Gd_2O_3 nanoparticles and AuNPs (g) Histogram displaying total counts in PHS upon loading Gd_2O_3 nanoparticles

By the rationale of the technique, high-energy gamma-rays seldom interact with nanoparticles. It is independent of species of nanoparticles.

For analysis, the attenuation lengths and interaction efficiencies of unloaded and loaded scintillators estimated for bulk materials are shown in Figure 4-20. The data is taken from the NIST XCOM photon cross sections database for the bulk materials. Toluene represents the liquid scintillator as it constitutes more than 99.2% of the scintillator. Nanoparticles are supposed to be distributed uniformly. Contributions of both the photoelectric effect and Compton scattering are included. The estimations consider the photons with energies ranging up to 2 MeV.

With the addition of nanoparticles into the liquid scintillator, the attenuation length significantly reduces for photons up to about 200 keV. The plot shows that the addition of nanoparticles enhances the interaction efficiencies. Meanwhile, the reduction in attenuation length is smaller for photons with greater energies than this 200 keV. Alongside, the interaction efficiency increases significantly for low-energy photons, which is reflected in Figure 4-8. For photons with energies greater than 500 keV (^{22}Na energy is 511 keV, 1.27 MeV), the increase in efficiency is only about 10% (maximum) even for the greatest amount of loading, where the overall efficiency itself is less than 20%.

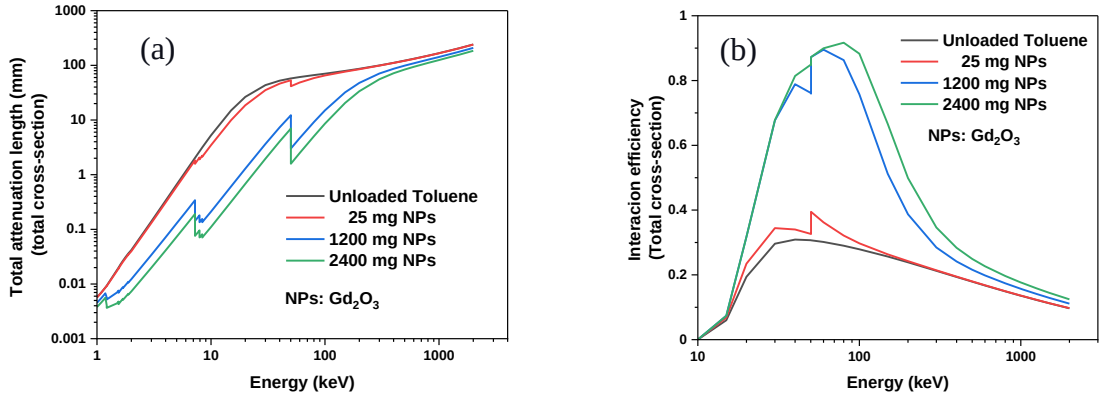

Figure 4-20 (a) Attenuation lengths and (b) Interaction probability of photons in an unloaded and loaded scintillator

Reduction in counts at higher loadings indicates that electrons energetic to traverse the layer of nanoparticles (such as those emitted upon interacting with low-energy photons) are not emitted upon interacting with high-energy photons. These analyses indicate that the probability of interaction of high-energy photons is low.

Taking the results of low and high-energy photons together, it is observed that only the low-energy photons interact with nanoparticles efficiently. Variations in the size of nanoparticles or energy of radiations displayed no considerable effect on the outcome.

4.2.3 Interactions of beta-radiations with nanoparticles

Figure 4-21 displays the variations in PHS of beta-radiations from $^{90}Sr/^{90}Y$ with a liquid scintillator upon loading the nanoparticles. When 5 mg Gd_2O_3 nanoparticles were loaded, the number of counts in PHS increased at lower channels. When the loading was increased to 10 mg, the number of counts was reduced at all channels. Figure 4-22 displays the variations in PHS of beta-radiations from ^{204}Tl and ^{147}Pm upon loading the nanoparticles. For demonstration purposes, the acquisition time in Figure 4-22 (b) was 20 minutes instead of the nominal 2 minutes. The number of counts increased at lower loadings at all channels. The quantity of loading varied with the species of nanoparticles. There appeared an optimum loading at which the extent of increase in counts is greatest. The trend in variation of counts was independent of species of nanoparticles for all beta-radiations.

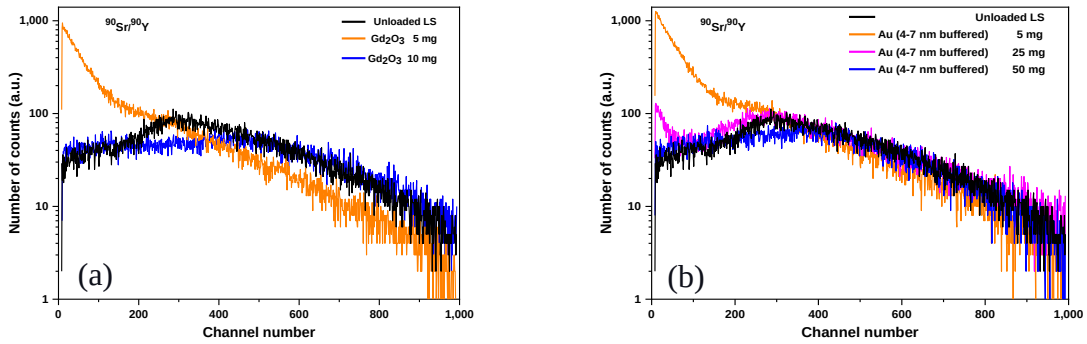

Figure 4-21 Variations in PHS of $^{90}Sr/^{90}Y$ with liquid scintillator upon loading (a) Gd_2O_3 nanoparticles and (b) AuNPs. Effects of species and loading are observed.

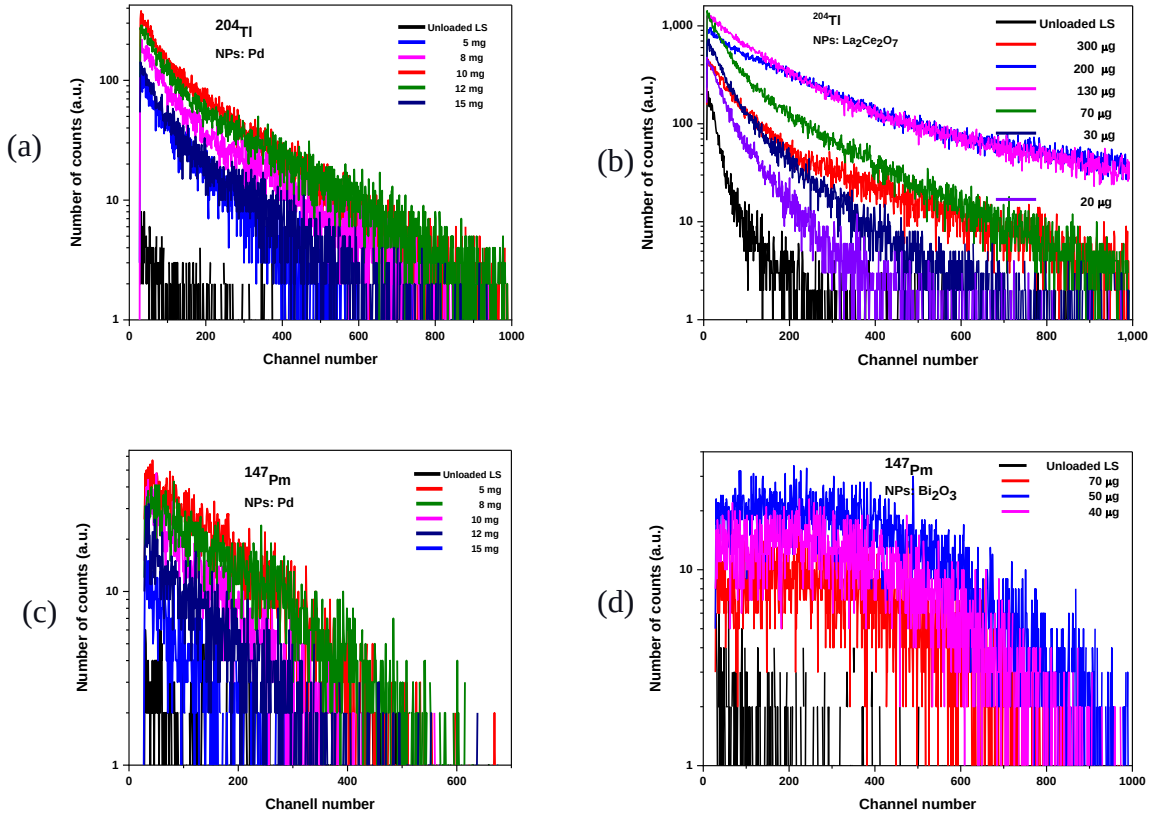

Figure 4-22 The variations in PHS of (a), (b) ^{204}Tl, and (c), (d)^{147}Pm with liquid scintillator upon loading different nanoparticles.

Going by the rationale of the technique, the interaction of beta-radiations with nanoparticles results in the emission of electrons from the nanoparticles. The presence of even a small component of gamma rays in the decay spectrum of a beta-ray source can bring ambiguity into the inference of beta-radiation interactions. Also, the bremsstrahlung can contribute to the enhancement of counts. ^{90}Sr/^{90}Y and ^{147}Pm are pure beta-emitters. Also, the interaction of beta-radiations enhances the counts in PHS of all species of nanoparticles. Taken together, the enhancement of counts in PHS of beta-radiations upon loading the nanoparticles is genuinely due to the emission of electrons from the nanoparticles.

The liquid scintillator is a good beta detector that detects betas directly. When a beta-ray strikes a nanoparticle, the interaction can generate electrons at the entry, inside the core, and at the exit of the nanoparticle, depending on the energy of incoming radiation. Some electrons generated at the core can exit the nanoparticle, depending on their initial energy and the distance to the edge. The increase in counts at lower channels is mainly due to the emission of low-energy electrons at the surfaces. Further, after having deposited some energy within a nanoparticle, beta-radiation may traverse the nanoparticle and continue to interact with the scintillator and/or the nanoparticle until it deposits its entire energy or exits the medium. The scintillator directly detects these transmitted beta-radiations. Thus, loading the nanoparticles into the liquid scintillator enhances the stopping power of the scintillator for beta-radiations.

Loading affects the outcome of the interaction of beta-radiations with an ensemble of nanoparticles. Since at lower loadings, a few nanoparticles are settled at the bottom, and the inter-particulate distances between the nanoparticles suspended in the liquid are large enough for beta-radiations to deposit their entire energy, increasing the number of counts in PHS is observed only at lower loadings. At higher loadings, the thickness of layers of nanoparticles is enough to attenuate the beta-radiations, and neighboring nanoparticles reabsorb the electrons emitted from the nanoparticles. A balance between these phenomena yields the greatest enhancement in counts (Figure 4-22).

The outcome of the interaction of beta-radiations is independent of the species of nanoparticles. The study of the effect of the size of nanoparticles could not be concluded since obtaining a small quantity (in micrograms) of the same nanoparticles differing only in size was challenging. The trials resulted in indistinguishable variations.

Beta-spectrum is a continuum having radiations up to end-point energy. Hence, inferring the effect of the energy of beta-radiations on the outcomes is hard. Determining the effect of energy requires arrangements to obtain monoenergetic electrons.

4.2.4 Interactions of alpha-radiations with nanoparticles

Figure 4-23 shows the variations in PHS of alpha radiations from ^{241}Am(α) with a liquid scintillator upon loading the nanoparticles. The number of counts in PHS increased upon loading the nanoparticles. They increased at all channels. Increased loading of nanoparticles reduced the counts. A similar trend was observed for all species of nanoparticles.

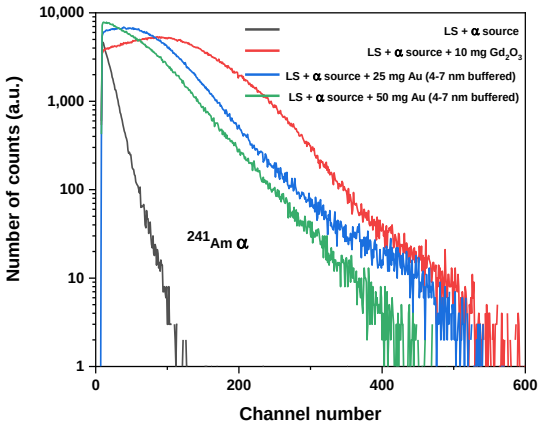

Figure 4-23 Variations in PHS of alpha-radiations from ^{241}Am(α) with liquid scintillator upon loading the nanoparticles.

Going by the rationale, alpha-radiations interact with the nanoparticles to cause the emission of electrons from the nanoparticles. ^{241}Am(α) emits gamma-rays also. As detailed in section 4.1.3.1, at 600 V HV, only the outcomes of alpha-radiation interaction are registered in the PHS.

Alpha radiations interact electrostatically to release numerous electrons from the nanoparticles, possibly through the emission of secondary electrons. An alpha particle may get transmitted through a nanoparticle after having deposited its partial energy within the nanoparticle. A large number of electrons emitted from the surfaces of the nanoparticles cause an increase in counts at lower channels. Increased loading of nanoparticles increases the density of target materials and thus reduces the number of counts as the electrons emitted get attenuated within the layer of nanoparticles. The interaction of alpha-radiations is independent of the species of nanoparticles.

Limited control over the positioning of the source disabled the study of the effects of the size of nanoparticles. It was challenging to repeatedly position this ~5 mm diameter disc with its face up inside a 22 mm diameter beaker. The effect of energy could not be ascertained due to the non-availability of another source.

4.3 Discussion

4.3.1 Features, capabilities, and limitations of the technique

The technique developed determines the outcome of the "simple physical interaction of ionizing radiations with nanoparticles." as demanded by the researchers[7]. There is no upper limit for the energy of incoming radiation. The set-up is scalable. The technique uses a liquid scintillator to directly detect the emission of fast electrons, thus obviating the need for a high vacuum. The technique is straightforward, quick, and nondestructive.

The technique can determine the relative efficacies of given nanoparticles for a given application. The importance of this is highlighted by the studies that have utilized practically synthesized nanoparticles of varying degrees of imperfection. Further, nanoparticles can be loaded in their final form in practical applications. Sample preparation is unwarranted. The technique enables the study of the effect of inorganic coating over the nanoparticles. This is useful for determining the suitable coating of nanoparticles.

However, the technique cannot detect the electrons emitted from the nanoparticles with energy lower than the scintillation threshold of the liquid scintillator. There is a lower limit for the energy of radiations, as they need to transmit to the bottom of the beaker unless the source can be immersed in the liquid scintillator. Limitations of the current study are compiled in section 6.3.

4.3.2 Comparison with literature and inputs for the studies

This section compares the results of this study with those in the literature. It also compiles the inputs for the studies concerning practical applications.

Since these are the first empirical results on the outcomes of the interaction of given ionizing radiation with given nanoparticles, a one-to-one comparison has not been possible. The section

considers and compares concerned aspects of the previous studies based on the parameter discussed.

Effect of Species

The present study finds and categorizes the species of nanoparticles as electron-emitting and photon-attenuating (Table 4-3). In literature, the enhancement of photon-detection efficiency of the plastic scintillator is repeatedly reported with the incorporation of selected species of nanoparticles such as Bi_2O_3, Gd_2O_3, HfO_2, $Hf_xSi_{1-x}O_2$, ZnO, ZrO_2 [56,57,83,58–60,65–67,70,80]. The same, incorporating a photon-attenuating nanoparticle, is not reported to the best of the survey. Meanwhile, the nanoparticles of both categories, viz. Bi, Bi_2O_3, BiO, CuO, Fe_2O_3, Fe_3O_4, Gd_2O_3, HfO_2, Pb, Pb_3O_4, PbO, PbO_2, $PbWO_4$, Sm_2O_3, TiO_2, W, WO_3, Zn, ZnO, ZrO_2, etc., are used for demonstrating nanoparticle-loaded gamma-ray shields [71,87,100,104,107–109,114,117,119,126]. Both the electron-emitting and photon-attenuating nanoparticles are effective for gamma-ray shielding.

Current findings established that the results obtained in chapter 3 are genuine. Notably, Pb, Sn, and W-based nanoparticles could have been the initial logical selection as dopants to enhance the gamma-detection efficiency. They possess high-Z, readily available, and the incorporation of atoms (not nanoparticles) of Pb and Sn into liquid and plastic scintillators enhances the gamma detection efficiency of the hosts, found in the 1960s as in ref. [74,75,130,172]. Sn and Pb-loaded scintillators are commercially available (e.g., BC-452 from Saint-Gobain, EJ-256 from Eljen Technologies). Thus, the present results indicate why only selected species of nanoparticles are repeatedly reported to have enhanced the gamma-detection efficiency of the plastic scintillators.

In the materials characterization technique of X-ray photoelectron spectroscopy (XPS), the energy of incoming photons in XPS is limited up to 1.5 keV, and the detection of photoelectrons emitted from outer shells is relied upon. Given the energy dependency of photon interaction with the bulk, the interaction in XPS need not represent those occurring with relatively high-energy photons. Nevertheless, Casta et al. used XPS to determine the electron emission from AuNPs to offer input for nanoparticle radiosensitization but observed that the number of photoelectrons emitted from AuNPs is only a few percent larger than those emitted by the Au bulk surface, contrary to their expectation [10]. In a computer tomography study, Chenjie et al. found that the extent of attenuation of photons by smaller AuNPs is greater than their larger counterparts or a commercial iodine-based contrast agent [179]. They attribute it to the increased surface area for smaller AuNPs and identify AuNPs as efficient attenuators and, thus, better contrast agents. However, using nanoparticles as radiosensitizers or dopants in plastic scintillators is motivated by the expected exit of photoelectrons or Auger electrons upon irradiation with photons of practically useful energies, owing to the smaller size feature of the nanoparticles [8,67]. In XPS, the electrons are emitted into the vacuum to get accelerated and detected. In the present setup, they are emitted into the liquid scintillator.

Effect of concentration

The present study finds that the optimum concentration of electron-emitting nanoparticles results in the greatest enhancement of counts in the PHS. Literature shows that the optimum loading of nanoparticles yields the greatest light yield[56,58,60,70,83]. The present finding that the gamma-attenuation efficiency of a polymer increases with increased loading of nanoparticles concurs with all the prior investigations [108,109,113,117,122,165].

Effect of size

Current work finds that the larger size of nanoparticles in certain species like Gd_2O_3 is not a critical factor in emitting electrons. Literature evidence that HfO_2 nanoparticles of 140 nm initial size [60], HfO_2 nanoparticles of 300 nm aggregated size [58], or $Hf_xSi_{1-x}O_2$ nanoparticles of tens of micrometer aggregation-size [60] enhances the number of counts in nanocomposites. Electrons emission is observed from Gd_2O_3 nanoparticles from 12 nm to those larger than 1000 nm. The current study finds that optimum-sized electron-emitting nanoparticles emit the greatest number of electrons. As modeled by Casta et al. [175], there exists an optimal radius of nanoparticles corresponding to maximum electron emission.

The increased size of photon-attenuating nanoparticles increases the extent of attenuation. This echoes several studies in literature[71,95,102,104,107,115,118,119,165,179,180].

Effect of energy of photons

The present work demonstrates that high-energy gamma rays seldom interact with nanoparticles. Most studies demonstrate the enhancement of gamma detection efficiency of the plastic scintillators for low-energy gamma rays[56,58,60,67,70,83,84]. However, few studies have demonstrated the enhancement of the gamma-detection efficiency of a plastic scintillator for ^{137}Cs by loading Gd_2O_3 [65] or HfO_2 [76] nanoparticles. They, incidentally, did not report the enhancement for low-energy photons, which could have been greater than that for high-energy photons.

The efforts to develop gamma-ray shields generally consider nanoparticles versus microparticles and low-energy gamma-rays versus high-energy ones for the study. The literature provides numerous reports that nanoparticles outperform microparticles in attenuating gamma-rays [87,91,96,100,102,105,106,109,113,117–123]. Multiple studies on gamma-ray attenuation report that nanoparticle-loaded polymers attenuate keV photons better than the MeV photons [71,87,96,102,104,105,107,108,113,117,118,121,165,180,181].

One article recognized that most studies do not attempt to explain why nanoparticles attenuate low-energy photons efficiently [122]. Some studies did it attribute it to the exceptionally high packing density of the nanoparticles achievable in nanocomposites [100,108,110,117] or to the large volume-fraction of grain boundaries possessed by nanocrystalline materials that act as effective sinks for radiations [100] or to higher photon interaction probability borne by the nanoparticles [105]. The results reason how the effective attenuation of low-energy gamma rays to their high-energy counterparts is intrinsic to the nanoparticles. Further, there appears to be a scale effect in intense interaction. Incorporating Pb, Sn, and W atoms enhance the gamma-counting efficiency of organic scintillators. It evidences that atoms of these materials emit

photoelectrons. However, the *nanoparticles* of these materials hinder the exit of electrons from them. Xu et al. found that the extent of attenuation of photons in computer tomography by AuNPs is greater than that by contrast agent solution containing All AuNPs attenuated better than the commercial iodine-based contrast agent [179].

4.3.3 Inputs on assumption and practical applications

Inputs on assumption

The interaction of gamma-rays with matter-at-nanoscale is assumed to be similar to that of the rays with matter-at-bulk [8,9,11,12,38]. The current results challenge this assumption.

Numerous Monte-Carlo simulations are performed based on the abovementioned supposition. Simulation results with AuNPs include that the electrons generated out of interactions of photons approximately 50 keV get emitted into the surroundings and can travel up to micrometers [50,178,182] (Figure 4-24); electrons generated by AuNPs on irradiation with high-energy photons reach distances up to hundreds of micrometers [16]; the mean range of the secondary electrons for a 50 kV_p source is nearly 3 µm [182]; incidence of ~55 keV photon would generate 40 μm ranged electrons [15]; An X-ray energy of 100 keV is estimated to produce an electron with a range of ~80 μm [58]; the energy deposited sharply peaks at long distances of 10 nm or more to the surface [38]; photoelectrons, fluorescent photons or characteristic X-rays travel longer distances of hundreds of nm [50] or fluorescent photons up to centimeters [15]. Auger electrons generated when 40 keV photons strike 20 nm AuNPs can reach distances of 250 nm [38,178]; low-energy electrons can escape the nanoparticles and travel over tens of nm in the surrounding [9]; Auger electrons are expected to carry lower energies, all < 10 keV with many at energies ~1 keV [38].

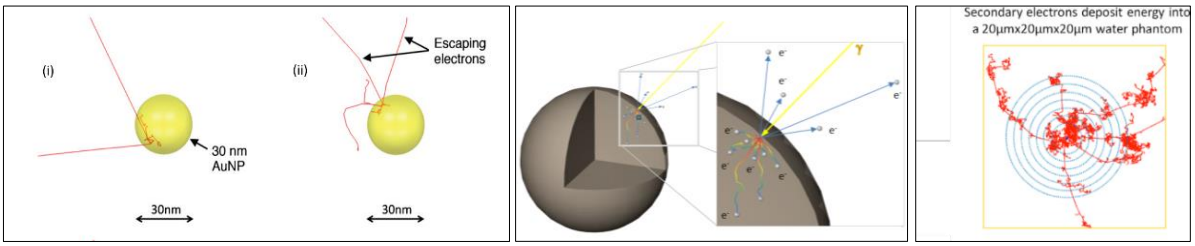

(a) (b) (c)

Figure 4-24 Simulation results. (a) The products from a single photoelectric absorption in an AuNP upon interacting with photons from (i) 6 MV source (ii) ^{125}I. Reproduced from [50] (b) Track of electrons induced by a photon outside and inside of a nanoparticle. Reproduced from [6] (c) Track of electrons from the nanoparticles. Reproduced from [178]

Further, while simulations consider water as the target medium [8,11,12] since the effective atomic number Z_{eff} and the density of the liquid scintillator used are comparable to those of the water, the electrons exiting the nanoparticles would invariably get detected in the scintillator.

Inputs for the debate over the mechanism of NPRS

Present results contribute a crucial input to the debate. A widely followed hypothesis states that the photoelectrons or Auger electrons emitted from the nanoparticles into the tumors originate

radiosensitization processes [8,9,17,22,24,28–31]. Literature explicitly comments that this hypothesis lacks definitive proof[7,8,10,26,183]. AuNPs, by far, are the most popular species of nanoparticles that demonstrate NPRS [6–9,17,24,25,39]. They are favored due to higher atomic number, ease of synthesis, control over size and shape, and ease of surface functionalization for biocompatibility[7–9,183]. However, the emission of Photoelectrons or Auger electrons from AuNPs is unobserved here. Photoelectrons emitted from Au upon interacting with gamma rays from ^{241}Am and ^{133}Ba typically carry about 46 and 67 keV energy, respectively. The estimated continuously slowing down average (CSDA) range of fast-electrons with these energies in Au is over 4000 nm and 6000 nm, respectively (physics.nist.gov). However, the transmission of photoelectrons within 4-7 nm of AuNPs is unobserved here. The energy of Auger electrons emitted from Au is expectedly small. Simulation of AuNPs irradiated with 100 keV photons yields Auger electrons with energies all ≤ 10 keV with many at energies ~1 keV [9]. Fe and Cu-based nanoparticles, upon irradiated with ^{241}Am, X-ray gun used or ^{133}Ba expectedly emit Auger electrons with energies around 5.5 and 6.9 keV, respectively. The emission of electrons from AuNPs with greater energy than the scintillation threshold of the liquid scintillator or at least 4 keV is unobserved here. Not all nanoparticles cause radiosensitization to emit photoelectrons into the surrounding.

In the case of Gd_2O_3, HfO_2 nanoparticles, numerous electrons are emitted from the nanoparticles upon interaction with low-energy photons. In terms of pre-clinical trials, these nanoparticles are ahead of others [7,8] There appear to be a few contradictory results concerning the radiosensitization using these nanoparticles with low-energy photons[7,8]. The exact mechanism of NPRS remains debatable.

Augmentation by electrons emitted supports the efficacy of brachytherapy and radiolabelled nanoparticle radiotherapy. Brachytherapy involves localized radiotherapy where radioactive isotopes internalized near malignant tissues, delivering higher doses of radiation including alpha, beta, and gamma-rays, proven beneficial as reviewed in [23,178,184]. Radiolabelling involves radiosensitization by administering nanoparticles labeled with proton/alpha/beta radionuclides into malignant tissues, as demonstrated in many studies [23,185,186].

The emission of low-energy electrons is another proposed model[8,187]. While some researchers hypothesize that the emission of electrons with much lower energies (all with energies approximately 10 keV, with many at energies lesser than 1 keV)[38,48], others debate whether such low energy electrons can cause required effects in water or tissues[8,16]. The current technique requires further characterization to scrutinize the emission of electrons with energy lower than 4 keV.

Inputs for the development of efficient, fast, large, and affordable gamma-ray detectors

Not all species of nanoparticles would suit as dopants. Based on the physical interaction alone, electron-emitting nanoparticles like Gd_2O_3, HfO_2, and ZrO_2 suit better. The emission of electrons with energy less than the scintillation threshold defeats the purpose of loading the nanoparticles into plastic scintillators to enhance the gamma detection efficiency of the hosts. Electron-emitting nanoparticles suit as dopants even if their starting size or aggregated size is

larger. Electron emission can be expected from an ensemble of nanoparticles till the concentration of nanoparticles reaches an optimum level. The selection of species of nanoparticles is more crucial than Z or the size of the nanoparticles. The optimum-sized electron-emitting nanoparticles emit the greatest number of electrons. The enhancement of gamma detection attenuation efficiency by loading the nanoparticles is feasible only for low-energy photons. Incidentally, new detectors are most required to detect low-energy gamma-rays [58,60,67,70,83].

All nanoparticles fully or partially absorb the energy of photoelectrons emitted from their constituent atoms, and the photoelectrons and scintillations share their energy with other nanoparticles. Thus, photoelectrons forfeit their characteristic leading to a loss of resolution. While most studies that enhanced gamma-detection efficiency of the plastic scintillators by loading the nanoparticles such as HfO_2, ZrO_2 [58,70,83] did not report the resolution achieved, Cai et al. reported 11.4% energy resolution for ^{137}Cs by loading Gd_2O_3 nanoparticles in polyvinyl-toluene [65]. This resolution is comparable but not significantly improved from inorganic scintillators. Hence, extending this approach to realize the detectors for spectroscopic studies warrants a 3-dimensional uniform distribution of monodisperse ultra-small nanoparticles at optimum concentration inside the scintillators. However, some applications require efficient counting of gamma-rays of known energy, such as medical imaging[68,143] or radioassays[75,172]. The latter is demonstrated in chapter 5.

Inputs for the development of radiation shields

In general, nanoparticles of any species would suit as a dopant inside the polymer to attenuate gamma-rays. Nanoparticles that efficiently convert the gamma-rays into electrons suit better, especially in applications like space electronics that forbid the emission and escape of energetic electrons from the radiation shields. Nanoparticles are efficient in shielding low-energy gamma-rays only. Incidentally, new shields are required to shield low-energy gamma rays typically used for diagnostic purposes [95,102,104,106,114]. Efficient attenuation of low-energy photons by nanoparticle-loaded polymers is intrinsic to the nanoparticles rather than packing-density.

4.3.4 Pointers for studies to explain new results

The primary objective of this thesis was to develop a novel technique for investigating the interaction of ionizing radiations with nanoparticles and to determine the effect of various factors, including nanoparticle species, size, and concentration, as well as the nature and energy of the ionizing radiations. The interpretation and explanation of the newly obtained results, however, necessitate further fundamental studies. This section presents a compilation of pointers potentially useful for additional investigation.

The first new result is that the interaction of low-energy photons varies with the species of nanoparticles. The interaction mechanism or electron transmission within these nanoparticles is distinct. As stated in the literature, the nanoparticles are generally small enough to confine their electrons and yield quantum effects, and the best example is Au [154]. The nanostructures are difficult to describe using either solid-state physics (solid materials) or quantum chemistry

(molecules and atoms). Determining which property changes in nanomaterials are due to confinement effects is difficult [69]. Present results rule out the involvement of the chemical composition of nanoparticles (W and WO_3 respond similarly, but Zn and ZnO differently) or magnetic properties of the materials (Fe_2O_3 and Pr_2O_3 respond similarly, but they both respond differently from Gd_2O_3). The responses differ among the nanoparticles of transition metals.

Nevertheless, it is observed that nanoparticles that attenuate the gamma-ray all appear non-white in the ambient. While sintered Gd_2O_3 nanoparticles retained their color, sintered ZnO nanoparticles turned black. The reduction in counts, however, is not due to color quenching, as established here. Though the interactions are atomic-scale phenomena, the electronic environment inside the nanoparticles dictates the transmission and exit of the electrons emitted. Thus, this variation might be related to the structure of the species of nanoparticles.

The second new result is the intense interaction of photons of various energies with nanoparticles. Rancoule et al., 2016 stated that densely packed metal particles scatter the radiations more intensely [31]. Scattering enriches the interaction cross-section of the particles for the photons [24]. Rayleigh scattering also increases the interaction of the photons [15]. Though this scattering is elastic, it is prominent for low-energy photons interacting with high-Z materials and indirectly increases the probability of interaction with a set of nanoparticles. Artemev hypothesized that when the dimensions of the nanoparticles match the wavelength of the photon, coherent scattering of photons by the particles turns substantial to cause extraordinary attenuation of X-rays [188]. However, the decreased counts in PHS after loading AuNPs indicate that photoelectrons emitting out of NPs, if any, are not detected through scintillation. Hence the hypothesis cannot be conclusively established in the present experiment. Another study suggests that with increased photon energy, reduced wavelength disallows coherent scattering [117].

4.4 Conclusions

This chapter contributes a technique that determines the outcome of the interaction of given ionizing radiation with given nanoparticles.

The outcomes of interactions of gamma-rays, X-rays, and beta- and alpha-radiations with about 25 types of nanoparticles investigated were determined. Effects of species, size, loading of nanoparticles, and type–the energy of radiations on the outcomes were ascertained. The results confirmed that the results obtained with WO_3 and PbO in the previous chapter were genuine. The salient results are captured in Figure 4-25. Further, it established that a range of energy exists for photons that interact with the nanoparticles intensely.

The strengths and weaknesses of the technique developed are discussed. The results obtained by directly determining the outcome of interactions are compared with those in the literature. The inputs for various applications and basic knowledge are compiled. The pointers for basic studies required to explain the new result are mentioned.

The next chapter details a study that demonstrates the enhancement of the gamma-counting efficiency of a liquid scintillator by loading nanoparticles into it, which would be useful for gamma-ray radioimmunoassay.

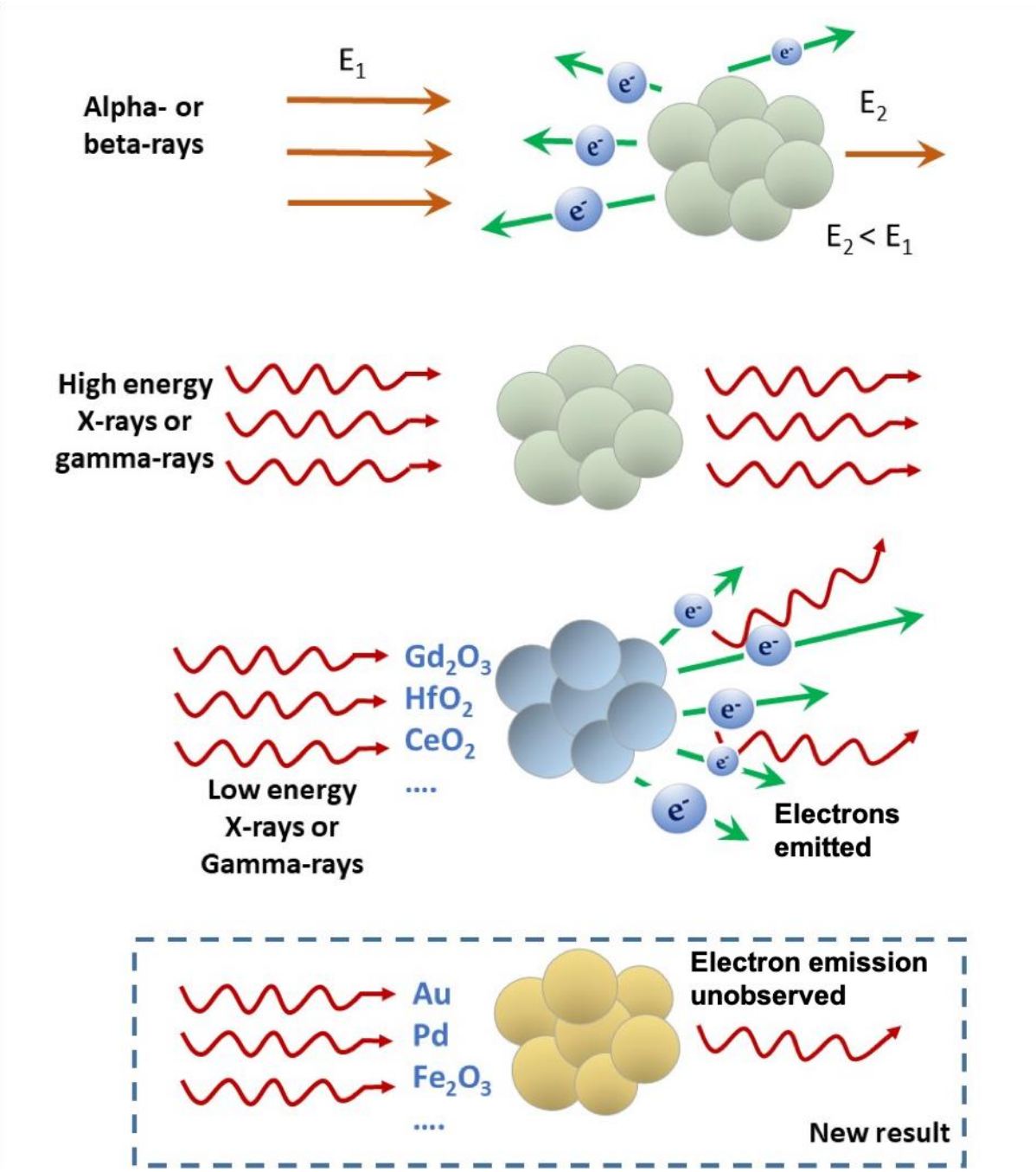

Figure 4-25 Graphics indicating the effect of species on the interaction of radiations

5 Chapter 5: Enhancing gamma-counting in liquid scintillation cocktails

This chapter presents a work that applies the knowledge gained in chapter 4 to overcome an enduring radiation physics challenge. The gamma-counting efficiency of a liquid scintillator is enhanced by loading Gd_2O_3 nanoparticles into the scintillator as a proof-of-principle for enabling the gamma-ray radioimmunoassay within the standard LSCs. The fifth objective of the thesis is addressed in this chapter.

5.1 Introduction

Achieving gamma-ray radioimmunoassay inside standard LSCs has been an enduring goal in the realm of radiation physics. It was not introduced in section 1.2 since it need not involve the interaction of radiations with the nanoparticles. The outcome of such interaction it utilized here for resolving the goal. Hence, the application is introduced here.

Radio-assay (also known as radioimmunoassay) is a technique to quantitatively analyze tiny concentrations of substances using radionuclides as tracers [189]. It detects and quantifies biological substances like antibodies, hormones, or contaminants in water or the environment [132]. The analyte is mixed with radionuclides and processed so that the vial's radioactivity corresponds to the analyte's concentration [189]. The level of radioactivity of the mixture is measured using a suitable instrument such as an LSC or spectrograph.

The technique of assays in LSCs is explained in several textbooks [132]. The RIA methods are based on competitive binding, as pictured in Figure 5-1. In these methods, an unlabeled antigen competes with a radiolabeled antigen to bind to an antibody with the appropriate specificity. When the mixtures of radiolabeled and unlabeled antigens are incubated with the corresponding antibody, the amount of free (not bound to antibody) radiolabeled antigen is directly proportional to the quantity of unlabeled antigen in the mixture [190]

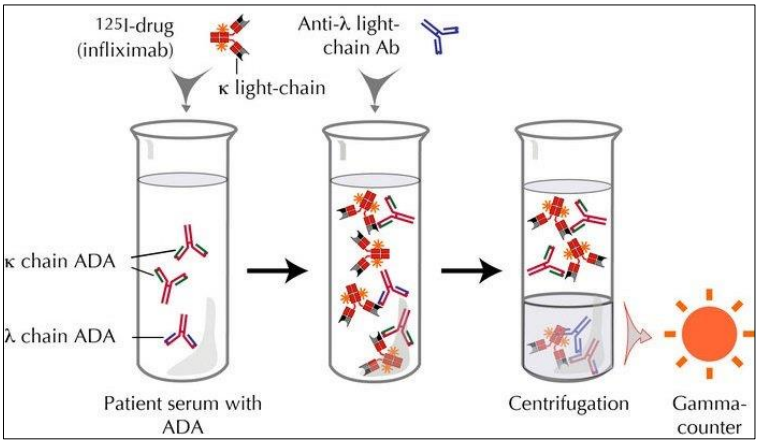

Figure 5-1 The principle of radioimmunoassay. An example of human serum is considered. Reproduced from [190]. ADA is Adenosine Deaminase

Radionuclide techniques offer better sensitivity than other analytical techniques, as a tiny mass of radionuclides is enough to generate considerable radioactivity. For example, 6.1 ng of ^{14}C or 1.6 pg of ^{125}I correspond to 1 kBq of activity [191], rendering their detectability.

Beta-emitting and gamma-emitting radionuclides are used in radioassay for different applications. Among the beta-emitters, ^{3}H, ^{14}C, and ^{32}P are popular due to their lower/optimum energies. Beta-assays are performed in LSC, standard instruments [132,147]. LSCs accommodate vials that contain the liquid scintillation cocktail mixed with the analyte (Figure 5-2). As beta-rays scintillate the liquid, a PMT placed next to the vial counts the scintillation pulses. Cocktails detect the beta-rays from these emitters with 10% to 100% efficiency [132]. The LSCs are simple, automated, standardized, and affordable [75,149,192].

While beta-assays are adequate for most applications, gamma-assays solve unique needs such as steroid receptor assays [75,136] or antigen-antibody interactions [193]. Further, labeling the same substance with beta and gamma radionuclides is required to ascertain the permeability of certain substances into different body parts, as in studies related to biological uptake and transport phenomena [194]. Radionuclides of ^{125}I, ^{55}Fe, and ^{57}Co are popular in gamma-assay due to their lower energies and shorter half-life [145,195].

However, the standard LSCs meant for beta-assay cannot count the gamma-rays due to the limited stopping power of constituents C, H, N, and O and the limited volume of liquid scintillation cocktails. Most gamma rays escape the LSC vials without interaction [149]. Hence, gamma-assays require a different instrument. A gamma-ray well counter is utilized for the purpose [192,194]. These counters have a geometric well that is bound by inorganic scintillators like NaI(Tl) that stop the gamma rays. A PMT is attached to the scintillator to count the scintillations. [130,196]. However, well-counters suffer hygroscopicity and self-absorption [1,192]. Notwithstanding that, employing a single, standard instrument for betas- and gamma-assays is preferable [192,193]. That would be feasible if the gamma-counting efficiency of the cocktails is enhanced such that the gamma rays are stopped within the LSC vials either fully or proportionately.

Efforts to enhance the gamma-counting efficiency of the cocktails are not new. One approach underway since the 1960s is to load high-Z materials into the cocktails to enhance the stopping power of the cocktail [75,129,130]. Ashcroft mixed a tetrabutyltin solution into the cocktail and achieved 51% counting efficiency for gamma-rays from ^{125}I against 48% with NaI(Tl) detector [75]. The interaction of gamma-rays with the dopants caused an increase in counts. However, the enhancement achieved by Ashcroft was contested by Horrock, stating that the enhancement could not only be due to the interaction of gamma-rays with loaded materials but also due to better counting of Auger or conversion electrons emitted by ^{125}I [172]. Horrocks proposed that the excitations are due mainly to the generation of Auger and conversion electrons during the decay of ^{125}I and calculated that only a minor portion (~8%) of it is the result of photons generated and, thus, a counting efficiency of 76% can be expected from an unquenched solution. This argument has remained unsettled for over five decades. Unfortunately, no further works are reported by Ashcroft.

Nevertheless, several attempts have been made towards achieving RIA in conventional LSCs. Ashcroft offered an innovative method of splitting the LSC vial into two portions (Figure 5-2). The outer portion was loaded with a tin-loaded liquid scintillator, and the inner one with the assay sample. Verslujis further improvised Ashcroft's design to accommodate a larger volume of the metal-loaded liquid scintillator. In 2006, Carles and Malonds recognized that cocktails containing heavy elements offer enhanced photon counting efficiency [129]. For X-rays from ^{55}Fe, the Cocktail (Ultima Gold Plus^{TM}) possessing 1.4% P and 0.2% S in addition to C, H, N, O yielded enhanced counting efficiency than the cocktail (Insta Gel^{TM}) possessing only C, H, N, O. Shoji, *et al.* loaded triethyl phosphate to a commercial cocktail. It demonstrated a greater gamma-counting efficiency for a loaded cocktail than its unloaded counterpart [130].

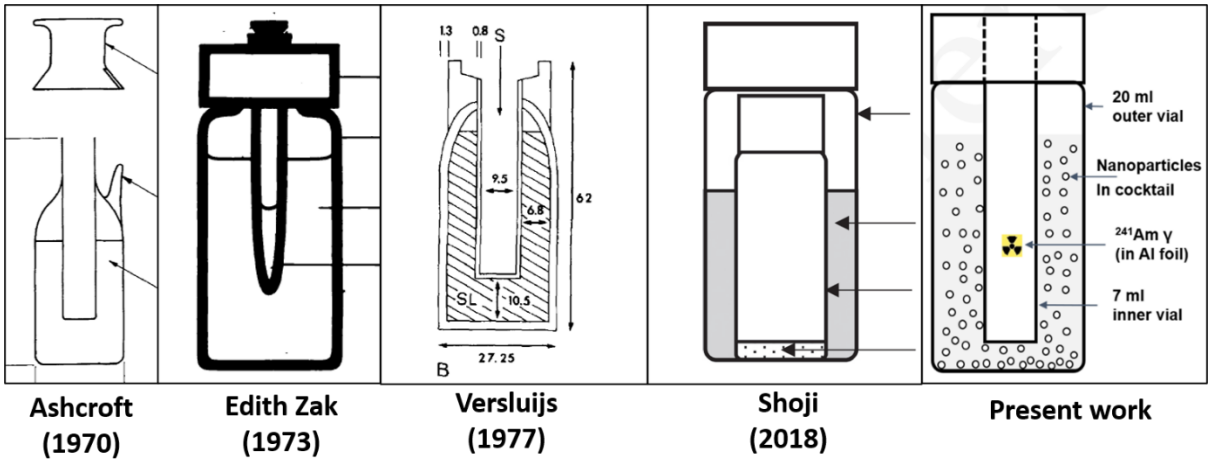

Figure 5-2 Innovative modifications of vials used in LSCs to stop and count gamma-rays within the vials. Reproduced from [75,130,197]

Despite these efforts, the goal of efficiently counting gamma-rays within the standard LSCs remains a challenge. Though alternate instruments such as accelerated mass spectrographs serve the radio-assays for other applications such as archaeology, geology, food, and environment, the radio-immunoassays for biomedical applications rely only on LSCs and well counters [192,194,196].

As learned in this thesis work, incorporating suitable nanoparticles into a liquid scintillator enhances the gamma detection efficiency of the host. This approach is attempted in this work. ^{125}I is a popular source of gamma-rays for radioassay. As sourcing ^{125}I turned challenging, the present work used a readily available ^{241}Am button source. The energy of gamma-rays from ^{241}Am 14 keV and 60 keV, and those from ^{125}I are 35 keV. The aim of this study was to demonstrate the feasibility of gamma-ray quantification using conventional liquid scintillation counters leading towards gamma-ray assay within conventional LSCs.

5.2 Materials and Method

5.2.1 Materials

The study used a Hidex Oy Triathler LSC, courtesy of brief access provided by a distributor. Triathler has one PMT. It has a 10 mm thick Pb to shield the background. Hidex supplied Aqualight+ Ultra Low Level^{TM} cocktail was used as the scintillator. A 20 ml and 7 ml

scintillation grade Pyrex glass vials sourced from Meridian Biotechnologies were used in the study. Their respective dimensions were 28 mm (diameter) × 61 mm (length) and 17 mm × 60 mm.

Gd_2O_3 nanoparticles 99.9% pure, 55 ± 0.8 nm average particle size were used. CeO_2 nanoparticles (99.9% pure, 38.5±1.7 nm average particle size) were also tried. $^{241}Am(\alpha)$ button source was utilized as the source of gamma-rays. Both nanoparticles were tried with the toluene-based cocktail used for developing the method. The results were similar in trend. Those with Aqualight+ Ultra Low Level^{TM} cocktail and Gd_2O_3 nanoparticles are presented.

5.2.2 Method

The setup is similar to that used by [198], as shown in Figure 5-2 and Figure 5-3. The gamma-ray source was wrapped in a 0.1 mm thick aluminum sheet before placing the source into the inner vial. The source was positioned about three fourth-down the inner vial. The wrapping provided positional stability for the source and attenuated alpha radiations emitted by the source. The inner vial was glued to the cap of the outer vial. The background counts measured were as low as 0.1 cps. The vial was positioned inside the measurement chamber using a plastic scintillation adapter. Orientation of the source to the PMT was ensured through a notch mark on the lid. All measurements used a full energy scale in PHS.

The PHS with an unloaded cocktail was obtained. The outer vial was loaded with about 8 ml of the cocktail, filling to about two-thirds of the volume. The vial was-demounted, and a given quantity of Gd_2O_3 nanoparticles was loaded into the cocktail. The mixture was thoroughly shaken for about 30 s to ensure proper dispersion of the nanoparticles, and the vial was mounted back. PHS with a nanoparticle-loaded liquid scintillator was obtained for different loadings under identical conditions. Acquisition time was 60 s.

Figure 5-3 Hidex Triathlon LSC. The vial and its cover are also shown

5.3 Result

Figure 5-4 displays the variations in PHS of ^{241}Am with unloaded and nanoparticle-loaded cocktails. The number of counts in the PHS increased with the loading of nanoparticles. Counts increased at all channels, and new counts appeared at higher channels. This trend was observed with each higher loading up to 1000 mg. Loading beyond 1000 mg reduced the number of counts from that of the previous loading.

Figure 5-4 (b) displays the histogram of the total number of counts in PHS. At optimum loadings, the number of counts in PHS was 3.4 times those of the unloaded cocktail.

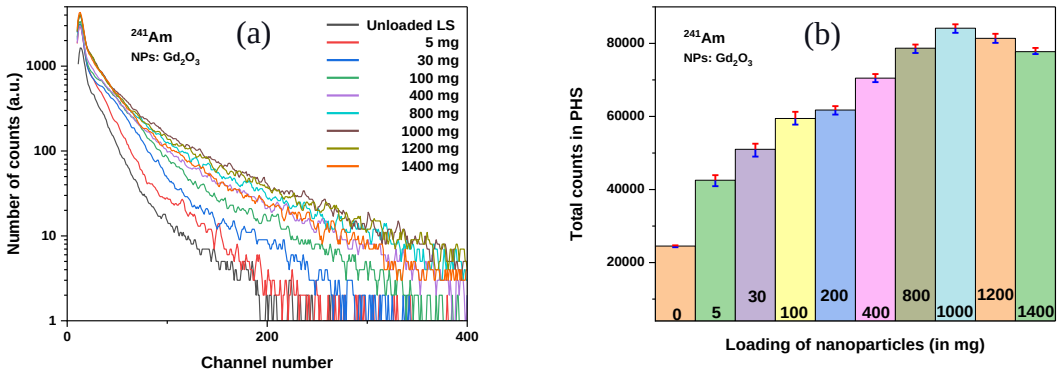

Figure 5-4 (a) Variations in PHS of ^{241}Am with an unloaded cocktail upon loading the nanoparticles. (b) Histogram indicating the variation in the total number of counts at different loading. The median value is plotted out of triplicate measurements.

5.4 Discussion

The results in Figure 5-4 are similar to those in Figure 3-8. The inference of results in Figure 3-8 applies to those in Figure 5-4. Though the number of counts reduces relative to the previous loading beyond the optimum loading, the number of counts remained more than those in the PHS for an unloaded cocktail for all the higher loadings tested.

The results resolve five-decades old apprehension. In 1970, Ashcroft demonstrated enhanced counting efficiency for ^{125}I to 51% [75]. In 1976, Horrocks demonstrated a counting efficiency of 76% for ^{125}I even in neat (unloaded) cocktails and raised merited apprehension that enhancement achieved by Ashcroft is due to better counting of Auger or conversion electrons emitted by ^{125}I [172]. Here, as ^{241}Am does not emit Auger or conversion electrons, the study establishes that the enhancement is due only to the interaction of gamma-rays with the high-Z matter.

The present study demonstrated the proof-of-principle of gamma-ray radioimmunoassay within standard LSCs using a ^{241}Am gamma source. The probability of interaction of gamma-rays from ^{125}I with the given nanoparticles is comparable to that of the gamma-rays from ^{241}Am. For routine usage, the cocktail suppliers can disperse the nanoparticles into the scintillator and ensure the reproducible preparation of samples. Inevitable variations in the physical properties

of nanoparticles synthesized in batches can be addressed by providing calibration curves for a batch of cocktails. The use of nanoparticles would require a standard operating procedure involving thorough shaking of the sample to ensure that the nanoparticles are dispersed and suspended uniformly. Direct addition of nanoparticles suffices unless the selected nanoparticles chemically interact with the cocktail. In this case, a surfactant may be used, and the attenuation of electrons by the surfactant is accounted.

Further studies may explore the utility of loading other nanoparticles, other sizes, and to other extents for efficient counting of gamma-rays from ^{125}I, ^{55}Fe, ^{57}Co, etc., radionuclides. The approach can be adapted to enhance the efficiency and, thus, sensitivity of beta-assays also. It would benefit the beta-assays involving tinier concentrations or flux-starving measurements, such as monitoring the natural radioactivity, contaminants from nuclear power stations or fuel reprocessing plants, contamination by nuclear fallouts, or surveying the synthetic additives in food etc. Alternately, the enhanced counting efficiency would reduce the time required for the assays. Typically counting times in flux starving measurements like carbon dating, archaeology, paleoethology etc., vary from 30 minutes to more than 30 hours [195].

5.5 Conclusions

This chapter proposed and implemented the concept of enhancing the number of scintillation counts in a conventional cocktail by incorporating nanoparticles of high-Z materials. The optimum loading of nanoparticles returns the greatest enhancement. This research has determined conclusively that the increased scintillation counting when high-Z materials are incorporated into liquid scintillators is the direct result of gamma-ray interactions with the heavy elements. Results thus resolve a long-standing ambiguity. Further studies can explore the nanoparticle of other species and sizes to efficiently count gamma rays from standard radionuclides like ^{125}I, ^{55}Fe, and ^{57}Co for gamma assays.

6 Chapter 6: Summary and further scope

The present chapter summarizes the work carried out in this thesis. It presents an account of how the aim and objectives of the thesis are accomplished. The chapter outlines the scope for future work.

6.1 Summary of the work

Ionizing radiations and nanomaterials represent major entities of Physics. While the knowledge of the interaction of ionizing radiations with matter-at-bulk has led to several vital applications and human safety, the interaction of ionizing radiation with matter-at-nanoscale remained nascent. Materials characterization techniques such as XRD, SEM, TEM, XPS, etc., involve the interaction of ionizing radiations with the matter at bulk, surface, and nano. However, the energy of radiations used is feeble compared to those used in various practical applications. They need not represent the interaction of radiations of other energies. Thus, there exists a gap in knowledge.

Beyond academic inquisitiveness, the interaction of ionizing radiations with nanoparticles is needed for practical applications such as nanoparticle radiosensitization for cancer treatment, the development of efficient-fast-large-affordable gamma-ray detectors, the development of Pb-free, efficient, light-weight gamma-ray shields, and Gamma-ray Radio-immunoassay. The first three applications rely on the interaction of ionizing radiations with nanoparticles as their first step. However, the studies concerning these applications involve multistage multi-variable experiments. Currently, the efficacy of chosen nanoparticle is determined only at the end of the experiment. The lack of knowledge on individual processes, such as the interaction of ionizing radiations with nanoparticles, has made interpreting the results challenging and thus has held the studies exploratory. Though laboratory scale detectors and shields have been realized, their upscaling is constrained by process-related issues. Shields for special applications like space seek nanoparticles that do not lead to bremsstrahlung.

Hence, there was a compelling need for empirical data and knowledge on the interaction of ionizing radiations with nanoparticles. It would determine better-suited nanoparticles for each application. Studies involving test-selected nanoparticles can address the remaining issues and propel the field implementation of the applications.

6.2 Conclusion from the thesis work

The present thesis aims to fill the gap in knowledge on the interaction of ionizing radiations with nanoparticles and provide empirical inputs to the studies concerning the practical applications. A novel experimental technique was developed to investigate the interaction between specific ionizing radiations and nanoparticles. This technique involves obtaining and comparing pulse height spectra (PHS) of the ionizing radiation with a liquid scintillator before and after loading the nanoparticles. By analyzing the variations in the spectra, the outcomes of these interactions can be determined. An increase in the number of counts in the pulse height

spectra suggests the emission of electrons from the nanoparticles into the surrounding environment. This indicates that the nanoparticles are interacting with the ionizing radiation and releasing electrons. Conversely, a reduction in counts signifies that the nanoparticles effectively attenuate the ionizing radiation, thereby decreasing the detected counts. Unvaried pulse height spectra indicate that the ionizing radiation is transmitting through the nanoparticles without interaction.

The experimental technique allows for the assessment of various factors, including the species, concentration, and size of the nanoparticles, as well as the nature and energy of the ionizing radiations. By varying these parameters, the impact of each on the interaction outcomes is evaluated.

In one application, the nanoparticles are loaded into a plastic scintillator to enhance the gamma accounting efficiency of the host material. This serves to improve the detection and measurement of gamma radiation. The results of this study motivated the development of a novel technique. In another application, the nanoparticles are loaded into a liquid scintillator to enhance the gamma-counting efficiency, making the scintillator suitable for use in radioimmunoassays.

The thesis targeted to fulfill the aim through five objectives. The objectives have been met, as enumerated hereunder.

First objective

The first objective is met by validating that the outcome of the interaction of gamma rays varies with the species of nanoparticles. The nanoparticles of Gd_2O_3, HfO_2, and Bi_2O_3 loaded into a plastic scintillator enhanced the gamma-detection efficiency of the host, but those of WO_3, and PbO, under identical conditions, reduced it. An investigation and analysis scrutinized the potential artifacts leading to such a result. Negation of the artifacts and critical literature review indicated that the result was genuine. It is speculated that nanoparticles of WO_3 and PbO interact with the gamma-rays but hinder the exit of electrons into the surrounding.

Second objective

The second objective is met by developing an experimental technique to directly determine the outcome of the interaction of given ionizing radiation with given nanoparticles. The technique validated the results observed with plastic scintillators directly. Further, the technique facilitates the study of interactions of radiations used in practical applications. It can determine the effect of species, size, and concentration of nanoparticles and the nature and energy of the ionizing radiations.

The technique relies on obtaining the PHS of given ionizing radiation with a liquid scintillator before and after loading the nanoparticles into the liquid scintillator under identical conditions and comparing the variations in the number of counts and shape of the spectrum to infer the outcome of the interaction. Interactions resulting in the emission of electrons from the nanoparticles increase the number of counts in PHS. The extent of the increase in the number

of counts signifies the abundance of electrons emitted. The shape of PHS with a nanoparticle-loaded liquid scintillator indicates the energy profile of the electrons emitted. Interactions resulting in the attenuation of ionizing radiation within the nanoparticle reduce the number of counts in PHS. The transmission of ionizing radiation without any interaction leaves the PHS unvaried.

Third objective:
The third objective is met by gaining empirical knowledge on the interaction of given ionizing radiations with given nanoparticles. The effects of nature and energy of ionizing radiations, species, size, and loading of the nanoparticles on the outcomes are studied. The interactions of alpha, beta, X-rays, and gamma radiations with about 25 types of nanoparticles are determined. The new results are identified, and pointers for their explanation are offered.

In summary,
among the photons, the interaction of low-energy photons (X-rays from ^{55}Fe or 40 kVp gun; and gamma-rays from ^{241}Am, ^{133}Ba) varies with the species of nanoparticles. Interaction of these photons with nanoparticles of Gd_2O_3, HfO_2, etc., results in the emission of electrons into the surrounding. These nanoparticles support the exit of electrons emitted from their constituent atoms. However, nanoparticles like Au, Pd, and WO_3 effectively attenuate low-energy photons. They possibly absorb the electrons emitted from their constituent atoms entirely or partially so that the exiting electron cannot scintillate the liquid scintillator.
Within low-energy photons, a range of energies induces intense interaction with the nanoparticles. Current results indicate that the range lies between 10 keV and 81 keV. This is another new result of the study. Photon-attenuating nanoparticles attenuated photons of all lower energies.

Low-energy photons interacting with an optimum concentration of electron-emitting nanoparticles produce a greater number of electrons. This effect is attributable to the ensemble of nanoparticles and, thus, is a secondary effect to the basic outcome of interactions. Optimum-sized electron-emitting nanoparticles emit more electrons into the surroundings upon interacting with low-energy photons. For photon-attenuating nanoparticles, increased concentration and increased size increase the extent of attenuation.

High-energy photons (those from ^{22}Na, ^{137}Cs, and ^{60}Co) transmit through all the nanoparticles without any interaction. No discernable effect is observed with variations in species or size of nanoparticles, nor with the variation in energy of photons. The extent of attenuation of photons increases with an increase in concentration for all nanoparticles.

Beta radiations interact with nanoparticles to cause the emission of electrons from the nanoparticles, independent of species of nanoparticles. The manifestation of outcomes is sensitive to the concentration of nanoparticles. An optimum concentration yields the greatest enhancement of the number of counts in PHS within small loadings. The outcome is independent of the species of nanoparticles.

Alpha-radiations interact with nanoparticles to cause the emission of electrons from the nanoparticles. The outcome is independent of the species of nanoparticles.

Fourth objective:
The fourth objective is met by comparing and contrasting the results of the present study with those available in the literature. The inputs from the present work for the studies concerning basic knowledge and practical applications involving the interaction of ionizing radiations with nanoparticles are identified.

The present study indicates that nanoparticle radiosensitization could originate through a mechanism other than the emission of photoelectrons or exclusively low-energy electrons, and the emission of photoelectrons from the nanoparticle could supplement it. The present study offers crucial input to explore other mechanisms.

For developing efficient-fast-large-affordable gamma-ray detectors, the results suggest using electron-emitting nanoparticles like Gd_2O_3, HfO_2, Bi_2O_3, and ZrO_2. They support the development of such detectors for low-energy photons as high-energy photons hardly interact with nanoparticles. The choice of nanoparticle species is more crucial than atomic number Z or the size or concentration of the nanoparticles. Since all nanoparticles absorb a portion of the energy of electrons emitted from their atoms, developing detectors for spectroscopic studies is feasible only with ultra-small nanoparticles dispersed uniformly throughout the detector.

To develop Pb-free, efficient gamma shields, the current findings encourage using photon-attenuating nanoparticles like Au, WO_3, Fe_2O_3, W, and Zn. Species like these are better suited than others for applications like Space electronics that forbid the emission and escape of energetic electrons from the radiation shields. The present results support the development of shields for low-energy or diagnostic photons, as the attenuation of high-energy photons through nanoparticle-loaded polymers is impractical.

Fifth objective:
The fifth objective is accomplished by applying the knowledge gained to demonstrate proof of principle for achieving gamma-ray radioimmunoassay within the standard LSCs. Incorporating 1000 mg of Gd_2O_3 nanoparticles into 8 ml of Aqualight+ Ultra Low Level™ cocktail enhanced the number of counts for gamma-rays from ^{241}Am by 3.4 times those from the unloaded cocktail in a standard LSC make.

Thus, the objectives of the study have been met. The new knowledge thus gained is relevant, important, and timely for ongoing applications.

6.3 Scope of further work

The scope for further work exists in five aspects: explanation of the new results through additional studies, overcoming the limitations of the present work, improvisation of the technique, determination of interaction of ionizing radiations with a whole arsenal of

nanoparticles, and the utilization of the results to meet associated goals in the field of radiation detection and measurement.

To overcome the limitations of the present work, characterizing the current set-up for the lowest energy that the electron striking the scintillator needs to carry to get detected would disclose the energy of electrons that photon-attenuating nanoparticles emit, if any. Present work could not characterize it for lesser energies than 4 keV due to the non-availability of the sources. Secondly, calibrating the channel numbers in PHS for the energy of electrons would quantify the energy of electrons emitted. It could not be performed here due to the non-availability of suitable sources. Further work could study AuNPs smaller than 4 nm to determine whether the smaller nanoparticles permit the exit of electrons. This work could not source them readily. The current work used one PMT. Using two PMTs enhances the accuracy of the measurements on the number of energy of the electrons emitted by minimizing the effects of possible large and unstable dark PMT current.

An inherent limitation of the technique is that it may not detect the electrons emitted with energy lesser than the scintillation threshold for the scintillator. Literature estimates the threshold as about 100 eV[149]. Alternate techniques need to be employed or developed for the same.
The interactions of the whole arsenal of ionizing radiations and the nanoparticles can be characterized to explore newer results, if any. Radiations include the photons < 4 keV and > 1.4 keV. The effect of beta-radiation energy can be studied with arrangements to obtain monochromatic radiations. It would help understand contrasting responses, make the simulation studies more reliable, and ascertain the most efficient nanoparticles for an application. While the advantage of nanoparticles is their amicability for modification, the set-up serves test bed for evaluating the utility of engineering or intentional modification of nanoparticles for the desired outcome of the interaction.

It turned out that the technique developed incidentally serves to enhance the counting efficiency of the liquid scintillator for alpha, beta, and gamma radiations. Such enhancement helps improvise the sensitivity of statistics and reduce the time required for reliable measurements. Specifically, enhancing the detection efficiency of liquid scintillators by loading nanoparticles benefits flux-starving measurements such as monitoring the natural radioactivity, contaminants from nuclear power stations or fuel reprocessing plants, contamination by nuclear fallouts, or survey the synthetic additives in food etc.[131]. Enhanced large signals help discriminate radiation species such as alpha vs. beta, gamma vs. neutron, etc. A brief attempt made on the latter is mentioned in Appendix-I.

References

1. Knoll, G. F. *Radiation Detection and Measurement*. (John Wiley & Sons, Inc., 2010).
2. Bagoria, L. Role Of Nanoparticles As Radioprotector. *Int. J. Creat. Res. Thoughts* **10**, (2022).
3. Wang, Z. L. *Characterization of nanophase materials*. *Particle and Particle Systems Characterization* vol. 18 (Wiley-VCH Verlag, 2001).
4. Roduner, E. Size matters: Why nanomaterials are different. *Chem. Soc. Rev.* **35**, 583–592 (2006).
5. Leroy, Claude, P.-G. R. *Principles of Radiation Interaction in Matter and Detection*. (World Scientific, 1998).
6. Karl, A. & Elsaesser, G. Biophysical Interaction of Nanoparticles and Radiations. (University of Ulster, 2011).
7. Brun, E. & Sicard-Roselli, C. Actual questions raised by nanoparticle radiosensitization. *Radiat. Phys. Chem.* **128**, 134–142 (2016).
8. Schuemann, J. *et al.* Roadmap for metal nanoparticles in radiation therapy: Current status, translational challenges, and future directions. *Phys. Med. Biol.* **65**, (2020).
9. Butterworth, K. T., McMahon, S. J., Currell, F. J. & Prise, K. M. Physical basis and biological mechanisms of gold nanoparticle radiosensitization. *Nanoscale* **4**, 4830–4838 (2012).
10. Casta, R. *et al.* Electronic emission of radio-sensitizing gold nanoparticles under X-ray irradiation: Experiment and simulations. *J. Nanoparticle Res.* **16**, 1–10 (2014).
11. Casta, R., Champeaux, J. P., Sence, M., Moretto-Capelle, P. & Cafarelli, P. Comparison between gold nanoparticle and gold plane electron emissions: a way to identify secondary electron emission. *Phys. Med. Biol.* **60**, 9095–9105 (2015).
12. Hajagos, T. J., Liu, C., Cherepy, N. J. & Pei, Q. High-Z Sensitized Plastic Scintillators: A Review. *Adv. Mater.* **30**, 1–13 (2018).
13. Khan, S. & Hossain, M. K. Classification and properties of nanoparticles. in *Metal Nanoparticle-Based Polymer Composites* 1–40 (2022).
14. Herold, D. M., Das, I. J., Stobbe, C. C., Iyer, R. V. & Chapman, J. D. Gold microspheres: A selective technique for producing biologically effective dose enhancement. *Int. J. Radiat. Biol.* **76**, 1357–1364 (2000).
15. Hainfeld, J. F., Dilmanian, F. A., Slatkin, D. N. & Smilowitz, H. M. Radiotherapy enhancement with gold nanoparticles. *J. Pharm. Pharmacol.* **60**, 977–985 (2010).
16. Cui, L. *et al.* Radiosensitization by gold nanoparticles: Will they ever make it to the clinic? *Radiother. Oncol.* **124**, 344–356 (2017).
17. Shiryaeva, E. S. *et al.* On the mechanism of radiation sensitization by gold nanoparticles under X-ray irradiation of oxygen-free aqueous organic solutions: A spin trapping study. *Radiat. Phys. Chem.* **193**, 109998 (2022).
18. Nambiar, S., Osei, E. K. & Yeow, J. T. W. Polymer nanocomposite-based shielding against diagnostic X-rays. *J. Appl. Polym. Sci.* **127**, 4939–4946 (2013).
19. Jia, S., Ge, S., Fan, X., Leong, K. W. & Ruan, J. Promoting reactive oxygen species generation: A key strategy in nanosensitizer-mediated radiotherapy. *Nanomedicine* **16**, 759–778 (2021).
20. Delaney, G., Jacob, S., Featherstone, C. & Barton, M. The role of radiotherapy in cancer treatment: Estimating optimal utilization from a review of evidence-based clinical guidelines. *Cancer* **104**, 1129–1137 (2005).
21. Zhang, Y. *et al.* Research progress on nano-sensitizers for enhancing the effects of radiotherapy. *Mater. Adv.* **3**, 3709–3725 (2022).
22. Pagáčová, E. *et al.* Challenges and contradictions of metal nano-particle applications for

radio-sensitivity enhancement in cancer therapy. *Int. J. Mol. Sci.* **20**, (2019).
23. Tarantino, S., Caricato, A. P., Rinaldi, R., Capomolla, C. & Matteis, V. De. Cancer Treatment Using Different Shapes of Gold-Based Nanomaterials in Combination with Conventional Physical Techniques. **15**, (2023).
24. Kwatra, D., Venugopal, A. & Anant, S. Nanoparticles in radiation therapy: A summary of various approaches to enhance radiosensitization in cancer. *Transl. Cancer Res.* **2**, 330–342 (2013).
25. Galain, I. *et al.* Enhancement of radiation response of breast cancer cells through the incorporation of Bi2S3 nanorods. *J. Nanoparticle Res.* **24**, 1–11 (2022).
26. Penninckx, S., Heuskin, A. C., Michiels, C. & Lucas, S. Thioredoxin reductase activity predicts gold nanoparticle radiosensitization effect. *Nanomaterials* **9**, 1–13 (2019).
27. Geng, F. *et al.* Thio-glucose bound gold nanoparticles enhance radio-cytotoxic targeting of ovarian cancer. *Nanotechnology* **22**, 285101 (2011).
28. Chen, Y., Yang, J., Fu, S. & Wu, J. Gold nanoparticles as radiosensitizers in cancer radiotherapy. *Int. J. Nanomedicine* **15**, 9407–9430 (2020).
29. Hainfeld, J. F., Slatkin, D. N. & Smilowitz, H. M. The use of gold nanoparticles to enhance radiotherapy in mice. *Phys. Med. Biol.* **49**, (2004).
30. Sukkar, F. A. Egyptian Journal of Chemistry: Preface. *Egypt. J. Chem.* **51**, 723–735 (2008).
31. Rancoule, C. *et al.* Nanoparticles in radiation oncology: From bench-side to bedside. *Cancer Lett.* **375**, 256–262 (2016).
32. Retif, P. *et al.* Monte Carlo simulations guided by imaging to predict the in vitro ranking of radiosensitizing nanoparticles. *Int. J. Nanomedicine* **11**, 6169–6179 (2016).
33. Kong, T. *et al.* Enhancement of radiation cytotoxicity in breast-cancer cells by localized attachment of gold nanoparticles. *Small* **4**, 1537–1543 (2008).
34. Bindhu, J., & Anupama, G. Radiosensitization: the new dogma in cancer treatment. *Austral-Asian J Cancer* **4**, 241–50 (2005).
35. Hiromichi Matsudaira; Akiko M. Ueno; Ikuko Furuno. Iodine contrast medium sensitizes cultured mammalian cells to X rays but not to γ rays. *Radiat Res* **84**, 144–148 (1980).
36. Liu, Y. *et al.* Metal-based NanoEnhancers for future radiotherapy: Radiosensitizing and synergistic effects on tumor cells. *Theranostics* **8**, 1824–1849 (2018).
37. Chithrani, D. B. *et al.* Gold nanoparticles as radiation sensitizers in cancer therapy. *Radiat. Res.* **173**, 719–728 (2010).
38. McMahon, S. J. *et al.* Biological consequences of nanoscale energy deposition near irradiated heavy atom nanoparticles. *Sci. Rep.* **1**, 1–10 (2011).
39. Luchette, M., Korideck, H., Makrigiorgos, M., Tillement, O. & Berbeco, R. Radiation dose enhancement of gadolinium-based AGuIX nanoparticles on HeLa cells. *Nanomedicine Nanotechnology, Biol. Med.* **10**, 1751–1755 (2014).
40. Kazmi, F. *et al.* Megavoltage radiosensitization of gold nanoparticles on a glioblastoma cancer cell line using a clinical platform. *Int. J. Mol. Sci.* **21**, 1–12 (2020).
41. Stewart, C. *et al.* First proof of bismuth oxide nanoparticles as efficient radiosensitisers on highly radioresistant cancer cells. *Phys. Medica* **32**, 1444–1452 (2016).
42. Coulter, J. A., Hyland, W. B., Nicol, J. & Currell, F. J. Radiosensitising Nanoparticles as Novel Cancer Therapeutics — Pipe Dream or Realistic Prospect ? *Clin. Oncol.* **25**, 593–603 (2013).
43. Roa, W. *et al.* Gold nanoparticle sensitize radiotherapy of prostate cancer cells by regulation of the cell cycle. *Nanotechnology* **20**, 375101 (2009).
44. Li, F. *et al.* Radiosensitizing Effect of Gadolinium Oxide Nanocrystals in NSCLC Cells Under Carbon Ion Irradiation. *Nanoscale Res. Lett.* **14**, (2019).

45. Wang, C. *et al.* Enhancement of radiation effect and increase of apoptosis in lung cancer cells by thio-glucose-bound gold nanoparticles at megavoltage radiation energies. *J. Nanoparticle Res.* **15**, 1–12 (2013).
46. Detappe, A. *et al.* Key clinical beam parameters for nanoparticle-mediated radiation dose amplification. *Sci. Rep.* **6**, 1–8 (2016).
47. Bilynsky, C., Millot, N. & Papa, A. L. Radiation nanosensitizers in cancer therapy—From preclinical discoveries to the outcomes of early clinical trials. *Bioeng. Transl. Med.* **7**, 1–22 (2022).
48. Her, S., Jaffray, D. A. & Allen, C. Gold nanoparticles for applications in cancer radiotherapy: Mechanisms and recent advancements. *Adv. Drug Deliv. Rev.* **109**, 84–101 (2017).
49. López-Valverde, J. A., Jiménez-Ortega, E. & Leal, A. Clinical Feasibility Study of Gold Nanoparticles as Theragnostic Agents for Precision Radiotherapy. *Biomedicines* **10**, 1214 (2022).
50. Lechtman, E. *et al.* Implications on clinical scenario of gold nanoparticle radiosensitization in regards to photon energy, nanoparticle size, concentration and location. *Phys. Med. Biol.* **56**, 4631–4647 (2011).
51. Byrne, H., McNamara, A. & Kuncic, Z. Impact of nanoparticle clustering on dose radio-enhancement. *Radiat. Prot. Dosimetry* **183**, 50–54 (2019).
52. Gilles, M., Brun, E. & Sicard-Roselli, C. Gold nanoparticles functionalization notably decreases radiosensitization through hydroxyl radical production under ionizing radiation. *Colloids Surfaces B Biointerfaces* **123**, 770–777 (2014).
53. Kobayashi, K., Usami, N., Porcel, E., Lacombe, S. & Le Sech, C. Enhancement of radiation effect by heavy elements. *Mutat. Res. - Rev. Mutat. Res.* **704**, 123–131 (2010).
54. Butterworth, K. T. *et al.* Variation of strand break yield for plasmid DNA irradiated with high-Z metal nanoparticles. *Radiat. Res.* **170**, 381–387 (2008).
55. Zwiehoff, S. *et al.* Enhancement of Proton Therapy Efficiency by Noble Metal Nanoparticles Is Driven by the Number and Chemical Activity of Surface Atoms. *Small* **18**, (2022).
56. Inoue, K. *et al.* Fast Scintillation X-Ray Detector Using Proportional-Mode Si-APD and a HfO2-Nanoparticle-Doped Plastic Scintillator. *IEEE Trans. Nucl. Sci.* **65**, 1012–1017 (2018).
57. Kagami, K. *et al.* High-energy X-ray detection capabilities of Hf-loaded plastic scintillators synthesized by sol–gel method. *J. Mater. Sci. Mater. Electron.* **31**, 896–902 (2020).
58. Sun, Y. *et al.* High-energy X-ray detection by hafnium-doped organic-inorganic hybrid scintillators prepared by sol-gel method. *Appl. Phys. Lett.* **104**, (2014).
59. Hiyama, F. *et al.* X-ray detection properties of plastic scintillators containing surface-modified Bi2O3 nanoparticles. *Jpn. J. Appl. Phys.* **57**, (2018).
60. Sato, A., Koshimizu, M., Fujimoto, Y., Kishimoto, S. & Asai, K. Fabrication of HfxSi1−xO2microparticle-loaded PVK-based plastic scintillators using the sol–gel method for high-energy X-ray detection at high counting rate. *J. Mater. Sci. Mater. Electron.* **32**, 28807–28818 (2021).
61. Schwoerer, H. *et al.* MeV X rays and photoneutrons from femtosecond laser-produced plasmas. *Phys. Rev. Lett.* **86**, 2317–2320 (2001).
62. Ledingham, K. W. D., McKenna, P. & Singhal, R. P. Applications for nuclear phenomena generated by ultra-intense lasers. *Science (80-.).* **300**, 1107–1111 (2003).
63. Lauck, R. *et al.* Low-afterglow, high-refractive-index liquid scintillators for fast-neutron spectrometry and imaging applications. *IEEE Trans. Nucl. Sci.* **56**, 989–993 (2009).
64. Hamel, M., Turk, G., Darbon, S. & Normand, S. Highly lead-loaded red plastic

scintillators as an X-ray imaging system for the laser Méga Joule. *IEEE Trans. Nucl. Sci.* **59**, 1268–1272 (2012).
65. Cai, W. *et al.* Synthesis of bulk-size transparent gadolinium oxide-polymer nanocomposites for gamma ray spectroscopy. *J. Mater. Chem. C* **1**, 1970–1976 (2013).
66. Gandini, M. *et al.* Efficient, fast and reabsorption-free perovskite nanocrystal-based sensitized plastic scintillators. *Nat. Nanotechnol.* **15**, 462–468 (2020).
67. Koshimizu, M. Composite scintillators based on polymers and inorganic nanoparticles. *Funct. Mater. Lett.* **13**, (2020).
68. Liu, C. High-Z Nanoparticle/Polymer Nanocomposites for Gamma-Ray Scintillation Detectors. (University of California, 2019).
69. Milbrath, B. D., Peurrung, A. J., Bliss, M. & Weber, W. J. Radiation detector materials: An overview. *J. Mater. Res.* **23**, 2561–2581 (2008).
70. Araya, Y. *et al.* Enhanced detection efficiency of plastic scintillators upon incorporation of zirconia nanoparticles. *Sensors Mater.* **27**, 255–261 (2015).
71. Li, Q. *et al.* Research on X-ray shielding performance of wearable Bi/Ce-natural leather composite materials. *J. Hazard. Mater.* **398**, (2020).
72. Bertrand, G. H. V. *et al.* Understanding the behaviour of different metals in loaded scintillators: Discrepancy between gadolinium and bismuth. *J. Mater. Chem. C* **3**, 6006–6011 (2015).
73. Dumazert, J. *et al.* Gadolinium-loaded Plastic Scintillators for Thermal Neutron Detection using Compensation. *IEEE Trans. Nucl. Sci.* **63**, 1551–1564 (2016).
74. Bertrand, G. H. V., Hamel, M. & Sguerra, F. Current Status on Plastic Scintillators Modifications. *Chem. - A Eur. J.* **20**, 15660–15685 (2014).
75. Ashcroft, J. Gamma Counting of lodine125 Using a Metal-Loaded Liquid Scintillator. *Anal. Biochem.* **37**, 268–275 (1970).
76. Liu, C. *et al.* Facile Single-Precursor Synthesis and Surface Modification of Hafnium Oxide Nanoparticles for Nanocomposite γ-Ray Scintillators. *Adv. Funct. Mater.* **25**, 4607–4616 (2015).
77. Magi, A. *et al.* Optimization of phosphor concentration of surface-modified Bi2O3 nanoparticle-loaded plastic scintillators for high-energy photon detection. *J. Mater. Sci. Mater. Electron.* **32**, 7987–7999 (2021).
78. McKigney, E. A. *et al.* Nanocomposite scintillators for radiation detection and nuclear spectroscopy. *Nucl. Instruments Methods Phys. Res. Sect. A Accel. Spectrometers, Detect. Assoc. Equip.* **579**, 15–18 (2007).
79. Pellegrin, S. M., Whitney, C. & Wilson, C. G. A multichannel nanoparticle scintillation microdevice with integrated waveguides for alpha, beta, gamma, X-ray, and neutron detection. *J. Microelectromechanical Syst.* **19**, 1207–1214 (2010).
80. Kishimoto, S., Koshimizu, M., Hiyama, F., Haruki, R. & Nishikido, F. Measurements of 73-keV X-ray time spectrum with avalanche-photodiode scintillation detector using Bi2O3-nanoparticle-doped plastic scintillator. *Nucl. Instruments Methods Phys. Res. Sect. A Accel. Spectrometers, Detect. Assoc. Equip.* **968**, 163908 (2020).
81. Darukesha, B. H. M., Radhakrishna, V. & Rajanna, K. Suitability of nanoparticles for gamma-ray applications. *Appl. Radiat. Isot.* **191**, (2023).
82. Toda, A. & Kishimoto, S. Bi 2 O 3 nanoparticle-loaded plastic scintillator for. *IEEE Trans. Nucl. Sci.* **70**, 164–172 (2023).
83. Toda, A. & Kishimoto, S. X-Ray Detection Capabilities of Plastic Scintillators Incorporated with ZrO2Nanoparticles. *IEEE Trans. Nucl. Sci.* **67**, 983–987 (2020).
84. Kishimoto, S. & Toda, A. High-Energy and High-Rate X-Ray Measurements Using HfO Nanoparticle-Loaded Plastic Scintillator. *IEEE Trans. Nucl. Sci.* **68**, 165–172 (2021).
85. Hammig M D. Nanoscale Methods to Enhance the Detection of Ionizing Radiation. in

Current Topics in Ionizing Radiation Research (ed. Nenoi, M.) 557–578 (InTech, 2012). doi:10.5772/35344.
86. Jin, Y. *et al.* Partial ligand exchange as a critical approach to the synthesis of transparent ytterbium fluoride-polymer nanocomposite monoliths for gamma ray scintillation. *J. Mater. Chem. C* **4**, 3654–3660 (2016).
87. Molina Higgins, M. C., Radcliffe, N. A., Toro-González, M. & Rojas, J. V. Gamma ray attenuation of hafnium dioxide- and tungsten trioxide-epoxy resin composites. *J. Radioanal. Nucl. Chem.* **322**, 707–716 (2019).
88. Ekinci, N. *et al.* Development of Tincal based polypropylene polymeric materials for radiation shielding applications: Experimental, theoretical, and Monte Carlo investigations. *Mater. Sci. Semicond. Process.* **146**, (2022).
89. Cucinotta, F. A. & Durante, M. Cancer risk from exposure to galactic cosmic rays: implications for space exploration by human beings. *Lancet Oncol.* **7**, 431–435 (2006).
90. Liu, P. *et al.* Evaluation of mercury stabilization mechanisms by sulfurized biochars determined using X-ray absorption spectroscopy. *J. Hazard. Mater.* **347**, 114–122 (2018).
91. Al-Hadeethi, Y., Sayyed, M. I., Barasheed, A. Z., Ahmed, M. & Elsafi, M. Preparation and radiation attenuation properties of ceramic ball clay enhanced with micro and nano ZnO particles. *J. Mater. Res. Technol.* **17**, 223–233 (2022).
92. Atxaga, G., Marcos, J., Jurado, M., Carapelle, A. & Orava, R. Radiation shielding of composite space enclosures. *Proc. Int. Astronaut. Congr. IAC* **8**, 6658–6667 (2012).
93. Chen, S. *et al.* Polymer nanocomposite for space applications. in *Proceedings of the IEEE Conference on Nanotechnology* 685–688 (Institute of Electrical and Electronics Engineers Inc., 2014). doi:10.1109/NANO.2014.6968141.
94. Mahdavi, M. & Amiri, M. A. Space radiation effects on future quantum satellites. *Aerosp. Sci. Technol.* **26**, 72–75 (2013).
95. Bijanu, A. *et al.* Metal-polymer composites for radiation protection: a review. *J. Polym. Res.* **28**, (2021).
96. Noor Azman, N. Z., Wan Mohamed, W. F. I. & Ramli, R. M. Synthesis and characterization of electrospun n-ZnO/n-Bi2O3/epoxy-PVA nanofiber mat for low X-ray energy shielding application. *Radiat. Phys. Chem.* **195**, 110102 (2022).
97. Sen, S., Schofield, E., O'Dell, J. S., Deka, L. & Pillay, S. The development of a multifunctional composite material for use in human space exploration beyond low-earth orbit. *JOM* **61**, 23–31 (2009).
98. Friedberg, W. & Copeland, K. *Ionizing Radiation in Earth's Atmosphere and in Space Near Earth*. *Federal Aviation Administration* (2011).
99. Noor Azman, N. Z. Design of Nanostructured Polymeric Materials for Radiation Shielding of Ionizing Radiations. (Curtin University, 2013).
100. Nambiar, S. Application of Nanomaterials for X-ray Shielding and Dosimetry in Diagnostic Radiology. (University of Waterloo, 2015).
101. Hannachi, E. *et al.* Synthesis, characterization, and performance assessment of new composite ceramics towards radiation shielding applications. *J. Alloys Compd.* **899**, 163173 (2022).
102. Asgari, M., Afarideh, H., Ghafoorifard, H. & Amirabadi, E. A. Comparison of nano/micro lead, bismuth and tungsten on the gamma shielding properties of the flexible composites against photon in wide energy range (40 keV–662 keV). *Nucl. Eng. Technol.* **53**, 4142–4149 (2021).
103. Elsafi, M. *et al.* Optimizing the gamma-ray shielding behaviors for polypropylene using lead oxide: A detailed examination. *J. Mater. Res. Technol.* **19**, 1862–1872 (2022).
104. McCaffrey, J. P., Shen, H., Downton, B. & Mainegra-Hing, E. Radiation attenuation by

lead and nonlead materials used in radiation shielding garments. *Med. Phys.* **34**, 530–537 (2007).
105. Tiamduangtawan, P., Kamkaew, C., Kuntonwatchara, S., Wimolmala, E. & Saenboonruang, K. Comparative mechanical, self-healing, and gamma attenuation properties of PVA hydrogels containing either nano- or micro-sized Bi2O3 for use as gamma-shielding materials. *Radiat. Phys. Chem.* **177**, 109164 (2020).
106. Karabul, Y. & İçelli, O. The assessment of usage of epoxy based micro and nano-structured composites enriched with Bi2O3 and WO3 particles for radiation shielding. *Results Phys.* **26**, (2021).
107. Wang, Y. *et al.* Advanced X-ray Shielding Materials Enabled by the Coordination of Well-Dispersed High Atomic Number Elements in Natural Leather. *ACS Appl. Mater. Interfaces* **12**, 19916–19926 (2020).
108. Ambika, M. R., Nagaiah, N. & Suman, S. K. Role of bismuth oxide as a reinforcer on gamma shielding ability of unsaturated polyester based polymer composites. *J. Appl. Polym. Sci.* **134**, 1–7 (2017).
109. Alavian, H., Samie, A. & Tavakoli-Anbaran, H. Experimental and Monte Carlo investigations of gamma ray transmission and buildup factors for inorganic nanoparticle/epoxy composites. *Radiat. Phys. Chem.* **174**, 108960 (2020).
110. Azman, N. Z. N. *et al.* Characteristics of X-ray attenuation in electrospun bismuth oxide/polylactic acid nanofibre mats. *J. Synchrotron Radiat.* **20**, 741–748 (2013).
111. Wahyuni, F., Sakti, S., Santjojo, D. & Juswono, U. Bismuth Oxide Filled Polyester Composites for X-ray Radiation Shielding Applications. *Polish J. Environ. Stud.* **31**, 1–6 (2022).
112. Iball, G. & Brettle, D. S. Organ and effective dose reduction in adult chest CT using abdominal lead shielding. *Br. J. Radiol.* **84**, 1020–1026 (2011).
113. Akman, F. *et al.* Impact of lead(II) iodide on radiation shielding properties of polyester composites. *Appl. Phys. A Mater. Sci. Process.* **126**, (2020).
114. Nambiar, S. & Yeow, J. T. W. Polymer-composite materials for radiation protection. *ACS Appl. Mater. Interfaces* **4**, 5717–5726 (2012).
115. Alavian, H. & Tavakoli-Anbaran, H. Comparative study of mass attenuation coefficients for LDPE/metal oxide composites by Monte Carlo simulations. *Eur. Phys. J. Plus* **135**, (2020).
116. Barabash, A., Barabash, D., Pertsev, V. & Panfilov, D. Polymer-Composite Materials for Radiation Protection. *Adv. Intell. Syst. Comput.* **983**, 352–360 (2019).
117. Li, R. *et al.* Effect of particle size on gamma radiation shielding property of gadolinium oxide dispersed epoxy resin matrix composite. *Mater. Res. Express* **4**, aa6651 (2017).
118. Botelho, M. Z. *et al.* X-ray transmission through nanostructured and microstructured CuO materials. *Appl. Radiat. Isot.* **69**, 527–530 (2011).
119. Noor Azman, N. Z., Siddiqui, S. A., Hart, R. & Low, I. M. Effect of particle size, filler loadings and x-ray tube voltage on the transmitted x-ray transmission in tungsten oxide-epoxy composites. *Appl. Radiat. Isot.* **71**, 62–67 (2013).
120. El-khatib, A. M., Elsafi, M., Sayyed, M. I., Abbas, M. I. & El-Khatib, M. Impact of micro and nano aluminium on the efficiency of photon detectors. *Results Phys.* **30**, 104908 (2021).
121. Mehrara, R., Malekie, S., Kotahi, S. M. S. & Kashian, S. Introducing a novel low energy gamma ray shield utilizing Polycarbonate Bismuth Oxide composite. *Sci. Rep.* **11**, 1–13 (2021).
122. Künzel, R. & Okuno, E. Effects of the particle sizes and concentrations on the X-ray absorption by CuO compounds. *Appl. Radiat. Isot.* **70**, 781–784 (2012).
123. Asari Shik, N. & Gholamzadeh, L. X-ray shielding performance of the EPVC

composites with micro- or nanoparticles of WO3, PbO or Bi2O3. *Appl. Radiat. Isot.* **139**, 61–65 (2018).
124. El-Toony, M. M., Eid, G., Algarni, H. M., Alhawimal, T. F. & Abel-hady, E. E. Synthesis and characterisation of smart poly vinyl ester / Pb2O3 nanocomposite for gamma radiation shielding. *Radiat. Phys. Chem.* **168**, 108536 (2020).
125. Mansouri, E., Mesbahi, A., Malekzadeh, R. & Mansouri, A. Shielding characteristics of nanocomposites for protection against X- and gamma rays in medical applications: effect of particle size, photon energy and nano-particle concentration. *Radiat. Environ. Biophys.* **59**, 583–600 (2020).
126. El-Sharkawy, R. M., Abdou, F. S., Gizawy, M. A., Allam, E. A. & Mahmoud, M. E. Bismuth oxide nanoparticles (Bi2O3 NPs) embedded into recycled- poly(vinyl chloride) plastic sheets as a promising shielding material for gamma radiation. *Radiat. Phys. Chem.* **208**, 110838 (2023).
127. More, C. V., Alsayed, Z., Badawi, M. S., Thabet, A. A. & Pawar, P. P. Polymeric composite materials for radiation shielding: a review. *Environ. Chem. Lett.* **19**, 2057–2090 (2021).
128. Darukesha, B. H. M., Radhakrishna, V. & Rajanna, K. Direct determination of the outcomes of interaction of X-rays/gamma-rays with nanoparticles. *Nucl. Instruments Methods Phys. Res. Sect. A Accel. Spectrometers, Detect. Assoc. Equip.* **1048**, 167922 (2023).
129. Grau Carles, A. & Grau Malonda, A. Computational aspects in modelling the interaction of low-energy X-rays with liquid scintillators. *Appl. Radiat. Isot.* **64**, 1515–1519 (2006).
130. Shoji, M. *et al.* Modification of LSC spectra of 125I by high atomic number elements. *Appl. Radiat. Isot.* **139**, 131–136 (2018).
131. Baratta, E. J. *Manual of Food Quality Control*. *FAO of the UN* (1997).
132. L'Annunziata, M. F., Tarancón, A., Bagán, H. & García, J. F. Liquid scintillation analysis: principles and practice. in *Handbook of Radioactivity Analysis* vol. 1 575–801 (Elsevier B.V., 2020).
133. NASA. Properties of Selected Radioisotopes. (1968).
134. Howard, D., Sebastian, S., Le, Q. V. C., Thierry, B. & Kempson, I. Chemical mechanisms of nanoparticle radiosensitization and radioprotection: A review of structure-function relationships influencing reactive oxygen species. *Int. J. Mol. Sci.* **21**, (2020).
135. Keller, J. M. Applied radiation measurements. in *Radioanalytical Chemistry* 134–162 (2007). doi:10.1007/0-387-34123-4_8.
136. L'Annunziata, M. F. Radiation Physics and Radionuclide Decay. in *Handbook of Radioactivity Analysis* 1–162 (Elsevier Inc., 2012). doi:10.1016/B978-0-12-384873-4.00001-3.
137. Kang, H. *et al.* Low energy beta emitter measurement: A review. *Chemosensors* **8**, 1–42 (2020).
138. El-Khatib, A. M. *et al.* Conductive natural and waste rubbers composites-loaded with lead powder as environmental flexible gamma radiation shielding material. *Mater. Res. Express* **7**, 105309 (2020).
139. Evans R. D. *The Atomic Nucleus*. (McGraw-Hill Book Company, 1955).
140. Claus Grupen, B. S. *Particle Detectors*. (Cambridge University Press, 2008).
141. Natali, D. & Sampietro, M. Detectors based on organic materials: Status and perspectives. *Nucl. Instruments Methods Phys. Res. Sect. A Accel. Spectrometers, Detect. Assoc. Equip.* **512**, 419–426 (2003).
142. Jagtap, S., Chopade, P., Tadepalli, S., Bhalerao, A. & Gosavi, S. A review on the progress of ZnSe as inorganic scintillator. *Opto-electronics Rev.* **27**, 90–103 (2019).

143. Dujardin, C. *et al.* Needs, trends, and advances in inorganic scintillators. *IEEE Trans. Nucl. Sci.* **65**, 1977–1997 (2018).
144. Young, S. A. Multifunctional Polymeric Micro- and Nanocomposite Fibers for Radiation Detection. (Tennessee, Knoxville, 2013).
145. Broda, R., Cassette, P. & Kossert, K. Radionuclide metrology using liquid scintillation counting. *Metrologia* **44**, (2007).
146. Barnett, J. M. Radon-222 in drinking water: liquid scintillation detection methods and estimated doses to the lungs. (Arizona State University, 1990).
147. Bransome, E. D. Liquid Scintillation C o u n t i n g in Nuclear Medicine. **3**, 389–399 (1973).
148. H Kara, O. A. M. A. *Radioanalytical Chemistry*. *Springer* vol. 7 (Springer, 2014).
149. Kessler, M. J. E. & Kessler, M. J. *Liquid Scintillation Analysis*. www.perkinelmer.com/liquid-scintillation (2015).
150. ASTM International. Standard Terminology Relating to Nanotechnology ASTM E2456-06(2020). (2020).
151. Buzea, C., Pacheco, I. I. & Robbie, K. Nanomaterials and nanoparticles: Sources and toxicity. *Biointerphases* **2**, MR17–MR71 (2007).
152. Baig, N., Kammakakam, I., Falath, W. & Kammakakam, I. Nanomaterials: A review of synthesis methods, properties, recent progress, and challenges. *Mater. Adv.* **2**, 1821–1871 (2021).
153. Mandal, G. & Ganguly, T. Applications of nanomaterials in the different fields of photosciences. *Indian J. Phys.* **85**, 1229–1245 (2011).
154. Mandal, A. Properties of nanoparticles. vol. 1 473–480 http://www.news-medical.net/health/Properties-of-Nanoparticles.aspx P (2006).
155. Singh, M., Goyal, M. & Devlal, K. Size and shape effects on the band gap of semiconductor compound nanomaterials. *J. Taibah Univ. Sci.* **12**, 470–475 (2018).
156. Liu, G. *et al.* Cu Nanowires Passivated with Hexagonal Boron Nitride: An Ultrastable, Selectively Transparent Conductor. *ACS Nano* **14**, 6761–6773 (2020).
157. Gao, F., Gu, Z. Melting Temperature of Metallic Nanoparticles. in *Handbook of Nanoparticles* (ed. Aliofkhazraei, M.) (Springer, 2015).
158. Quadros, M. E. & Marr, L. C. Environmental and human health risks of aerosolized silver nanoparticles. *J. Air Waste Manag. Assoc.* **60**, 770–781 (2010).
159. Chinthala, M., Balakrishnan, A., Venkataraman, P., Manaswini Gowtham, V. & Polagani, R. K. *Synthesis and applications of nano-MgO and composites for medicine, energy, and environmental remediation: a review*. *Environmental Chemistry Letters* vol. 19 (Springer International Publishing, 2021).
160. Forsberg, B. J. & Burlin, T. E. Microdosimetry I. Use of secondary electron emission. *Acta Oncol. (Madr).* **19**, 115–127 (1980).
161. Gimåker, M. & Granberg, H. *DCC review: Graphite materials - Production from biomass?* (2021).
162. Xue, L. *et al.* Solid-state nanopore sensors. *Nat. Rev. Mater.* **5**, 931–951 (2020).
163. Korin, E., Froumin, N. & Cohen, S. Surface Analysis of Nanocomplexes by X-ray Photoelectron Spectroscopy (XPS). *ACS Biomater. Sci. Eng.* **3**, 882–889 (2017).
164. Sato, A. Fabrication of Hf x Si 1 2 x O 2 microparticle-loaded PVK- based plastic scintillators using the sol – gel method for high-energy X-ray detection at high counting rate. *J. Mater. Sci. Mater. Electron.* **32**, 28807–28818 (2021).
165. Elsafi, M., Sayyed, M. I., Almuqrin, A. H., Gouda, M. M. & El-khatib, A. M. Analysis of particle size on mass dependent attenuation capability of bulk and nanoparticle PbO radiation shields. *Results Phys.* **26**, 104458 (2021).
166. Britvich, G. I., Vasil'chenko, V. G., Lapshin, V. G. & Solov'ev, A. S. New heavy plastic

scintillators. *Instruments Exp. Tech.* **43**, 36–39 (2000).
167. Awaja, F., Zhang, S., Tripathi, M., Nikiforov, A. & Pugno, N. Cracks, microcracks and fracture in polymer structures: Formation, detection, autonomic repair. *Prog. Mater. Sci.* **83**, 536–573 (2016).
168. Perera, H. *et al.* Rapid two-dimensional dose measurement in brachytherapy using plastic scintillator sheet: linearity, signal-to-noise ratio, and energy response characteristics. *Int. J. Radiat. Oncol.* **23**, 1059–1069 (1992).
169. Ghaseminejad, M. & Gholamzadeh, L. Investigation of x-ray attenuation property of modification PbO with graphene in epoxy polymer Investigation of x-ray attenuation property of modi fi cation PbO with graphene in epoxy polymer. *Mater. Res. Express Pap.* **8**, 035008 (2021).
170. Turkevich, J., Stevenson, P. C. & Hillier, J. A study of the nucleation and growth processes in the synthesis of colloidal gold. *Discuss. Faraday Soc.* **11**, 55–75 (1951).
171. Zhang, Y., Zheng, D., Talaei, S. & Abasi, M. Albumin stabilized Pt nanoparticles as radiosensitizer for sensitization of breast cancer cells under X-ray radiation therapy. *Inorg. Chem. Commun.* **140**, 109423 (2022).
172. Horrocks, D. L. Measurement of 125I by Liquid Scintillation Methods. *Nucl. Instruments Methods* **133**, 293–301 (1976).
173. Prins, T. J. Organic Scintillators Containing High-Z Nanoparticles. (University of California, 2020).
174. Tarancón, A., Bagán, H. & García, J. F. Plastic scintillators and related analytical procedures for radionuclide analysis. *J. Radioanal. Nucl. Chem.* **314**, 555–572 (2017).
175. Casta, R., Champeaux, J. P., Cafarelli, P., Moretto-Capelle, P. & Sence, M. Model for electron emission of high-Z radio-sensitizing nanoparticle irradiated by X-rays. *J. Nanoparticle Res.* **16**, (2014).
176. Lynch, I. *et al.* The nanoparticle-protein complex as a biological entity; a complex fluids and surface science challenge for the 21st century. *Adv. Colloid Interface Sci.* **134**–**135**, 167–174 (2007).
177. Haupert, F. & Wetzel, B. Reinforcement of Thermosetting Polymers by the Incorporation of Micro- and Nanoparticles. in *Polymer Composites* 45–62 (Springer-Verlag, 2005). doi:10.1007/0-387-26213-x_3.
178. Lin, Y., McMahon, S. J., Scarpelli, M., Paganetti, H. & Schuemann, J. Comparing gold nano-particle enhanced radiotherapy with protons, megavoltage photons and kilovoltage photons: A Monte Carlo simulation. *Phys. Med. Biol.* **59**, 7675–7689 (2014).
179. Chenjie, X., Tung, G. A. & Shouheng, S. Size and concentration effect of gold nanoparticles on X-ray attenuation as measured on computed tomography. *Chem. Mater.* **20**, 4167–4169 (2008).
180. Nambiar, S., Osei, E. K. & Yeow, J. T. W. Effects of particle size on X-ray transmission characteristics of PDMS/Ag nano- and microcomposites. in *IEEE-NANO 2015 - 15th International Conference on Nanotechnology* 1358–1361 (2015). doi:10.1109/NANO.2015.7388888.
181. Kawady, N. A., Elkattan, M., Salah, M. & Galhoum, A. A. Fabrication, characterization, and gamma ray shielding properties of PVA-based polymer nanocomposite. *J. Mater. Sci.* **57**, 11046–11061 (2022).
182. Leung, M. K. K. *et al.* Irradiation of gold nanoparticles by x-rays: Monte Carlo simulation of dose enhancements and the spatial properties of the secondary electrons production. *Med. Phys.* **38**, 624–631 (2011).
183. Coughlin, B. P. *et al.* Evidence for biological effects in the radiosensitization of leukemia cell lines by PEGylated gold nanoparticles. *J. Nanoparticle Res.* **22**, 1–12 (2020).

184. Lacombe, S., Porcel, E. & Scifoni, E. Particle therapy and nanomedicine: state of art and research perspectives. *Cancer Nanotechnol.* **8**, (2017).
185. McLaughlin, M. F. *et al.* Gold Coated Lanthanide Phosphate Nanoparticles for Targeted Alpha Generator Radiotherapy. *PLoS One* **8**, 2–9 (2013).
186. Silva, F., Campello, M. P. C. & Paulo, A. Radiolabeled gold nanoparticles for imaging and therapy of cancer. *Materials (Basel).* **14**, 1–32 (2021).
187. Haume, K. *et al.* Gold nanoparticles for cancer radiotherapy: a review. *Cancer Nanotechnol.* **7**, (2016).
188. Artem'ev V. Attenuation of x rays by ultradisperse media. *Tech. Phys. Lett.* **23**, 5–9 (1997).
189. Chase, G. D. Applications of Liquid Scintillation Counting To Radioimmunoassay. in *Liquid Scintillation Counting, Recent Applications and Development* vol. II 489–502 (Academic Press, 1980).
190. Bikash Dwivedi. Radioimmunoassay- Principle, Uses and Limitations. *Microbe Notes* https://microbenotes.com/radioimmunoassay-principle-uses-and-limitations/.
191. Tölgyessy, J. & Harangozó, M. Radiochemical Methods | Food and Environmental Applications. in *Encyclopedia of Analytical Science* 79–86 (Elsevier, 2005). doi:10.1016/B0-12-369397-7/00526-4.
192. Buck A. Rhodes. Liquid Scintillation Counting of Radioiodine. *Int. J. Appl. Radiat. Isot.* **16**, 65–70 (1965).
193. Herscowitz, H. B. & McKillip, T. W. A simple method for liquid scintillation counting of 125Iodine and 51Chromium used in antigen binding and cytotoxicity studies. *J. Immunol. Methods* **4**, 253–262 (1974).
194. Akanuma, S. ichi *et al.* ATP-binding cassette transporter A1 (ABCA1) deficiency does not attenuate the brain-to-blood efflux transport of human amyloid-β peptide (1-40) at the blood-brain barrier. *Neurochem. Int.* **52**, 956–961 (2008).
195. Wilde, C. & Ottewell, D. A practical guide to gamma-counting in radioimmunoassay. *Ann. Clin. Biochem.* **17**, 1–9 (1980).
196. da Costa, O. L. *et al.* Gamma spectrometry of iodine-125 produced in IEA-R1 nuclear reactor, using HPGe detector and fixation into epoxy matrix disc. *Appl. Radiat. Isot.* **169**, 1–6 (2021).
197. Versluijs, F. An improved counting vial for measurement of low-energy gamma rays in liquid scintillation counters. *Anal. Biochem.* **80**, 249–257 (1977).
198. Helman, E. Z. & Ting, P. Counting of beta and gamma emitters used in clincal radioimmunoassays and competitive-binding assays by liquid scintillation counters. *Clin. Chem.* **19**, 191–196 (1973).
199. Medalia, J. *Detection of nuclear weapons and materials: Science, technologies, observations*. *Detection of Nuclear Weapons and Materials* (2010).
200. Whitney, C., Pellegrin, S. M. & Wilson, C. A nanoparticle doped micro-Geiger counter for multispecies radiation detection. *J. Microelectromechanical Syst.* **18**, 998–1003 (2009).
201. Stone, R. Researchers rise to challenge of replacing helium-3. *Science (80-.).* **353**, 15–16 (2016).
202. Vladimirov, A. G. *et al.* Synthesis of composite Si-B nanoparticles by the laser-induced pyrolysis method. *Laser Phys. Lett.* **11**, (2014).
203. Ellis, M. E., Duroe, K. & Kendall, P. A. Pulse-shape discrimination scintillators for homeland security applications. *Int. J. Mod. Phys. Conf. Ser.* **44**, 1660214 (2016).
204. Maguire, John A, Z. Y. and T. M. *Boron and gadolinium neutron capture therapy for cancer treatment*. (World Scientific, 2012).

Appendix-I: Interaction of neutrons with nanoparticles

A brief study on the interaction of neutrons with nanoparticles is presented here.

Neutrons are uncharged particles that reside inside the nucleus of an atom owing to the strong nuclear force [1]. They spontaneously get emitted from excited nuclei. Detecting neutrons is crucial for space travel, high-energy physics experiments, and nuclear security [1]. While medical isotopes can produce low-energy beta and gamma radiation, fissionable materials emit neutrons and high gammas[1,199]. The emission of neutrons is almost exclusive to fissionable materials, as not much else generates neutrons[200].

However, neutron detection is challenging [1,74,140]. Neutrons interact with matter rarely, that too with the nucleus of the suitable materials[1,74]. The probability of interaction of neutrons is greater when the mass and size of the target material nuclei are comparable to those of neutron[1]. H, He, Li, and B are popular neutron targets [74]. Gd is another popular neutron target since it has the greatest neutron cross-section[136].

The general scheme of detection of neutrons is shown in Figure A.1-0-1.

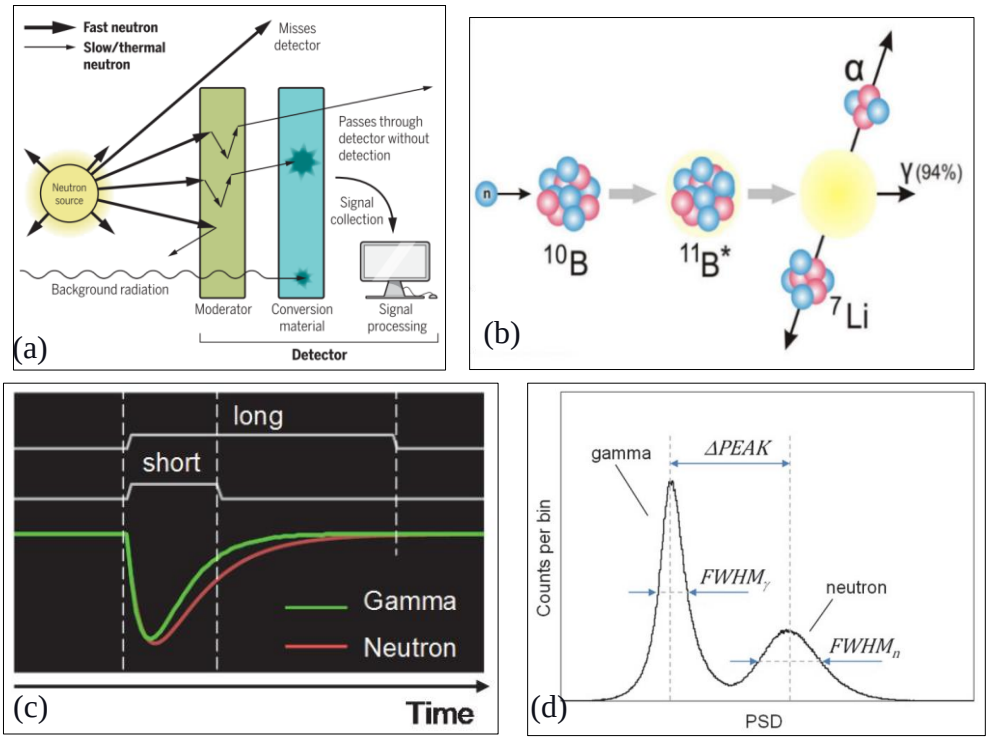

Figure A.1-0-1 (a) Scheme of neutron detection Adapted from [201] (b) Interaction of neutrons. Adapted from [202] (c) Gamma and neutron pulse Characteristics. Adapted from [203] (d) Shape discriminated pulses. Adapted from [203]

Upon interaction with the suitable targets, the neutron may either disappear and be replaced by one or more secondary radiations or undergo a significant change in the energy to become slow neutrons [1]. Secondary radiations usually include charged particles (like beta and alpha) and gamma rays. Further, slow neutrons interact with the nuclei of the same materials to emit gamma rays and charged particles. The scintillation light pulse of particles has a longer tail than that of gamma rays, owing to how the particles lose their energy in the scintillator. These pulses are digitized and discriminated based on the characteristic decay times.

In this pulse shape discrimination technique, higher detection or higher efficiency of the detector defines the pulses well and separate from each other. This separation called the figure of merit (FoM), distinguishes the neutron and gamma-ray interactions occurring in a given detector. The larger the pulse sizes, the better the FoM. Better the FoM, unambiguous the detection.

As demonstrated in this thesis work, the liquid scintillator loaded with Gd_2O_3 nanoparticles enhances the pulse sizes for gamma and electrons. The interaction of neutrons with Gd is shown below [204].

$$[^{157}Gd + n_{th}] \Rightarrow [^{158}Gd] \Rightarrow [^{158}Gd + \gamma + 7.9\ MeV]$$

$\hookrightarrow$ Internal conversion electrons

Hence, the Gd_2O_3 nanoparticle-loaded liquid scintillator should efficiently detect internal conversion electrons and thus enhance the FoM. The following study was conducted with this rationale.

A-1.1 Materials and Method

The am-Be source and the Gd_2O_3 nanoparticles used are mentioned in sections 3.2.2 and 4.1.2. Pulse shape discriminator model 2620 was sourced from RSD.

The outcomes of the interaction of neutrons with nanoparticles were determined in two modes. The variations in the PHS of neutrons for the unloaded liquid scintillator upon loading the nanoparticles were obtained first. This was similar to studying the interactions of gamma rays. The basic setup for either mode was the same as in section 4.1.3.1. Secondly, the technique of pulse shape discrimination was adopted. For this, a pulse shape discriminator replaced CSPA and MCA in Figure 2-12. The neutron source was placed about 50 cm away from the beaker. Whenever required for analysis, to attenuate the gamma rays from the Am-Be source so that only neutrons strike the samples, a sheet of 20 mm thick lead between the source and detector. LLD was kept at 25.

A-1.2 Results

Figure A.1-0-2a presents the variations in PHS of radiations from the Am-Be source with an unloaded liquid scintillator upon loading the nanoparticles. The response is similar in trend to that of the ^{241}Am source in Figure 4-7. When a 20 mm thick Pb-sheet was placed between the

source and the detector, the gamma rays were eliminated, and no variation was observed in the number of counts [Figure A.1-0-2 (b)].

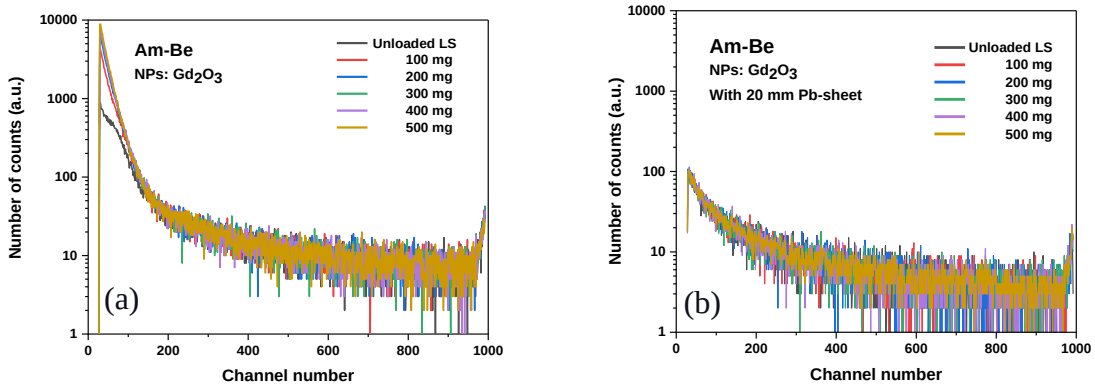

Figure A.1-0-2 Variations in PHS of neutrons with unloaded liquid scintillator upon loading Gd_2O_3 nanoparticles (a) without Pb-sheet placed (b) with Pb-sheet placed

Figure A.1-0-3 displays the pulse shape discriminated output. The number of counts due to gamma-radiation interaction is increased, while those for neutrons remain unchanged.

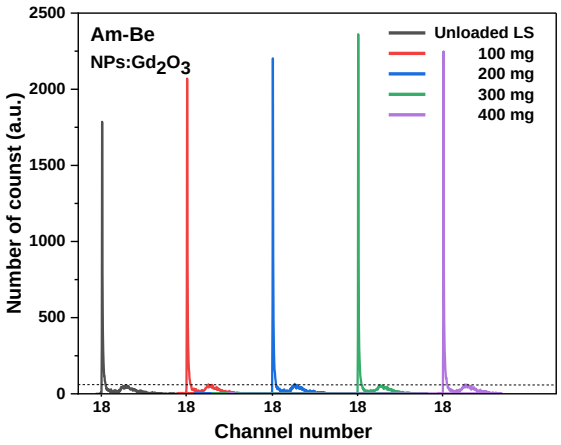

Figure A.1-0-3 Pulse shape discriminated response of Gd_2O_3 nanoparticle loaded liquid scintillator for neutrons from Am-Be. The channel numbers are repeated on X-axis.

A-1.3 Discussion

When both the neutrons and gamma rays strike the nanoparticles [Figure A.1-0-2(a)], the electrons emitted from the nanoparticles upon interacting with the gamma rays cause the number of counts to increase. The interaction of gamma rays is similar in trend to that in Figure 4-7. However, the enhancement due to the expected interaction of beta-radiations with nanoparticles was unobserved. Had the internal conversion electrons released from ^{158}Gd interacted with the liquid scintillator, the number of counts would have increased. It is possible that the neutrons interacted with the Gd nanoparticles, and the beta-radiation was emitted into the liquid scintillator. However, these experiments were conducted with loadings of 100 mg and above. The loading of hundreds of milligrams of nanoparticles resulted in a high

concentration inside the scintillator or formed a layer at the bottom. The electrons emitted from the nanoparticles might have been absorbed by others or scattered, reducing their energy lower than the detection threshold of fast-electrons inside the liquid scintillator. Hence, experiments with lower loadings are required. It was realized later that to enhance the beta-detection efficiency, the loading needs to be extremely small (section 4.2.3), and then this experiment could not be repeated within the time frame of this thesis work. Thus, a large scope exists for improving the quality of pulse shape discrimination by loading the nanoparticles into the organic scintillators at lower loadings.

A-1.4 Conclusions

A brief study on the interaction of ionizing radiations from Am-Be source with nanoparticles demonstrated the interaction of gamma rays with Gd_2O_3 nanoparticles. Further experiments at lower loadings of nanoparticles could enhance the quality of pulse shape discrimination.

Appendix-II: Effect of shape of nanomaterials

This appendix presents the study of the effect of the shape of nanomaterials. It was conducted initially to establish that the outcome of the interaction of ionizing radiation with nanoparticles is distinct from that of the radiation with nanofilm.

The arrangement made is shown in Figure A.2-0-1. This was part of the main setup (section 4.1.3.1). A glass substrate sputtered with a 70 nm thick HfO_2 layer was placed inside the beaker with sputtered layer facing the PMT head. A liquid scintillator was loaded into the beaker, and a PHS of ^{241}Am was obtained. About 10 mg of HfO_2 nanoparticles were loaded into the scintillator, and the PHS was obtained.

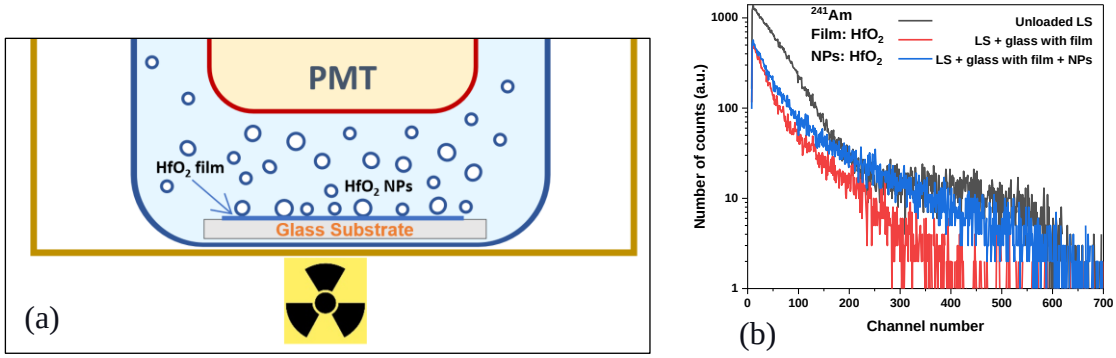

Figure A.2-0-1 (a) Arrangement to study the effect of the shape of nanomaterials (b) Variations in PHS of ^{241}Am with liquid scintillator upon placing HfO_2 film over the glass and then HfO_2 nanoparticles over the film

Figure A.2-0-1b shows the outcomes. The number of counts in PHS was reduced upon the introduction of the nanofilm-sputtered substrate. The radiation flux at the scintillator is reduced as the substrate attenuates a portion of radiation. Though the atoms inside the nanofilm emit electrons, the electrons get attenuated within the film. When HfO_2 nanoparticles were dispersed over the substrate, the number of counts in PHS increased as the gamma rays interacted with the nanoparticles to cause the emission of electrons into the scintillator. Thus, it was established that the emission of electrons from the nanoparticles is unique to nanoparticles but not to nanofilms.

Applied Radiation and Isotopes 191 (2023) 110519

Contents lists available at ScienceDirect

Applied Radiation and Isotopes

journal homepage: www.elsevier.com/locate/apradiso

Suitability of nanoparticles for gamma-ray applications

B.H.M. Darukesha [a,b,*], V. Radhakrishna [a], K. Rajanna [b]

[a] U R Rao Satellite Centre, Indian Space Research Organisation, Bengaluru, 560 017, India
[b] Department of Instrumentation & Applied Physics, Indian Institute of Science, Bengaluru, 560 012, India

ARTICLE INFO

Keywords:
Interaction of radiation with nanoparticles
Nanoparticle-loaded plastic scintillators
Nanocomposites
Pb-free gamma-ray shields

ABSTRACT

While measuring the relative gamma-to-electron conversion efficiencies of nanoparticles by incorporating them into plastic scintillator and comparing the number of counts in pulse height spectrum for gamma-rays from ^{241}Am, WO_3, and PbO nanocomposites offered lesser scintillation counts than their unloaded counterparts. As investigated, these nanoparticles absorb a major portion of outgoing electron energy such that exiting electrons turn incapable of scintillating the medium. This observation hints why only selected species of nanoparticles successfully enhance the gamma-counting efficiency of plastic scintillators.

1. Introduction

Fast-efficient-large-affordable gamma-ray detectors are needed for synchrotron-based materials characterization studies, nuclear non-proliferation, medical imaging, high energy physics, etc. (Kagami et al., 2020; Magi et al., 2021; Sun et al., 2014). Plastic scintillators are fast-scalable-affordable but are inefficient gamma-detectors. The incorporation of high-Z materials into plastic scintillators through organo-metallic ligands to enhance the gamma-detection efficiency of the hosts has been pursued since the 1960s. (G. H. V. Bertrand et al., 2015; Dumazert et al., 2016). While this approach facilitates the uniform distribution of high-Z materials, it limits the loading of dopants due to the limited solubility of the ligands. Further, even at small loadings, the quenching results in a severe reduction of light yield in such composites (Cai et al., 2013).

In a recent approach, the nanoparticles of high-Z materials are incorporated into plastic scintillators to enhance the gamma-detection efficiency of the latter. (Kishimoto and Toda, 2021; Koshimizu, 2020; Pellegrin et al., 2010; Sato et al., 2021). As reasoned, nanoparticles interact with incoming gamma-radiations and emit electrons into the scintillator to increase the scintillation counts and thus enhance the gamma-detection efficiency. (Kishimoto and Toda, 2021; Koshimizu, 2020; Pellegrin et al., 2010). Various studies so far have demonstrated that incorporating Bi_2O_3, Gd_2O_3, HfO_2, $Hf_xSi_{1-x}O$, and ZrO_2 nanoparticles enhances the gamma detection efficiency of the host scintillators (Araya et al., 2015; Cai et al., 2013; Hiyama et al., 2018; Inoue et al., 2018; Kishimoto and Toda, 2021; Liu et al., 2015; Magi et al., 2021; Sato et al., 2021; Sun et al., 2014; Toda and Kishimoto, 2020). However, the demonstration of nanoparticle-loaded scintillators is limited to a laboratory scale due to the issues related to the upscaling process (Cai et al., 2013; Hajagos et al., 2018; Koshimizu, 2020). Such process issues preferably be addressed using nanoparticles that efficiently convert the gamma-rays into electrons in the first place.

With a target to determine the better-suited nanoparticles to develop fast-efficient-large- gamma-ray detectors for applications in Space-based astronomy, we aimed to measure relative gamma-to-electron conversion efficiency for the available nanoparticles. We realized the unloaded and Gd_2O_3, HfO_2, Bi_2O_3, WO_3, and PbO nanoparticle-loaded plastic scintillators (nanocomposites), obtained pulse height spectrum (PHS) of gamma-rays from ^{241}Am for each nanocomposite and compared it with PHS for the unloaded scintillator, all under identical conditions. Nanocomposite loaded with a highly efficient dopant nanoparticle yields greater enhancement of scintillation counts at peak energy channels compared to those in the PHS for unloaded scintillator.

Remarkably, WO_3 and PbO nanocomposites yielded lesser scintillation counts than the unloaded scintillator. After a detailed investigation, we speculate that WO_3 and PbO nanoparticles interact with the gamma-rays; their constituent atoms emit the electrons, but these nanoparticles attenuate the electrons within themselves or absorb the energy of outgoing electrons to the extent that electrons exit with energy insufficient to scintillate the host. This result is significant because it (a) ascertains that not all nanoparticles, even if high-Z, suit as dopants in plastic scintillators for enhancing the gamma-detection efficiency of the latter (b) hints why only certain species of nanoparticles are successful in enhancing the gamma-counting efficiency of the plastic scintillators and (c) enables the selection of better-suited nanoparticles for a given

* Corresponding author. U R Rao Satellite Centre, Indian Space Research Organisation, Bengaluru, 560 017, India.
E-mail address: darukeshabhm@iisc.ac.in (B.H.M. Darukesha).

https://doi.org/10.1016/j.apradiso.2022.110519
Received 7 April 2022; Received in revised form 29 September 2022; Accepted 15 October 2022
Available online 19 October 2022

application. The objective of this article is to present the experiments, results, and our discussion.

The nanoparticles were selected based on their higher atomic numbers, enabling better gamma-to-electron conversion. Radioactive source ^{241}Am was chosen since the energy of gamma-rays emitted by this source (principal energy at 60 keV) is comparable to those of interest in practical applications. It is reported earlier that loading the nanoparticles into polystyrene solvent leads to the sedimentation of nanoparticles (Araya et al., 2015). Hence, BC-490, a viscus partially-polymerized formulation of plastic scintillators, was used to ensure that the nanoparticles stayed suspended in the scintillator. As reported, the higher loading of nanoparticles adversely affects the gamma-detection efficiency of the loaded plastic scintillators(Sato et al., 2021). Hence, we limited the maximum loading to a sufficiently low level of 2 wt%.

2. Experiments

2.1. Materials and their characterization

Nanoparticles of Gd_2O_3, WO_3, and PbO were sourced from Nanoshell. Bi_2O_3 and HfO_2 were sourced from Sigma-Aldrich and Ottokemi, respectively. Saint-Gobain's BC-490, a vinyl-toluene solvent-based partially-polymerized formulation, was used to realize plastic scintillators. Standard plastic scintillator EJ212 was sourced from Eljen Technologies to compare the performance of the unloaded plastic scintillator realized. Radioactive source ^{241}Am supplied by the Board of Radiation & Isotope Technology (BRIT), India, was utilized.

The purity of the nanoparticles was determined using the energy dispersive spectroscope, Oxford ESD system model INCA Pentafet attached to Carl Zeiss SEM model EVO 50. All five species of nanoparticles were purer than 99.9%. The size of nanoparticles was determined through dynamic light scattering using NanoBrook ZetaPALS (90°, 658 nm, 25 °C). The nanoparticles and de-ionized water mixture were ultra-sonicated for about 15 min before loading into the cuvette. Three replicate measurements for 1 min each were carried out. Size in nm and polydiversity indices of nanoparticles were Gd_2O_3 (55 ± 1, 0.292), HfO_2 (77 ± 3, 0.333), Bi_2O_3 (120 ± 2, 0.361), WO_3 (82 ± 1, 0.351), and PbO (141 ± 2, 0.299).

The crystalline phase of the nanoparticles was confirmed with an X-ray diffraction (XRD) system (Rigaku SmartLab) using Cu $K\alpha$ X-rays in a 2θ–θ setup. The chemical composition of nanoparticles was affirmed by X-ray Photoelectron Spectroscopy (XPS) with a SPECS spectrometer (SPECS Surface Nano Analysis GmbH, Germany) using non-monochromatic Al K_α radiation (1486.6 eV) as an X-ray source operated at 300 W (12 kV, 12.5 mA). All the survey spectra were obtained with a pass energy of 50 eV with a step increment of 1 eV, and individual core level spectra were recorded with a pass energy and step increment of 40 and 0.05 eV, respectively. The nanoparticle sample was mounted on the sample holder and kept in the preparation chamber at ultrahigh vacuum at 8×10^{-8} mbar for 5 h in order to desorb any volatile species present on the surface. After 5 h, the sample was placed into the analyzer chamber with UHV at 5×10^{-10} mbar.

The absorbance spectra of the nanoparticles were obtained with Analytik Jena Specord-S600 UV–Vis spectrophotometer. The nanoparticles were loaded into the de-ionized water, mixed thoroughly, and diluted to obtain the spectrum. The extent of dilution was different for different nanoparticles.

2.2. Realization of nanocomposites

The realization of unloaded plastic scintillators followed the method outlined in the datasheet of BC-490. All reagents were used as received. The solvent and the catalyst were mixed in proportion in a beaker. The mixture was added to the resin. Vacuum settling was performed to get rid of air bubbles for 10 min at 10 mbar. To realize the nanocomposites, nanoparticles were incorporated into the formulation at this stage. Nanoparticles were added to the mixture directly by weight. Loadings were 2 wt%, 1 wt%, and 0.5 wt%. The mixture was manually stirred and cast into glass test-tube molds (inner diameter of 9 mm and height of 12 mm). The mixture (of solvent, catalyst, and resin) for unloaded plastic scintillators was also cast into the molds. Vacuum settling was performed again at 10 mbar for 10 min for all scintillators. All molds were immersed in de-ionized water maintained at 47 °C for 14 days inside an oven. Later, the water was drained, and the molds were stored at 80 °C in a nitrogen atmosphere for 8 h. The glass was broken in running water. Three samples for each variation were realized.

The scintillators thus realized were cut to 10 mm thickness. The slab of plastic scintillator EJ212 was machined to the same dimensions. All faces of all scintillators were polished using a micro grinder and 0.05 μm sized alumina powder. The scintillators were wrapped with reflecting aluminized mylar sheets on the side and top.

The cross-sectional microscopic images of the nanocomposites were acquired by a Field Emission Scanning Electron Microscope (FE-SEM), Carl Zeiss Ultra 55, equipped with secondary electron detectors and a backscattered electron detector.

2.3. Measurement of relative gamma-to-electron conversion efficiency

Measurement of gamma-to-electron conversion efficiency of the nanocomposites followed the method of determining the gamma-detection efficiency of the nanocomposites found in the literature (Araya et al., 2015; Hiyama et al., 2018; Kagami et al., 2020). The setup had a photomultiplier tube (PMT) (ET Enterprises 9078B) positioned vertically up inside a light-tight enclosure. The scintillators were placed over the head of the PMT with their uncovered side facing the PMT. They were optically coupled to the PMT head with Dow-corning DC 3500 grease. An aluminum plate covered the enclosure from the top. The cover had an aperture (10 mm in diameter) in the center, optically closed with a thin aluminum foil. The gamma-source disc was positioned over the plate. Gamma-rays reach the plastic scintillator after passing through the aluminum foil. The output of PMT was fed to a multichannel analyzer (MCA, Amptek 8000A) through a charge-sensitive pre-amplifier cum shaping amplifier (Amptek A-203). Data were acquired for 60 s. PHS for unloaded, loaded, and standard plastic scintillators were obtained under identical measurement conditions.

2.4. Measurement of relative gamma-attenuation efficiency

Gamma shielding efficiency was determined using the standard procedure of measuring the transmitted portion of gamma rays through the nanocomposites (Wang et al., 2020). The greater the shielding efficiency of the nanocomposite, the lesser the transmitted portion and thus the greater reduction of counts in PHS. A CdTe photon detector (Amp-Tek XR-100T) was positioned over the source disc at a height of ~11 mm. Each scintillator was placed in the gap between the source and the detector. CdTe detector output was connected to the AMP-TEK PX5 package, the output of which is the required PHS. PHS was acquired for 120 s.

3. Results and discussion

Fig. 1 presents the nanocomposites alongside the unloaded plastic scintillators. Each sample is a cylinder of 10 mm thickness and 9 mm diameter. As observed, the process has yielded good quality unloaded, loaded, and standard plastic scintillators.

Fig. 2 displays pulse height spectra for scintillators for gamma-rays from ^{241}Am with 1 wt% for all nanocomposites. The spectrum of unloaded plastic scintillators closely matched that of EJ212. Full-energy peaks for unloaded scintillator and EJ212 were located at channels around 110. Those for the nanocomposites were roughly located between channel 80 for Bi_2O_3 and 90 for Gd_2O_3 nanocomposites. Thus,

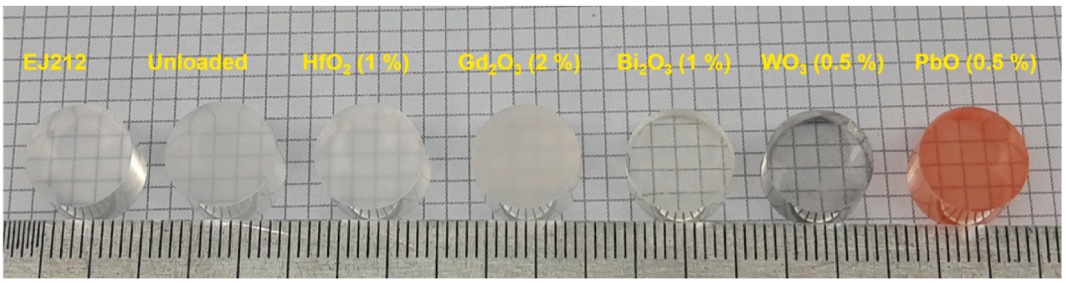

Fig. 1. Unloaded, nanoparticle-loaded and standard plastic scintillators used in the study. The extent of loading is in wt.% Scintillators with different loadings are chosen to display the variations in transparency, as discussed.

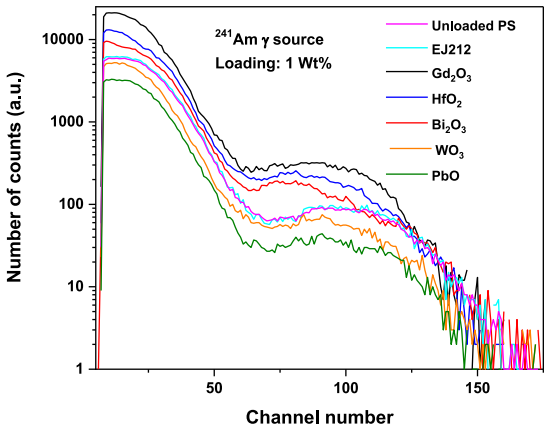

Fig. 2. Pulse height spectra of standard plastic scintillator EJ212, unloaded plastic scintillator realized out of BC-490, and different nanocomposites, for gamma-rays from ^{241}Am, obtained under identical conditions.

upon loading the nanoparticles, the centroids of the full-energy peaks shifted to lower channels. Total counts under the PHS increased for nanocomposites of Gd_2O_3, HfO_2, and Bi_2O_3 but decreased for those of WO_3 and PbO. The counts increased or decreased at all channels for a given nanocomposite. The increase in counts was greater for Gd_2O_3 nanocomposites.

Fig. 3 shows the effect of loading on the variations in PHS. For Gd_2O_3, HfO_2, and Bi_2O_3 nanocomposites, counts increased with loading. A 2 wt% Gd_2O_3 nanocomposite yielded a greater increase than others (overall, 4.2 times that of an unloaded plastic scintillator, considering the sum of the counts over the entire spectrum). Counts remained reduced for WO_3 and PbO nanocomposites at all loadings, and the variations in counts for different loadings were negligible.

Fig. 4 exhibits the relative gamma-attenuation efficiencies of nanocomposites. Histogram compares the total counts in PHS formed by the gamma-rays transmitted through the nanocomposites relative to those through an unloaded scintillator. EJ212 and unloaded plastic scintillators transmitted almost equal flux. The extent of transmission varied between the nanocomposites. In general, increased loading of any nanoparticle reduced the extent of transmission.

The results are inferred here. The PHS for unloaded plastic scintillator is formed due to the interaction of gamma-rays with constituent C, H, N, and O atoms (Fig. 2). The variations in PHS for nanocomposites are due to the outcome of the interaction of gamma-rays with the dopant nanoparticles. An electron exiting the nanoparticle causes additional scintillation leading to increased counts in PHS. The counts vary at all channels as electrons can exit the nanoparticles with all possible energies. Shifting of the centroids of the full-energy peak positions towards

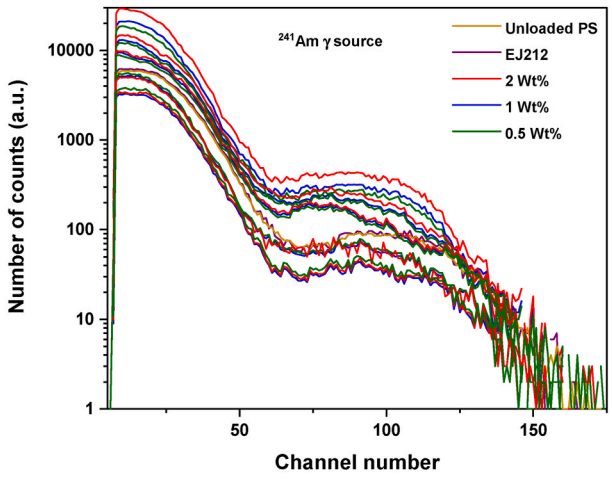

(a)

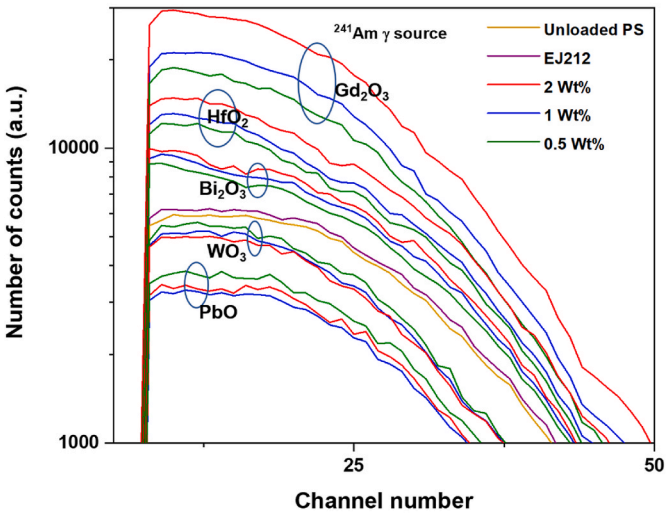

(b)

Fig. 3. (a) Effect of loading on the variations in PHS for nanocomposites. **(b)** Enlarged version of (a).

lower channels for nanocomposites indicates that the scintillation light yield reduces upon the incorporation of nanoparticles. It is consistent with the literature (Araya et al., 2015; Hiyama et al., 2018; Kagami et al., 2020; Liu et al., 2015; Magi et al., 2021; Sato et al., 2021; Toda and

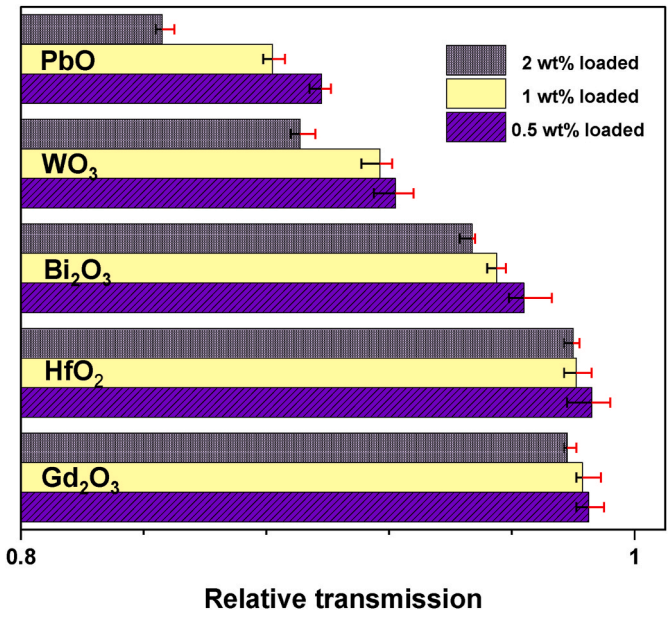

Fig. 4. Relative gamma transmission efficiencies of nanocomposites for gamma-rays from ^{241}Am. Of the data for three samples, the median value was drawn.

Kishimoto, 2020). The root cause of the reduction in scintillation light yield is being debated as fluorescence quenching, self-absorption loss due to scattering of light by the nanoparticles, etc. (G. H. V. Bertrand et al., 2015; Cai et al., 2013; Hajagos et al., 2018; Liu et al., 2015). Further, the extent of light yield reduction varies with the nanoparticle species, as found here. While maintaining the light yield of nanocomposites is a requirement (Koshimizu, 2020), literature reports that the scintillation light yield can be increased at optimum loadings of nanoparticles, i.e., 10 wt% of ZrO_2 (Araya et al., 2015), 20 wt% ZrO_2 (Toda and Kishimoto, 2020), 20% of HfO_2 (Inoue et al., 2018), 10 wt% HfO_2 (Sun et al., 2014), attributed to the increased probability of interaction of gamma-rays with the scintillator (Hiyama et al., 2018).

In line with the purpose of the present study, we focus the discussion on the total number of counts in PHS that indicates the variations in gamma-to-electron conversion efficiencies of the nanoparticles. The total number of counts in the PHS reflects the interacting radiation events. The variations in total counts in PHS occur due to the differences in the interactions of gamma-rays (i.e., the number of events detected). In the current experiments, the input flux in each case is the same. The extent of the increase in counts in PHS is used to assess the relative suitability of the nanoparticles.

Counts increase at all channels for Gd_2O_3, HfO_2, and Bi_2O_3 nanocomposites (Fig. 2). Increased loading of these nanoparticles increases the interaction events resulting in the enhancement of counts (Fig. 3). The literature indicates shifting of full-energy peaks with the extent of loading also (Araya et al., 2015; Toda and Kishimoto, 2020). However, such shifting is unobserved here since the variations in loading in the present study are relatively much smaller compared to those in the literature [(say, 20%, 40%, 60%, etc., by Toda and Kishimoto (2020)]. All results in Fig. 4 are as expected. For gamma-attenuation measurements, the host plastic scintillator serves merely as a conformable polymer (Fig. 4). All nanocomposites shielded the gamma-rays. Increased loading of nanoparticles enhanced the extent of shielding owing to increased interaction events. The results in Fig. 4 correspond to those obtained while developing efficient, light-weight gamma-ray shields by loading the nanoparticles of high-Z materials into conformable polymers (Alavian and Tavakoli-Anbaran, 2020; Ambika et al., 2017; Asgari et al., 2021; Bijanu et al., 2021; Q. Li et al., 2020; R. Li et al., 2017; McCaffrey et al., 2007; Nambiar and Yeow, 2012; Wang et al., 2020). Though initially not intended, we include the results as they indirectly indicate the gamma-attenuation efficiency of the typical nanoparticles used as dopants in conformable polymers.

Thus, we had five key observations: incorporation of Gd_2O_3, HfO_2, and Bi_2O_3 nanoparticles enhanced the scintillation counts; increased loading of these three nanoparticles increased the counts; incorporation of each nanoparticle enhanced the gamma-shielding efficiency of the host polymer; increased loading of nanoparticles increased the gamma-shielding; and, the incorporation of WO_3, PbO nanoparticles into the plastic scintillator reduced the scintillation counts.

The first four of the above observations are as expected and concur with those in the literature. Cai et al. (2013) and Liu et al. (2015) incorporated Gd_2O_3 and HfO_2, respectively, and demonstrated enhanced gamma detection efficiencies for nanocomposites. Kishimoto and Toda achieved 7.2 times better detection efficiency with HfO_2 nanoparticles than a commercially available 5 wt% Pb-loaded plastic scintillator EJ-256 (Kishimoto and Toda, 2021). Magi et al. enhanced the detection efficiency of the scintillators for high-energy photons by incorporating Bi_2O_3 nanoparticles (Magi et al., 2021). The effect of increased loading of Gd_2O_3, HfO_2, and BiO_3 nanoparticles is in line with previous reports(Araya et al., 2015; Hiyama et al., 2018; Kagami et al., 2020; Sato et al., 2021; Toda and Kishimoto, 2020). Fifth observation, the reduction in scintillation counts from a plastic scintillator upon incorporating WO_3, and PbO nanoparticles into the scintillator (Figs. 2 and 3), demands detailed analysis. Such observation is unreported earlier.

A nanocomposite offers increased counts consequent to a series of processes: the nanoparticle interacts with the gamma-ray; the electron emitted from a constituent atom undergoing the interaction exits the nanoparticle with enough energy to scintillate the medium; and finally, the nanocomposite does not absorb the scintillation before the scintillation reaches the PMT. These series occur in Gd_2O_3, HfO_2, and Bi_2O_3 nanocomposites. In WO_3, PbO nanocomposites, the nanoparticles interact with the gamma-rays, as manifested by the reduction in counts. Otherwise, the transmission of gamma-rays through nanoparticles without interaction leaves the counts unaltered. A nanocomposite offers reduced counts attributable to various reasons like optical quenching; large initial or aggregated size of the nanoparticles attenuating the electron; loss of transparency due to the self-absorption of scintillation by the nanoparticles, or, as we speculate, the given nanoparticles absorb the energy of the electrons to the extent that electrons exit with energy insufficient to cause the scintillation.

The presence of a nanoparticle inside the plastic scintillator causes optical quenching (Kessler and Kessler, 2015). All nanoparticles quench. However, if quenching were a determining factor, the enhancement of counts by 4.2 times by Gd_2O_3 nanocomposite and reduction of counts by 0.7 times for WO_3 and 0.5 times for PbO nanocomposites would be improbable. In the latter cases, additional scintillation, if generated, would balance the loss of counts due to optical quenching and thus at least maintain the counts, if not increase. This condition is true for any nanocomposite, particularly at these lower loadings. From Fig. 3, the change in counts for increased loading is disproportionate to the concentration of the nanoparticles. The quenching leads to the shift in full-energy peak position in PHS. Such shift is not seen here as the loading variations are much smaller than those in the literature. Thus, quenching is not the reason for reduced counts.

A nanoparticle larger than the range of electrons inside the material can attenuate the electrons emitted from its atoms. Photoelectrons emitted from WO_3 and PbO atoms interacting with gamma-rays from ^{241}Am could be K_α energies of 48 keV and 44 keV from W and Pb atoms, respectively. The continuous-slowing-down approximation (CSDA) range of a 45 keV electron in W and Pb is about 42 μm and 76 μm, respectively. Thus, the starting size of currently used nanoparticles is not a deterrent. The nanoparticles aggregated during the realization of nanocomposites (Fig. 5).

As in the micrographs, the nanoparticles have aggregated from less

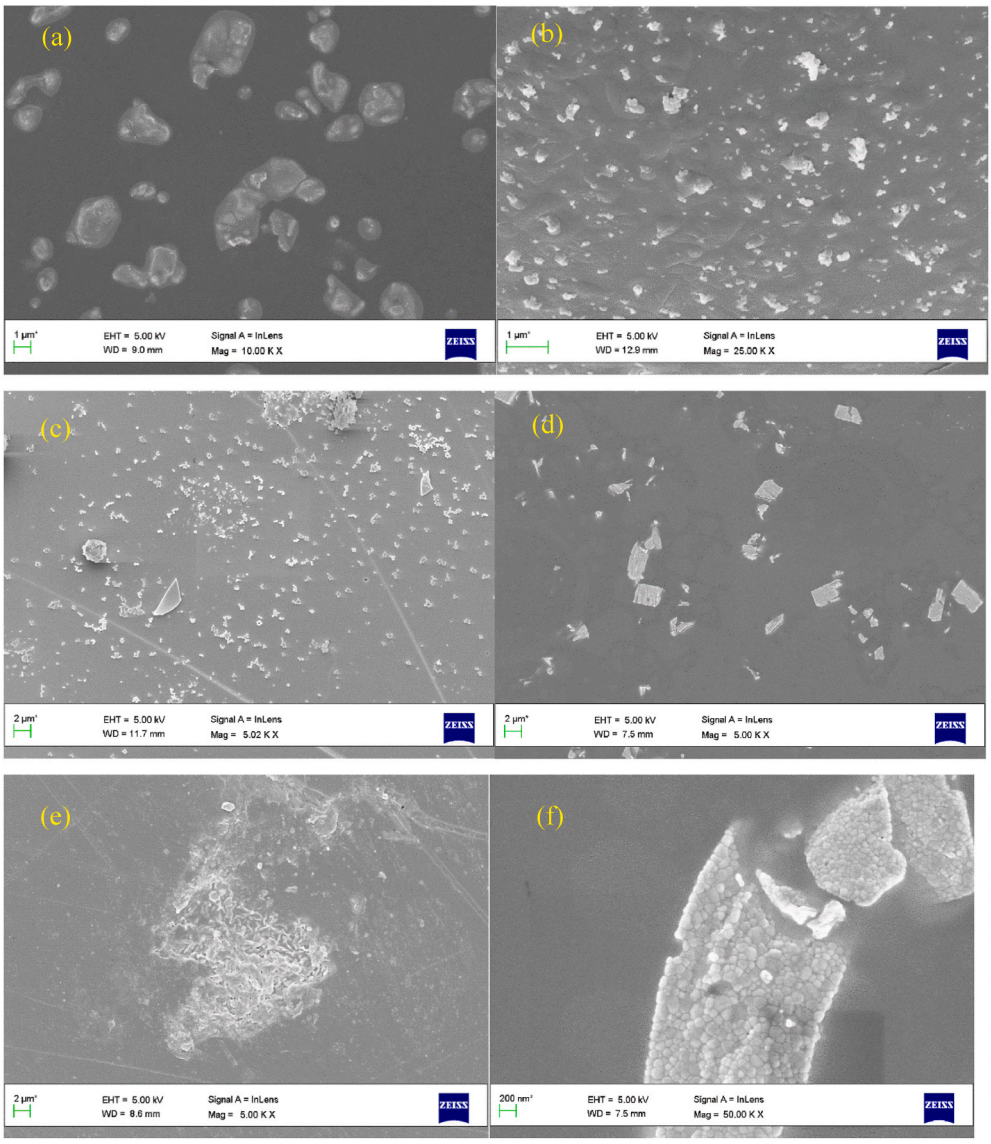

Fig. 5. Scanning electron micrographs of a plain of **(a)** Gd_2O_3 **(b)** HfO_2 **(c)** Bi_2O_3 **(d)** WO_3 **(e)** PbO nanocomposites. **(f)** Magnified view of plain of WO_3 nanocomposite. All are 0.5 wt% loaded nanocomposites.

than a hundred nm to about half a micrometer. The aggregated sizes of WO_3 and PbO nanoparticles are comparable to those of the other nanoparticles. Alongside, the literature evidences the enhancement of counts from nanocomposites containing $Hf_xSi_{1-x}O_2$ nanoparticles aggregated to hundreds of micrometers (Sato et al., 2021). HfO_2 nanoparticles aggregated to sizes as large as 300 nm have enhanced the counts (Sun et al., 2014). Hence, the aggregation of nanoparticles inside the plastic scintillators does not necessarily hinder the exit of electrons.

The loss of transmission due to self-absorption of scintillation by the nanoparticles could reduce the number of counts. The color of WO_3 and PbO indicates that these nanoparticles absorb light at some wavelength region, which may suppress the scintillation photons. To investigate this potential artefact, the absorption spectra were obtained for the nanoparticles (Fig. 6). The spikes observed at 356 nm are noise generated during the change of lamps. PPO (fluor) scintillation occurs from 350 nm to 400 nm, with a peak at 360 nm. POPOP (wavelength shifter) emits light from 380 nm to 450 nm, with a peak at 420 nm. However, none of the nanoparticles exhibit absorption of photons at these wavelengths. No unusual response is observable in absorption spectra of WO_3, PbO nanoparticles, relative to that of the others. The absorption of scintillation would result in the shift of full-energy peak to the lower channels.

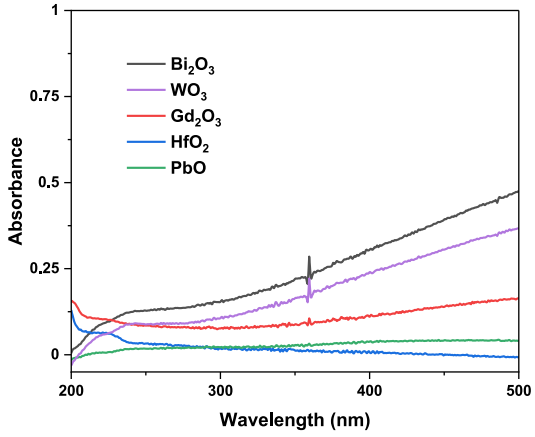

Fig. 6. Absorption spectra of the nanoparticles used.

The colour of WO_3 or PbO nanocomposites indicate that their absorption spectra may have peaks or tails in wavelengths outside the scintillation region. Thus, reduced counts in WO_3 and PbO nanocomposites are not caused by the self-absorption of scintillation by the nanoparticles.

The number of physical processes leading to increased or decreased scintillation counts from a nanocomposite is limited. The potential artifacts are negated. However, we are unable to explain why and how WO_3 and PbO nanocomposites reduce the counts. We speculate that WO_3 and PbO nanoparticles interact with the gamma-rays; their constituent atoms emit the electrons, but these nanoparticles absorb the electrons within themselves wholly or partially such that an electron exits the nanoparticles with energy insufficient to scintillate the host or the scintillation light generated is below the detection threshold of the PMT. The scintillation threshold of the PVT-based plastic scintillator used is typically 100 eV (Perera et al., 1992) but far greater than that and challenging to determine in practice (Kessler and Kessler, 2015). While all nanoparticles reduce the energy of exiting electrons, WO_3 and PbO nanoparticles reduce it severely. The above speculation needs more basic experimental results. Currently, no experimental technique exists to distinctly determine the emission or attenuation of electrons from given nanoparticles upon irradiation with gamma-rays of a given energy. The question remains open for a solution.

Meanwhile, the literature repeatedly reports the enhancement of gamma-detection efficiency of a plastic scintillator with the incorporation of only selected species of nanoparticles such as HfO_2, Gd_2O_3, ZrO_2, Bi_2O_3 (Araya et al., 2015; Cai et al., 2013; Hiyama et al., 2018; Inoue et al., 2018; Kagami et al., 2020; Kishimoto and Toda, 2021; Liu et al., 2015; Magi et al., 2021; Sato et al., 2021; Sun et al., 2014; Toda and Kishimoto, 2020). Since the loading of Pb, Sn atoms (not the nanoparticles) into liquid and plastic scintillators enhances the gamma-detection efficiency of the hosts, as demonstrated and utilized since the 1960s (Ashcroft, 1970), the nanoparticles of these materials were the logical first choice as dopants in plastic scintillators for enhancing the gamma-detection of efficiency of the hosts. In another application, the nanoparticles of high-Z materials are loaded into conformable polymers to develop Pb-free, light-weight, efficient gamma-ray shields required in radiation research and technology, medical diagnosis and therapy, nuclear power stations, space exploration, non-destructive inspection, resource finding, waste management, etc. (Alavian et al., 2020; Ambika et al., 2017; Q. Li et al., 2020; R. Li et al., 2017; McCaffrey et al., 2007; Molina Higgins et al., 2019; Nambiar, 2015; Nambiar and Yeow, 2012; Noor Azman et al., 2013; Wang et al., 2020). Such composite gamma-shields are realized by the incorporation of nanoparticles of Bi, Bi_2O_3, BiO, CuO, Fe_2O_3, Fe_3O_4, Gd_2O_3, HfO_2, Pb, Pb_3O_4, PbO, PbO_2, $PbWO_4$, Sm_2O_3, TiO_2, W, WO_3, Zn, ZnO, ZrO_2 into various conformable polymers (as reviewed or studied in Ref. (Alavian and Tavakoli-Anbaran, 2020; Asgari et al., 2021; Bijanu et al., 2021; Ghaseminejad & Gholamzadeh, n.d.; Karabul and İçelli, 2021; R. Li et al., 2017; Mehrara et al., 2021; Molina Higgins et al., 2019). The present observations hint at why only selected species of nanoparticles are repeatedly reported to enhance the gamma-detection efficiency of the host plastic scintillators.

The present results render additional implications. While developing nanocomposite gamma-shields, it is assumed that WO_3 and PbO nanoparticles interact with gamma-rays and emit photoelectrons, and the polymer absorbs the electrons. By the first assumption, WO_3 and PbO nanocomposites should enhance PHS counts, which is not the case in practice. Present results suggest that in WO_3, PbO nanoparticles, the electrons are attenuated not by the polymer but by the nanoparticles themselves, to the most extent. Further, the literature attributes the remarkable gamma-shielding ability of the nanocomposites to the exceptionally high packing density of the nanoparticles (Ambika et al., 2017; Azman et al., 2013). The present results contribute an additional reason for the same.

For the original purpose of the study, results determine that, among the ones tested, Gd_2O_3 HfO_2, and Bi_2O_3 nanoparticles convert the gamma rays into electrons more efficiently, with Gd_2O_3 offering the best conversion efficiency. They are better suited as dopants in plastic scintillators to develop efficient gamma-detectors. WO_3 and PbO, on the other hand, suit as dopants in conformable polymers to develop efficient gamma-ray shields, as they seem to be absorbing the gamma-rays. Thus, present results enable the selection of better-suited nanoparticles for a given application.

4. Conclusions

Relative gamma-to-electron conversion efficiencies of Gd_2O_3, HfO_2, Bi_2O_3, WO_3, and PbO nanoparticles for gamma radiations from ^{241}Am are determined. The first three nanoparticles efficiently convert the gamma-rays into scintillation photons. Within them, Gd_2O_3 nanoparticles offered the greatest gamma-to-electron conversion efficiency. Thus, the first three nanoparticles suit as dopants in plastic scintillators to enhance the gamma-detection efficiency of the host. WO_3 and PbO nanoparticles reduce the number of scintillation counts of the host. They interact with the gamma-rays; their constituent atoms emit the electrons, but, possibly, these nanoparticles absorb the electrons within themselves wholly or partially such that an electron exits the nanoparticles with energy insufficient to scintillate the host. The results indicate that WO_3 and PbO nanoparticles are better suited as dopants in polymers to realize gamma-shields and hint at why only selected species of nanoparticles have been repeatedly reported to enhance the gamma-counting efficiency of the plastic scintillators. The method and results enable the selection of better-suited nanoparticles for a given application.

CRediT authorship contribution statement

B.H.M. Darukesha: Writing – original draft, Validation, Methodology, Investigation, Formal analysis, Conceptualization. **V. Radhakrishna:** Writing – review & editing, Validation, Supervision, Formal analysis, Data curation. **K. Rajanna:** Writing – review & editing, Supervision, Resources.

Declaration of competing interest

The authors declare that they have no known competing financial interests or personal relationships that could have appeared to influence the work reported in this paper.

Data availability

Data will be made available on request.

Acknowledgments

Authors thank Dr. M Ravindra at RNSIT and Dr. MM Nayak at CeNSE, IISc for guidance and support. They thank MNCF at IISc and Dr. Sarat Kumar Dash at Indian Space Research Organisation (ISRO) for the characterization of the nanoparticles. BHMD acknowledges the discussions and instrumentation support from Shri Srikar Paavan Tadepalli and Shri Koushal Vadodariya at Space Astronomy Group, ISRO. Supervision of Smt. M A Lalitha Abraham, Radiation Safety Officer at ISRO, is highly regarded.

References

Alavian, H., Samie, A., Tavakoli-Anbaran, H., 2020. Experimental and Monte Carlo investigations of gamma ray transmission and buildup factors for inorganic nanoparticle/epoxy composites. Radiat. Phys. Chem. 174 (October 2019), 108960 https://doi.org/10.1016/j.radphyschem.2020.108960.

Alavian, H., Tavakoli-Anbaran, H., 2020. Comparative study of mass attenuation coefficients for LDPE/metal oxide composites by Monte Carlo simulations. Euro Phys. J. Plus. 135 (1) https://doi.org/10.1140/epjp/s13360-020-00164-7.

Ambika, M.R., Nagaiah, N., Suman, S.K., 2017. Role of bismuth oxide as a reinforcer on gamma shielding ability of unsaturated polyester based polymer composites. J. Appl. Polym. Sci. 134 (13), 1–7. https://doi.org/10.1002/app.44657.

Araya, Y., Koshimizu, M., Haruki, R., Nishikido, F., Kishimoto, S., Asai, K., 2015. Enhanced detection efficiency of plastic scintillators upon incorporation of zirconia nanoparticles. Sensor. Mater. 27 (3), 255–261. https://doi.org/10.18494/sam.2015.1090.

Asgari, M., Afarideh, H., Ghafoorifard, H., Amirabadi, E.A., 2021. Comparison of nano/micro lead, bismuth and tungsten on the gamma shielding properties of the flexible composites against photon in wide energy range (40 keV–662 keV). Nucl. Eng. Technol. 53 (12), 4142–4149. https://doi.org/10.1016/j.net.2021.06.022.

Ashcroft, J., 1970. Gamma counting of Iodine125 using a metal-loaded liquid scintillator. Anal. Biochem. 37, 268–275.

Azman, N.Z.N., Siddiqui, S.A., Haroosh, H.J., Albetran, H.M.M., Johannessen, B., Dong, Y., Low, I.M., 2013. Characteristics of X-ray attenuation in electrospun bismuth oxide/polylactic acid nanofibre mats. J. Synchrotron Radiat. 20 (5), 741–748. https://doi.org/10.1107/S0909049513017871.

Bertrand, G.H.V., Dumazert, J., Sguerra, F., Coulon, R., Corre, G., Hamel, M., 2015. Understanding the behaviour of different metals in loaded scintillators: discrepancy between gadolinium and bismuth. J. Mater. Chem. C 3 (23), 6006–6011. https://doi.org/10.1039/c5tc00387c.

Bijanu, A., Arya, R., Agrawal, V., Tomar, A.S., Gowri, V.S., Sanghi, S.K., Mishra, D., Salammal, S.T., 2021. Metal-polymer composites for radiation protection: a review. J. Polym. Res. 28 (10) https://doi.org/10.1007/s10965-021-02751-3.

Cai, W., Chen, Q., Cherepy, N., Dooraghi, A., Kishpaugh, D., Chatziioannou, A., Payne, S., Xiang, W., Pei, Q., 2013. Synthesis of bulk-size transparent gadolinium oxide-polymer nanocomposites for gamma ray spectroscopy. J. Mater. Chem. C 1 (10), 1970–1976. https://doi.org/10.1039/c2tc00245k.

Dumazert, J., Coulon, R., Hamel, M., Carrel, F., Sguerra, F., Normand, S., Mechin, L., Bertrand, G.H.V., 2016. Gadolinium-loaded plastic scintillators for thermal neutron detection using compensation. IEEE Trans. Nucl. Sci. 63 (3), 1551–1564. https://doi.org/10.1109/TNS.2016.2535278.

Ghaseminejad, M., & Gholamzadeh, L. (n.d.). Investigation of X-Ray Attenuation Property of Modification PbO with Graphene in Epoxy Polymer Investigation of X-Ray Attenuation Property of Modi Fi Cation PbO with Graphene in Epoxy Polymer.

Hajagos, T.J., Liu, C., Cherepy, N.J., Pei, Q., 2018. High-Z sensitized plastic scintillators: a review. Adv. Mater. 30 (27), 1–13. https://doi.org/10.1002/adma.201706956.

Hiyama, F., Noguchi, T., Koshimizu, M., Kishimoto, S., Haruki, R., Nishikido, F., Fujimoto, Y., Aida, T., Takami, S., Adschiri, T., Asai, K., 2018. X-ray detection properties of plastic scintillators containing surface-modified Bi2O3 nanoparticles. Jpn. J. Appl. Phys. 57 (5) https://doi.org/10.7567/JJAP.57.052203.

Inoue, K., Koshimizu, M., Hiyama, F., Asai, K., Nishikido, F., Haruki, R., Kishimoto, S., 2018. Fast scintillation X-ray detector using proportional-mode Si-apd and a HfO2-nanoparticle-doped plastic scintillator. IEEE Trans. Nucl. Sci. 65 (4), 1012–1017. https://doi.org/10.1109/TNS.2018.2807801.

Kagami, K., Koshimizu, M., Fujimoto, Y., Kishimoto, S., Haruki, R., Nishikido, F., Asai, K., 2020. High-energy X-ray detection capabilities of Hf-loaded plastic scintillators synthesized by sol–gel method. J. Mater. Sci. Mater. Electron. 31 (2), 896–902. https://doi.org/10.1007/s10854-019-02597-y.

Karabul, Y., İçelli, O., 2021. The assessment of usage of epoxy based micro and nano-structured composites enriched with Bi2O3 and WO3 particles for radiation shielding. Results Phys. 26 https://doi.org/10.1016/j.rinp.2021.104423.

Kessler, M.J.E., Kessler, M.J., 2015. Liquid Scintillation Analysis. www.perkinelmer.com/liquid-scintillation.

Kishimoto, S., Toda, A., 2021. High-energy and high-rate X-ray measurements using HfO nanoparticle-loaded plastic scintillator. IEEE Trans. Nucl. Sci. 68 (2), 165–172. https://doi.org/10.1109/TNS.2020.3048943.

Koshimizu, M., 2020. Composite scintillators based on polymers and inorganic nanoparticles. Fuct. Mater. Lett. 13 (6) https://doi.org/10.1142/S1793604720300030.

Li, Q., Wang, Y., Xiao, X., Zhong, R., Liao, J., Guo, J., Liao, X., Shi, B., 2020. Research on X-ray shielding performance of wearable Bi/Ce-natural leather composite materials. J. Hazard Mater. 398 https://doi.org/10.1016/j.jhazmat.2020.122943.

Li, R., Gu, Y., Wang, Y., Yang, Z., Li, M., Zhang, Z., 2017. Effect of particle size on gamma radiation shielding property of gadolinium oxide dispersed epoxy resin matrix composite. Mater. Res. Express 4 (3), aa6651. https://doi.org/10.1088/2053-1591/aa6651.

Liu, C., Hajagos, T.J., Kishpaugh, D., Jin, Y., Hu, W., Chen, Q., Pei, Q., 2015. Facile single-precursor synthesis and surface modification of hafnium oxide nanoparticles for nanocomposite γ-ray scintillators. Adv. Funct. Mater. 25 (29), 4607–4616. https://doi.org/10.1002/adfm.201501439.

Magi, A., Koshimizu, M., Watanabe, A., Yoko, A., Seong, G., Tomai, T., Adschiri, T., Haruki, R., Nishikido, F., Kishiomto, S., Fujimoto, Y., Asai, K., 2021. Optimization of phosphor concentration of surface-modified Bi2O3 nanoparticle-loaded plastic scintillators for high-energy photon detection. J. Mater. Sci. Mater. Electron. 32 (6), 7987–7999. https://doi.org/10.1007/s10854-021-05522-4.

McCaffrey, J.P., Shen, H., Downton, B., Mainegra-Hing, E., 2007. Radiation attenuation by lead and nonlead materials used in radiation shielding garments. Med. Phys. 34 (2), 530–537. https://doi.org/10.1118/1.2426404.

Mehrara, R., Malekie, S., Kotahi, S.M.S., Kashian, S., 2021. Introducing a novel low energy gamma ray shield utilizing Polycarbonate Bismuth Oxide composite. Sci. Rep. 11 (1), 1–13. https://doi.org/10.1038/s41598-021-89773-5.

Molina Higgins, M.C., Radcliffe, N.A., Toro-González, M., Rojas, J.V., 2019. Gamma ray attenuation of hafnium dioxide- and tungsten trioxide-epoxy resin composites. J. Radioanal. Nucl. Chem. 322 (2), 707–716. https://doi.org/10.1007/s10967-019-06714-3.

Nambiar, S., 2015. Application of Nanomaterials for X-Ray Shielding and Dosimetry in Diagnostic Radiology. University of Waterloo.

Nambiar, S., Yeow, J.T.W., 2012. Polymer-composite materials for radiation protection. ACS Appl. Mater. Interfaces 4 (Issue 11), 5717–5726. https://doi.org/10.1021/am300783d.

Noor Azman, N.Z., Siddiqui, S.A., Hart, R., Low, I.M., 2013. Effect of particle size, filler loadings and x-ray tube voltage on the transmitted x-ray transmission in tungsten oxide-epoxy composites. Appl. Radiat. Isot. 71 (1), 62–67. https://doi.org/10.1016/j.apradiso.2012.09.012.

Pellegrin, S.M., Whitney, C., Wilson, C.G., 2010. A multichannel nanoparticle scintillation microdevice with integrated waveguides for alpha, beta, gamma, X-ray, and neutron detection. J. Microelectromech. Syst. 19 (5), 1207–1214. https://doi.org/10.1109/JMEMS.2010.2067435.

Perera, H., Williamson, J.F., Monthofer, S.P., Binns, W.R., Klarmann, J., Fuller, G.L., Wong, J.W., 1992. Rapid two-dimensional dose measurement in brachytherapy using plastic scintillator sheet: linearity, signal-to-noise ratio, and energy response characteristics. Int. J. Radiat. Oncol. Biol. Phys. 23 (5), 1059–1069. https://doi.org/10.1016/0360-3016(92)90914-4.

Sato, A., Koshimizu, M., Fujimoto, Y., Kishimoto, S., Asai, K., 2021. Fabrication of HfxSi1−xO2microparticle-loaded PVK-based plastic scintillators using the sol–gel method for high-energy X-ray detection at high counting rate. J. Mater. Sci. Mater. Electron. 32 (24), 28807–28818. https://doi.org/10.1007/s10854-021-07265-8.

Sun, Y., Koshimizu, M., Yahaba, N., Nishikido, F., Kishimoto, S., Haruki, R., Asai, K., 2014. High-energy X-ray detection by hafnium-doped organic-inorganic hybrid scintillators prepared by sol-gel method. Appl. Phys. Lett. 104 (17) https://doi.org/10.1063/1.4875025.

Toda, A., Kishimoto, S., 2020. X-ray detection capabilities of plastic scintillators incorporated with ZrO2Nanoparticles. IEEE Trans. Nucl. Sci. 67 (6), 983–987. https://doi.org/10.1109/TNS.2020.2978240.

Wang, Y., Ding, P., Xu, H., Li, Q., Guo, J., Liao, X., Shi, B., 2020. Advanced X-ray shielding materials enabled by the coordination of well-dispersed high atomic number elements in natural leather. ACS Appl. Mater. Interfaces 12 (17), 19916–19926. https://doi.org/10.1021/acsami.0c01663.

Nuclear Inst. and Methods in Physics Research, A 1048 (2023) 167922

Contents lists available at ScienceDirect

Nuclear Inst. and Methods in Physics Research, A

journal homepage: www.elsevier.com/locate/nima

Direct determination of the outcomes of interaction of X-rays/gamma-rays with nanoparticles

B.H.M. Darukesha [a,b,*], V. Radhakrishna [a], K. Rajanna [b]

[a] U R Rao Satellite Centre, Indian Space Research Organisation, Bengaluru 560017, India
[b] Department of Instrumentation & Applied Physics, Indian Institute of Science, Bengaluru 560012, India

ARTICLE INFO

Keywords:
Interaction of radiations with nanoparticles
Fast and efficient gamma-detectors
Nanoparticle loaded plastic scintillators
Nanoparticle radiosensitization
Pb-free radiation shields

ABSTRACT

An experimental technique to determine the outcome of the interaction of gamma-rays with the given nanoparticles is contributed. The interactions involve gamma-rays of energies used in practical applications. The technique determines the outcomes directly. The variations in the number of counts and shape of pulse height spectra obtained before and after loading the nanoparticles into a liquid scintillator for given gamma-ray irradiation under identical conditions reveal the outcome of the interactions. Results reveal that the interaction of low-energy gamma-rays such as those from ^{241}Am, ^{133}Ba with the nanoparticles tested resulted in the emission of electrons from the nanoparticles. Among the nanoparticles tested, Gd_2O_3 emitted the greatest number of electrons. Photons with energy lying between 14 keV and 81 keV undergo greater interaction with the nanoparticles than those with other energies. High-energy gamma-rays transmit through the nanoparticles without interaction. The technique distinguishes the abundance and energy profile of electrons emitted from different nanoparticles upon irradiation with gamma-rays. Results enable test-selection of nanoparticles for applications such as the development of fast-efficient-large-affordable gamma-detectors, nanoparticle radiosensitization for cancer treatment, and the development of Pb-free efficient radiation shields for healthcare workers.

1. Introduction

The development of simultaneously fast, efficient, large, and affordable gamma-ray detectors is a long-standing goal in radiation physics [1–3]. The availability of such detectors extends the research and application of gamma-rays or high-energy X-rays. They are currently needed for nuclear resonance scattering measurements [1,3–5] detection of illicit traffic of special radionuclides across international borders [6,7], and medical imaging techniques [6,8–10]. These applications involve photons with typical energies of tens of keV X-rays from Synchrotrons [11], 60 keV gamma-rays emitted by ^{241}Am (a progeny of ^{241}Pu), and 40 keV–150 keV of diagnostic X-rays [8,10,12].

Currently used inorganic scintillators are efficient gamma-ray detectors but are slow. Solid-state detectors are either inefficient or slow, depending on the thickness of the depletion layer [1]. Both these types are available in small sizes and are costly to operate. On the other hand, organic scintillators are fast, scalable, and affordable but are inefficient. If only their gamma-detection efficiency is enhanced, the transformed plastic scintillators fill the gap of fast-efficient-large-affordable gamma-detectors.

One means of enhancing the gamma-detection efficiency of plastic scintillators is to increase their $Z_{eff.}$ For this purpose, nanoparticles of high-Z materials are incorporated into the plastic scintillators in a recent approach. As hypothesized, the incoming gamma-rays readily interact with dopant nanoparticles and cause the emission of photoelectrons from the atoms of nanoparticles to produce additional scintillation in the plastic and thus enhance the gamma-detection efficiency of the host [13–15]. Theoretically, this approach is feasible [16]. Experimentally, several studies have demonstrated the enhancement of gamma-detection efficiency of plastic scintillators by incorporating various nanoparticles like Gd_2O_3, HfO_2, Bi_2O_3, ZrO_2, etc. [3–5,13,17–21] the detectors have remained in a laboratory scale. Currently, the efficacy of the chosen nanoparticle is determined indirectly by measuring the enhancement of the gamma-counting efficiency of loaded plastic scintillators [1,3,4,17]. However, challenges related to the processes of incorporation of nanoparticles and upscaling [6,14,18] lead to inconclusive results. Such challenges include undue aggregation of the nanoparticles [4] or the generation of a gap between the nanoparticle and the host, adversely affecting the transmission of electrons or scintillation through them [22]. Consequently, the studies have remained exploratory.

Although the current materials characterization techniques reveal the outcome of X-ray photons interaction with nanomaterials, the

* Corresponding author at: U R Rao Satellite Centre, Indian Space Research Organisation, Bengaluru 560017, India.
E-mail address: darukeshabhm@iisc.ac.in (B.H.M. Darukesha).

https://doi.org/10.1016/j.nima.2022.167922
Received 29 March 2022; Received in revised form 24 November 2022; Accepted 11 December 2022
Available online 17 December 2022
0168-9002/

energy of photons they involve (up to about 1.5 keV) is low compared to energies involved in practical applications [23,24]. Such practical applications are discussed in Section 3.3. Interactions of ionizing radiations with matter-at-nanoscale are assumed to be similar to those of the radiations with matter-at-bulk [9,25]. The nanomaterials, however, exhibit nanoscale effects on the outcomes of interaction with non-ionizing radiations, like with visible light [26], owing to their finite size and large surface-to-volume ratio. Thus, the outcomes of the interaction of ionizing radiations with nanoparticles could differ. Further, as the nanoparticles studied in different works vary in species, purity, size, aggregation, etc., the results of a given work are not extendable to the others. Hence, it is prudent to determine the outcome of the interaction of gamma-rays of given energy with the given nanoparticles *experimentally* before subjecting the nanoparticles to detailed investigation.

The objectives of the present work, thus, are (a) the development of an empirical, direct, and quick technique to determine the outcome of the interaction of gamma-rays of given energy with the given nanoparticles and (b) ascertain the effects of energy of gamma-rays, size, and concentration of the nanoparticles on the outcome of the interaction. The results would qualitatively benchmark the nanoparticles for the abundance and energy profile of the electrons they emit on irradiation with given photons and thus determine the most suited nanoparticles for the application. They benefit two other applications involving the interaction of gamma-rays with the nanoparticles: nanoparticle radiosensitization for cancer treatment [25] and the development of Pb-free light-weight efficient radiation shields [27,28], as discussed later. With the preliminary investigation of nanoparticles using the proposed method, further studies can utilize test-selected nanoparticles to facilitate the identification and resolution of process-related issues and thus propel the field implementation of the applications. The work presents a qualitative and comparative study. Measurement of efficiencies, accuracy of recorded spectra, or the numerical analysis of the spectra, however, have not been part of present work.

2. Materials and method

2.1. Materials

Nanoparticles studied were (source, purity, size in nm, polydiversity index) Gd_2O_3 (Nanoshel, 99.9%, 55 ± 0.8, 0.292), HfO_2 (Otto Chemie, 99.6%, 76.6 ± 3.2, 0.333), LaF_3 (Lab Chemie, 99.7%, 41.9 ± 2.3, 0.298), ZnO (Nanoshel, 99.9%, 73.0 ± 3.3, 0.316), ZrO_2 (Tosho, 99.9%, 36.8 ± 1.5, 0.286). The purity of nanoparticles was characterized with energy-dispersive X-ray spectroscopy using Oxford ESD system model INCA PentaFET attached to *Carl Zeiss* SEM model EVO 50. Nanoparticle sizes were determined through dynamic light scattering using NanoBrook ZetaPALS (90°, 658 nm, 25 °C). The nanoparticles and de-ionized water mixture were ultra-sonicated for about 15 min before loading. Three replicate measurements for one minute each were carried out.

The crystallinity of the nanoparticles was analyzed with an X-ray diffraction system (Rigaku SmartLab) using Cu $K\alpha$ X-rays in a 2θ–θ setup. The crystallite grain size of Gd_2O_3 nanoparticles calculated from the Debye–Scherrer equation using powder X-ray analysis software (Rigaku SmartLab Studio II) was 36 nm.

The elemental composition of the nanoparticles was confirmed with X-ray photoelectron spectroscopy. Spectra for these nanoparticles were recorded with a SPECS spectrometer (SPECS Surface Nano Analysis GmbH, Germany) using non-monochromatic Al-K_α radiation (1486.6 eV) as an X-ray source operated at 300 W (12 kV, 12.5 mA). All the survey spectra were obtained with a pass energy of 50 eV with a step increment of 1 eV. Individual core level spectra were recorded with a pass energy and step increment of 40 eV and 0.05 eV, respectively.

It was challenging to obtain nanoparticles that vary only in size. Hence, 55 nm sized Gd_2O_3 nanoparticles procured were sintered in a regular oven for 4 h at 900 °C and 1300 °C to obtain Gd_2O_3 nanoparticles of larger sizes. Sintered nanoparticles were (purity, size in nm and polydiversity index) 99.9%, 179.9 ± 5.7, 0.347, and 99.8%, 1249.2 ± 112.1, 0.249, respectively. Additionally, smaller-sized Gd_2O_3 (Nanoshel, 99.9%, 12.96 ± 0.6, 0.428) were sourced. Unless specified, the Gd_2O_3 nanoparticles refer to 55 nm-sized.

A liquid scintillation cocktail consisting of 6 g 2,5-Diphenyloxazole (PPO) and 0.2 g 1,4-bis(5-phenyloxazol-2-yl) benzene (POPOP) in 1 L of toluene was used as the liquid scintillator for its ready availability. It was sourced from SRL Chemicals, Mumbai, India (srlchem.com, product #46069). Radioactive sources ^{55}Fe, ^{241}Am, ^{133}Ba, ^{22}Na, ^{137}Cs, ^{60}Co supplied by BRIT, India, and a 40 kVp X-ray gun sourced from Moxtek (Model: Magnum) were used. The X-ray gun was operated at 38 kVp.

2.2. Measurement system and method

Fig. 1 illustrates the setup. The light-tight enclosure was realized from vacuum pipes (inner diameter of 40 mm, thickness of 1.5 mm) and flanges. The bottom cover of the enclosure (~3.5 mm thick aluminum) was detachable. A photomultiplier tube (PMT) (ET Enterprises 9078B, ~19 mm diameter) was hung vertically down. A 12 mm diameter, 0.1 mm thick aluminum window was created at the center of the bottom cover. The radioactive source discs (~3 mm thick, ~10 mm diameter) placed in steel enclosures were placed below the bottom cover such that the axis of the source, window, beaker, and PMT coincide. A glass beaker (~22 mm inner diameter, ~1.5 mm thickness, ~80 mm long) was placed inside the enclosure such that a ~7 mm thick liquid scintillator stays below the PMT head. Immersion of PMT head in the liquid scintillator ensured efficient optical coupling. The beaker was wrapped with a 0.05 mm thick aluminized Mylar sheet for reflecting the scintillations into the beaker. The output of PMT was connected to a data acquisition system through a charge-sensitive pre-amplifier cum pulse-shaper (Amptek A203) and a multichannel analyzer (MCA, Ametek, MCA-8000 A). ADMCA data acquisition tool (www.amptek.com/software) was used to acquire the data on a computer. While studying the interaction of X-rays from ^{55}Fe, the glass beaker was replaced by a (~25 mm diameter, 0.5 mm thick) polytetrafluoroethylene beaker.

The chart on the bottom right side of the setup shows the possible variations in PHS. The emission of electrons from the Nanoparticles results in an increase in counts. The attenuation of radiations within the nanoparticles would reduce the counts. Transmission of radiation without any interaction with the nanoparticles leaves the PHS unvaried.

Initially, about 6 mL of liquid scintillator was poured into the beaker. Pulse height spectrum (PHS) of the gamma radiation source with the liquid scintillator was acquired. Acquisition time was 120 s. The given quantity of nanoparticles was loaded into the liquid scintillator. The loading was direct by weight. The nanoparticles were weighed using a Genius Sartorius 10 microgram resolution scale. The mixture (along with the beaker) was sonicated using a 300 W sonicator at 35 kHz for 15 min, and the beaker was loaded into the light-tight enclosure. PHS of given gamma-ray source with nanoparticle-loaded liquid scintillator was obtained under identical measurement conditions. The procedure was repeated for different loadings.

The operating HV was 800 V for experiments with ^{241}Am and X-rays, 600 V for that with ^{55}Fe, and 700 V for ^{133}Ba. Generally, higher HV is preferred since it efficiently accelerates the electrons such that a greater number of electrons are ejected from the photocathode. At greater HVs than these, the counts registered with nanoparticles loaded inside the liquid scintillator saturate the channels. The background count rates were as low as 0.7, 2.4, and 3.8 cps for HVs at 600 V, 700 V and 800 V, respectively. Count rates with radiation sources positioned below empty beakers were indistinguishable from the background count rates for all sources except for X-rays from the gun. The background count- rate was high (35 cps) for 38 kVp X-rays from the gun. Possibly, X-rays strike the dynodes to cause the release of electrons. However, with a liquid scintillator inside the beaker, the

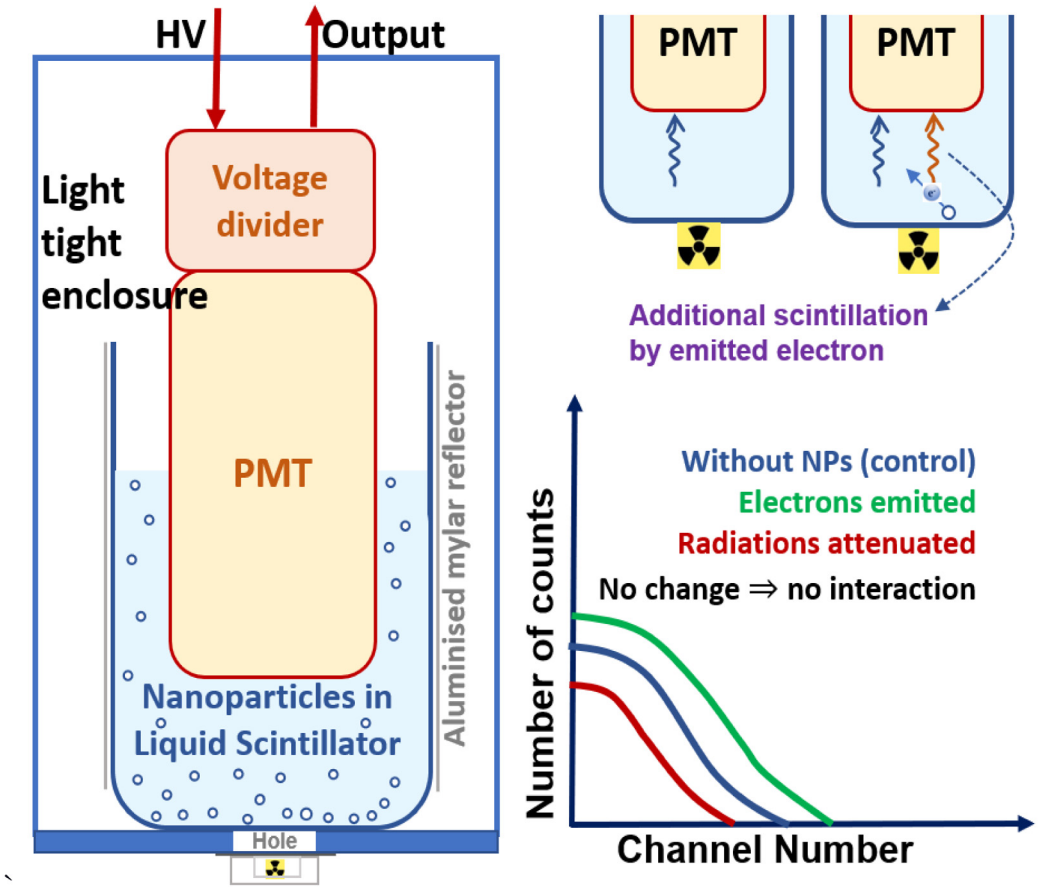

Fig. 1. Schematic setup of the method developed to directly determine the outcomes of the interaction of given gamma-rays with given nanoparticles. The graphic on the right displays the rationale of the method.

count rate for X-rays was as high as 14850 cps. CSPA required ± 9 V. The greatest variations in counts observed were within ~0.5% for unloaded liquid scintillators and ~1% for nanoparticle-loaded liquid scintillators at 800 V HV measured over a dozen acquisitions. The variations were lesser in these in other cases.

The phenomena occurring inside a liquid scintillator counter are described in the literature [29,30]. Briefly, once the readout setup is established, the beaker into which the liquid scintillator is poured is positioned inside the light-tight chamber, HV for PMT is turned on, the radioactive source is placed, and the photons strike the liquid scintillator. Photons interact with C, H, N, and O atoms of the liquid scintillator and undergo the photoelectric or Compton effect. Photoelectrons or recoil electrons emitted excite the solvent or flour molecules inside the liquid scintillator. The excitation energy received by the solvent is transferred to flour molecules. Upon de-excitation, these molecules scintillate. Scintillation reaches the PMT head to get converted as electrons to be read out by the subsequent instruments to be displayed as PHS. When the nanoparticles are loaded into the liquid scintillator, the photons interact with the atoms inside the nanoparticles, either through photoelectric or Compton scattering. Electrons thus emitted exit the nanoparticles and interact with the liquid scintillator, leading to similar consequences as stated above for the electrons emitted from the atoms of the liquid scintillator.

3. Results and discussion

Fig. 2 presents the variation in PHS of gamma-rays from ^{241}Am with an unloaded liquid scintillator upon loading Gd_2O_3 nanoparticles into the scintillator. Pulse height spectra without and with the nanoparticles are obtained under identical measurement conditions. The number of counts in PHS increased upon loading the nanoparticles. At this stage, it was needed to establish that the variations in PHS are due only to the outcome of interactions, and thus the method is genuine.

For the given acquisition time of 120 s, the recorded maximum energy of electrons emitted from the unloaded liquid scintillator corresponds to channel 400. The appearance of counts beyond channel 400 within the given acquisition time upon loading the nanoparticles confirms the enhanced interaction of the gamma rays with the atoms inside the nanoparticles and the emission of electrons from the nanoparticles into the scintillator.

A simple experiment was carried out to further confirm the emission of *electrons* upon the interaction of gamma-rays with nanoparticles. Loading 50 mg Gd_2O_3 nanoparticles into the liquid scintillator enhanced PHS counts (Fig. 3). Adding 1 mL of water into this mixture reduced this enhancement and brought the total count level down. Water, immiscible and denser than the liquid scintillator, occupies the volume below the scintillator. Some nanoparticles suspend in water. Though the interaction of gamma-rays with nanoparticles suspended inside the water may cause the emission of electrons from the nanoparticles, water molecules being non-fluorescent dissipate such excitations non-radiatively. The water layer reduces the flux of photons striking the liquid scintillator staying over it. The interaction of gamma-rays reaching the liquid scintillator and the nanoparticles suspended in the scintillator yields a finite number of counts in the PHS.

Withdrawal of gamma-source in the middle of acquisition reduced the count rate to the background, affirming that the nanoparticles used are non-radioactive. The contribution of radioluminescence of the nanoparticles to the increase in counts is found negligible as the irradiation of nanoparticles *alone* inside the beaker returned a PHS identical to the level of the background of scintillator without nanoparticles.

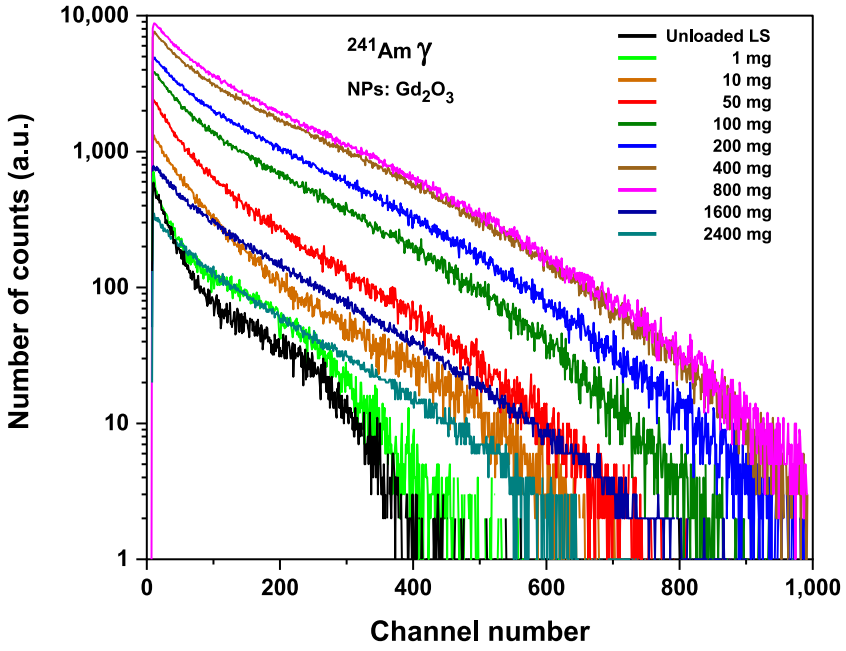

Fig. 2. The variations in PHS of gamma-rays from ^{241}Am with unloaded liquid scintillator upon loading Gd_2O_3 nanoparticles into the scintillator. The effect of loading is also displayed.

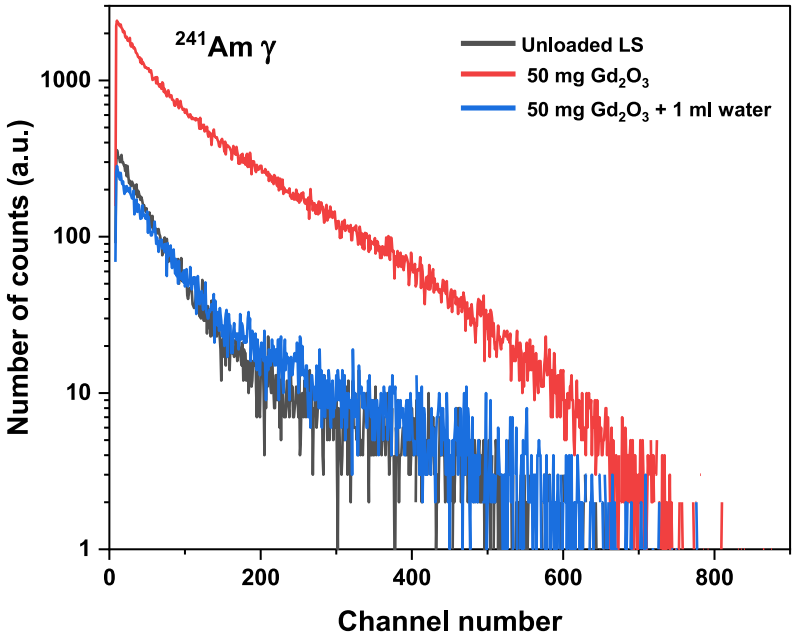

Fig. 3. The variations in PHS of gamma-rays from ^{241}Am with unloaded liquid scintillator upon loading Gd_2O_3 nanoparticles and the water.

The photoluminescence quantum efficiencies of the Gd_2O_3 nanoparticles were experimentally determined outside of the liquid scintillator. Internal photoluminescence quantum yield (PLQY) (ratio of the number of photons emitted to the number of photons absorbed by the sample) of Gd_2O_3 nanoparticles was characterized with a Hitachi F7000 spectrophotometer, and the external PLQY (ratio of the number of photons emitted to the number of photons incident on the sample) was estimated. External PLQYs was 9.32% and 9.83% at wavelengths of peak emission of the flour (360 nm) and the wavelength shifter (420 nm), respectively. The contribution of photoluminescence of the nanoparticles to the increase in counts is negligible compared to that occurring through the emission of electrons from the nanoparticles followed by scintillation. Thus, we conclude that the outcome of the interaction of gamma-rays with the nanoparticles varies the PHS.

Interaction of photons with nanoparticles expectedly involves photoelectric effect *or* Compton scattering with various probabilities depending on photons energy and interaction cross-section. The electrons emitted cause scintillations and increased the number of counts. The PHS of gamma-rays from ^{241}Am and ^{133}Ba with a CdTe photon detector is shown in Fig. 4. It was obtained by hanging vertically down Amptek XR-100T inside the empty beaker (no liquid scintillator, no nanoparticles) (Fig. 4c). The detector was positioned closely above the bottom of the beaker in the setup, and the output of the detector is analyzed through a digital pulse processor Amptek PX5. PHS obtained upon loading Gd_2O_3 nanoparticles into the beaker is also shown in Fig. 4. Upon loading 10 mg of nanoparticles, the net counts decreased to about 0.80 and 0.85 times in Fig. 4 a and b, respectively. The counts remained lower than those in unloaded for 100 mg loadings. Results

were similar without or with the liquid scintillator. The reduced flux of gamma-rays at the detector by introducing nanoparticles confirms the interaction of gamma-rays with the nanoparticles. Further, since this detector has a Be window, the chances of electrons emitted from the nanoparticles reaching the detector are low. Thus, it is the emission of electrons from the nanoparticles that genuinely increase the number of counts in the PHS.

Thus, the technique involves loading the nanoparticles into a liquid scintillator and use the liquid scintillation counting technique, a practical means of quantitative analysis of low-energy betas emitted from the radionuclides mixed with the scintillator [31]. Though a liquid scintillator is a low-efficient X-rays or gamma-ray detector, its efficiency in detecting electrons is utilized. The immersion of nanoparticles inside the liquid scintillator causes the emitted electrons from the nanoparticles upon interacting with the gamma-rays to interact with the scintillator liquid and cause additional scintillation.

3.1. Interaction of low-energy gamma-rays

X-rays from ^{55}Fe, X-ray gun, and gamma-rays from ^{241}Am, ^{133}Ba are low-energy. As observed from Fig. 2, the number of counts increases with the amount of nanoparticle loading and new counts appear at higher channels. As we infer, the loading of nanoparticles increases the interaction of gamma-rays within the medium. The number of electrons emitted into the scintillator also increases. As gamma-ray interacts with an atom inside the nanoparticle, a photoelectron emitted from the atom exits the nanoparticle when the range of the nanoparticles in the material is sufficiently larger. A photoelectron exiting the nanoparticle can lose part of its energy to other atoms along its track inside the nanoparticle making the energy of the exiting electron vary to different degrees, thereby not yielding any characteristic peak in PHS.

3.1.1. Effect of loading (concentration) of nanoparticles

The increased number of counts and appearance of counts at higher channels continue with increased loading (Fig. 2). As we infer, increased loading increases both the packing density and the concentration of the nanoparticles suspended in the liquid. Increased thickness of the layer of nanoparticles increases the number of interactions. Further, it enhances the probability of interaction of gamma-rays and thus increases the number of counts. However, it also increases the probability of attenuation due to scattering of electrons or scintillation photons. The relative dominance of these probabilities dictates the net counts at a given loading.

On a side note, the nanoparticles stay suspended inside the liquid scintillator at lower loadings. At higher loadings, however, a portion of them forms a thin visible layer at the bottom of the beaker with time. Increased loading quickens the formation of the layer. For instance, while about 10 mg Gd_2O_3 nanoparticles stay suspended in the scintillator for several hours, 100 mg loading forms about a 2 mm thick layer in about half an hour. Since the acquisition time is as low as 2 min, the condition of suspension of nanoparticles inside the scintillator at the beginning and end of acquisition is practically the same. The optimum thickness of a layer of nanoparticles results in the greatest enhancement of counts. Around this loading, though photoelectrons emitted from the nanoparticles in lower layers may not reach the liquid scintillator, the gamma-rays can reach the top few layers of nanoparticles and cause increased counts. Beyond this loading, the nanoparticle layer imitates bulk material and attenuates the gamma-rays. Notably, this loading effect does not hinder the essential requirement of determining the outcome of the interaction of gamma-rays with the nanoparticles. Since the loading effect can obscure it, the basic outcome of the interaction is preferably studied at lower loadings of nanoparticles. Further, viscous liquid scintillators can be utilized since precipitation is greater for even larger particles.

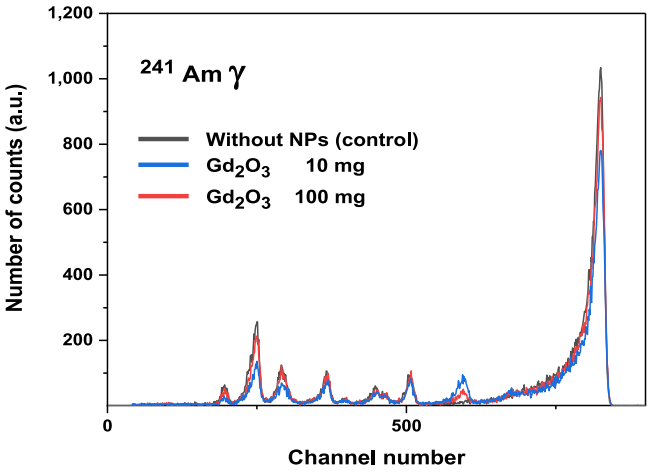

(a)

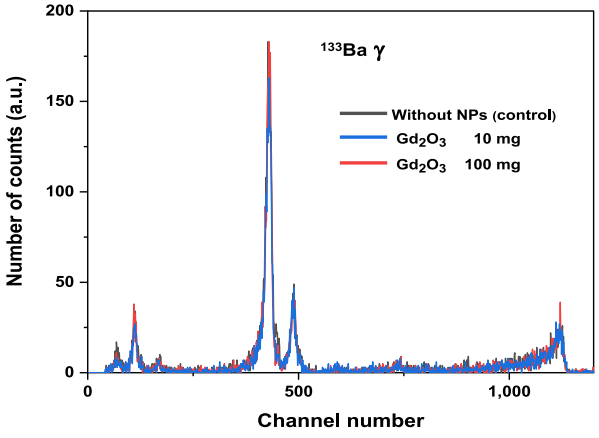

(b)

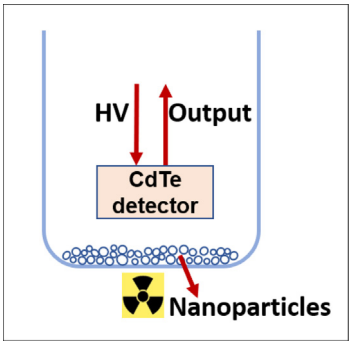

(c)

Fig. 4. The variations in PHS of gamma-rays from in (a) ^{241}Am and (b) ^{133}Ba with CdTe detector upon loading Gd_2O_3 nanoparticles. (c) The position of CdTe photon detector while obtaining the above spectra.

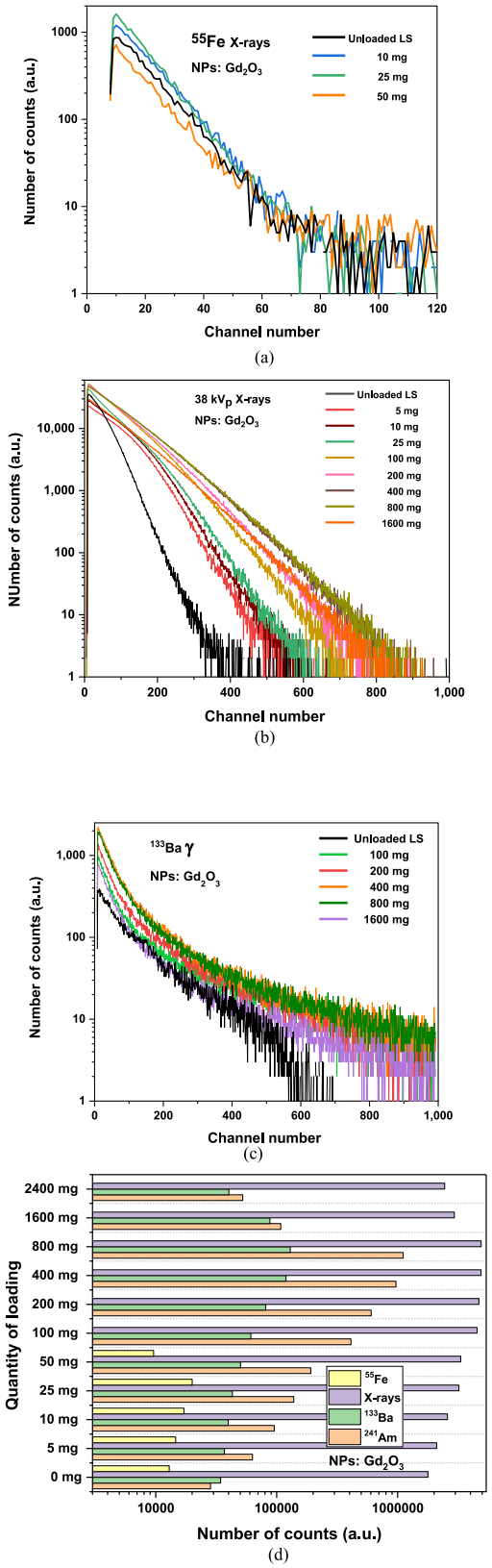

Fig. 5. The variations in PHS of X-rays from (a) ^{55}Fe and (b) 38 kVp gun, and gamma-rays from (c) ^{133}Ba with unloaded liquid scintillator upon loading Gd_2O_3 nanoparticles at different concentrations (d) Histogram displaying the extent of enhancement of counts for low-energy gamma-rays all the loadings tried.

3.1.2. *Effect of energy*

The extent of enhancement in counts varies with the energy of X-rays/gamma-ray (Fig. 5d). The maximum enhancements in counts when photons from ^{55}Fe (6.8 keV maximum) (Fig. 5a), 38 kVp gun (~10 keV weighted average) (Fig. 5b), ^{241}Am (14 keV, 60 keV) (Fig. 2), and ^{133}Ba (81 keV, 356 keV) (Fig. 5c) interacted with Gd_2O_3 nanoparticles were about 1.5, 3.8, 39.2 and 2.8 times, respectively. This trend is observed for all the nanoparticles tested here. Thus, photons within an energy range undergo greater interaction with the nanoparticles than those with other energies.

3.1.3. *Effect of size of nanoparticles*

Among the different sized Gd_2O_3 nanoparticles tried here, those of 180 nm yielded the greatest enhancement of counts interacting with gamma-rays from ^{241}Am (Fig. 6). However, 180 nm need not be optimum for Gd_2O_3 nanoparticles.

The increased size of the nanoparticles increases the number of interactions within a single nanoparticle. It, however, increases the probability of attenuation of photoelectrons inside the nanoparticles. A photoelectron emitted from a core atom can exit the nanoparticle when the distance from the interacting atom to the edge of the nanoparticle is shorter than the range of electrons inside the nanoparticle material. Thus, an optimum size for nanoparticles results in the emission of the greatest counts. In the present study, 180 nm-sized nanoparticles showed maximum detection efficiency.

3.1.4. *Study of the outcomes with different nanoparticles*

The outcomes of the interaction of HfO_2, LaF_3, ZnO, and ZrO_2 nanoparticles with each of the X-rays and gamma-rays tested increased the number of counts, with a similar trend to that of Gd_2O_3 nanoparticles. The sizes of the nanoparticles are mentioned in the methods section. As expected, the extent of variation in PHS varied with nanoparticles (Fig. 7). Variations in the number of electrons emitted and the energy profile of the electrons emitted are distinctly observed. Since the sizes of nanoparticles also vary, it is not easy to make a further inference.

Above variations are expected as these nanoparticles vary in composition (atomic number, Z), density, size and size distribution, purity, etc. Also, weight-based loading means fewer numbers and lesser surface area of denser nanoparticles. Further, since these nanoparticles vary in species, purity, and size, the further inference is challenging. Notably, the results in Fig. 7 affirm that the method can distinguish between the outcomes of the interaction of the same radiation with different nanoparticles (species/sizes) in terms of the number of electrons emitted and the energy profile of the electrons. This technique is direct, quick, and straightforward.

3.2. *Interaction of high-energy gamma-rays*

Gamma-rays from ^{22}Na, ^{137}Cs, and ^{60}Co are considered high-energy gamma-rays. The outcome of interactions of ^{137}Cs with Gd_2O_3 nanoparticles is shown in Fig. 8, while the extents of variation in the number of counts on interaction with high-energy gamma-rays are displayed in the histogram.

The enhancement of counts was insignificant when the high-energy gamma-rays interact with Gd_2O_3 nanoparticles. Results were the same for other nanoparticles tested. The greatest variations in counts for loadings between 1 mg and 200 mg of Gd_2O_3 nanoparticles were 1.1 and 0.8 times that for unloaded liquid scintillator, respectively. Unlike in Fig. 2 for low energy X-rays, the variation of the number of counts in Fig. 8 did not follow any trend for us to conclude the effectiveness of the addition of nanoparticles. The interaction efficiency of high-energy photons in a liquid scintillator does not considerably increase with the addition of nanoparticles. Thus, the addition of nanoparticles into the liquid scintillator has been ineffective in significantly enhancing the detection of high-energy photons.

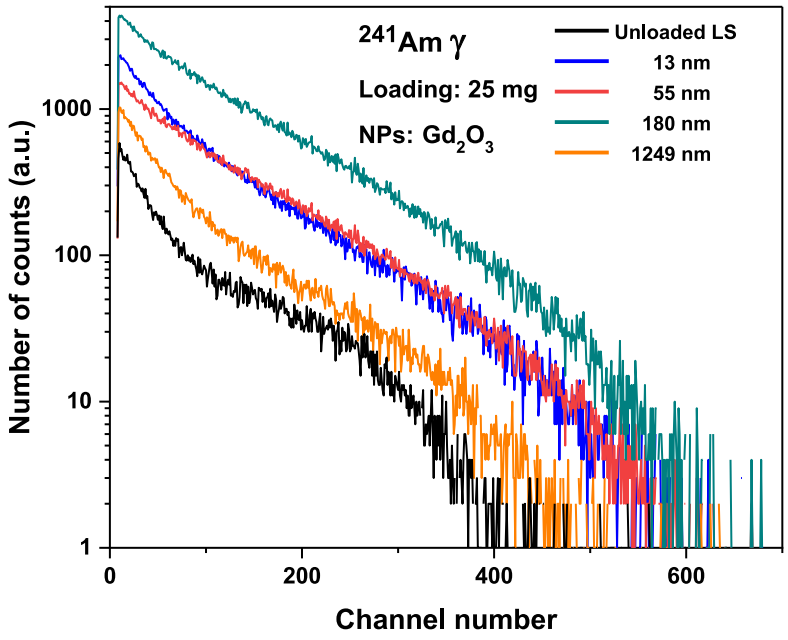

Fig. 6. The variations in PHS of gamma-rays from ^{241}Am with unloaded liquid scintillator upon loading Gd_2O_3 nanoparticles of different sizes.

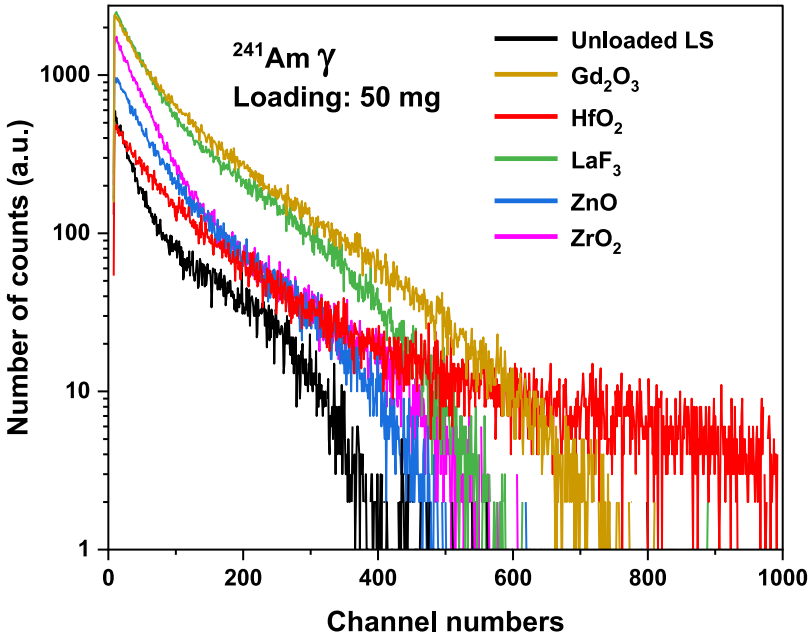

Fig. 7. The variations in PHS of gamma-rays from ^{241}Am with unloaded liquid scintillator upon loading different nanoparticles.

3.3. Novelty of the results and their impact

The present study contributes empirical results on the outcome of the interaction of X-rays or gamma-rays of energies beneficial in practical applications, as discussed below. The ability of the technique to benchmark the nanoparticles directly and quickly for the abundance and energy profile of the electrons they emit on irradiation with given photons and the existence of a range of energy of photons that undergo greater interaction with nanoparticles than the photons of other energies constitute new results.

The method and the results potentially impact three applications that anticipate the emission of electrons from the nanoparticles upon irradiation with X-rays or gamma-rays. The method developed here determines better-suited nanoparticles for the applications. The current studies for these applications involve multivariable, multistage experiments. For example, studies for NPRS involve variables such as the energy of photons, species, size, distribution, the retention time of nanoparticles administered into the tissues, and physical, chemical, and biological stages before the efficacy of the nanoparticles are determined [24,25]. There are contradicting results discussed and debated in the literature [24,32,33]. The researchers seek a mechanistic understanding of the processes. In view of this, the certainty achieved in the first of the process stages facilitates researchers to address other parameters and or subsequent stages. Based on the rationale introduced, for the development of fast-efficient-large-affordable gamma-ray detectors, nanoparticles of Gd_2O_3, HfO_2, ZrO_2 suit better. Results of the current study accord those in the literature, where encouraging results involving these nanoparticles are repeatedly reported [1,3,4,9,13,17,18,21] The optimum concentration of nanoparticles yielding better results is also reflected in these works. In the current setup, the concentration

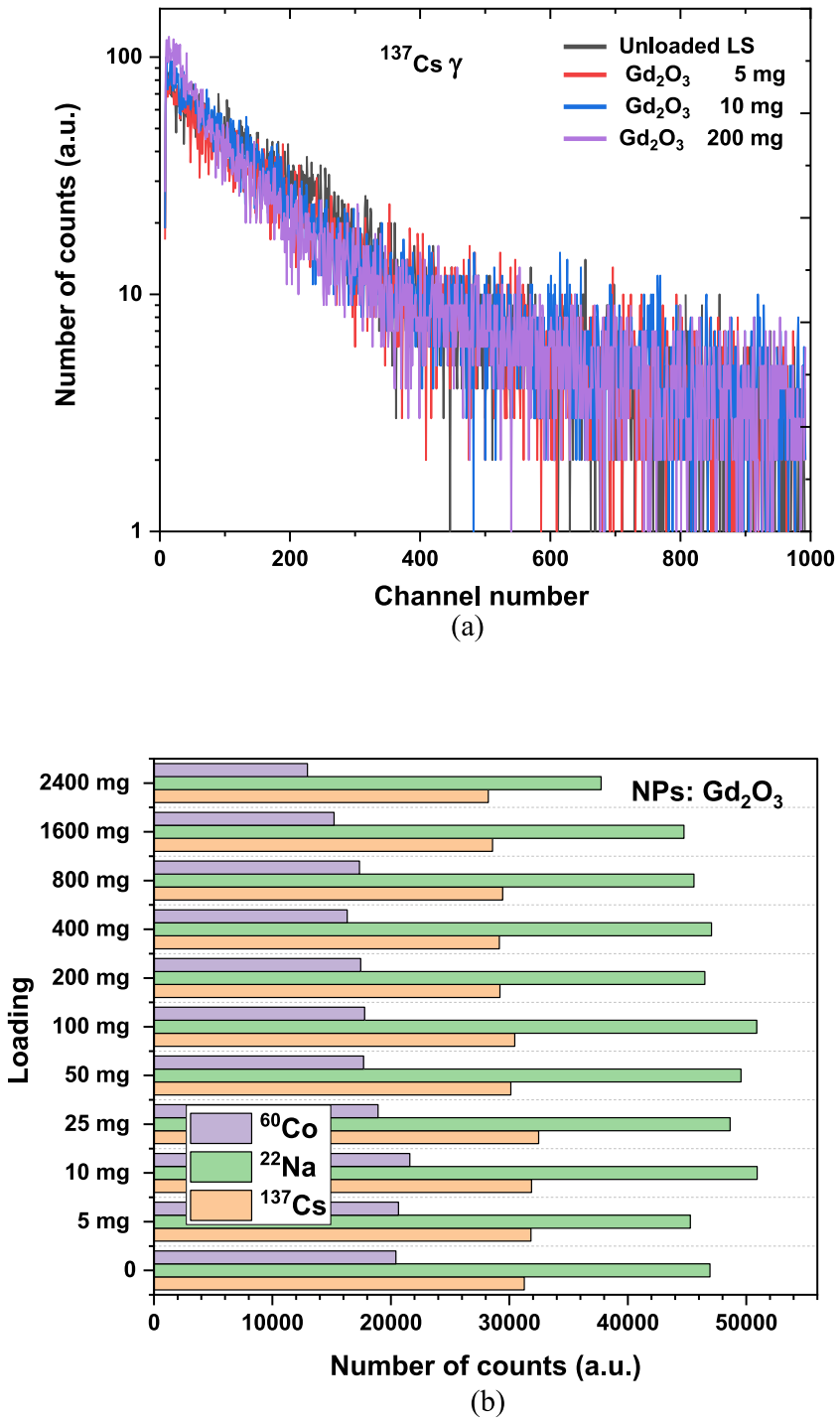

Fig. 8. (a) The variations in PHS of gamma-rays from ^{137}Cs with unloaded liquid scintillator upon loading Gd_2O_3 nanoparticles of 55 nm size (b) Histogram displaying the extent of enhancement of counts for high-energy gamma-rays from ^{137}Cs, ^{22}Na, and ^{60}Co.

achieved by loading 800 mg of Gd_2O_3 nanoparticles (Fig. 2) is found to be optimum. The process for realizing large detectors without developing the physical cracks between the nanoparticles and the host, as displayed in [22], can now involve these nanoparticles.

Nanoparticle radiosensitization is an approach targeting to enhance the efficacy of radiotherapy in cancer treatment. Per the widely followed hypothesis, the nanoparticles administered into the tumors interact more readily with the incoming radiations than the tumor materials to emit electrons into the tumor to cause chemical and biological effects to eradicate the tumor or inhibit its growth. This application appears far from field implementation despite intense research for nearly two decades. Responding to a few unanticipated results, researchers argue over the exact mechanism of radiosensitization [24,25,32,33]. Few studies have demonstrated radiosensitization with MeV X-rays [34–36]. Present results empirically establish that the electrons are not released efficiently by the nanoparticles when irradiated with MeV photons. The radiosensitization in such cases may be occurring through an alternate mechanism. The present results are significant for nanoparticle radiosensitization for an additional reason. The Z_{eff}, and density of the liquid scintillator are approximately the same as those of water,

the greatest constituent of biological tissues. Calibration of channel numbers for the energy of the electrons would quantitatively ascertain the energy profile of the electrons emitted. Empirical data on the range of electrons emitted from the nanoparticles into water enables clinicians to choose appropriate nanoparticle–gamma combinations to protect healthy cells surrounding a malignant tissue.

In developing Pb-free light-weight efficient radiation shields for radiation workers, space exploration and non-destructive inspection [12,28,37–39] nanoparticles are incorporated into conformable polymers. Nanoparticles interact and convert incoming gamma rays into electrons which are absorbed within the polymer. Though laboratory-scale shields are demonstrated by various studies [12,28,37–39], their upscaling is hindered by process-related challenges such as embrittlement, tear, crack, split [40,41]. Process-related issues are desirably resolved with better-suited nanoparticles. Further, the nanoparticles that emit less energetic electrons suit better since the high-energy electrons can generate Bremsstrahlung [12]. The present study ascertains that Gd_2O_3, LaF_3 nanoparticles suit better than HfO_2 nanoparticles as a dopant in polymers for developing such shields (Fig. 7).

The selection of nanoparticles for given applications relies on the outcome of the interaction of radiations with the nanoparticles. The results are highly repeatable, and the variations in the outcomes upon the change in species, size, loading of nanoparticles, and type & energy of the radiations are distinctly observable. Thus, the nanoparticle selection method is reliable. Further, the measurement system can be improved with two or three PMTs to ensure stability and make it suitable for distinguishing the number and energy of emitted electrons. The quantitative measurement of the energy profile of the electrons emitted is feasible once the channel numbers are calibrated. Researchers with a known source or calibrated detector for reference could easily accomplish it.

4. Conclusions

The study contributed an experimental technique that determines the outcome of the interaction of gamma-rays with the nanoparticles. The technique determines the outcomes directly and quickly. Low-energy gamma-rays such as those from ^{241}Am, ^{133}Ba interact with nanoparticles to cause the emission of electrons from the nanoparticles tested. There exists a range of X-rays and gamma-rays that undergo greater interaction with the nanoparticles than the photons of other energies. High energy gamma-rays such as those from ^{137}Cs transmit through the nanoparticles without much interaction. The technique can distinguish the number and energy profiles of electrons emitted from different nanoparticles upon irradiation with given gamma-rays. Further, the calibration of channel numbers enables the determination of the actual energy of the electrons emitted. The results help identify better-suited nanoparticles for a given application. With such test-selected nanoparticles, issues faced in subsequent steps or processes of practical applications can be addressed to quicken the field implementation of the applications.

CRediT authorship contribution statement

B.H.M. Darukesha: Conceptualization, Investigation, Methodology, Validation, Writing – original draft. **V. Radhakrishna:** Formal analysis, Methodology, Resources, Supervision, Writing – review & editing. **K. Rajanna:** Resources, Supervision, Writing – review & editing.

Declaration of competing interest

The authors declare that they have no known competing financial interests or personal relationships that could have appeared to influence the work reported in this paper.

Data availability

Data will be made available on request.

Acknowledgments

The authors thank Dr. Aruna S T of National Aerospace Laboratories (CSIR-NAL), Bengaluru, for providing several nanoparticles for the study and sintering the nanoparticles. They thank Dr. M M Nayak at CeNSE, IISc, and Dr. M Ravindra at RNSIT for their guidance and encouragement. Authors thank MNCF at IISc; Dr. Parthasarathi Bera at NAL; Dr. Sarat Kumar Dash at Indian Space Research Organisation (ISRO); Dr. SMM Kennedy at SSNCE, Kalavakkam for characterization of nanoparticles. BHMD acknowledges the discussions and instrumentation support from Shri Srikar Paavan Tadepalli and Shri Koushal Vadodariya at Space Astronomy Group, ISRO. Supervision of Smt. M A Lalitha Abraham, Radiation Safety Officer at ISRO, is regarded.

Funding

This research did not receive any specific grant from funding agencies in the public, commercial, or not-for-profit sectors.

References

[1] K. Kagami, et al., High-energy X-ray detection capabilities of Hf-loaded plastic scintillators synthesized by sol–gel method, J. Mater. Sci., Mater. Electron. 31 (2) (2020) 896–902, http://dx.doi.org/10.1007/s10854-019-02597-y.

[2] J. Ashcroft, Gamma counting of Iodine125 using a metal-loaded liquid scintillator, Anal. Biochem. 37 (1970) 268–275.

[3] Y. Sun, et al., High-energy X-ray detection by hafnium-doped organic–inorganic hybrid scintillators prepared by sol–gel method, Appl. Phys. Lett. 104 (17) (2014) http://dx.doi.org/10.1063/1.4875025.

[4] A. Sato, Fabrication of Hf × Si 1 2 × O 2 microparticle-loaded PVK- based plastic scintillators using the sol–gel method for high-energy X-ray detection at high counting rate, J. Mater. Sci., Mater. Electron. (2021) http://dx.doi.org/10.1007/s10854-021-07265-8.

[5] A. Magi, et al., Optimization of phosphor concentration of surface-modified Bi_2O_3 nanoparticle-loaded plastic scintillators for high-energy photon detection, J. Mater. Sci., Mater. Electron. 32 (6) (2021) 7987–7999, http://dx.doi.org/10.1007/s10854-021-05522-4.

[6] T.J. Hajagos, C. Liu, N.J. Cherepy, Q. Pei, High-Z sensitized plastic scintillators: A review, Adv. Mater. 30 (27) (2018) 1–13, http://dx.doi.org/10.1002/adma.201706956.

[7] J.H. Ely, E.R. Siciliano, R.T. Kouzes, Comparison of NaI(Tl) scintillators and high purity germanium for vehicle portal monitor applications, IEEE Nucl. Sci. Symp. Conf. Rec. 3 (C) (2004) 1584–1587, http://dx.doi.org/10.1109/nssmic.2004.1462543.

[8] S. Gundacker, et al., Experimental time resolution limits of modern SiPMs and TOF-PET detectors exploring different scintillators and Cherenkov emission, Phys. Med. Biol. 65 (2) (2020) http://dx.doi.org/10.1088/1361-6560/ab63b4.

[9] M. Gandini, et al., Efficient, fast and reabsorption-free perovskite nanocrystal-based sensitized plastic scintillators, Nat. Nanotechnol. 15 (6) (2020) 462–468, http://dx.doi.org/10.1038/s41565-020-0683-8.

[10] M.J. Willemink, M. Persson, A. Pourmorteza, N.J. Pelc, D. Fleischmann, Photon-counting CT: Technical principles and clinical prospects, Radiology 289 (2) (2018) 293–312, http://dx.doi.org/10.1148/radiol.2018172656.

[11] S. Kishimoto, M. Koshimizu, F. Hiyama, R. Haruki, F. Nishikido, Measurements of 73-keV X-ray time spectrum with avalanche-photodiode scintillation detector using bi2o3-nanoparticle-doped plastic scintillator, Nucl. Instrum. Methods Phys. Res. A 968 (April) (2020) 163908, http://dx.doi.org/10.1016/j.nima.2020.163908.

[12] S. Nambiar, Application of Nanomaterials for X-Ray Shielding and Dosimetry in Diagnostic Radiology, University of Waterloo, 2015.

[13] A. Toda, S. Kishimoto, X-ray detection capabilities of plastic scintillators incorporated with ZrO_2 Nanoparticles, IEEE Trans. Nucl. Sci. 67 (6) (2020) 983–987, http://dx.doi.org/10.1109/TNS.2020.2978240.

[14] M. Koshimizu, Composite scintillators based on polymers and inorganic nanoparticles, Funct. Mater. Lett. 13 (6) (2020) http://dx.doi.org/10.1142/S1793604720300030.

[15] S.M. Pellegrin, C. Whitney, C.G. Wilson, A multichannel nanoparticle scintillation microdevice with integrated waveguides for alpha, beta, gamma, X-ray, and neutron detection, J. Microelectromech. Syst. 19 (5) (2010) 1207–1214, http://dx.doi.org/10.1109/JMEMS.2010.2067435.

[16] J. Medalia, Crs report for congress detection of nuclear weapons and materials: Science, technologies, observations jonathan medalia specialist in nuclear weapons policy, 2010.
[17] Y. Araya, M. Koshimizu, R. Haruki, F. Nishikido, S. Kishimoto, K. Asai, Enhanced detection efficiency of plastic scintillators upon incorporation of zirconia nanoparticles, Sensors Mater. 27 (3) (2015) 255–261, http://dx.doi.org/10.18494/sam.2015.1090.
[18] W. Cai, et al., Synthesis of bulk-size transparent gadolinium oxide-polymer nanocomposites for gamma ray spectroscopy, J. Mater. Chem. C 1 (10) (2013) 1970–1976, http://dx.doi.org/10.1039/c2tc00245k.
[19] M. Fernández-García, J.A. Rodriguez, Metal oxide nanoparticles, in: Encyclopedia of Inorganic and Bioinorganic Chemistry, John Wiley & Sons, Ltd, 2011.
[20] F. Hiyama, et al., X-ray detection properties of plastic scintillators containing surface-modified Bi_2O_3 nanoparticles, Japan. J. Appl. Phys. 57 (5) (2018) http://dx.doi.org/10.7567/JJAP.57.052203.
[21] K. Inoue, et al., Fast scintillation X-ray detector using proportional-mode Si-APD and a HfO_2-nanoparticle-doped plastic scintillator, IEEE Trans. Nucl. Sci. 65 (4) (2018) 1012–1017, http://dx.doi.org/10.1109/TNS.2018.2807801.
[22] M.D. Hammig, Nanoscale methods to enhance the detection of ionizing radiation, in: M. Nenoi (Ed.), Current Topics in Ionizing Radiation Research, InTech, 2012.
[23] R. Casta, et al., Electronic emission of radio-sensitizing gold nanoparticles under X-ray irradiation: Experiment and simulations, J. Nanopart. Res. 16 (4) (2014) 1–10, http://dx.doi.org/10.1007/s11051-014-2348-8.
[24] E. Brun, C. Sicard-Roselli, Actual questions raised by nanoparticle radiosensitization, Radiat. Phys. Chem. 128 (2016) 134–142, http://dx.doi.org/10.1016/j.radphyschem.2016.05.024.
[25] J. Schuemann, et al., Roadmap for metal nanoparticles in radiation therapy: Current status, translational challenges, and future directions, Phys. Med. Biol. 65 (21) (2020) http://dx.doi.org/10.1088/1361-6560/ab9159.
[26] M. Faraday, Experimental relations of gold (and other metals) to light, Philos. Trans. R. Soc. 147 (1857) 145–181, [Online]. Available: http://rstl.royalsocietypublishing.org/cgi/doi/10.1098/rstl.1857.0011.
[27] S. Nambiar, E.K. Osei, J.T.W. Yeow, Effects of particle size on X-ray transmission characteristics of PDMS/Ag nano- and microcomposites, in: IEEE-NANO 2015-15th Int. Conf. Nanotechnol., 2015, pp. 1358–1361, http://dx.doi.org/10.1109/NANO.2015.7388888.
[28] Q. Li others, Research on X-ray shielding performance of wearable Bi/Ce-natural leather composite materials, J. Hazard. Mater. 398 (2020) http://dx.doi.org/10.1016/j.jhazmat.2020.122943.
[29] M.F. L'Annunziata, A. Tarancón, H. Bagán, J.F. García, Liquid Scintillation Analysis: Principles and Practice, Vol. 1, 2020.
[30] M.J.E. Kessler, M.J. Kessler, Liquid scintillation analysis, waltham, 2015, [Online]. Available: Www.perkinelmer.com/liquid-scintillation.
[31] R. Broda, P. Cassette, K. Kossert, Radionuclide metrology using liquid scintillation counting, Metrologia 44 (4) (2007) http://dx.doi.org/10.1088/0026-1394/44/4/S06.
[32] K.T. Butterworth, S.J. McMahon, F.J. Currell, K.M. Prise, Physical basis and biological mechanisms of gold nanoparticle radiosensitization, Nanoscale 4 (16) (2012) 4830–4838, http://dx.doi.org/10.1039/c2nr31227a.
[33] S. Penninckx, A.C. Heuskin, C. Michiels, S. Lucas, Thioredoxin reductase activity predicts gold nanoparticle radiosensitization effect, Nanomaterials 9 (2) (2019) 1–13, http://dx.doi.org/10.3390/nano9020295.
[34] F. Geng, et al., Thio-glucose bound gold nanoparticles enhance radio-cytotoxic targeting of ovarian cancer, Nanotechnology 22 (28) (2011) 285101, http://dx.doi.org/10.1088/0957-4484/22/28/285101.
[35] D.B. Chithrani, et al., Gold nanoparticles as radiation sensitizers in cancer therapy, Radiat. Res. 173 (6) (2010) 719–728, http://dx.doi.org/10.1667/RR1984.1.
[36] M. Luchette, H. Korideck, M. Makrigiorgos, O. Tillement, R. Berbeco, Radiation dose enhancement of gadolinium-based aguix nanoparticles on HeLa cells, nanomedicine nanotechnology, Biol. Med. 10 (8) (2014) 1751–1755, http://dx.doi.org/10.1016/j.nano.2014.06.004.
[37] R. Li, Y. Gu, Y. Wang, Z. Yang, M. Li, Z. Zhang, Effect of particle size on gamma radiation shielding property of gadolinium oxide dispersed epoxy resin matrix composite, Mater. Res. Express 4 (3) (2017) aa6651, http://dx.doi.org/10.1088/2053-1591/aa6651.
[38] H. Alavian, A. Samie, H. Tavakoli-Anbaran, Experimental and Monte Carlo investigations of gamma ray transmission and buildup factors for inorganic nanoparticle/epoxy composites, Radiat. Phys. Chem. 174 (2019) (2020) 108960, http://dx.doi.org/10.1016/j.radphyschem.2020.108960.
[39] M.C. Molina Higgins, N.A. Radcliffe, M. Toro-González, J.V. Rojas, Gamma ray attenuation of hafnium dioxide- and tungsten trioxide-epoxy resin composites, J. Radioanal. Nucl. Chem. 322 (2) (2019) 707–716, http://dx.doi.org/10.1007/s10967-019-06714-3.
[40] Y. Wang others, Advanced X-ray shielding materials enabled by the coordination of well-dispersed high atomic number elements in natural leather, ACS Appl. Mater. Interfaces 12 (17) (2020) 19916–19926, http://dx.doi.org/10.1021/acsami.0c01663.
[41] J.P. McCaffrey, H. Shen, B. Downton, E. Mainegra-Hing, Radiation attenuation by lead and nonlead materials used in radiation shielding garments, Med. Phys. 34 (2) (2007) 530–537, http://dx.doi.org/10.1118/1.2426404.

ISSN 1066-3622, Radiochemistry, 2022, Vol. 64, No. 3, pp. 393–398. © Pleiades Publishing, Inc., 2022.

Enhancing the Gamma-Counting Efficiency of a Liquid Scintillation Cocktail by Incorporation of Nanoparticles

B. H. M. Darukesha[a,b,*], V. Radhakrishna[a], and K. Rajanna[b]

[a] *U R Rao Satellite Centre, Indian Space Research Organization, Bengaluru, 560017 India*
[b] *Department of Instrumentation and Applied Physics, Indian Institute of Science, Bengaluru, 560012 India*
**e-mail: darukesha@gmail.com*

Received December 24, 2021; revised March 14, 2022; accepted March 21, 2022

Abstract—The scintillation counts in a conventional liquid scintillation cocktail Aqualight + Ultra Low Level™ for γ-rays from ^{241}Am are enhanced by a factor of 3.4 by incorporating Gd_2O_3 nanoparticles. The nanoparticles efficiently stop and convert the γ-rays into electrons, which cause additional scintillation in the cocktail. Results resolve a decades-old ambiguity by establishing that the enhancement is due only to the interaction of γ-rays with the nanoparticles. Efficient counting of γ-rays enables γ-assays within standard liquid scintillation counters.

Keywords: liquid scintillation counters, scintillation cocktails, radioimmunoassay, high-*Z* nanoparticles, ^{125}I gamma counting

DOI: 10.1134/S1066362222030171

INTRODUCTION

Radioassay allows quantitative analysis of tiny concentrations of substances using radionuclides as tracers [1]. It is used to detect and quantify biological substances like antibodies, hormones, or contaminants in water or the environment. In general, the analyte and radionuclides are mixed and processed so that the level of radioactivity in the vial corresponds to the concentration of the analyte [1]. The level of radioactivity of the mixture is measured using a suitable instrument. Radionuclide techniques offer better sensitivity than other analytical methods do, because a tiny mass of radionuclides is enough to generate considerable radioactivity [2]. For example, 6.1 ng of ^{14}C or 1.6 pg of ^{125}I correspond to 1 kBq of activity [2], rendering their detectability.

Radioassays use β- and γ-emitting radionuclides for different applications. Among β-emitters, ^{3}H, ^{14}C, and ^{32}P are popular because of their lower/optimum energies. β-Assays are performed in liquid scintillation counters (LSCs), which have become standard instruments. LSCs accommodate vials that contain a liquid scintillation cocktail (Fig. 1) mixed with an analyte. As β-rays scintillate the liquid, a photomultiplier tube placed next to the vial counts the scintillation pulses. Cocktails detect the β-rays from these emitters with 10 to 100% efficiency [3]. The counting efficiency is better for the average decay energies of over 100 keV [3]. The LSCs are simple, automated, standardized, and affordable [4, 5].

While β-assays serve most purposes, γ-assays are uniquely necessary for some applications, such as steroid receptor assays [4, 6]. The studies related to biological uptake and transport phenomena demand the labeling of certain substances with both β- and γ-emitting radionuclides to ascertain the permeability of the substance into different parts of the body [7]. γ-Emitters such as ^{125}I, ^{55}Fe, and ^{57}Co are popular radionuclides due to their lower energies and shorter half-life [8, 9]. However, the standard LSCs cannot count the γ-rays because of low stopping power of constituent C, H, N, O and the limited volume of liquid scintillation cocktails used. Most γ-rays escape from the LSC vials without interaction. Therefore, γ-assays require a different instrument, γ-ray well counter, which employs inorganic scintillators like NaI(Tl) [10]. These counters have a geometric well bound by inorganic scintillators that stop the γ-rays. A photomultiplier tube is attached to the scintillator to count the scintillations. Well counters suffer from hygroscopicity and are cumbersome. Also, it is preferable to employ a single, standard instrument for both β- and γ-assays [11]. It would be feasible by en-

hancing the γ-counting efficiency of the cocktails so that the γ-rays be stopped within the LSC vials either fully or proportionately. Further, maximizing the scintillation counts within the detection medium improves the detection efficiency.

One approach to enhance the γ-counting efficiency of LSC cocktails is to load high-*Z* materials into the cocktails to enhance the stopping power of the cocktail. Efforts have been underway since the 1960s to accomplish this goal. Ashcroft mixed a tetrabutyltin solution into the cocktail and achieved 51% counting efficiency for γ-rays from ^{125}I, against 48% with NaI(Tl) detector [4]. The interaction of γ-rays with the dopants caused an increase in counts. However, the enhancement achieved by Ashcroft was contested to be not necessarily due to the interaction of γ-rays with the loaded materials but also due to better counting of Auger or conversion electrons emitted by ^{125}I [12]. The argument has remained unsettled for over five decades.

Nevertheless, Ashcroft had innovatively split the LSC vial into two portions (Fig. 1). The outer portion was loaded with a tin-loaded liquid scintillator, and the inner one, with the assay sample. Verslujis further improvised Ashcroft's design to accommodate a larger volume of the metal-loaded liquid scintillator (Fig. 1) [13]

In 2006, Carles and Malonds recognized that the cocktails possessing heavy elements enhance the counting efficiency for the photons [15]. For X-rays from ^{55}Fe, cocktail (Ultima Gold Plus™) possessing 1.4% P and 0.2% S in addition to C, H, N, and O yielded higher counting efficiency than the cocktail (Insta Gel™) possessing only C, H, N, and O did. Recently, Shoji et al. loaded triethyl phosphate into a commercial cocktail and demonstrated higher γ-counting efficiency for the loaded cocktail compared to its unloaded counterpart [14]. Despite these efforts, the goal of efficiently counting γ-rays within the standard LSCs remains a challenge. Though alternative instruments such as accelerated mass spectrographs are used for radioassays in archaeology, geology, food industry, and environment, radioimmunoassays for biomedical applications rely on LSCs and well counters [7, 10].

Nanoscience and nanotechnology offer novel possibilities for readdressing the long-standing challenges. Literature finds that incorporating high-*Z* material nanoparticles such as Gd_2O_3, ZrO_2, and Bi_2O_3 into the plastic scintillators enhances the gamma detection efficiency of the host [16, 17]. The objective of this study is to implement the approach of loading high-*Z* nanoparticles for enhancing the scintillation counts in conventional liquid scintillator cocktails. The present study used readily available ^{241}Am γ-source.

EXPERIMENTAL

Gd_2O_3 nanoparticles were sourced from Nanoshel, the United States. Nanoparticles were 99.9% pure as characterized by energy-dispersive X-ray spectroscopy using Oxford ESD system model INCA Pentafet attached to Carl Zeiss SEM model EVO 50. The size of the nanoparticles was determined by dynamic light scattering using NanoBrook ZetaPALS (90°, 658 nm, 1 min, 25°C). The measurements were triplicated. The average size of the nanoparticles was 55 ± 0.8 nm.

The crystalline phase of the nanoparticles was analyzed with an X-ray diffraction (XRD) system (Rigaku SmartLab) using CuK_α X-rays in a 2θ–θ setup. The crystallite grain size of the nanoparticles, calculated from the Debye–Scherrer equation using powder X-ray analysis software (Rigaku SmartLab Studio II), was 36 nm. Figure 2 shows a transmission electron microscopic image of the nanoparticles obtained with an FEI-Titan Themis 300 kV microscope.

The internal photoluminescence quantum yield (PLQY) of Gd_2O_3 nanoparticles was determined with a Hitachi F7000 spectrophotometer, and the external PLQY was estimated. The internal and external PLQYs were 12.36 and 13.86%, respectively.

The study used a Hidex Oy Triathler liquid scintillation counter thanks to brief access provided by the distributor. Hidex-supplied Aqualight+ Ultra Low Level™ cocktail was used as the scintillant. 20- and 7-mL scintillation grade Pyrex glass vials sourced from Meridian Biotechnologies were used in the study. Their respective dimensions were 28 mm (diameter) × 61 mm (length) and 17 mm × 60 mm. ^{241}Am was utilized as a γ-source. The trials were also conducted with CeO_2 nanoparticles (99.9%, 38.5 ± 1.7 nm). Both nanoparticles were tried with a toluene-based cocktail (srlchem.com, product #46069; 6 g of 2,5-diphenyloxazole [PPO] and 0.2 g of 1,4-bis(5-phenyloxazol-2-yl) benzene [POPOP] in 1 L of toluene). The results were similar in trend.

The setup is sketched in Fig. 1. The γ-ray source was wrapped in a 0.1 mm thick aluminum sheet before placing the source into the inner vial. The source was positioned about three fourth down the inner vial. The

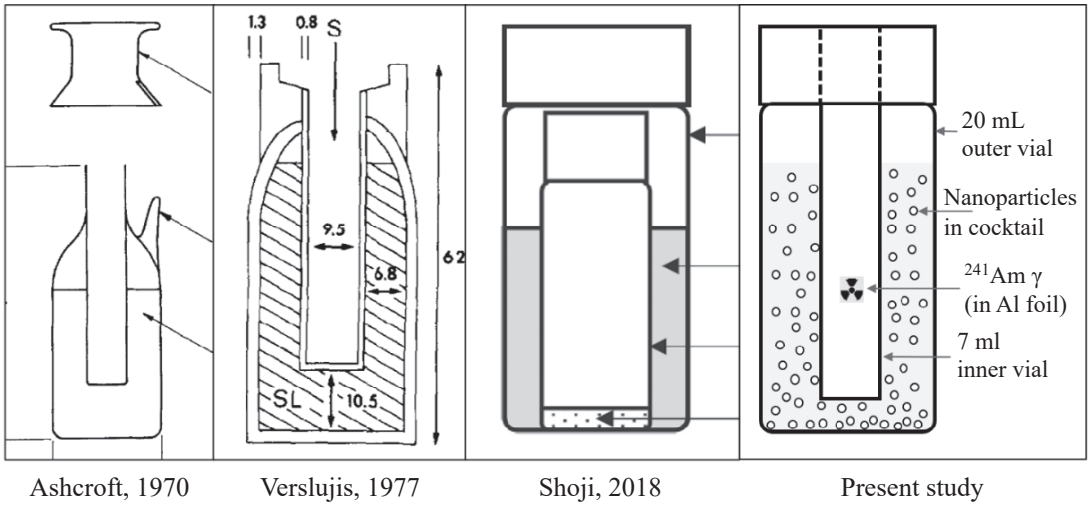

Fig. 1. Innovative modifications of vials used in liquid scintillation counters to stop and count γ-rays within the vials. Tin-loaded liquid scintillator was accommodated in the outer part of the vial (Ashcroft), the volume of the outer part of the vial was increased (Verslujis), and triethyl phosphate was loaded into the liquid scintillator (Shoji). Nanoparticles of high-*Z* materials are directly loaded into the liquid scintillator (present study). The first three images are reproduced with permission [4, 13, 14].

wrapping provided the positional stability for the source and attenuated α-radiations emitted by the source. The inner vial was glued to the cap of the outer vial. The background was as low as 0.1 cps. The vial was positioned inside the measurement chamber using a plastic scintillation adapter. All measurements used a full energy scale. Pulse height spectra were acquired for 60 s.

The pulse height spectrum (PHS) for a neat (unloaded) cocktail was obtained. This PHS serves as the control. The vial was demounted and mounted back with a given quantity of Gd_2O_3 nanoparticles loaded into the cocktail. Weight-based loading ensured better control over the increment of loading. The mixture was thoroughly shaken for about 30 s to ensure proper dispersion of the nanoparticles. PHS for nanoparticle-loaded liquid scintillator was obtained for different loadings under identical conditions.

RESULTS

Figure 3a displays the pulse height spectra (PHS) obtained for unloaded and nanoparticle-loaded cocktails for ^{241}Am. The number of counts in the PHS increased with the loading of nanoparticles. Fresh counts appeared at higher channels than channel 200. These variations were observed for each loading till 1000 mg. Further loading of nanoparticles reduced the counts from that of the previous. Figure 3b displays the histogram of total counts in PHS. The greatest increase in counts was 3.4 times that of the unloaded liquid scintillator.

DISCUSSION

The pulse height spectrum (PHS) for an unloaded cocktail (Fig. 3a) is characteristic, and it serves as the control. Upon loading the nanoparticles, the incoming

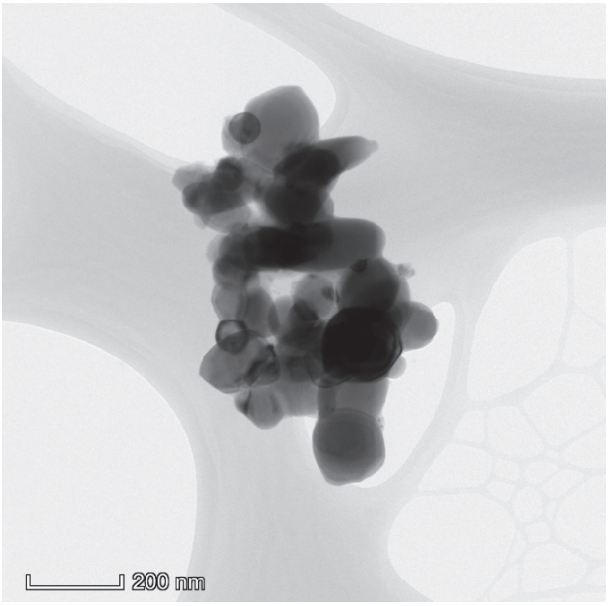

Fig. 2. A high-resolution transmission electron micrograph of Gd_2O_3 nanoparticles.

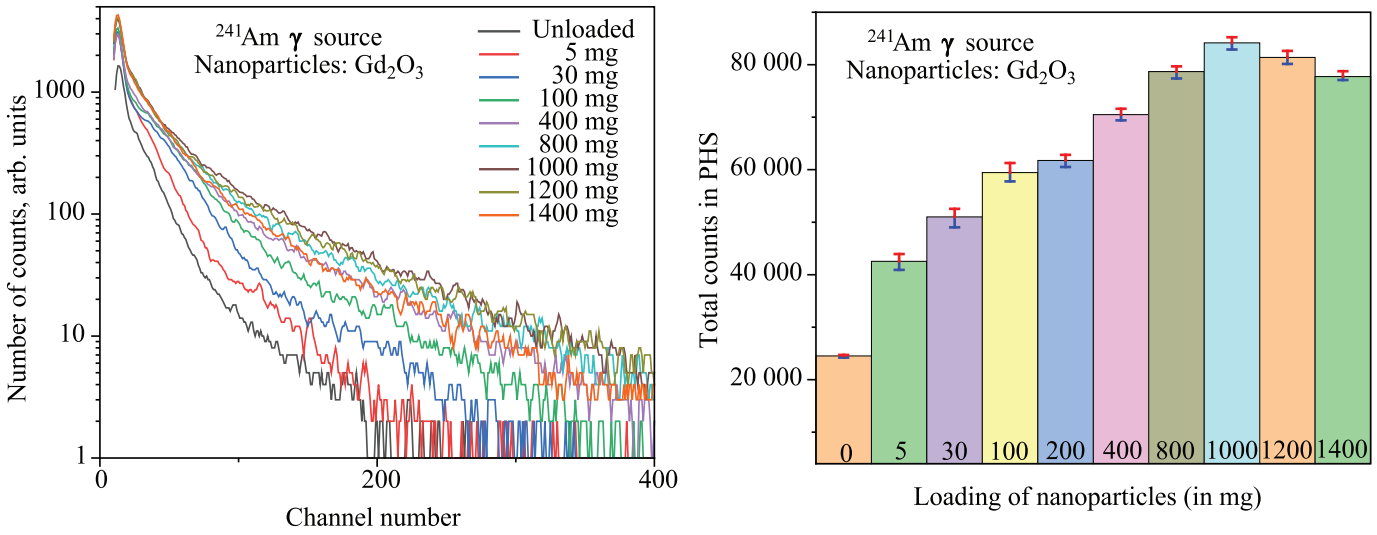

Fig. 3. (a) Variations in pulse height spectrum for unloaded liquid scintillator for ^{241}Am γ-rays upon loading different quantities of nanoparticles; (b) variation in the counts at different nanoparticle loadings. The median of triplicate readings is plotted.

γ-rays interact with the nanoparticles, causing the emission of electrons from the nanoparticles that scintillate the liquid. The appearance of counts beyond channel 200 in Fig. 3a affirms the emission of electrons from the nanoparticles. The electrons (photoelectrons or Compton-scattered electrons) emitted from an atom inside the nanoparticle lose part of their energy to other atoms along the track. Thus, photoelectrons lose their characteristic feature and strike the cocktail with all possible energies. Further, the exiting electrons undergo absorption or scattering on other nanoparticles or walls of the container, as illustrated in [18]. The same is true for the scintillation photons. Down-conversion of electron energy, thus, yields relatively large counts at lower channels.

Increased loading of nanoparticles increases the probability of interaction. However, it also increases the probability of absorption or scattering of electrons and/or scintillation photons by the nanoparticles. Increased loading increases the counts until the probability of interaction overweighs the rest. Beyond the optimum loading, however, the counts decrease relative to the previous loading. The counts, nonetheless, remained greater than those in the PHS for unloaded liquid scintillator till a greater loading that we tested.

Our results concur with those in the literature where loading of heavy elements enhanced the γ-counting efficiency of the cocktails. Whereas in previous studies [4, 14, 19] high-*Z* materials were loaded as organometallic ligands, in the present study they are loaded as nanomaterials, commencing a novel approach. The use of ^{241}Am resolves an apprehension expressed five decades ago. In 1970, Ashcroft demonstrated enhanced counting efficiency for ^{125}I to 51% [4]. In 1976, Horrocks demonstrated a counting efficiency of 76% for ^{125}I even in neat (unloaded) cocktail and raised merited apprehension that enhancement achieved by Ashcroft is due to better counting of Auger or conversion electrons emitted by ^{125}I [12]. The uncertainty remained unresolved till now. As Auger or conversion electrons are not emitted from ^{241}Am, the present results establish that the enhancement is due only to the interaction of γ-rays with the high-*Z* matter unambiguously. The contribution from the photoluminescence from Gd_2O_3 nanoparticles (~14%) is negligible compared to the enhancement of around 340%.

Compared to the atom loaded in the previous study, the nanoparticles improve the interaction probability. Also, the current approach of direct loading of nanoparticles is quicker and easier than loading high-*Z* materials through organometallic ligands. Experience shows that, while a portion of nanoparticles precipitates, the rest stays suspended. The nanoparticles suspended inside the scintillant interact with the γ-rays. The suspended portion continues to stay suspended for long enough time for the experiment. The variations in total counts were within 1% for 10 min of acquisition. The procedure and conditions were maintained identical across the experiments. The present study proposed and implemented the approach using a ^{241}Am γ-source. We would consider

^{125}I γ-source in further studies. Since the γ-rays from these sources possess lower energies than those from ^{241}Am, the probability of interaction of γ-rays with the given nanoparticles would be encouragingly better.

Further studies may deal with the utility of other nanoparticles of other species, size, and the extent of their loading for efficient counting of γ-rays from ^{125}I, ^{55}Fe, ^{57}Co, etc. The approach can be adapted for enhancing the efficiency and thus sensitivity of β-assays also. The nanoparticles would interact with the β-rays and emit electrons, as they do in a scanning electron microscope, and thus increase the number of counts for the same input. The sensitivity thus enhanced would benefit the assays involving tinier concentrations and flux-starving measurements. For routine usage, the cocktail suppliers can disperse the nanoparticles into the scintillant and ensure the reproducible preparation of samples. Inevitable variations in physical properties of nanoparticles synthesized in batches can be addressed by providing calibration curves for a batch of cocktails. Direct addition of nanoparticles suffices unless the selected nanoparticles chemically interact with the cocktail, in which case a surfactant may be used, and attenuation of electrons by the surfactant is accounted.

CONCLUSIONS

The concept of enhancing the number of scintillation counts in a conventional cocktail by incorporating nanoparticles of high-*Z* materials is proposed and implemented. Optimum loading of nanoparticles returns the greatest enhancement. It is established that the enhancement of scintillation counts upon loading high-*Z* materials into the liquid scintillators is due genuinely to the interaction of γ-rays with the high-*Z* matter, thus resolving a decades-old ambiguity. Further studies can explore the nanoparticles of other species and sizes for efficient counting of γ-rays from standard radionuclides like ^{125}I, ^{55}Fe, and ^{57}Co for γ-assays.

ACKNOWLEDGMENTS

Authors thank Noki Technologies, Hyderabad, India, for offering the liquid scintillation counter and the cocktail. The technical expertise of Shri Varun Kashyap is highly regarded. They thank Dr. M.M. Nayak and Dr. M. Ravindra for valuable discussions. They also thank MNCF at IISc and Dr. Sarat Kumar Dash at Indian Space Research Organisation (ISRO) for characterizing the nanoparticles.

FUNDING

This research did not receive any specific grant or funding.

CONFLICT OF INTEREST

The authors declare that they have no conflict of interest.

REFERENCES

1. Chase, G.D., *Liq. Scintillation Counting, Recent Applications and Development,* Peng, C.-T., Horrocks, D.L., and Alpen, E.L., Eds., Academic, 1980, vol. II, p. 489.
2. Tölgyessy, J. and Harangozó, M., *Encyclopedia of Analytical Science,* Worsfold, P., Townshend, A., and Poole, C., Eds., Elsevier, 2005, 2nd ed., p. 79. https://doi.org/10.1016/B0-12-369397-7/00526-4
3. L'Annunziata, M.F., Tarancón, A., Bagán, H., and García, J.F., *Liquid Scintillation Analysis: Principles and Practice,* L'Annunziata, M.F., Ed., Academic, 2020, vol. 1, p. 575. https://doi.org/10.1016/B978-0-12-814397-1.00006-6
4. Ashcroft, J., *Anal. Biochem.,* 1970, vol. 37, no. 2, p. 268.
5. LSABooklet_012129_01.pdf, Kessler, M.J.E., Ed., https://www.perkinelmer.co.jp/Portals/0/resource/products_ls/ls_cocktails/pdf/LSABooklet_012129_01.
6. L'Annunziata, M.F., *Radiation Physics and Radionuclide Decay,* Elsevier, 2012, 3rd ed. https://doi.org/10.1016/B978-0-12-384873-4.00001-3
7. Akanuma, S., Ohtsuki, S., Doi, Y., Tachikawa, M., Ito, S., Hori, S., Asashima, T., Hashimoto, T., Yamada, K., Ueda, K., Iwatsubo, T., and Terasaki, T., *Neurochem. Int.,* 2008, vol. 52, no. 6, pp. 956–961. https://doi.org/10.1016/j.neuint.2007.12.002
8. Broda, R., Cassette, P., and Kossert, K., *Metrologia,* 2007, vol. 44, no. 4, p. S36. https://doi.org/10.1088/0026-1394/44/4/S06
9. Wilde, C. and Ottewell, D., *Ann. Clin. Biochem.,* 1980, vol. 17, no. 1, p. 1. https://doi.org/s10.1177/000456328001700101
10. Costa, O.L. da, Souza, D.C.B. de, Castanho, F.G., Feher, A., Moura, J.A., Souza, C.D., Oliveira, H.B., Máduar, M.F., Zeituni, C.A., and Rostelato, M.E.C.M., *Appl. Radiat. Isot.,* 2021, vol. 169, ID 109568. https://doi.org/10.1016/j.apradiso.2020.109568
11. Herscowitz, H.B. and McKillip, T.W., *J. Immunol. Meth.,* 1974, vol. 4, no. 2, p. 253.

https://doi.org/10.1016/0022-1759(74)90068-4

12. Horrocks, D.L., *Nucl. Instrum. Meth.,* 1976, vol. 133, no. 2, p. 293.
13. Versluijs, F., *Anal. Biochem.,* 1977, vol. 80, no. 1, p. 249, https://doi.org/10.1016/0003-2697(77)90643-1
14. Shoji, M., Aso, T., Hara, M., Benii, R., Kato, Y., Furusawa, T., and Yoshimura, T., *Appl. Radiat. Isot.,* 2018, vol. 139, p. 131. https://doi.org/10.1016/j.apradiso.2018.04.038
15. Carles, A.G. and Malonda, A.G., *Appl. Radiat. Isot.,* 2006, vol. 64, nos. 10–11, p. 1515. https://doi.org/10.1016/j.apradiso.2006.02.066
16. Hajagos, T.J., Liu, C., Cherepy, N.J., and Pei, Q., *Adv. Mater.,* 2018, vol. 30, no. 27, p. 1. https://doi.org/10.1002/adma.201706956
17. Koshimizu, M., *Funct. Mater. Lett.,* 2020, vol. 13, no. 6, article 2030003. https://doi.org/10.1142/S1793604720300030
18. Tarancón, A., Bagán, H., and García, J.F., *J. Radioanal. Nucl. Chem.,* 2017, vol. 314, no. 2, p. 543. https://doi.org/10.1007/s10967-017-5494-5
19. Bransome, E.D., Jr., *Semin. Nucl. Med.,* 1973, vol. 3, no. 4, p. 389.